SCALABLE AND DURABLE MACRO-MICRO-NANOMANUFACTURING OF FUNCTIONAL INTERFACES AND DEVICES

BY

MUHAMMAD JAHIDUL HOQUE

DISSERTATION

Submitted in partial fulfillment of the requirements
for the degree of Doctor of Philosophy in Mechanical Engineering
in the Graduate College of the
University of Illinois Urbana-Champaign, 2022

Urbana, Illinois

Doctoral Committee:

Associate Professor Nenad Miljkovic, Chair and Director of Research
Professor Anthony Jacobi
Professor Placid Ferreira
Assistant Professor Marianne Alleyne

ABSTRACT

Around 70% of global electricity is produced from steam-cycle power plants. Utilizing a hydrophobic condenser surface within the steam cycle has potential to enhance the overall cycle efficiency by up to 2%, demonstrating a profound impact on the global energy landscape as well as on carbon footprint. Moreover, past research has shown that mixed-liquid repellency (hybrid wettability) of condenser surface can significantly enhance the condenser performance. However, main challenges are scalable fabrication of mixed hydrophobicity or hybrid/ biphilic surfaces, and lack of durability of the hydrophobic promoters. Also, traditional hydrophobic chemistry is not suitable in many applications (organic Rankine cycles) where low surface tension liquids are used, alternatives are proposed with limited focus on durability improvement. Here, we develop a simple, scalable, rapid stamping method for hybrid surface fabrication which is substrate and coating independent. From fundamental physics-based understanding of hydrophobic layer degradation mechanism, we develop a robust hydrophobic coating for steam condensation, which has outstanding mechanical and thermal properties that enable durability in moist (> 3 years condensation), abrasive (> 5000 cycles), and high temperature (> 300°C) environments. For condenser surface where low surface tension liquids are used, we demonstrate design methods and longevity statistics and develop fundamental design guidelines for creating durable hydrophobic surfaces. In contrast to generation, the electric energy from power plant is used in all electronic devices and rapid miniaturization of electronics had led to significant growth in the power density of modern devices and systems, which demands effective thermal management to avoid unwanted failure due to overheating. Here, by adapting device level macro-machining and additive manufacturing we develop advanced thermal solutions for both air and liquid cooled electronics for different mobile applications. Our developed air cooled (modular heat sink) and liquid cooled (polymer-metal hybrid cold plate) based advanced thermal solutions offer system level volumetric and gravimetric power density enhancement, also improve the system reliability by enabling isothermalization of devices. The techniques and insights presented here will open new avenue of research to adapt advanced multiscale manufacturing to improve the performance of different energy systems.

To my parents,

Abdul Aziz Bhuiyan

&

Dilruba Begum

ACKNOWLEDGMENTS

I want to start with thanking my advisor, Prof. Nenad Miljkovic. Nenad, thank you so much for everything! You made my PhD journey the utmost satisfying time in my life so far. Thank you for guiding me with kindness, supports, patience, promptness, scientific rigor, creative ideas, and generosity. Thank you for believing me and allowing me to pursue my own ideas and research directions while keeping me on track. You inspired me by being a great example of someone with an innate passion for his work, which I have strived to emulate and will continue to do so in my life. You have always supported me whatever I did, and have guided me well throughout my Ph.D. I could not have asked for a better adviser!

I would also like to thank my thesis committee members Professor Anthony M. Jacobi, Professor Placid Ferreira, and Professor Marianne Alleyne for providing very insightful comments and guidance that have greatly improved the quality of my thesis and deepened my understanding of the content. I thank Professor Jacobi for helping me to connect the dots between the fundamental scientific development and societal impact in the long run. I would like to thank Professor Ferreira for his insights on different aspects of advanced manufacturing to solve challenging energy problems. I would like to thank Professor Alleyne for insightful directions to integrate the nature-inspired design to real life engineering problem solutions.

The major share of my PhD lesson came from collaborators at UIUC, other schools and industries. I have received significant help from my lab mates in the Energy Transport Research Lab Laboratory (ETRL) and I want to thank all of them. Four former ETRL postdocs Dr. Xiao Yan, Dr. Longnan Li, Dr. Jiaqi Li and Dr. Soumyadip Sett showed me great supports both in

research and personal life throughout the past few years. I especially thank Dr. Xiao Yan, who was my officemate in DCL, UIUC. Xiao, I enjoyed and will miss our conversation about new ideas while we were sitting in the office or drinking tea or having lunch in the restaurants on green street. Xiao, thank you for your guidance and collaboration. You helped me to broaden my research focus and connect the dots. I also like to thank former ETRL PhD students Dr. Junho Oh, Dr. Hyeongyun Cha and Dr. Moonkyung Kim who showed me the fascinating world of fluids and surface science when I started working in the lab. And I have always enjoyed the friendship and high-quality collaborations that I had with my peers at ETRL, especially with Dr. Alperen Günay, Dr. Jingcheng Ma, Kazi Fazle Rabbi, Ho Chan Chang, and Aniket Lad. Moreover, I would like to thank other ETRL members Kalyan Boyina, James Carpenter, Nithin Upot, Tarek Gebrael, Yashraj Gurumukhi, Mohamed Mousa, Wuchen Fu, Junyoung Lee, Majid Linjawi, Siavash khodakarami for their support. Finally, I also want to thank many helpful UIUC research facility staffs such as Dr. Kathy Walsh, Dr. Julio Soares, Dr. Fubo Rao, and Dr. Tao Shang for their patience, trainings, helpful guidance, and insightful discussions. I am very lucky to have the chance to work with all these brilliant people, without whom it would not be possible to write this dissertation. I would like to thank Prof. Seik Kim and Hohyun Keum for their support on the PDMS stamping paper (Chapter 2). I would like to thank Dr. Andrew Stillwell (ECE, UIUC) and Dr. Robert Pilawa (UC Berkley) for their collaboration and continuous support on the modular heat sink project (Chapter 5). I would like to thank the collaborators from University of Arkansas, Dr. Alan Mantooth, Dr. Yue Zhao, Dr. David Huitink, Yuheng Wu, Mohammad Hazzaz Mahmud, and Bakhtiyar Mohamamd Nafis for their support on the hybrid cold plate project (chapter 6). Moreover, I acknowledge funding support from the advanced research projects agency-energy (ARPA-E) and center for power optimization of electro-thermal systems (POETS).

I will always be grateful to my minions (undergrads) who have helped me during the experiments and simulations over the last five and half years. Without you guys, it would have taken me twice as much time to complete my Ph.D.: Derrick Liu, Haoyun (Aaron) Qiu, Mansoor Qureshi, Jackson Stermer, Sakshi Agarwal, Brisa McGrath, and Bruno Funez.

I was also very fortunate to make many good friends at UIUC. Their warm friendship is gratefully cherished.

I want to show my special and deep appreciation to my family. My beloved wife, Sadia Anjum Ashrafi (Trisha), has always been showing unconditional love and support to me. Trisha, thank you so much for tolerating me, being with my frustrations and joys, giving me the courage when I was feeling down and for all your sacrifices. Trisha, for the last four years we both are graduate student at UIUC, even in your busy schedule you always made time for me and supported me. I am truly grateful to you. I would also like to thank the best gift of my life, my daughter, Anahi Rubasha Hoque. Anahi, your beautiful smile, tight hugs, and all those two-word sentences those you learned while I am writing this thesis were my strength and pushed me to work hard. “Baba (father)” is sorry for not spending enough time with you.

I lost my father almost eight years back, but I always cherish the lessons he taught me. His lessons about life and reality always helped to tackle all problems and made a strong-practical man. I dedicate my PhD degree to him and my mother. My mother, who is living 8500 miles away, has been always a support system for me. Thank you, mother, for your support and sacrifice. For the last 17 years I couldn’t spend continuous 30 days with you but you never complaint instead inspired me to pursue my dreams. I also like to thank my siblings. It’s the utmost sacrifices that they made, and I have nothing in return but making good use of my time and grow into a better human being, as they always expect me to be.

TABLE OF CONTENTS

LIST OF FIGURES

LIST OF TABLES

CHAPTER 1. INTRODUCTION

1.1. Background

Condensation heat transfer is crucial to the energy-efficient operation of a range of applications such as building environmental control,[1] power generation,[2] and high-heat-flux thermal management.[3] Steam condensing on high- or low-surface-energy substrates forms a liquid film or distinct droplets, respectively.[4, 5] The latter, termed dropwise condensation, is desired due to its 10X higher heat transfer coefficient.[6, 7] To further enhance dropwise condensation heat transfer, researchers have recently proposed the use of suitably designed superhydrophobic (SHP) surfaces.[8-13] When two or more condensate droplet coalesce on an ultra-low adhesion nanostructured superhydrophobic surface, the resulting droplet jumps away from the surface. This process is termed coalescence-induced droplet jumping and is fundamentally governed by inertial-capillary energy conversion.[9, 12] By enabling droplet jumping, the average droplet size on the surface is reduced, decreasing the condensate thermal resistance and enhancing the overall heat transfer by $\geq$ 2X when compared to dropwise condensation.[14] However, the enhancement is fundamentally limited by the significantly decreased individual droplet growth rate associated with superhydrophobic states having large *apparent* contact angle.[15] Surfaces with spatially varying wettability, commonly referred to as hybrid or biphilic surfaces, have the potential to overcome condensation-related limitations of homogeneous superhydrophobic surfaces by striking a balance between the advantages of hydrophobicity and hydrophilicity.[16] Hybrid or biphilic surfaces have been shown to enhance fog harvesting,[17-22] icing prevention,[23-25] condensation and boiling heat transfer.[16, 26-32] Furthermore, hybrid surfaces increase flooding resistance when compared to homogenous superhydrophobic surfaces,[27] a key limitation to the implementation of superhydrophobic

materials for condenser applications. However, significant challenges remain related to the manufacture of hybrid patterns on large area samples. Unlike scalable homogenous functional surfaces,[33] past hybrid surface fabrication processes, typically involving conventional mask-based lithography with selective removal of the background material,[16, 17, 34] direct-patterning by inkjet printing,[35, 36] laser processing,[37] and a direct combination or stacking of materials with distinct wettabilities [22, 24] have not focused on scalabilty. All of the aforementioned techniques are substrate dependent, are not scalable (~ cm), and suffer from long fabrication times (~ hours).

Wettability control requires functionalization of the surfaces with hydrophobic coating. However, designing a suitable hydrophobic coating has been the main decades-long challenge to deploying dropwise condensation in real power systems. To overcome this challenge, five coating requirements need to be met simultaneously. 1) The coating needs to be fabricated scalably and must be applicable to a variety of potential substrate materials. Typical condensers in a power station are fabricated from different metals or metal alloys depending on the region, and they are relatively large (~10 m) often containing thousands of tubes in a bundle. 2) The coating needs to be thin (< 5 μm) so that the coating parasitic thermal resistance does not off-set the benefit of high dropwise condensation heat transfer coefficient[38]. 3) The coating needs to resist delamination caused by the condensate capillary force. Specifically, condensation-induced blistering, which is the most direct coating degradation mechanism, enables condensate penetration between the interface of the coating through surface defects. This penetration causes localized pressure, and gradually results in complete coating delamination[39]. 4) The coating must be thermally stable at elevated temperature steam environments. 5) The coating needs to resist mechanical abrasion during condenser fabrication, assembly, maintenance, and operation. Classical artificial

hydrophobic materials such as low surface energy polymers cannot meet these requirements and cannot be utilized due to their low elastic modulus, and poor thermal and mechanical stability. In an attempt to finally craft durable hydrophobic coatings, past strategies have generally focused on optimizing the coating geometric and structural design. By doing so, these have demonstrated that coating robustness can be enhanced by surface structures which act as a protective or sacrificial armor[40-42]. However, these hierarchical protective structures make the overall coating thick (> 10 μm), and unusable for condensation heat transfer. Furthermore, armor approaches are relatively difficult to scale to arbitrary substrates and materials. Thus far, little progress has been made on enhancing the coating intrinsic properties in order to overcome the durability challenge.

Usage of low surface tension liquid has grown substantially in recent years due to their implementation as alternative energy sources, biofuels, and refrigeration applications.[11, 43-47] Traditional hydrophobic or superhydrophobic surfaces fail to repel low surface tension liquids,[48, 49] with adsorption of organic contaminants such as proteins, cells or bacteria compromising repellency.[50-52] Although complex re-entrant geometries can achieve repellency of deposited low surface- tension liquids,[53-55] they fail during condensation, where the presence of random nucleation sites leads to flooding and film formation.[56, 57] Hence, the development of durable surfaces that are repellant to low surface tension fluids are needed. Inspired by the Nepenthes pitcher plant, a new class of surface called the slippery liquid-infused porous surface (SLIPS) has been proposed.[58] Due to their superior repellant properties to a variety of liquids, SLIPS have been demonstrated to promote stable dropwise condensation of low surface tension organic vapors and enhanced dropwise condensation heat transfer.[59-62] The life span of SLIPS is of crucial importance for both system performance and economic considerations. A lack of fundamental

understanding of condensation-induced degradation mechanisms has held back the successful development and demonstration of surfaces capable of achieving stable dropwise condensation. One of the largest barriers to success is the long experimental timescale required to quantify life span. A limited number of studies have focused on conducting long-term condensation durability tests on functional surfaces.[63-69] To the best of our knowledge, no study has quantified the long-term (multi-month) condensation durability of SLIPS. The majority of past work has focused on short term robustness quantification for icing/frosting, biofouling, corrosion, and ageing.[70-77]

In contrast to generation, the electric energy from power plant is used in all electronic devices and rapid miniaturization of electronics had led to significant growth in the power density of modern devices and systems, which demands effective thermal management to avoid unwanted failure due to overheating. Macroscale device level advanced design consideration has profound impact on performance improvement of energy systems. Such as in thermal management of air/liquid cooled power electronics. For air cooled based thermal solution, heat sink is very common. In the past, researchers have optimized different parameters of air-cooled heat sink topologies focusing on heat sink design [78-81], heat sink fabrication processes [82-84], different power electronics system layouts [85, 86], various heat sink geometries [87, 88], heat sink materials [89], hybrid cooling approaches [90, 91], coolant flow modifications [92], and overall thermal performance [93-95]. With the integration of power converters into mobile machinery such as aircraft, ships, on-road vehicles, or off-road equipment, a desire exists to enhance converter power density and performance without integration penalty [96, 97]. The heat sink in an air-cooled power converter is typically the heaviest part [92, 98]. A key parameter governing the required heat sink is the thermal performance of the gap pad between the PCB and heat sink. Although gap

pads are required for electrical isolation and mechanical compliance, their added thermal impedance stemming from their poor thermal conductivity (< 5 W/(m·K)) ensures oversizing of heat spreading components to minimize non-pad thermal resistances and hence enhance overall junction-to-air heat transfer. The need for coupling of the heat sink with multiple heat generating components operating at different voltage potentials inherently increases complexity and mass. To ensure compliance, the heat sink is oversized to overlap with all components to and to ensure that the gap pad material is present at the interface of all devices to provide electrical isolation. In many applications, especially for high density power electronics, the air cooling is not sufficient. Liquid cooled cold plate based thermal solution is used in those applications. Traditional commercial off-the-shelf (COTS) cold plates are all metal and heavy. So, COTS cold plate provides limited scope of system level volumetric and gravimetric power density enhancement. Moreover, isothermal profile generation, which is needed for system reliability improvement, is challenging due to limited design freedom of COTS cold plate.

1.2. Outline of The Dissertation

The dissertation aims to understand and develop the solutions of the problems outlined above. The dissertation consists of seven interconnected chapters where nano-to-macroscale advanced manufacturing methods are demonstrated for overcoming different challenges discussed above to improve surface to device level performance enhancement in different energy systems.

Chapter 2 presents a simple, rapid, and scalable stamping method to manufacture hybrid surfaces on arbitrarily sized materials. Chapter 3 investigates and uncover important new physical effects and uses them to develop a unique multilayer micro-scale thick coating to finally solve a decades-old challenge of durable (years) hydrophobicity. In continuation of the durability

investigation, chapter 4 further studies and develops guidelines for manufacturing scalable and durable slippery liquid infused (SLIPS) hydrophobic surfaces for low-surface-tension fluids. Finally, when focus to macro-scale device level cooling solution such as heat sink and cold plate, it is observed that the micromanufacturing creates the scope to improve thermal performance of the systems. To enhance the volumetric and gravimetric energy density of the system, chapter 5 and 6 develop aggressive thermal solutions for air cooled (modular heat sink and liquid cooled (polymer-metal hybrid cold plate) electronics focusing on macro-machining and additive manufacturing. Chapter 7 presents detailed conclusions from this study.

CHAPTER 2

High-Throughput Stamping of Hybrid Functional Surfaces

2.1. Introduction

Inspired by nature [99, 100], engineered structured surfaces have attracted great interest due to their self-cleaning,[101] electrostatic energy harvesting,[102] anti-dew,[103, 104] anti-icing,[105-107] and enhanced heat transfer[33, 62, 108-112] performance. Of these phase change processes, water vapor condensation has seen a particular focus due to its wide utilization in power generation,[113] thermal management,[114] and air-conditioning.[115-117] To enhance condensation using functional surfaces, researchers have recently proposed coalescence induced droplet jumping[9, 10, 13, 118-121] on rationally designed superhydrophobic surfaces as a means to remove droplets from the surface. Droplet jumping on superhydrophobic surfaces can enhance condensation heat transfer by more than 100% when compared to state of the art dropwise condensation.[33, 122] The superhydrophobicity of a surface relies on successfully maintaining air gaps between micro/nanostructures.[123] Recent studies have shown that the water repellency of homogeneous superhydrophobic surfaces is lost at high subcooling,[109, 124] due to 'flooding' of the surface stemming from condensate droplet transition to the Wenzel state. In addition to flooding, many superhydrophobic surfaces do not enable spatial control of heterogeneous nucleation due to the high nucleation energy barrier stemming from the presence of homogeneous

*This chapter was mostly reprinted (adapted) with permission from *Langmuir* 2020, 36, 21, 5730–5744. Copyright © 2020 American Chemical Society. Muhammad Jahidul Hoque is the first author and he contributed to the study via conducting experiments, analyzing data, and writing the manuscript. Dr. Nenad Miljkovic and Dr. Seok Kim guided the research and revised the manuscript and are the corresponding authors.

low-surface energy chemistry. To overcome these limitations, researchers have demonstrated the spatial control of heterogeneous nucleation by manipulating the local intrinsic wettability of the surface.[24, 125, 126] Surfaces with spatially varying wettability, commonly referred to as hybrid or biphilic surfaces, have the potential to overcome condensation-related limitations of homogeneous superhydrophobic surfaces by striking a balance between the advantages of hydrophobicity and hydrophilicity.[16]

Hybrid or biphilic surfaces have been shown to enhance fog harvesting,[17-22] icing prevention,[23-25] condensation and boiling heat transfer.[16, 26-32] As was the case of the lotus leaf, hybrid surfaces were inspired from natures Namib Desert beetles, which harvests water via its dorsal surface comprising of microscale wax-free hydrophilic bumps distributed on a wax-coated superhydrophobic background.[127, 128] Water vapor is captured and collected at the hydrophilic bumps, while the superhydrophobic background promotes water drainage.[17, 128] Hybrid surfaces induce spatial control of heterogeneous nucleation[24, 126] and enhance droplet growth due to the reduced thermodynamic energy barrier for nucleation[126] and droplet conduction thermal resistance.[129] Condensation heat transfer on rationally designed hybrid surfaces shows a 63% enhancement when compared to state-of-the-art dropwise condensation.[16] Furthermore, hybrid surfaces increase flooding resistance when compared to homogenous superhydrophobic surfaces,[27] a key limitation to the implementation of superhydrophobic materials for condenser applications.

Significant challenges remain related to the manufacture of hybrid patterns on large area samples. Unlike scalable homogenous functional surfaces,[33] past hybrid surface fabrication processes, typically involving conventional mask-based lithography with selective removal of the background material,[16, 17, 34] direct-patterning by inkjet printing,[35, 36] laser processing,[37]

and a direct combination or stacking of materials with distinct wettabilities[22, 24] have not focused on scalabilty. All of the aforementioned techniques are substrate dependent, are not scalable (~ cm), and suffer from long fabrication times (~ hours).

In this chapter, we show a simple, rapid, and scalable stamping method to pattern well-defined hydrophobic and hydrophilic regions on arbitrarily sized materials, which overcome the challenges of conventional hybrid surface micro and nanomanufacturing. The microtip-patterned polydimethylsiloxane (PDMS) stamps were utilized to form arrays of hydrophilic regions on homogenous hydrophobic and superhydrophobic surfaces. To demonstrate hybrid wettability, water condensation phenomena were visualized which resulted in the spatial control of heterogeneous nucleation, with droplets initiating on hydrophilic domains as small as 1 μm. To demonstrate the versatility of our stamping approach, a variety of coating materials and substrates with hydrophobic and superhydrophobic backgrounds were tested. In addition to nucleation, the self-organization, droplet growth dynamics, and coalescence induced jumping behavior on a variety of different hybrid surfaces was analyzed. The stamping technique developed here not only enables the scalable manufacture of substrates having spatial control of heterogeneous nucleation of water, but presents design guidelines for the development of scalable hybrid surfaces for the study of controlled phase change phenomena such as frosting, icing, evaporation, and boiling.

2.2. PDMS Micro-Tip Stamp Fabrication

The fabrication of the microtipped stamp involved molding and demolding of PDMS (Sylgard 184, Dow Corning; 5:1 mixture of base to curing agent) against negative templates as illustrated in Figures 2.1(a-d).[130, 131] The negative template consists of an Si wafer (100) and an epoxy layer (SU8 50, MicroChem Corp., 250 μm thick). To define pyramidal pits (Fig. 2.1a) the Si wafer was anisotropically wet etched in a potassium hydroxide (KOH) solution at 80ºC with a lithographically patterned mask made of silicon nitride (SiN, 100 nm thick, formed using PECVD, PlasmaTherm), which takes around 2~3 hours. After etching the Si wafer to form square openings (5 × 5 mm, Figure 2.1b) epoxy was spun coated and lithographically patterned on the wafer. Casting the prepolymer to PDMS (base oligomer and crosslinking agent) against the functionalized (trichlorosilane, United Chemical Technology) surface of the negative template, thermally curing the PDMS at 70ºC for >1 h (Fig. 2.1c), and demolding it from the negative template, produces the desired elastomeric microtipped stamp (Fig. 2.1d), which takes total of about 2.5 hours. The isometric image of a fabricated microtipped stamp is shown in Figure 2.1(e), with a top-view magnified image in Figure 2.1(f). Figures 2.1(h), and 2.1(i) illustrate key schematics of the pyramidal dimensions on the stamps. As shown in Table 1, four different microtipped stamps were fabricated following the same procedures, and keeping the same base to base spacing (b = 25 μm) while changing the squared base size (a = 30 μm to 60 μm). The pyramid spacing was selected for three reasons. First, the particular spacing ensured that pyramids were distinguishable and do not interfere with one another when the stamp is placed against surface for patterning. Second, with denser spacing, the hydrophilic patterns on the functional substrate would be too close to each other, making observation of the water droplet wettability contrast difficult. Lastly, with reduced base spacing, the pyramid height reduces (assuming the same angle dictated by the anisotropic wet

etch). Creating stamps with shorter pyramid heights places a constraint on surface alignment needs. The alignment between the PDMS stamp, and surface to be stamped needs to be tighter in order to obtain a homogeneous pattern across a large area substrate. The height of each microtip is determined by the pyramid base size, since the etch rate of 111 crystal plane is significantly lower than that of 100 or 110 plane (Table 2.1).

Table 2.1 Summary of the dimensions of the fabricated PDMS stamps. Symbols represent dimensions outlined in Figure 2(h, i). Uncertainty for all reported dimensional measurements was ± 500 nm.

Base, a [µm]	Spacing, b [µm]	Pitch, c [µm]	Height, h [µm]
30	25	55	53
40		65	70
50		75	88
60		85	105

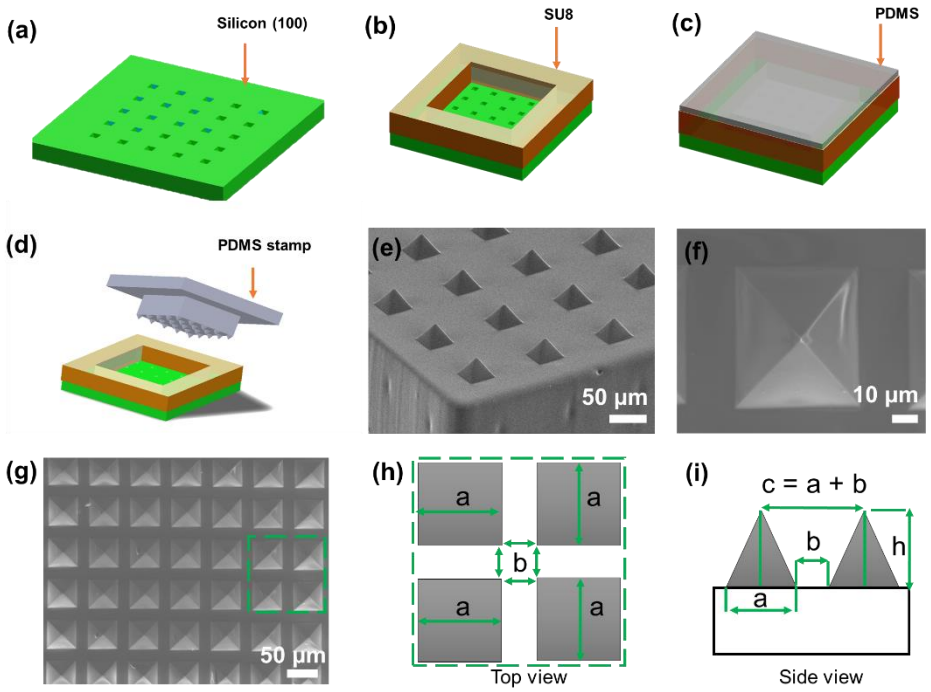

Figure 2.1 Schematic of the microtipped PDMS stamp and surface fabrication process flow. (a) Formation of multiple pits using KOH etching on a polished Si wafer. (b) Patterning using photolithography of SU8. (c) PDMS molding of the stamp. (d) Stamp removal after curing at 70ºC for 1 hour. (e) Isometric-view scanning electron microscopy (SEM) image of a fabricated microtipped stamp. (f) Top-view SEM image of an individual tip. (g) Top-view SEM image of the fabricated PDMS pyramid structure for a dense stamp design. Schematics showing key pyramidal dimensions for (h) top and (i) side views.

2.3. Hybrid Surface Fabrication using Stamping

Hybrid surface fabrication is a two-step method involving functionalization and stamping. Figure 2.2 illustrates the fabrication steps for post-stamped (Fig. 2.2a-d) and pre-stamped (Fig. 2.2e-h) self-assembled monolayer (SAM) based hybrid surfaces. For both stamping methods, fabrication starts with cleaning smooth substrates for hybrid surfaces having hydrophobic backgrounds, or fabricating micro/nanostructures for hybrid surfaces having superhydrophobic backgrounds[132]. To fabricate the post-stamped hybrid surface, the substrate is first functionalized with Heptadecafluorodecyltrimethoxy-silane (HTMS, TCI America, CAS #: 83048-65-1) using atmospheric pressure vapor phase deposition (Fig. 2.2a).[133] Briefly, the substrates were placed in a glass beaker with a vial of HTMS toluene solution (5% v/v). A glass lid was placed on top to seal the container, followed by heating in an atmospheric pressure oven (Thermo Scientific, Lindberg Blue M) at 80 ± 5°C for 3 hours to allow conformal HTMS SAM deposition [132]. After SAM deposition, the functionalized surface was stamped with the pre-fabricated PDMS micro-tipped stamp (Fig. 2.2b), resulting in selective removal of the HTMS SAM and creation of the hybrid surface (Fig. 2.2d). To facilitate the alignment and stamping, a precise three-axis stage was used (Newport). The substrate was fixed to a reference plate and the stamp was allowed to move vertically to come in contact with the substrate. For both pre and post stamping, 5 to 10 N/cm^2 pressures were applied on the back side of the PDMS stamp, as measured by weight calibration on the back face area. For pre-stamping, the applied load and the strong adhesion of PDMS to the substrate surface ensure great affixation of the PDMS stamp even after releasing the load. Hence, the stamp was kept attached to the substrate to act as a mask for HTMS SAM deposition without an applied load (other than gravitational forces). The substrate, stamp, and HTMS solution were placed into the oven (Fig. 2.2e) and the sample functionalized using

vapor phase deposition.[133] The pre-stamped functionalized surface was then removed from the oven with the PDMS tips still attached to the sample (Fig. 2.2f), which is removed by fixing the substrate on a stage while vertically pulling the stamp away from the surface in the normal direction. Once the PDMS sample was removed, the hybrid surface was formed with hydrophilic uncoated spots where the PDMS tips were in contact with the substrate (mask), and an HTMS SAM coated hydrophobic background (Fig. 2.2h). It is important to note, we tried using solid Si micropillar stamps for hybrid surface fabrication. The solid stamps had limited success due to alignment issues, stiffness of the stamp features, and potential for gap formation. Notably, pre-stamping did not work due to the presence of microscale gaps between the pillars and substrate prior to SAM functionalization. Table 2.2 provides a comparison of the developed stamping technique with conventional methods.[24, 126, 134-142] The techniques developed here are simple, rapid, and scalable.

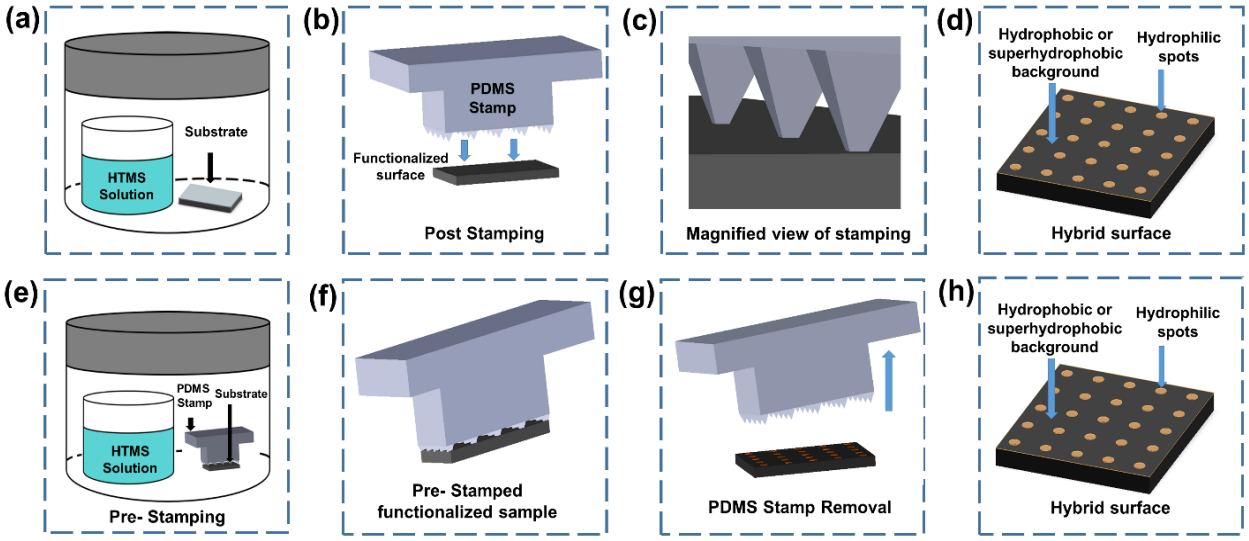

Figure 2.2. Schematics of the fabrication steps for post-stamped and pre-stamped hybrid surfaces. To fabricate post-stamped hybrid surfaces (a) the sample is functionalized with an HTMS SAM, (b) stamped, resulting in (c) selective removal of the HTMS SAM and creation of the (d) hybrid surface. To fabricate pre-stamped hybrid surfaces, (e) the PDMS stamp is preloaded to the sample to mask functionalization of HTMS SAM. (f) The pre-stamped functionalized surface is removed from the oven with the PDMS tips attached, and (g) the PDMS sample is removed, resulting in the creation of the (h) hybrid surface with hydrophilic uncoated spots where the PDMS tips were in contact with the substrate, and HTMS SAM hydrophobic background.

Table 2.2. Comparison of the developed stamping technique with currently avaiable hybrid surface fabrication techniques.

Fabrication Process		**Lithography**	**Inkjet Printing**	**Bottom Up**	**Spray Coating**	**Stamping**
Timescale	**Prototyping**	~hours	~hours	~hours	~ hours	~ hours
	Mass Manufacturing				~minutes	~ seconds
Reusability*		N/A	N/A	N/A	N/A	Stamp is reusable
Scalability		~ cm	~ cm	~ cm	~ m	~ m
Pattern Uniformity		High	High	High	Poor	High
Substrate Independence		No	No	No	Yes	Yes
Cost	**Equipment**	High	Medium	Medium	Medium	High: Mold Low: Stamp
	Labor		Low		Low	Low
	Material		Medium		Medium	
Reference		[16, 17, 34, 143, 144]	[35, 36, 145, 146]	[24, 147, 148]	[149]	Micro-printing[125, 130, 131, 150] Stamping - this work

***Reusability is used here with respect to the stamp only, and not the coating material that is removed.**

The stamping techniques (pre and post) are substrate and coating independent. The timescale for prototyping of a new mold and stamp is ~4 hours, which is comparable to existing methods (Table 2.2). However, the manufacturing timescale is ~1 second. Moreover, the same mold and stamp can be used repeatedly. We created more than 100 samples using the same stamp with negligible quality difference between the hybrid surfaces from first to last. Use of PDMS as the stamp material was done in order to ensure good mechanical compliance when the stamp contacts the substrate. Previously, elastomeric PDMS stamps were used for transfer printing in micro-masonary [130, 131] and to pattern surfaces for condensation applications.[125, 150] Past studies have used PDMS stamps to achieve micro-contact printing where a PDMS stamp was coated with functional coating after which it was stamped against the substrate to transfer print the coating.[125, 150] Our work differs in that the PDMS micro-tips are used to stamp the already functionalized substrate to selectively remove the coating. To demonstrate the versatility of our approach, seven different hybrid surfaces were fabricated using post and pre-stamping (Table 2.3). For post-stamping, we studied HTMS, polymeric octafluorocyclobutane (C_4F_8),[151] as well as slippery omniphobic

covalently attached liquids (SOCAL)[152] deposited on polished Si wafers. With pre-stamping, the PDMS stamp acts as a mask and the HTMS creates monolayer irrespective of the substrate. This was not possible with C_4F_8 and SOCAL based hybrid surfaces due to their different coating recipes and inability to place arbitrary materials in the C_4F_8 deposition chamber. Hence for pre-stamping, only the HTMS SAM was used. To fabricate hybrid surfaces having superhydrophobic backgrounds, microstructured copper oxide (CuO) on bulk copper (Cu) substrates[33] and nanostructured boehmite (AlO(OH)) on bulk aluminum (Al) substrates were used.[153] To obtain smoother hybrid surfaces and to enable better visualization, boehmite nanostructures were also formed on sputtered Al on a Si wafer. The superhydrophilic boehmite nanoblades were developed on a silicon sputtered Al surface. In doing so, silicon wafers were first ultrasonically cleaned with acetone for 5 min and rinsed with ethanol, IPA, and DI water and dried with a clean nitrogen stream. Then a 50 nm thick Al layer was sputtered on the cleaned Si wafer using an AJA Orion-8 Magnetron Sputtering System and to form the nanoblades, the Al coated Si wafer was placed in hot DI water at 90ºC for 10 minutes. To fabricate the superhydrophobic boehmite nanoblade surface, boehmite surfaces were functionalized with HTMS (TCI America, CAS #: 83048-65-1). After surface fabrication, all coated surfaces were stamped using four pyramidal designs (c = 55, 65, 75, and 85 µm). Ellipsometric characterization of smooth Si wafers coated with HTMS, C_4F_8 and SOCAL coating showed thicknesses of 2.5 nm,[153] 100 nm,[154] and 4 nm,[152, 155] respectively.

Table 2.3. Substrate material, coating material, apparent advancing (θ_a), and apparent receding (θ_r) contact angles of water droplets on the background material (non-stamped), and manufacturing method used to develop the hybrid surfaces. All samples were prepared using four pyramidal pitches having c = 55, 65, 75, and 85 μm (Fig. 2.1i).

Substrate	Coating	Coating Thickness*	Apparent Contact Angle	Wetting to Water	Stamping
Si Wafer	HTMS	2.5 nm	$\theta_a = 111° \pm 1°$ $\theta_r = 103° \pm 2°$	Hydrophobic	Post
	C_4F_8	100 nm	$\theta_a = 121° \pm 1°$ $\theta_r = 99° \pm 1°$		
	SOCAL	4 nm	$\theta_a = 103 \pm 1°$ $\theta_r = 102 \pm 1°$		
	Boehmite + HTMS	2.5 nm	$\theta_a = 166 \pm 3°$ $\theta_r = 164 \pm 3°$	Superhydrophobic	
	HTMS		$\theta_a = 111 \pm 1°$ $\theta_r = 103 \pm 2°$	Hydrophobic	Pre
Cu Tab	CuO + HTMS		$\theta_a = 170 \pm 3°$ $\theta_r = 168 \pm 3°$	Superhydrophobic	Post
Al Tab	Boehmite + HTMS		$\theta_a = 169 \pm 2°$ $\theta_r = 165 \pm 4°$	Superhydrophobic	Post

*Considering only the thickness of functionalizing layer

2.4. Experimental Procedures

Optical Microscopy: A customized top-view microscopy setup (Fig. 2.3) was built using an upright optical microscope (Eclipse LV100, Nikon) linked to a high-resolution camera (Nikon DS-Qi2), which was used to observe top-view condensation behavior on the hybrid surfaces.[141, 156] The setup consisted of a cold stage (TP104SC-mk2000A, Instec) that held the sample horizontally and cooled the sample surface to 5 ± 0.5°C to condense water vapor from the laboratory ambient air having a temperature $T_a = 22 \pm 0.5$°C and relative humidity $\Phi = 45 \pm 5\%$ (Roscid Technologies, RO120). With the help of two objective lenses 20X and 50X (TU Plan Fluor EPI, Nikon) condensate behavior was recorded at 4 frames per second (fps). An LED light source (SOLA SM II Light Engine, Lumencor) was selected for illumination due to its high intensity but low power consumption (2.5 W) that minimized heat generation at the surface due to light absorption. Moreover, the flexibility of manual control of increasing the camera exposure time and reducing the condenser aperture diaphragm opening size helped us to minimize local heating effects during

condensation experiments. Additional details of the visualization technique can be found elsewhere.[141, 157-159]

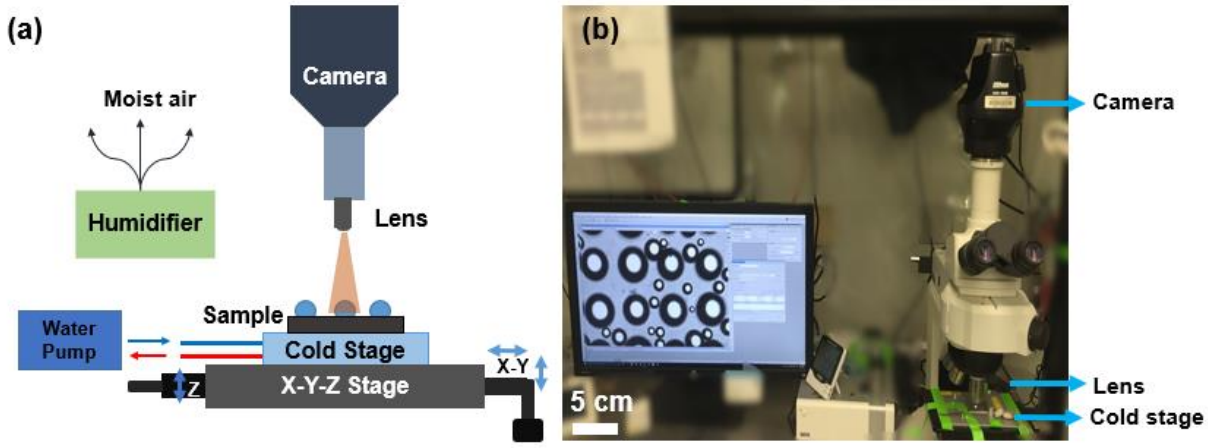

Figure 2.3. (a) Schematic and (b) photograph of the experimental setup used to test condensation behavior on the fabricated hybrid surfaces. To control the environmental humidity, a cool mist humidifier was placed adjacent to the microscope, which was curtained off from the rest of the laboratory environment.

Environmental Scanning Electron Microscopy (ESEM): Microscale condensation experiments were also studied with the fabricated hybrid surfaces using ESEM (FEI Quanta FEG 450, FEI Company). The water vapor pressure in the ESEM chamber was maintained between 1067 to 1200 Pa. Samples were placed on a cold stage and in order to achieve nucleation of water droplets on the sample from the saturated water vapor inside of the chamber. The cold stage temperature was maintained between 8 to 9.5°C. To visualize and capture images, a beam potential of 20 kV was maintained. To limit droplet heating effects, the electron beam current was carefully controlled.[160]

Side-View Droplet Jumping Imaging: To study coalescence-induced droplet jumping and to eliminate interference from multiple droplets, we interfaced a high-speed camera (Phantom v711, Vision Research) with a piezoelectric micro-goniometer (MCA-3, Kyowa Interface Science). The

sample was horizontally placed on a movable stage with three-dimensional positioning ability. Back illumination was supplied by an LED source (TSPA22x8, AITECSYSTEM). The piezoelectric dispenser was placed above our surface with a spacing ranging from 5 to 10 mm. To grow droplets on the substrate, the piezoelectric dispenser was turned on to generate monodisperse droplets having diameters ranging from 30 to 40 μm. Thus, monodisperse droplets accumulated on the sample surface by coalescing to form a single droplet with targeted size. The piezoelectric dispenser had voltage and frequency control. During experiments, 7 V and 10-100 Hz were used and no droplet resonance was observed for these operating conditions. A customized cage was set up to screen external airflow disturbances to the dispensed and deposited droplets. Imaging was performed at a 25X magnification with a capture rate of 13,001 fps. Experiments were conducted in ambient conditions $T_a = 22 \pm 0.5$°C and $\Phi = 45 \pm 5\%$ (Roscid Technologies, RO120). Additional details of the visualization technique can be found elsewhere.[159]

Hybrid Sample Surface Chemistry: The diameters of stamped spots on the hybrid surfaces were small (~ 1 μm). Chemical analysis utilizing X-Ray photoelectron spectroscopy (XPS), or Energy-dispersive X-ray spectroscopy (EDS) of individual spots was challenging as the analyzed data included the spectrum of the surrounding homogenous background material along with the underlying substrate. To overcome these spatial-resolution challenges, two 20 mm × 20 mm superhydrophobic boehmite surfaces were fabricated. The superhydrophilic boehmite nanoblades were developed on a silicon sputtered Al surface and also on mirror polished Al plate (6061 Al, McMaster). In doing so, both silicon wafers and Al plates were first ultrasonically cleaned with acetone for 5 min and rinsed with ethanol, IPA, and DI water and dried with a clean nitrogen stream. A 50 nm thick Al layer was sputtered on the polished Si wafer using an AJA Orion-8 Magnetron Sputtering System and to form the nanoblades, the Al coated Si wafer was placed in

hot DI water at 90ºC for 10 minutes. Whereas, after cleaning the Al plates were kept in hot DI water at 90ºC for 60 minutes. To fabricate the superhydrophobic boehmite nanoblade surface, both boehmite surfaces were functionalized with HTMS (TCI America, CAS #: 83048-65-1. After functionalization, the boehmite nanowire surfaces became superhydrophobic with apparent contact angles $\theta_a \approx 169^o$ and $\theta_r \approx 165^o$. Then PDMS (Sylgard 184, Dow Corning; 5:1 mixture of base to curing agent) was poured in a well-cleaned 2 inch diameter glass Petri dish up to a pre-marked height so that the thickness of the PDMS was 4 mm. The PDMS was then thermally cured at 70°C for 1 h in a vacuum furnace (Thermo Scientific, Lindberg Blue M). A 20 mm × 20 mm PDMS flat elastomer was cut and one of the two superhydrophobic surfaces was stamped. X-ray photoelectron spectroscopy was then perform on both the PDMS stamped and unstamped surfaces to compare the surface chemistry change after stamping. The XPS was performed using a monochromatic Al Kα source (Kratos Axis Ultra, Kratos Analytical). The size of the source beam was 2 mm x 2 mm, and the size of the analyzed region was 0.3 mm x 0.7 mm. The instrument was maintained at a pressure of 10^{-7} Pa during the experiments. The spectra were post-processed with CasaXPS software to determine the change in composition of the sample surfaces.

2.5. Characterization of the Hybrid Surface

To prove that the stamping method can selectively remove HTMS molecules or structures, we conducted SEM and XPS studies of pre and post-stamped samples. Figure 2.4 shows that stamping induces hydrophilicity at locations where the PDMS micro tip contacts the HTMS SAM. For structured surfaces, stamping not only removes HTMS, but also can remove the structure. Figure 2.4(a) shows top-view SEM images of post-stamped nanostructured boehmite on a Si wafer. Prior to stamping, the boehmite was uniform (Fig. 2.4b). After stamping, mechanical

contact and adhesion to the PDMS tips resulted in the removal of the boehmite from the Si wafer (Fig. 2.4c). Removal of the superhydrophobic boehmite layer during stamping resulted in exposure of the hydrophilic substrate, and preferential heterogeneous nucleation of water droplets on the exposed hydrophilic spots as observed with ESEM (Fig. 2.4d to 2.4f).

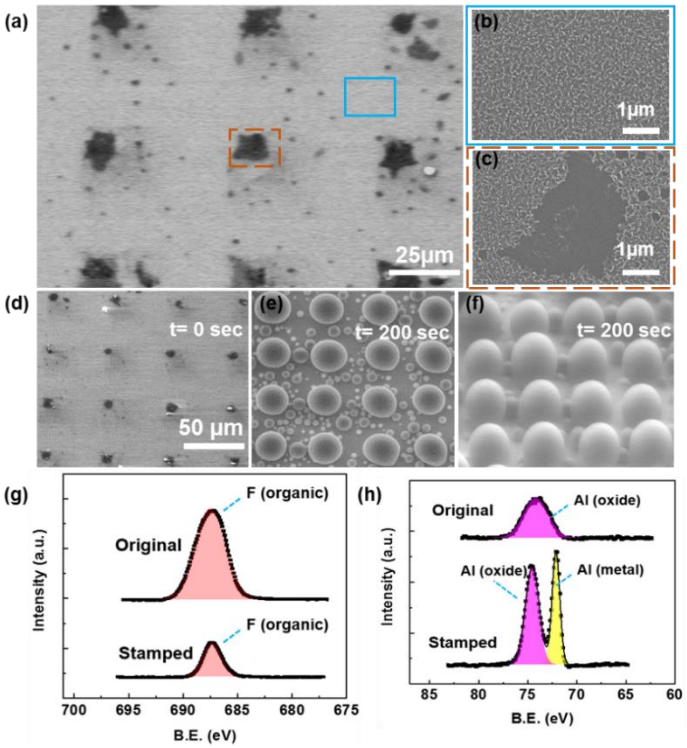

Figure 2.4. (a) Top-view SEM images of the stamped hybrid surfaces. (b) Magnified view of the blue solid box in (a) showing the un-stamped superhydrophobic background consisting of boehmite nanostructures. (c) Magnified view of the brown dotted box in (a) showing the stamped section with boehmite removed. Time-lapse ESEM (d)-(e) top view and (f) 30º tilted images of water vapor condensation on the stamped hybrid surface. Due to removal of the superhydrophobic boehmite layer during stamping, the hydrophilic Si wafer is exposed, resulting in preferential heterogeneous nucleation of water droplets. High-resolution XPS spectra showing the (g) F 1s and (h) Al 2p peaks on the original and stamped hybrid surfaces.

To further quantify the removal efficacy, XPS analysis elucidated the cause of patterned hydrophilicity. After stamping, HTMS was indeed partially removed as evidenced by the decreased intensity of the characteristic fluorine (F) peak (Fig. 2.4g). The XPS results point to a damage mechanism of HTMS due to the remnants of a small F peak, rather than the ideal removal

of all molecules via stamping. Due to the small size of the stamped spots, we could not characterize the apparent contact angle locally to identify intrinsic wettability. Furthermore, due to the removal of boehmite nanostructures, the underlying Al substrate was exposed (Fig. 2.4h) as evidenced by the appearance of a strong Al peak after stamping.

2.6. Water Droplet Nucleation on Hybrid Surfaces

Condensation experiments were conducted using optical microscopy (Fig. 2.3) on both pre and post-stamped hybrid surfaces having hydrophobic and superhydrophobic backgrounds. Figure 2.5(a), shows atmospheric water vapor condensation on a pre-stamped HTMS-coated hybrid surface with a hydrophobic background having $c = 65$ μm (Fig. 2.1i). At time $t = 0$, defined as the time when condensation was first observed, water droplets nucleate on the stamped hydrophilic regions. At later times (5 min < t < 10 min), due to the presence of defects in the SAM coating as well as elevated supersaturations as the sample cools down further, secondary droplets appeared in the field of view that nucleated between stamped features. The growth rate of primary droplets growing on the hydrophilic spots was higher than secondary droplets, with secondary droplets eventually engulfed by the faster growing parent droplets on the hydrophilic spots, depicting the stamp pattern.[161] During coalescence of secondary and primary droplets, two mechanisms dictate the motion of secondary droplets towards primary droplets, hence, maintaining the stamp pattern. The smaller size of secondary droplets results in a higher Laplace pressure when compared to their primary counterparts, resulting in coalescence and motion of the liquid from smaller to larger droplets.[151, 162] Furthermore, the presence of hydrophilic regions implies higher contact angle hysteresis,[140, 142, 163] with greater mobility of secondary droplets due to their growth on homogeneous hydrophobic or superhydrophobic backgrounds.

To compare the nucleation behavior under identical atmospheric conditions for the background and stamped regions, we characterized the average spacing (l) between nucleating droplets. The average spacing between spatially random nucleating droplets on the homogeneous hydrophobic background was l = 10.5 ± 3.5 μm (Fig. 2.6). The spacing can be used to estimate a nucleation site density ($\sim 1/l^2$), which was determined to be 10^{10} droplets/m^2 on the homogenous coated background. This nucleation density was within the range of previous experimental values 10^9 -10^{15} droplets/m^2, [164-167] and is dictated by the quality of the coating and number of exposed defect sites.[151] However, the distance between microscale primary droplets nucleating on the hydrophilic regions was 1.6 ± 0.45 μm, indicating significant wettability contrast and hence lower nucleation energy barrier for the hydrophilic spots. The local nucleation site density on the stamped hydrophilic regions was 44X higher when compared to the homogenous background.

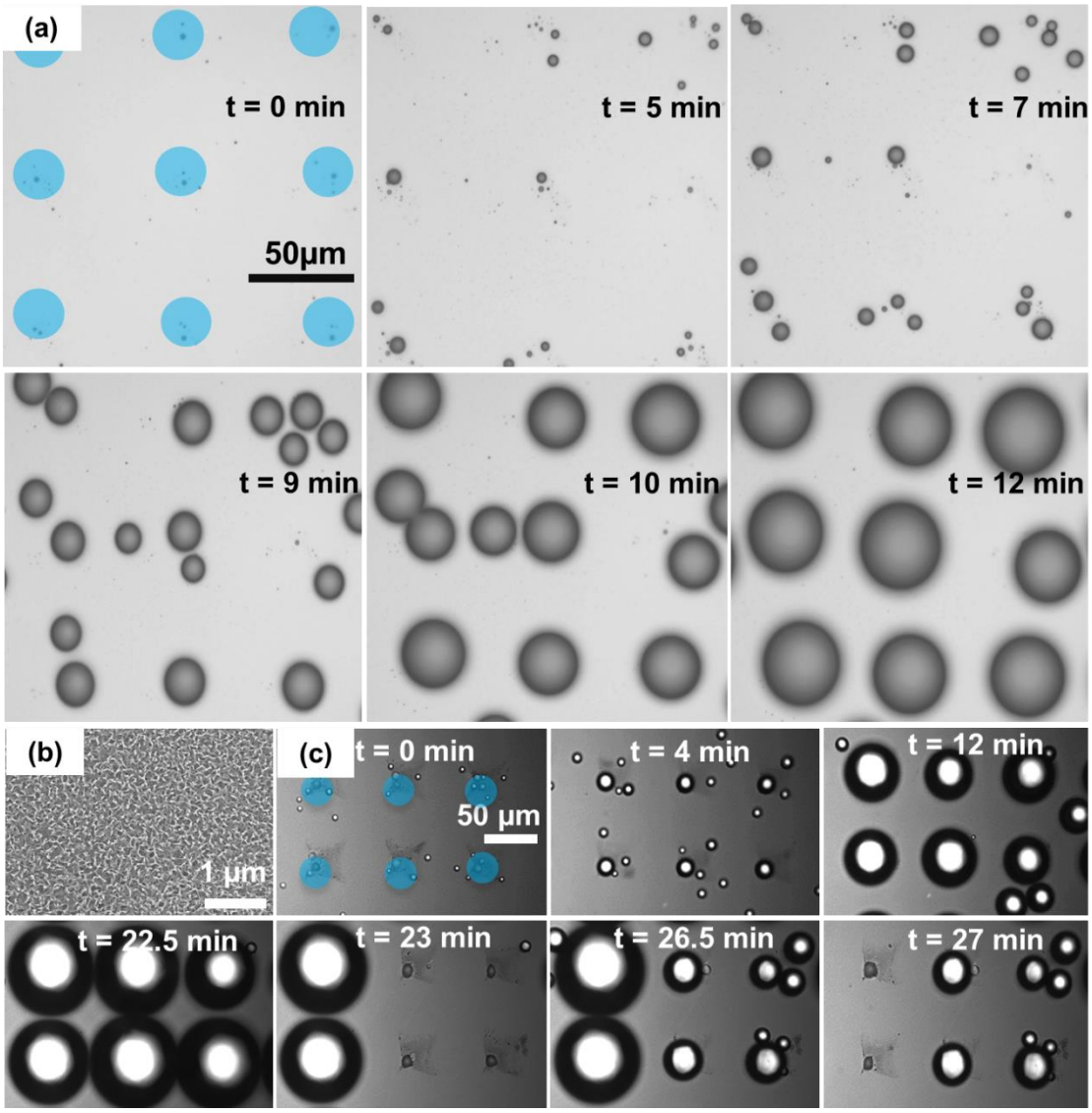

Figure 2.5. Top-view optical microscopy (OM) images of atmospheric water vapor condensation. Condensation on a (a) pre-stamped HTMS-coated hybrid surfaces having hydrophobic background with $c = 65$ μm (Fig. 1i). At $t = 0$, the hydrophilic stamped regions are false colored blue for clarity. Time $t = 0$ was defined as the time when water nuclei were first observed. For $0 < t < 5$ min, nucleation of droplets occurred mainly on the hydrophilic stamped regions. At later times ($5 < t < 10$ min), secondary droplets appeared in the field of view. (b) SEM image of the nanostructured boehmite surface used to create superhydrophobic background hybrid surfaces. (c) Top-view high-speed OM time-lapse images of droplet nucleation on the hybrid boehmite surface demonstrating continuous nucleation, self-organization, coalescence, jumping, and re-nucleation.

Hybrid surfaces having superhydrophobic backgrounds showed similar condensation behavior. Figure 2.5(b) shows SEM images of the SAM-coated boehmite surface used to create hybrid surfaces having a superhydrophobic background. Figure 2.5(c) shows top-view optical microscopy time-lapse images of droplet nucleation and growth on the hybrid boehmite surface. In addition to continuous nucleation, and self-organization (as observed in Fig. 2.5a), the surface showed coalescence, jumping, and re-nucleation. In addition to the exemplary results of Figure 1.5, condensation behavior on pre-stamped HTMS-coated hybrid surfaces having $c = 55$ μm, post-stamped HTMS-coated hybrid surfaces having $c = 75$ and 85 μm, post-stamped SOCAL surfaces, C_4F_8-coated hybrid surfaces, and a CuO-HTMS hybrid surface, were analyzed and are shown in Figure 2.7.

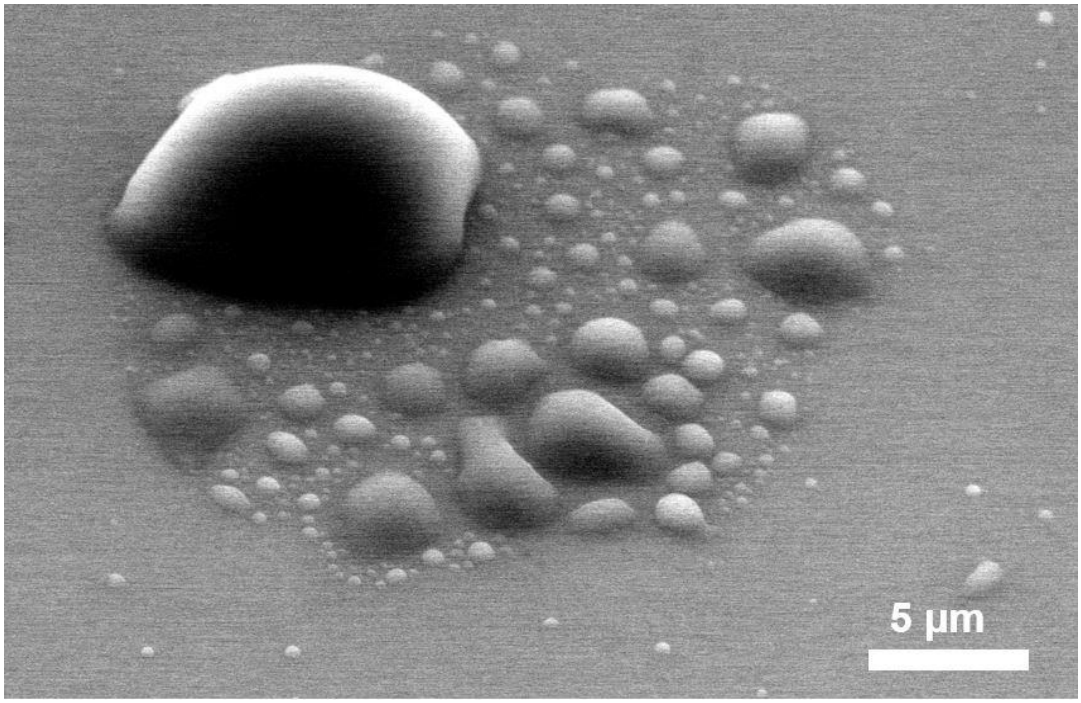

Figure 2.6. Top-view environmental scanning electron microscopy (ESEM) image of primary droplets nucleating on a stamped hydrophilic spot (center), and secondary droplets forming on coated the hydrophobic background (bottom left).

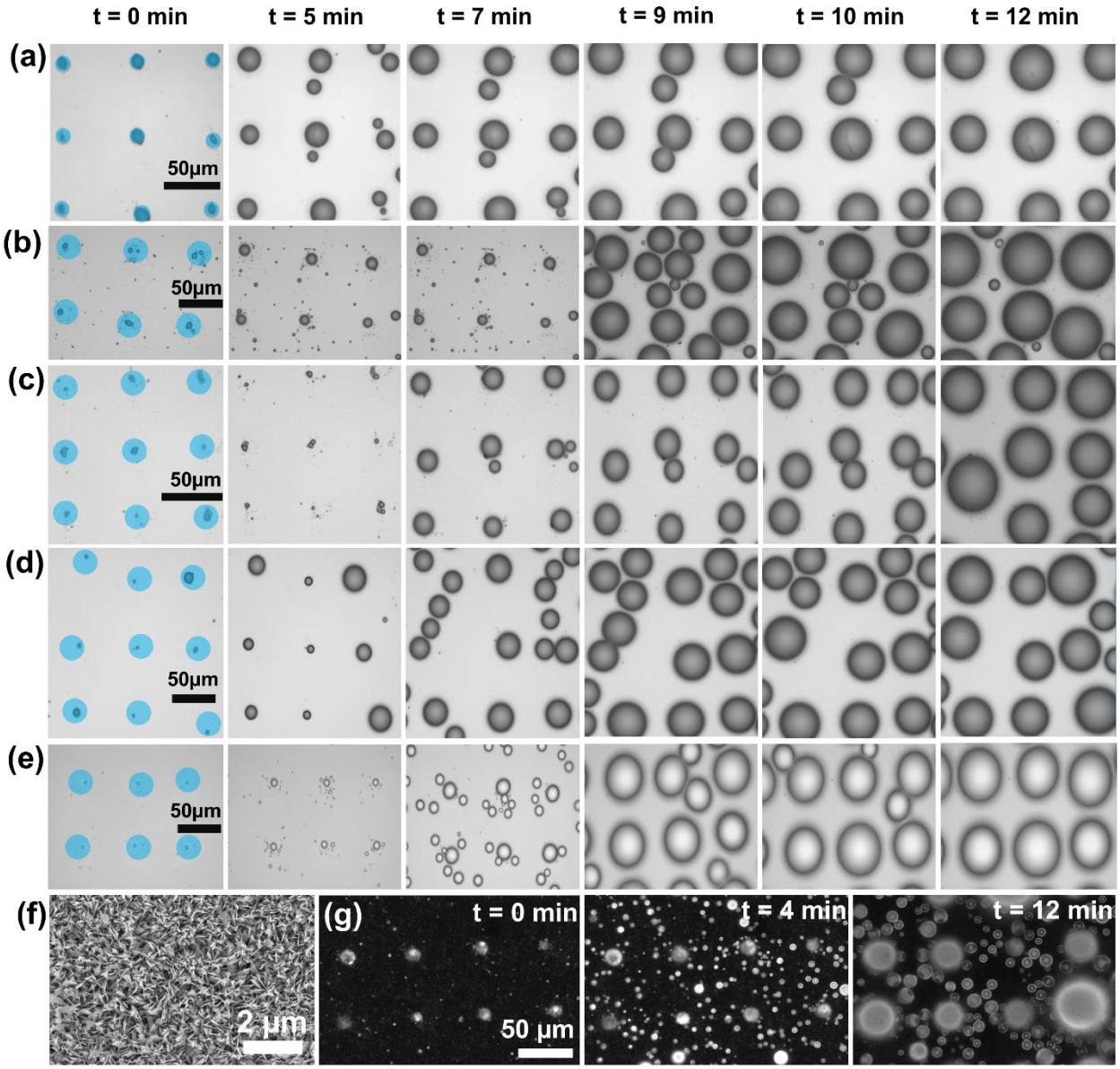

Figure 2.7. Top-view optical microscopy images of atmospheric water vapor condensation. Individual rows represent different samples, while columns represent different times. Condensation on (a)-(b) post-stamped HTMS-coated hybrid surface having $c = 75$ μm and $c = 85$ μm pitch, (c) pre-stamped HTMS-coated hybrid surfaces having $c = 55$ μm pitch, respectively, (d) a post-stamped SOCAL surface, and (e) a C_4F_8-coated hybrid surface. For $t = 0$, the hydrophilic stamped regions are false colored blue for clarity. The time $t = 0$ was defined as the time when water nuclei were first observed. (f) SEM image of the nanostructured CuO surface used to create the hybrid surfaces with a superhydrophobic background. (g) Top-view high-speed optical microscopy time lapse images of droplet nucleation and growth on the hybrid CuO surface demonstrating spatial control of heterogeneous nucleation with poor control of adjacent nucleation of small water droplets.

2.7. Coalescence Induced Droplet Jumping

Due to the removal of nanostructures at the PDMS-substrate contact regions, the stamped superhydrophobic surface showed hybrid wettability with local hydrophilicity distributed against the background of global superhydrophobicity. To confirm the hybrid wetting of the stamped surface, we visualized the droplet-surface interaction during droplet coalescence and jumping. Visualization was performed by dispensing two equally-sized water droplets (R = 188 ± 4 μm) on the surface using the piezoelectric microdroplet dispensing and positioning system.[159, 168] Placing of the stamped samples on the side-view setup showed that droplets impinging on the superhydrophobic background resulted in frequent rebound and lack of microscale droplet formation. Motion of the stage and sample until droplets impinged on the stamped features, resulting in droplet formation, was done in order to locate the periodic stamped regions.

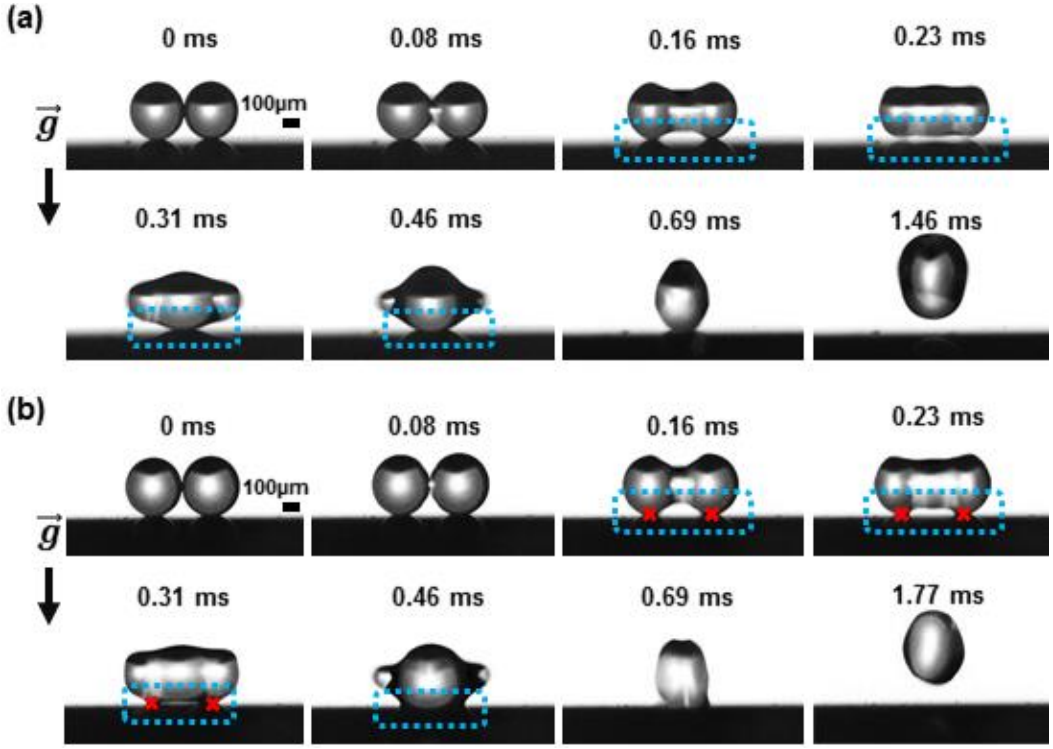

Figure 2.8. Side-view high-speed time-lapse images of droplet coalescence induced jumping on the (a) homogeneous superhydrophobic and (b) hybrid boehmite surface. From t = 0.23 to 0.69 ms, coalescence dynamics on the hybrid surface showed clear signs of pinning due the presence of hydrophilic spots, resulting in delayed droplet jumping. The pinning spots are demarked by red crosses.

Figure 2.8, shows that the merged droplet had delayed separation from the hybrid surface during the liquid bridge development stage (t = 0.16 to 0.31 ms) due to the additional adhesion stemming from the hydrophilic spots.[159] As a result of the local pinning, the coalesced droplet on the hybrid surface showed a reduced jumping velocity of 0.11 m/s, 34% lower than observed on the unstamped superhydrophobic surface (0.17 m/s), where liquid-surface separation (t = 0.23 ms, Fig 2.8a) was observed prior to the eventual droplet detachment.

The hybrid surfaces increase droplet density and mobility, resulting in frequent enhancement of multi-droplet jumping.[169, 170] Figure 2.9(a), shows false colored time-lapse high-speed images of six droplet coalescence-induced jumping. In contrast to the homogenous superhydrophobic surfaces, the hybrid surfaces induced controlled nucleation of primary droplets which improved droplet mobility towards the hydrophilic stamped regions, yielding enhancement of multi-droplet jumping. Figure 2.9(b) shows that on a homogenous superhydrophobic surface, 70% of jumping events included two droplets (N = 2).

However, for the hybrid surface, two-droplet jumping decreased to 25% due to the increase in N > 2 events. For $N \geq 6$, the hybrid surface showed a 14X higher rate of jumping. It is important to note, although the hybrid surfaces showed a significantly higher probability of multi-droplet jumping, fewer total jumping events occurred when compared to the homogeneous superhydrophobic surface due to the additional surface-droplet adhesion that prevented small droplets (comparable to or smaller than the hydrophilic spot size, ≈ 3 μm) from departing upon coalescence, further confirming the effectiveness of the hydrophilicity of the stamped spots.

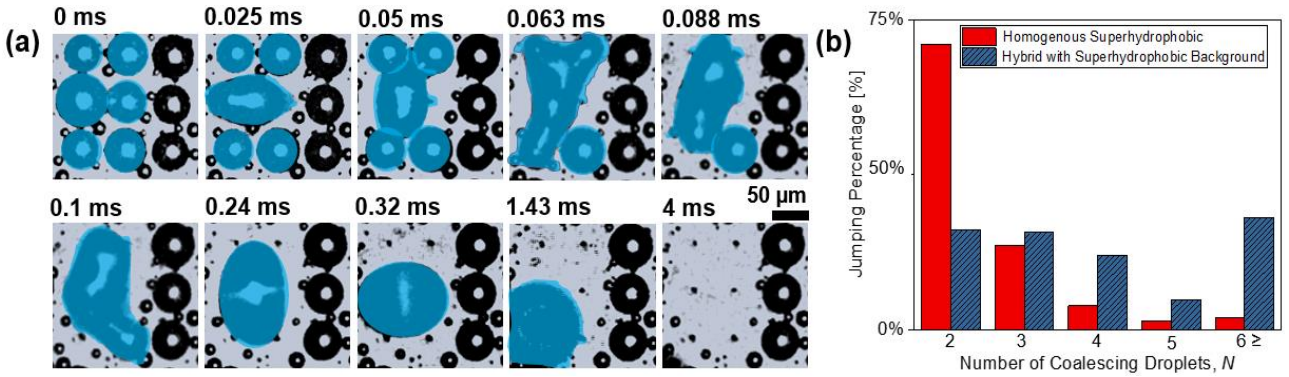

Figure 2.9. Multi-droplet coalescence induced jumping. (a) False-color time-lapse top-view high-speed images of a droplet cluster (N = 6) coalescing and jumping from the hybrid surface with a superhydrophobic background. (b) Percentage of jumping events as a function of the total number of droplets partaking in the jumping event (N) on the hybrid surface (hatched blue bars) and homogenous superhydrophobic surface (solid red bars). The percentage was obtained by normalizing the number of events with the total number of observed jumping events on the surface over a time span of 20 minutes, which was ≈ 350 and ≈ 165 for the homogeneous and hybrid surfaces, respectively.

2.8. Dynamics of Droplet Growth and Self-Organization

Hybrid surfaces having superhydrophobic backgrounds are capable of inducing multidroplet jumping which has the potential to improve condensation heat transfer.[28, 149] Moreover, these surfaces show higher droplet nucleation density, and self-organization behavior, compared to hybrid surfaces with hydrophobic backgrounds. Figures 2.10(a) and (b) show droplet nucleation and growth dynamics on a hydrophobic hybrid surface and superhydrophobic hybrid surface, respectively. As observed in Figure 2.10(c), during the initial stages of water vapor condensation, the growth rate of secondary droplets (shaded red band) on the hydrophobic hybrid surface is comparable to primary droplets growing on the hydrophilic regions (shaded blue band). On superhydrophobic hybrid surfaces (Figure 2.10d) the growth rate of primary and secondary droplets was approximately the same for $0 < t < 450$ s. During this initial phase, droplets grew mainly via direct molecule accommodation at the liquid-vapor interface and no interaction with

adjacent droplets occurred. Due to the presence of non-condensable gases in the experiment, the growth rates of droplets on the hydrophobic and superhydrophobic hybrid surfaces were identical during the initial stages of condensation for isolated droplets. However, once droplets begin to interact and coalesce, the growth dynamics of primary droplets began to diverge on the two surfaces. The divergence was mainly due to the motion of secondary droplets towards primary droplets in the stamped region during coalescence, resulting in a sudden jump in growth rate ($t >$ 450 s) for primary droplets (Fig. 2.10c). For $t >$ 450 s, re-nucleation of isolated secondary droplets occurred having growth rates slower than primary droplets due to their coalescence mediated growth. Due to higher droplet mobility on the superhydrophobic hybrid surface (*i.e.* lower contact angle hysteresis of the background) as well as the higher fraction of exposed condensing area near the contact line, primary droplets growing on the superhydrophobic surface showed higher growth rates when compared to secondary droplets (Fig. 2.10d).

For $t >$ 900 s, the majority of the hybrid surface was covered by coalesced droplets (Fig. 2.11). Coalesced droplets on the surface yielded irregular patterns, with the SHP demonstrating vigorous droplet jumping with fresh droplets re-nucleating at the stamped hydrophilic spots.

The superhydrophobic hybrid surface also exhibited higher nucleation effectiveness (η) compared to the hydrophobic surface (Fig. 2.10e). The nucleation effectiveness (η) was defined as the ratio of primary droplets, n_{p} which nucleated on stamped regions to the total number of droplets ($n_{\mathrm{p}} + n_{\mathrm{s}}$) nucleating on the surface, where n_{s} represents the number of secondary droplets ($\eta = n_p/(n_p + n_s)$). For hydrophobic hybrid surfaces, η had a local minimum for $0 \leq t \leq$ 450 s (Fig.10e). During initial nucleation ($t = 0$ s), multiple droplets formed in the hydrophilic regions due to the low nucleation energy barrier, with a limited number of secondary droplets forming on the background ($n_{\mathrm{p}} > n_{\mathrm{s}}$), resulting in a high η. For longer times ($0 < t <$100 s), a

number of secondary droplets (n_s) nucleated on the surface, while the number of primary droplets decreased due to the coalescence of droplets in the hydrophilic regions, decreasing η. For $t > 100$ s, secondary droplets began to coalesce with the primary droplets resulting in $n_p \gg n_s$, and hence increased η. Due to the better self-organization behavior on the superhydrophobic hybrid surface (Fig. 2.10e), the local minimum was shallower at early stages of condensation ($0 \leq t \leq 200$ s). Due to higher droplet mobility, faster growing primary droplets engulfed secondary droplets, increasing the effectiveness, which approaches $\eta = 1$ in later stages of condensation.

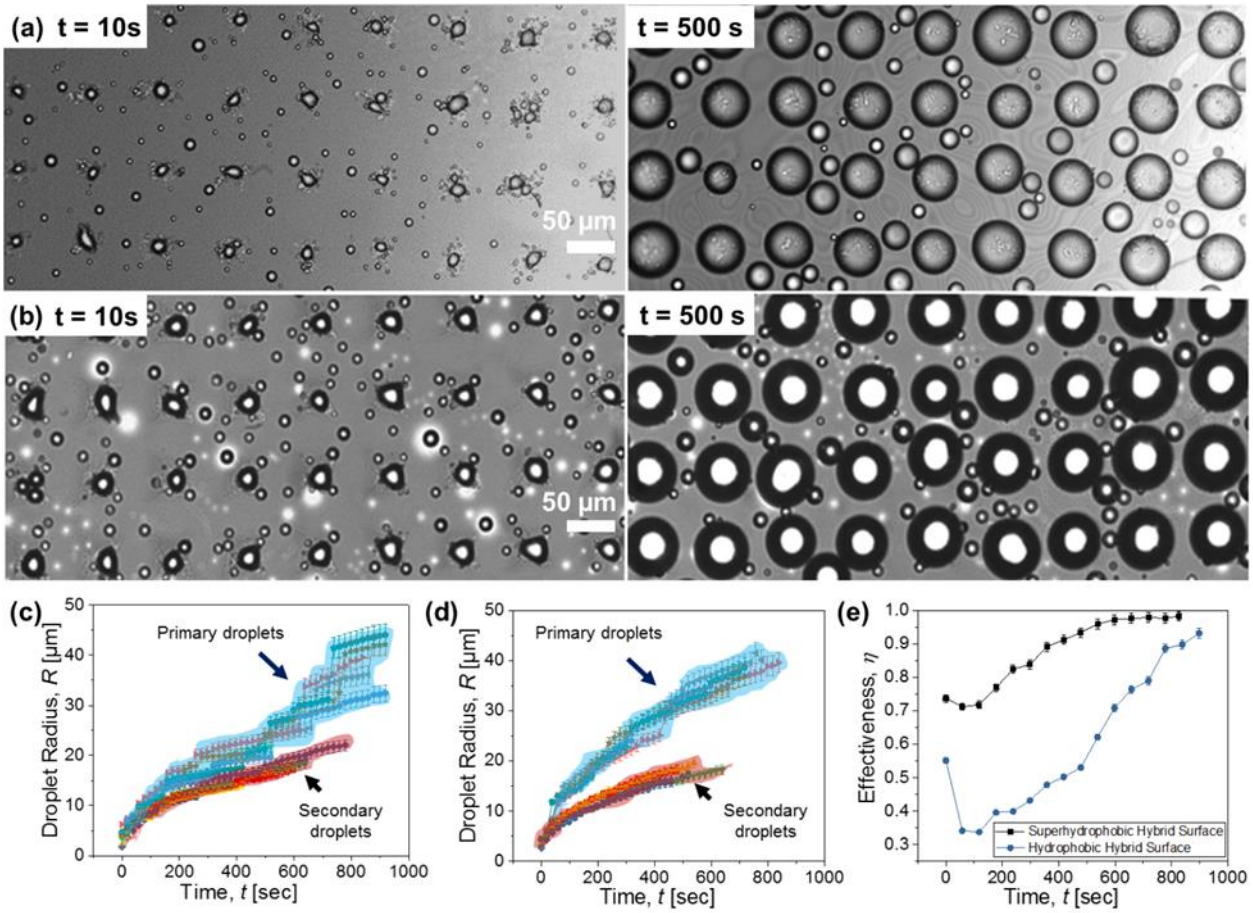

Figure 2.10. Top-view optical microscopy images of water vapor condensation on the (a) hydrophobic and (b) superhydrophobic hybrid surfaces. Growth rate of primary droplets (artificially shaded light blue) which nucleate on stamped spots and secondary droplets (shaded red) as a function of time on the (c) hydrophobic, and (d) superhydrophobic hybrid surfaces. (e) Nucleation effectiveness (η) on the hydrophobic and superhydrophobic hybrid surfaces. Error bars were obtained with propagation of error analysis.

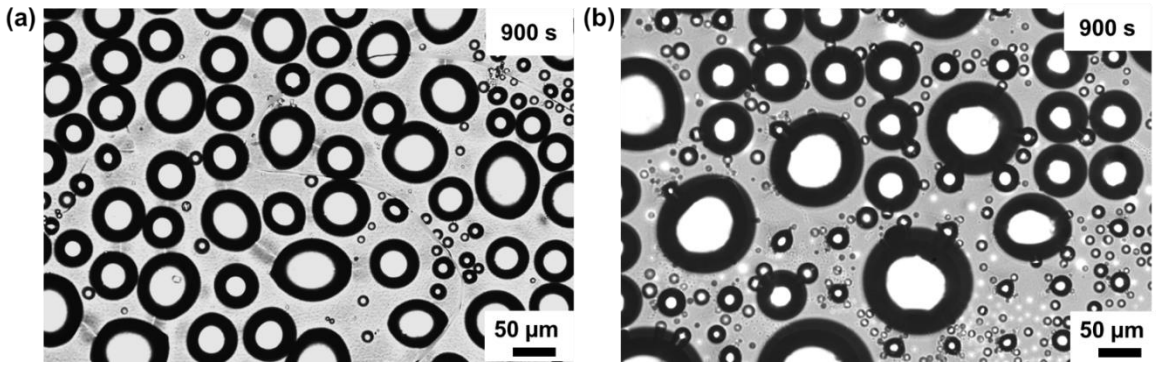

Figure 2.11. Top-view optical microscopy images of atmospheric water vapor condensation on (a) hydrophobic, (b) superhydrophobic hybrid surface at longer time showing irregular droplets pattern due to droplet coalescence and re-nucleation of fresh droplets, this corresponds to the Figure 7 in the manuscript.

2.9. Discussion

Previous studies have shown that asymmetric droplet-surface adhesion is responsible for non-perpendicular droplet departure which promotes multi-droplet jumping and enhances condensate removal.[159, 169, 171-174] Indeed, as observed on our stamped surfaces having superhydrophobic backgrounds, six or more droplets ($N > 6$) with similar sizes were involved in a single droplet jumping event in the absence of surface-structure mediated oblique jumping[159, 173] or jumping relay.[172, 175] The asymmetric adhesion that causes the multi-droplet jumping observed here (Fig. 2.9a) may be due to the slight difference in stamped spot areas (Fig. 2.4a). A larger stamped area provides more local nucleation sites, resulting in a larger droplet size prior to coalescence. Additionally, large surface pinning sites act as pivots for rotation of the coalesced droplets, thus promoting in-plane motion of the merged droplet that is beneficial to multi-droplet jumping.[159] To achieve droplet jumping involving more droplets, it will be interesting to incorporate stamp tips with differing sizes, shapes, and patterns into a single stamp to fabricate hybrid surfaces with an optimized multi-droplet jumping performance by altering droplet coalescence and jumping dynamics through delicately tuning asymmetric surface pinning.

Though we have shown that the presented stamping method based on mechanical stamp-substrate contact is effective for introducing hybrid wettability on various coatings, molecular diffusion at the stamp-coating interface might promise an alternate way to alter local surface chemistry. Indeed, interface diffusion is a common phenomenon at metal/ceramic interfaces present in numerous energy and electronic devices.[176, 177] In the future, it would be interesting to study interfacial atomic or molecular diffusion and its effects on local surface wettability by creating different interface diffusivities between the stamp and substrate. Furthermore, work is needed to study the effects of the developed stamping technique on thicker coatings (> 100 nm thick), key to demonstrate durability of the hybrid surface. The week long tests conducted here represent a good starting point, however are insufficient to demonstrate durability [132].

Though PDMS is a robust elastomer, as shown by the negligible degradation after 100 uses, the key limitation of our approach is the sensitivity of the pyramidal micro tips to stamping load. Under pressure, the micro tips have elastic deformation. At elevated loading, the square shaped pyramid base becomes visible on the surface. At loads < 5 N/cm^2, no significant stamp marks appear on the surface, whereas for > 5 N/cm^2, the square pattern becomes more obvious (Fig. 2.12). For samples stamped with 10 to 50 N/cm^2 loads, droplets showed higher adhesion to the surface during condensation experiments. The higher adhesion occurred because the tips remove the coating from larger areas with increased stamping load, which results in jumping of larger size droplets [159].

Although controlling the hydrophilic spot size while stamping was enabled due to the elastomeric properties of the PDMS stamp, future work is needed to enable tighter control of spot size variation due to its importance on both nucleation density and jumping behavior. In addition, spot pitch (spacing) plays a key role in condensation and boiling.[26, 30, 178-180] Smaller pitch

leads to denser hydrophilic spots with lager nucleation site density and higher work of adhesion that delays droplet detachment. Indeed, previous studies on biphilic surfaces have suggested an optimal pitch in terms of jumping-droplet condensation heat transfer.[16] Future work is needed to examine the fabrication limitations of creating stamps what can enable variable spot pitch not considered in this study.

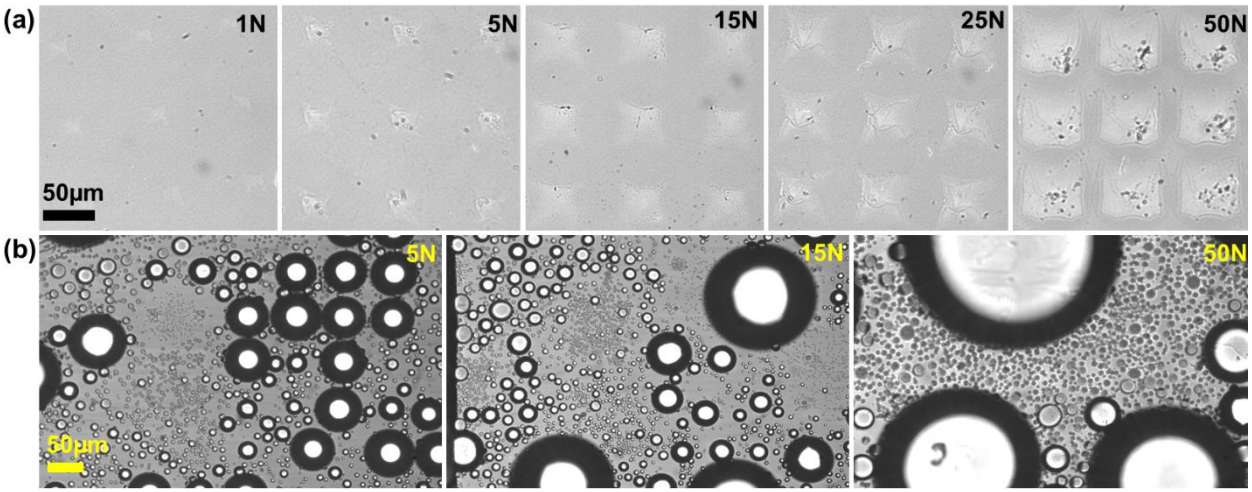

Figure 2.12. Top-view optical microscopy images of (a) hybrid surfaces stamped with different stamping loads, and (b) water vapor condensation on the stamped hybrid surfaces (with 5N, 15N, and 50N loads) after 10 minutes of condensation. Surfaces stamped with larger loads showed large size droplets involved in jumping due to higher pinning.

Non-elastomeric (metal or resin) materials that are not deformable are good candidates for future stamps that can create hydrophilic spot sizes. Additively manufactured stamps with nano-tipped features are a potential solution to tackle the elasticity issue of PDMS. Moreover, nano 3D printing can be used to make negative templates of nano tipped resin stamps, which can be used to generate nanotip metal stamps by electrodeposition of metal on the template.

In this study, the microtip pitch range (c = 55 to 85 μm) was too narrow to study meaningful droplet dynamics and jumping behavior. Micro tips with pyramidal geometries were fabricated due to the advantages of well-controlled fabrication using anisotropic etching in Si and also to

obtain small radii of curvature (less than ~100 nm) at the pyramid tips under no preload conditions.[131] Hence, fabrication of hybrid surfaces with nanometer scale pitch is challenging with the developed method. A promising method to overcome this challenge is to integrate the stamp with a programmable three-axis stage to mimic the stitching approach.[181, 182] High resolution stitching through programmable offset stamping not only enables higher hydrophilic spot density using low complexity stamps, but increases the scalability of the fabrication technique. Significant opportunities exist to extent the approach developed here for hybrid surface fabrication on curved surfaces (tubes) using roll-to-roll methods.[183-185] Roll-to-roll manufacturing of curved hybrid surfaces would involve two adjacent rollers, where the first roller (the donor) would have the micro/nano scale features while a second roller (the target) would be a coated sample. The fabricated hybrid tube surfaces with variable spot sizes and pitches can be used to visualize condensation phenomena and also study condensation heat transfer performance. Indeed, condensation on hybrid or biphilic surfaces has been shown to enhance heat transfer by allowing selective drainage of the condensate film on hydrophilic regions.[186-189] In addition to roll-to-roll, future work is needed to develop the stamping approach on surfaces having multi-axis curvature[190] or even arbitrary shaped surfaces, using flat stamps.

2.10. Conclusions

In this work, we demonstrated a simple, scalable and rapid stamping technique to fabricate hybrid surfaces. The technique involves using a pre-fabricated stamp, which is reusable and can be used to stamp various coated hydrophobic/superhydrophobic surfaces. The hybrid surfaces fabricated here show approximately 44X higher droplet nucleation site density enhancement. Atmospheric vapor condensation and coalescence-induced droplet jumping experiments showed that

superhydrophobic hybrid surfaces possess global superhydrophobicity with local hydrophilicity, resulting in an almost 14X improvement in multi-droplet jumping compared to homogenous superhydrophobic surfaces. The hybrid surfaces fabricated here demonstrate spatially controlled heterogeneous nucleation of condensation, enhance droplet nucleation density, and a narrower droplet distribution. Our study not only presents an effective and high-throughput approach to fabricating hybrid surfaces using a facile stamping technique, but also provides insights into the interplay between the dual wettability of the hybrid functional surfaces during condensation heat transfer.

CHAPTER 3

Resilient Hydrophobic Surfaces Enabled by Multi-Layer Fluorinated Diamond Like Carbon

3.1. Introduction

In chapter 2, we demonstrated a simple method for developing mixed wettability surfaces, which requires functionalization of the surfaces with hydrophobic coating. However, designing a suitable hydrophobic coating has been the main decades-long challenge to deploying dropwise condensation in real power systems. To overcome this challenge, five coating requirements need to be met simultaneously (Fig 3.1). 1) The coating needs to be fabricated scalably and must be applicable to a variety of potential substrate materials. Typical condensers in a power station are fabricated from different metals or metal alloys depending on the region, and they are relatively large (~10 m) often containing thousands of tubes in a bundle. 2) The coating needs to be thin (< 5 μm) so that the coating parasitic thermal resistance does not off-set the benefit of high dropwise condensation heat transfer coefficient[38]. 3) The coating needs to resist delamination caused by the condensate capillary force. Specifically, condensation-induced blistering, which is the most direct coating degradation mechanism, enables condensate penetration between the interface of the coating through surface defects. This penetration causes localized pressure, and gradually results in complete coating delamination[39]. 4) The coating must be thermally stable at elevated temperature steam environments. 5) The coating needs to resist mechanical abrasion during

*This chapter was mostly reprinted (adapted) with permission from *Nature Energy*. 2022, *Submitted*. Copyright © 2022 Nature Energy. Muhammad Jahidul Hoque, Longnan Li, Jingcheng Ma equally contributed to the work. As the lead first author Muhammad Jahidul Hoque contributed to the study via sample fabrication, conducting experiments, analyzing data and writing the manuscript. Dr. Nenad Miljkovic guided the research and revised the manuscript and is the co-corresponding author.

condenser fabrication, assembly, maintenance, and operation. Classical artificial hydrophobic materials such as low surface energy polymers cannot meet these requirements and cannot be utilized due to their low elastic modulus, and poor thermal and mechanical stability.

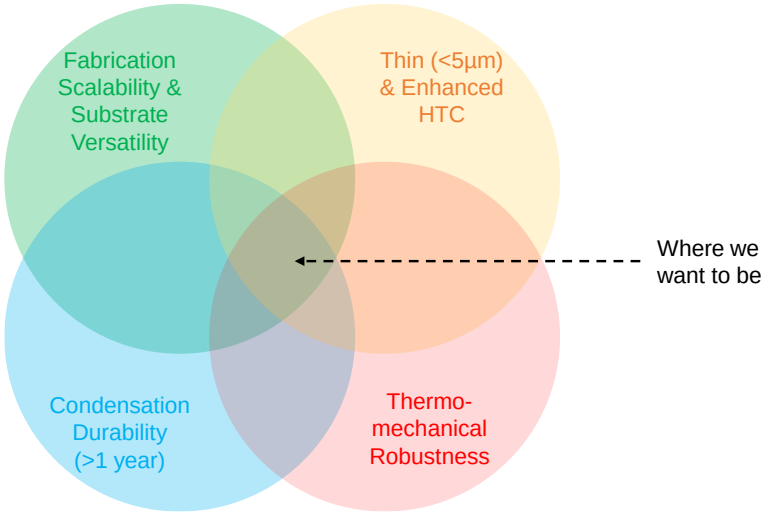

Figure 3.1. Focal point of fabricating a robust hydrophobic coating for energy applications.

In an attempt to finally craft durable hydrophobic coatings, past strategies have generally focused on optimizing the coating geometric and structural design. By doing so, these have demonstrated that coating robustness can be enhanced by surface structures which act as a protective or sacrificial armor[40-42]. However, these hierarchical protective structures make the overall coating thick (> 10 μm), and unusable for condensation heat transfer. Furthermore, armor approaches are relatively difficult to scale to arbitrary substrates and materials. Thus far, little progress has been made on enhancing the coating intrinsic properties in order to overcome the durability challenge.

Interestingly, a coating material which can potentially achieve the required coating intrinsic properties for steam condensation applications is diamond-like carbon (DLC). The intrinsic properties of DLC thin films gives them the desired mechanical and thermal stability[191-193].

Moreover, the abrasion resistance and corresponding interfacial adhesion of these DLC coatings can be enhanced by adapting multilayer designs[194, 195]. However, the utilization of such structures for phase-change heat transfer has been under-explored. Specifically, the majority of the past studies have explored tribological, medical, mechanical, wettability, and dielectric property improvement with a focus on altering the fabrication method, recipe modification, and doping. [194, 196-204] Limited focus has been places on substrate versatility, or the long-term sustainability of enhanced properties. Furthermore, no past study has synergistically considered the crucial parameters required to achieve robust hydrophobic coating design or demonstrated continual dropwise condensation under sustained long-term (> 1 year) steam exposure.

In this chapter, we demostarte a hydrophobic coating synthesis and application approach using multilayer fluorinated diamond-like carbon (F-DLC) that meets all requirements to enable the sustained dropwise condensation of steam. By using scalable co-deposition of a short chain fluorocarbon with well-established DLC (a-C:H), we demonstrated a hydrophobic coating having a surface energy characteristics of non-polar polymers, with a high Young's modulus approaching that of metals. We demonstrate the versatility of F-DLC on a wide range of substrates including crystalline, non-crystalline and common engineering metals, all showing similar surface energy after coating. Multilayer fluorinated diamond-like carbon not only demonstrates enhanced dropwise condensation heat transfer, but also durability in moist environments for a period of more than three years. Characterization of the compatibility of multi-layer F-DLC in elevated air and inert gas temperature environments exceeding 300ºC and sustainability after 5000 mechanical abrasion cycles demonstrates thermo-mechanical resiliency. The outcomes of our work not only develop a low surface energy coating capable of implementation for a plethora of versatile applications, they demonstrate a means to overcome fundamental barriers for generating

hydrophobic surfaces that can achieve extended lifetime during exposure to harsh thermo-mechanical environments, thus paving the way for direct enhancement of energy efficiency for a majority of large-scale energy production infrastructure.

3.2. Hydrophobic Coating Design Strategy

The rational design of the multi-layer F-DLC coating was guided by our physics-based understanding of condensation-induced blistering. The quantitative parameter that describes blistering, Ω, demonstrates that delamination of a hydrophobic coating will occur if $\Omega > 1$ [39]. Specifically, Ω is governed by the pinhole size, R_{d}, the base radius of the pinhole-adjunct delaminated region, R_{b0}, the liquid-vapor surface tension of the working fluid (water) γ, as well as the coating intrinsic properties including its wet adhesion G, Young's modulus E and thickness h:

$$\Omega = \left(\frac{1.04R_{\mathrm{b0}}}{R_{\mathrm{d}}}\right)\left(\frac{\gamma^4}{EG^3h}\right)^{\frac{1}{4}}. \tag{3.1}$$

For a typical 100-nm thick fluoropolymer deposited on a metal ($R_{\mathrm{b0}} \approx 5R_{\mathrm{d}}$, $E \approx 1$ GPa, $G \approx 10\ \mathrm{mJ/m^2}$), $\Omega \approx 3.6$. Hence, polymers are unable to prevent delamination, unless their thicknesses exceed 10 μm (where $\Omega \approx 1.0$). Our multi-layer F-DLC coating decreases Ω by using several synergistic and rationally selected approaches. By co-depositing short-chain PFCs with the top DLC (a-C:H) surface, we enable high Young's modulus of E = 78 GPa and low surface energy of ~ 30 mJ/m^2. By deploying a well-established titanium bonding layer approach, we enable an interfacial toughness of ~ 10 J/m^2. Utilizing the Ti-DLC-FDLC multilayer, we eliminate pinholes, resulting in an ultra-low $\Omega < 4 \times 10^{-3}$ via the design of a 1-μm thick multi-layer F-DLC coating.

The Ti-DLC-FDLC multilayer focuses primarily on blistering and delamination, and satisfying abrasion resistance and high temperature stability requires further layer design. In addition to the aforementioned 3-layer design, we included an additional layer of co-deposit DLC and silica (a-C:H:Si:O) between the DLC (a-C:H) layer and the Titanium adhesion layer, which we termed DLN. Such design is well-adapted in conventional DLC multilayers to 1) Enhance the adhesion with the Ti layer by silica infusion, 2) provides good thermal stability and acts as stress reliever, and 3) further decrease the pinhole density. As a result, the multilayer F-DLC coating designed here not only promises reliable adhesion between the coating and a variety of arbitrary substrates, it also decreases interfacial stresses from abrasion or thermal expansion by increasing the numbers of layered interfaces.

3.3 Experimental Procedures

F-DLC Nanofabrication Method. The four-layer F-DLC coating manufacturing process uses a combination of PVD sputtering and PACVD. The Ti layer is sputtered on the substrate and while the remaining three layers are deposited with PACVD in a vacuum chamber at 250ºC. On the Ti coated substrate, DLN is deposited by PACVD. Hydro-carbonated DLN gases integrated with silicon and oxygen provide the deposition of a soft DLN (a-C:H:Si:O) layer. Next the DLC layer is deposited in the same environment. Finally, the fluorine precursor in liquid form is introduced to the system which is then vaporized and co-deposited with the final DLC layer at the end of the deposition process yielding a top fluorinated DLC (f-DLC) layer.

Cross Sectional SEM. The cross-section imaging of a multilayer F-DLC coating on a polished silicon substrate was prepared through focused ion beam (FIB, Thermo Scios2 Dual-Beam

SEM/FIB) milling. The ion beam voltage and current were set into 30 kV and 15 nA, respectively. After milling, the coating cross-section was imaged by ultra-high resolution SEM.

Energy Dispersive X-ray Spectroscopy (EDS) analysis. Qualitative chemical element analysis for each layer of the F-DLC coating was conducted with EDS (JEOL JSM 7000F Analytical SEM/EDS). The accelerating voltage was set to 10 kV during the analysis.

X-ray photoelectron spectroscopy (XPS). XPS was performed using a monochromatic Al Kα-source (Kratos Axis Ultra, Kratos Analytical). The size of the source beam was 2 mm× 2 mm, and the size of the analyzed region was 0.3 mm × 0.7 mm. The instrument was maintained at a pressure of 10^{-7} Pa during the experiments. The spectra were post processed with CasaXPS software to determine the change in composition of the sample surfaces.

Time-domain Thermo-reflectance (TDTR). Prior to thermal conductivity measurement, the sample was coated with a 111 ± 2 nm-thick Al film by magnetron sputtering (AJA Orion3 Sputter Coater). It was assumed that the film was free of adsorbed water because the sputtering procedure involved pumping the sputter chamber down to $\approx 1.33\times10^{-5}$ Pa. The TDTR system uses a mode-locked Ti:sapphire laser tuned to 785 nm and a repetition rate of 74.6 MHz.[39] The output laser was split into separate pump and probe beams by a polarizing beam splitter. The power of the pump beam was set to 10 mW, and the probe beam power was set to 5 mW. The intensity of the pump beam was modulated with an electro-optic modulator at $f = 10.1$ MHz synchronized with an RF lock-in amplifier. The time delay of the arrival of the pump and probe beam to the surface was adjusted by a mechanical delay stage in the path of the probe beam. The pump and probe beams were overlapped on the sample and the beams were focused using a 5X objective lens. The laser spot size was ≈ 10.7 μm. A photodiode was used to detect the reflected probe beam and the light from the pump beam was blocked from reaching the detector by spatial filtering and two-tint

wavelength filtering. The signal was measured by a lock-in amplifier connected to the photodiode. The thickness of F-DLC (1.65 ± 0.05 μm) is measured by cross-section SEM imaging. $\sqrt{kC} = (1.07 \pm 0.05) \times 10^{-3}$ (W·s$^{1/2}$)/(m·K). The heat capacity of amorphous carbon film is usually within the rage of 2.5 J/(cm^3·K),[205] hence the thermal conductivity of the film $k = 0.46 \pm 0.05$ W/(m·K). The error comes from experimental uncertainty (~10%).

Surface Energy Measurement. The surface energy was measured by the contact angle method[206] using Fowkes theory and the Young-Dupre equation.[207] The dispersive, E^{d} and polar, E^{p} components of the free surface energy were determined by measuring the intrinsic advancing contact angle between the surface and two test liquids with known surface energy components. A non-polar test liquid, diiodomethane was first used to obtain the dispersive component, E^{d} , where the polar component, E^{p} is negligible. Then, deionized (DI) water was used to obtain the polar component, E^{p} with known dispersive component, E^{d} from the previous measurement. All apparent contact angles were measured using a microgoniometer (MCA-3, Kyowa Interface Science).

Atmospheric Water Vapor Condensation Experiment. To induce water droplet condensation in the atmospheric laboratory environment having air temperature T_{a} = 25 ± 1ºC and a relative humidity *RH* = 50 ± 5% (RO120, Roscid Technologies), we placed the samples horizontally on a cold stage (Linkam T95-PE) and reduced the stage temperature to T_{c} = 2.0 ± 0.1ºC to enable observation of water vapor condensation on the substrates using a top-view optical microscopy (Nikon Eclipse LV100) coupled to a monochrome camera (Nikon DS-Qi2).[132]

HTMS SAM Hydrophobic Surface Fabrication. Polished aluminium and copper tabs were first ultra-sonicated in acetone (10 min), followed by IPA (10 min), then thoroughly rinsed in DI water and dried under a clean N_2 gas stream. To fabricate the hydrophobic surface, the Al and Cu tabs were functionalized with heptadecafluorodecyltrimethoxy-silane (HTMS, TCI America, CAS #: 83048-65-1) using the vapor phase deposition method.[208] Briefly, the substrates were placed in a glass beaker with a vial of HTMS toluene solution (5% v/v). A glass lid was placed on top to seal the container, followed by heating in atmospheric pressure oven (Thermo Scientific, Lindberg Blue M) at 80± 5°C for 3h to allow conformal HTMS SAM deposition.

Long-term Condensation Durability. The durability tests were performed in a customized vacuum compatible environmental chamber (Kurt J. Lesker). The main environmental box chamber (16 inch by 16 inch by 16 inch in size) consists of a front door to access all samples inside, 10 view ports (DN100CF, Kurt J. Lesker), and 17 feedthrough apertures for various components. The front door was sealed with a rubber gasket; all CF flanges were sealed with silver plated copper gaskets; and, KF flanges were sealed with stainless steel centering rings accompanied by nitrile rubber O-rings. Resistive heating cables (AWH-101-040D, HTS/Amptek) were wrapped around the exterior of the chamber walls to prevent condensation on the inside chamber walls and view ports. The heaters were controlled by a voltage regulator (DNG-600PH-DK, Lutron). The chamber wall temperature was maintained at $\approx 40^{o}$C throughout the experiment. Heating cables were insulated to prevent unnecessary condensation and limit heat losses to the ambient environment. Cooling water was supplied to the aluminum cold plates in the chamber from a large capacity chiller (Merlin M150, Thermo Fisher Scientific) via KF fluid feedthroughs (Kurt J. Lesker). To monitor the coolant water flow rate, an electromagnetic flow meter (FMG93-PVDF, Omega) with an accuracy of ±1% of the reading was integrated along the coolant inlet line.

To remove non-condensable gasses prior to the experiments, a bellows valve (Ideal Vacuum) was attached to the top of the environmental chamber and connected to a rotary vane vacuum pump (KJLC-RV212, Kurt J. Lesker). An inline liquid nitrogen (LN2) cold trap (Kurt J. Lesker) was incorporated into the line from the environmental chamber to the vacuum pump via bellows tubes (Kurt J. Lesker) to remove any moisture from the pumped air from inside of chamber, which also helps produce a lower base pressure and achieve faster pump down. A secondary bellows valve (Kurt J. Lesker) was integrated onto a tee flange between the vacuum pump and the LN2 trap to release the vacuum to ambient once the pump down process is finished. In order to monitor the pressure within the chamber, a vacuum pressure transducer (925 Micro Pirani, MKS) was installed on top of the chamber. A tertiary bellows valve was attached to the environmental chamber as a leak port between inside of the chamber and the ambient to release the vacuum once the experiments are finished.

A secondary stainless-steel water reservoir (or degassing chamber) was installed to supply water vapor inside the environmental chamber. The water reservoir was connected to the environmental chamber via bellows tubes (Kurt J. Lesker) and two diaphragm valves (SS-DSS4, Swagelok). Bellows tubes were wrapped with tape heaters (HTWC101-010, Omega) to prevent condensation and icing during the pump down process. Five 6.35 mm (1/4 inch) diameter access tubes were welded directly on top of the degassing chamber flange and were attached with three independent diaphragm vales (SS-DSS4, Swagelok), a pressure relief valve, and a thermocouple. The first diaphragm valve was connected to the vapor supply line connecting the top of the water reservoir to bottom of the environmental chamber. The second valve was connected to the liquid condensate drainage line connecting the bottom of the water reservoir to the environmental chamber. The third value was connected the top of the water reservoir to the ambient air to establish a water filling

port. The water reservoir was wrapped by a resistive heater (AWH-101-040D, HTS/Amptek) and insulated to limit heat losses. Heating power was controlled by a voltage regulator (DNG-600PH-DK, Lutron). To prevent over-pressurization of the water vessel, the water temperature was monitored using a K-type thermocouple located inside the water reservoir. A pressure relief valve (SS-RL3S4 , Swagelok) was set at 303.975 kPa (3 atm) to prevent overpressure. The mass of the water reservoir was monitored with a digital mass scale (CPWplus 75, Adam Equipment Inc.).

Four cold plates (12.0 inch by 3.5 inch, CP10G05, Lytron) forming heat sinks were installed inside the environmental chamber using aluminum frames and connected to the external chiller loop to promote condensation. The heat sinks were customized to hold up to 40 specimens (1 inch by 2 inch samples sizes). Screw threads were created on each cold plate to mount samples. The samples were mounted on the heat sinks using Polyether ether ketone (PEEK) screws and washers (Misumi), while the other sides of the cold plates were insulated with PEEK sheets (Misumi) to limit condensation outside of the specimen area. The PEEK material was chosen as an insulation material due to its low outgassing rate, low thermal conductivity, and excellent chemical and thermal resistance. The PEEK screws were chosen in order to limit potential for galvanic or electrochemical corrosion when connecting dissimilar sample materials to the aluminum cold plate.

In order to monitor temperatures within the system, K-type thermocouple bundles were connected to the chamber via thermocouple feedthroughs (TFT5KY00008B, Kurt J. Lesker). Inside the chamber, the temperature of the cold plates, side walls, water vapor, and collected condensate were monitored throughout the three year experiment. The thermocouples and pressure transducer were electrically connected to a data acquisition (DAQ) system which was built on a CompactDAQ Chassis (cDAQ-9174, National Instruments). All collected data was analyzed with in-house LabVIEW code. The DAQ system includes a thermocouple module (NI-9213, National

Instruments), a digital signal module (NI-9423, National Instruments), an analog signal module (NI-9209, National Instruments), and a terminal block (NI-9923, National Instruments). Finally, multiple DSLR Cameras (K-50, Pentax) were placed in line with all view ports on the chamber for visual recording of steam condensation process on samples to track coating degradation.

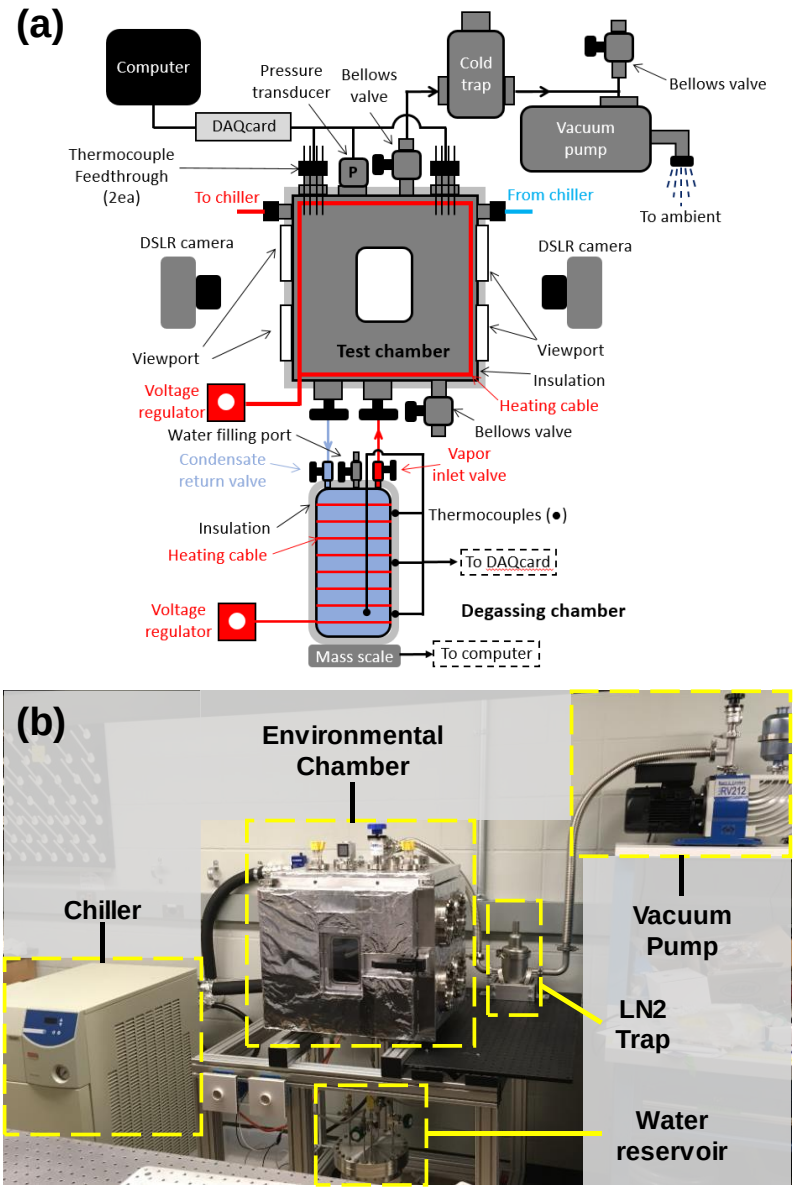

Figure 3.2. (a) Schematics of experimental setup (not to scale). (b) Photograph of the experimental setup from the front.

A set of strict procedures were followed to ensure consistency throughout the experiments. First, the chamber interior and sample mounting rig were thoroughly cleaned with isopropyl alcohol (IPA) to remove any contaminants. The water reservoir was filled with deionized (DI) water. The heating cables wrapping the environmental chamber were energized to maintain the chamber walls at ≈ 40ºC. The chamber walls were heated to dry out the inside of the chamber prior to pump down and prevent condensation during the experiments. The test samples were mounted on the aluminum cold plates using PEEK screws and PEEK washers. Then, the test rig with cold plates were connected to the coolant line. Simultaneously, thermocouples were attached to cold plates and chamber walls.

Given the long period of the durability test (> 1 month), a leak test was performed to ensure that no leaks were present before each experimental trial. All diaphragm valves on the degassing chamber and the leak port bellows valve on the environmental chamber was closed. The LN2 trap was filled with LN2. The bellows valve connecting the vacuum pump to the ambient was closed, and another bellows valve connecting the environmental chamber and LN2 trap was opened. Then, the vacuum pump was turned on to initiate the pump down process. The chamber pressure was monitored using the pressure transducer. In the middle of pump down process, the large capacity chiller was turned on, and the coolant temperature was set to 10°C. The inflow rate of the coolant was monitored using the electromagnetic flowmeter. This process took approximately one hour to achieve the target vacuum conditions ($P < 5$ Pa). Whenever necessary, the LN2 trap was refilled. The LN2 trap was cleaned midway during the pump down process, since frost would form on the LN2 trap and block the vacuum line during pump down. When the target pressure was achieved, the valve connecting the environmental chamber and the LN2 trap was closed, and the pump was turned off. Then, the valve connecting the vacuum pump and the ambient was opened to release

vacuum in the pump line. The chamber was left under vacuum for >24 hours to perform the leak test, and the chamber pressure was monitored with the pressure transducer. The leak rate was characterized to acquire the fidelity of the data. The initial leak rate was controlled to less than 1 Pa/min, with the long term leak rate controlled to less than 0.1 Pa/min. When the leak test was finished, the vacuum was released by opening the valve connecting the environmental chamber and the ambient.

Once the leak test was finished, the experiment was initiated. The vapor supply diaphragm valve and the water filling valve on the water reservoir were opened, and the tape heater around the water reservoir was turned on with the voltage regulator set to maximum output to boil the water. During the boiling process, the excess water that spilled from the water reservoir was removed. In the meantime, most of the dissolved gas in the water was removed. The temperature of the water and reservoir were monitored using thermocouples. Once the water temperature reaches slightly higher than 100°C for at least 10 minutes, the voltage regulator was turned down, and all the valves were closed. Then, the vacuum pump down process was repeated.

When the target pressure ($P < 5$ Pa) inside the environmental chamber was reached, the bellows valve connecting the environmental chamber and LN2 trap was closed, the vacuum pump was turned off, and the valve connecting the vacuum pump and the ambient was opened to release the vacuum. Immediately after closing the bellows valve on the environmental chamber, the vapor supply valve and condensate drainage valve on the water reservoir were opened. Steady state conditions were typically reached after approximately 30 min of full operation. Throughout the experiments, the data (temperatures, pressure, and mass scale) was collected, and the images of each sample were recorded using the DSLR cameras.

Bond Number Calculation to Predict Filmwise to Dropwise Condensation Transition. The droplet Bond number is defined as $\mathrm{Bo} = R_\mathrm{f}^2/l_\mathrm{y}^2$, where R_f is the characteristic lateral length of the liquid droplet, taken to be its final equilibrium radius immediately before departure. The droplet departure size R_f can be calculated from a force balance between the gravitational body and contact line pinning forces and is defined as:[154]

$$R_\mathrm{f} = \sqrt{\left[\frac{6\gamma\,(\cos\theta_\mathrm{r} - \cos\theta_\mathrm{a})\sin\theta_\mathrm{e}}{\pi\rho g(2 - 3\cos\theta_\mathrm{e} + \cos^3\theta_\mathrm{e})}\right]},$$

where θ_a, and θ_r are the apparent advancing and receding contact angles, θ_e is the equivalent contact angle immediately before shedding from the condensing surface, defined as:

$$\theta_\mathrm{e} = \cos^{-1}(0.5\cos\theta_\mathrm{a} + 0.5\cos\theta_r).$$

Here, l_y represents the capillary length defined as, $l_y = \sqrt{\gamma/\rho g}$, where γ and ρ are the condensate surface tension and density, respectively, and g is the gravitational constant. A previous study showed that the critical Bond number, $\mathrm{Bo}_\mathrm{crit} \approx 1.4$, forms the transition boundary, with Bo > 1.4 indicating filmwise condensation transition.[154]

3.4. Nanofabrication and Structure Properties

The F-DLC fabrication process is a multi-layer film comprised of a primary adhesion layer deposited via physical vapor deposition (PVD) sputtering followed by plasma assisted physical vapor deposition (PACVD) to build the remaining three layers. The PACVD coating is done in a vacuum chamber at 250ºC, maintaining localized filaments to assist in homogenous plasma conditions throughout the vessel. Hydro-carbonated DLN gases which give the elemental structure were introduced in the system which was deposited on the Ti-coated substrate. Then a fluorine precursor as a liquid form is introduced to the system which was vaporized and co-deposited with

the DLC layer at the end of the deposition process. In our study, a ~0.29 µm-thick layer of PVD sputtered Titanium (Ti) on the substrate ensures strong adhesion between the subsequent multi-layer deposition and the substrate. The Ti PVD process is followed by the deposition of a ~0.3 µm-thick DLN (a-C:H:Si:O) intermediate layer, a ~0.51 µm-thick DLC (a-C:H) layer, and finally a ~0.5 µm-thick fluorinated DLC (f-DLC) layer (a-C:H:O:Si:F), in sequential order.

Cross-sectional SEM of the coating shows a total thickness of ~1.65 ± 0.05 µm (Fig. 3.3a inset). As shown in Fig. 3.3a, energy-dispersive X-ray spectroscopy (EDS) analysis of each layer ensures the presence of the required respective components. The multi-layer F-DLC film not only generates a pinhole-free coating but also improves the mechanical resiliency of the surface.

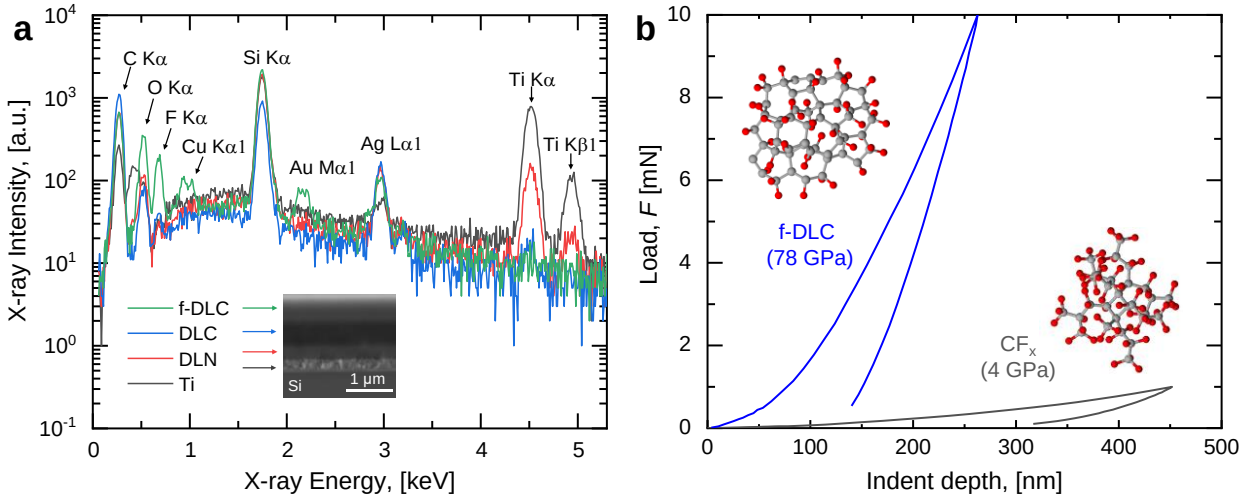

Figure 3.3. Design and structure of F-DLC. (a) Layer structure and chemistry of F-DLC obtained from EDS. Peaks of Au and Cu stem from impurities present in the EDS chamber. Inset: cross-sectional SEM image of F-DLC deposited on a polished silicon wafer. (b) Load-depth curve showing F-DLC has a ~20X higher Young's modulus when compared to amorphous C-F materials. Inset: schematics of the atomic structures of the top f-DLC coating in the F-DLC stack and the amorphous C-F coating.

To evaluate and compare the elastic properties, nanoindentation (Hysitron TI 950 TriboIndenter) was performed on both the F-DLC multiplayer coating and a control sample consisting of an amorphous carbon-fluorine (CFx) film of equivalent thickness. The depth of the indent was controlled by the applying force from the indenting tip (Berkovich TI-0039 standard

tip, Bruker) to the samples. As shown in Fig. 3.2b, the F-DLC coating shows a ~20X higher Young's modulus when compared to amorphous carbon-fluorine materials.

3.5. Surface Characterization and Wettability

The thermal conductivity of the fabricated multi-layer F-DLC sample was measured using time-domain thermoreflectance (TDTR). Figure 3.4a shows the surface reflectivity change as a function of the time delay Δt between the pump and probe pulses for the test sample, yielding a thermal conductivity of the coating of k = 0.46 ± 0.05 W/(m·K) by assuming a volumetric heat capacity consistent with previous measurements on DLC materials, $C = 2.5$ J/(cm^3·K).[209] Due to the limited thermal penetration depth of the TDTR measurement, $d = \sqrt{k/\pi C f} \sim$ 100 nm, we measure the thermal conductivity of the top fluorinated f-DLC layer. As the top f-DLC layer is the most amorphous among all layers due to the fluorination process, it has the lowest thermal conductivity of all layers, ensuring that our measurement represents the lower-bond thermal conductivity of the entire multilayer coating.

The mechanical properties of DLC-like materials are strongly related to the hybridization of sp^2 and sp^3 carbon bonding. To quantitatively measure the carbon composition of the top layer, we used X-ray photoelectron spectroscopy (XPS, Fig. 3.4b). The main peak of the C1s spectrum was decomposed into three components: the sp^3 (C-C) bond at 284.4 eV, the sp^2 (C=C) bond at 285.2 eV and the C-O or C=O bonds at 286.6 eV. We did not observe noticeable amounts of C-Si bonding, which should be located at ~283 eV. The area of the decomposed peaks indicates that relative content of the sp^3 and sp^2 bonds is 47 ± 10% and 35 ± 10%, respectively, where the uncertainties were calculated from the uncertainty of the sp^2 peak position (0.1 eV). The relative content result indicates that although the top layer contains fluorine, the carbon bonding structure

does not deviate appreciably from typical DLC materials and maintains a high Young's modulus and hardness (Fig. 3.3b). The F1s spectrum showed that most fluorine atoms are bonded with carbon by covalent and semi-ionic C-F bonds.

The surface energy (E_s) of the F-DLC coating was measured by probing the advancing contact angle of deionized (DI) water and diiodomethane (Dii) on the F-DLC surface, which yielded E_s = 24 ± 1 mJ/m^2. Details of the surface energy measurement can be found in the Experimental Section.[206] Although the surface energy is 25% higher when compared to Teflon-like materials having surface energy of ~20 mJ/m^2, the F-DLC coating maintains a ~20X higher Young's modulus. Figure 3.4d shows the surface energy and Young's modulus of many commonly used engineering materials, demonstrating that F-DLC combines the merits of both low surface energy and high mechanical modulus.

To demonstrate versatility, we deposited F-DLC on a variety of substrates, showing substrate-independent wetting. The wettability of the F-DLC coated substrates were determined by performing water contact angle measurements using a microgoniometer (MCA-3, Kyowa Interface Science). The apparent advancing contact angle on an F-DLC coated smooth silicon wafer (University Wafer) is, $\theta_a = 97.5 \pm 1°$ (Fig. 3.4e). Figure 3.4e shows the apparent advancing (θ_a) and receding (θ_r) contact angles of water on a wide variety of F-DLC coated substrates. A slight variation in the apparent advancing contact angle (θ_a), and contact angle hysteresis ($\Delta\theta = \theta_a - \theta_r$) among the substrates occurred due to the variability in topological homogeneity (roughness) of the surfaces.[154] Surface roughness homogeneity also affects the droplet distribution and droplet shapes during water droplet condensation. Figure 3.4f shows top view optical microscopy images of atmospheric water vapor condensation on the different F-DLC

coated substrates demonstrating spherical droplet morphologies with highly mobile contact lines, key to attaining high quality hydrophobicity.

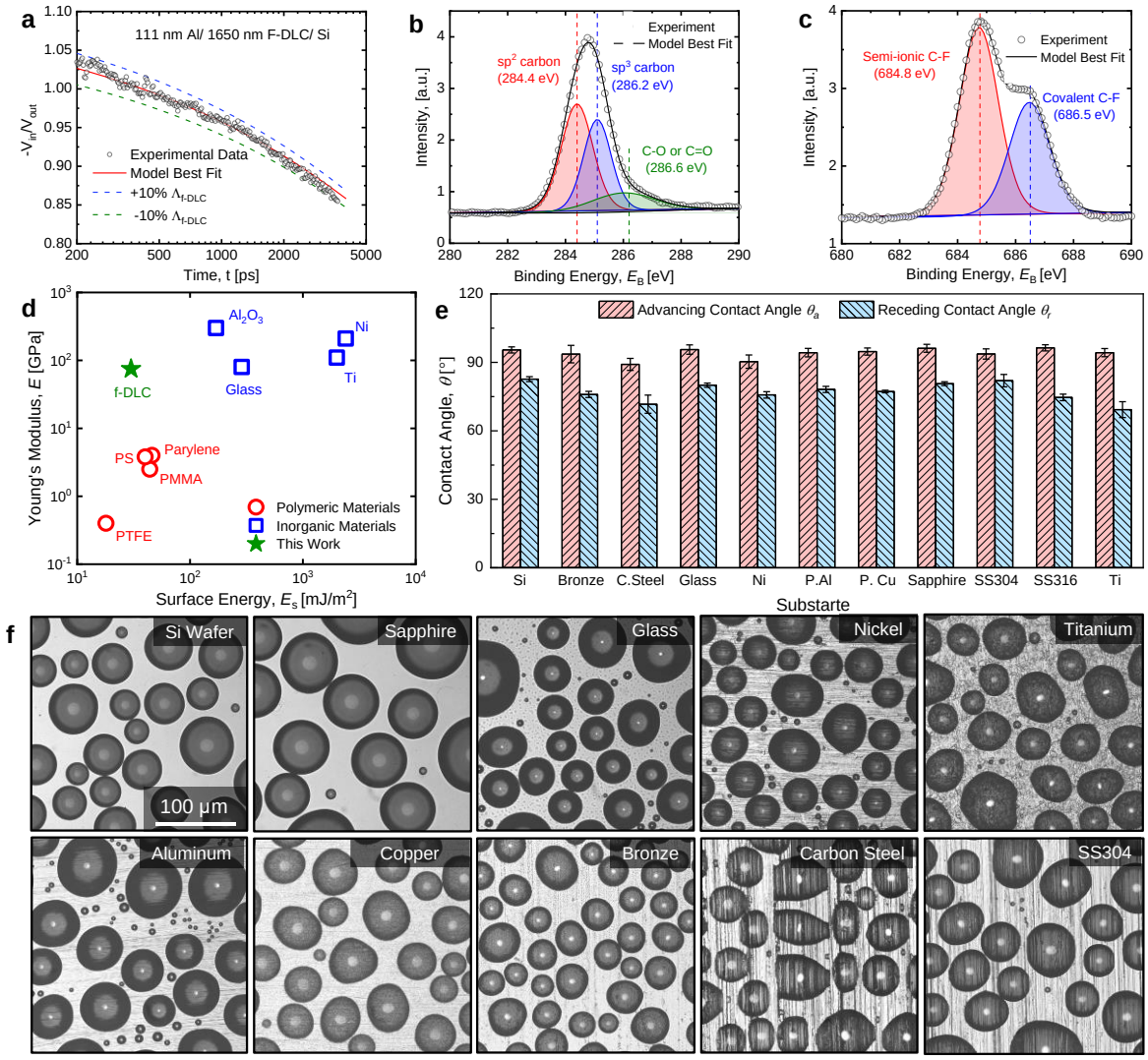

Figure 3.4. Surface characterization, wettability, and versatility of F-DLC coatings. (a) TDTR surface reflectivity as a function of the time delay Δt between pump and probe pulses on the F-DLC coating. The measured thermal conductivity was k = 0.46 ± 0.05 W/(m·K). The TDTR sample consisted of a 111 nm sputtered Al layer on a 1650 nm F-DLC multi-layer stack. (b) X-ray photoelectron spectroscopy (XPS) of the C1s peak demonstrating the three components consisting of sp^3 (C-C) bonds at 284.4 eV, sp^2 (C=C) bonds at 285.2 eV, and C-O or C=O bonds at 286.6 eV. (c) The XPS F1s spectrum showed the highest amount of fluorine atoms are bonded with carbon by covalent and semi-ionic C-F bonds. (d) Surface energy and Young's modulus of different commonly used engineering materials, showing that F-DLC combines the merit of both low surface energy and high mechanical modulus. (e) Measured apparent advancing and receding contact angles of DI water droplets on a variety of substrates coated with F-DLC. (f) Optical microscopy top-view images of atmospheric water vapor condensation on the different F-DLC coated substrates, showing the substrate versatility with similar hydrophobicity of the F-DLC coating.

3.6. Steam Condensation Heat Transfer Performance

Due to the demonstrated F-DLC conformity, low surface energy, and good thermal conductivity compared to polymeric hydrophobic coatings, the F-DLC coating has high potential to enhance condensation heat transfer performance. To determine the overall condensation heat transfer performance, an F-DLC coated copper (Cu) tube was fabricated following the same process described for the flat coupons and condensation heat transfer experiments were performed in a chamber with a controlled environment (Fig. 3.5a). Condensation heat transfer behavior and condensate shedding was benchmarked by comparison to an uncoated Cu tube sample having identical diameter and length. Prior to performing the experiments, the water vapor supply was boiled, and the test chamber was evacuated to a pressure $P < 1$ Pa to eliminate noncondensable gases and eliminate diffusional mass transfer resistances, key to obtaining high fidelity measurements.[210-213] Throughout the experiments, the chamber pressure and temperature were continuously monitored to ensure saturated conditions. The temperature of the sample tubes was independently controlled via a cooling loop, and the inlet and outlet tube temperatures were measured using high accuracy resistance temperature detectors to determine the coolant enthalpy change and relate it to the measured condensation heat flux. For all experiments, the cooling water inlet temperature was kept constant at 7 ± 1°C with a coolant flow rate of 8 ± 0.2 L/min, resulting in fully turbulent internal flow with Reynolds number, $Re_D = 24{,}000$. Condensation heat transfer performance was tested within the vapor pressure range of $3.5 < P_v < 10$ kPa, which are common conditions used for condensers in steam cycle power generation applications.[214, 215] The complete description of the experimental setup with all components is discussed in detail in the published work.[216, 217]

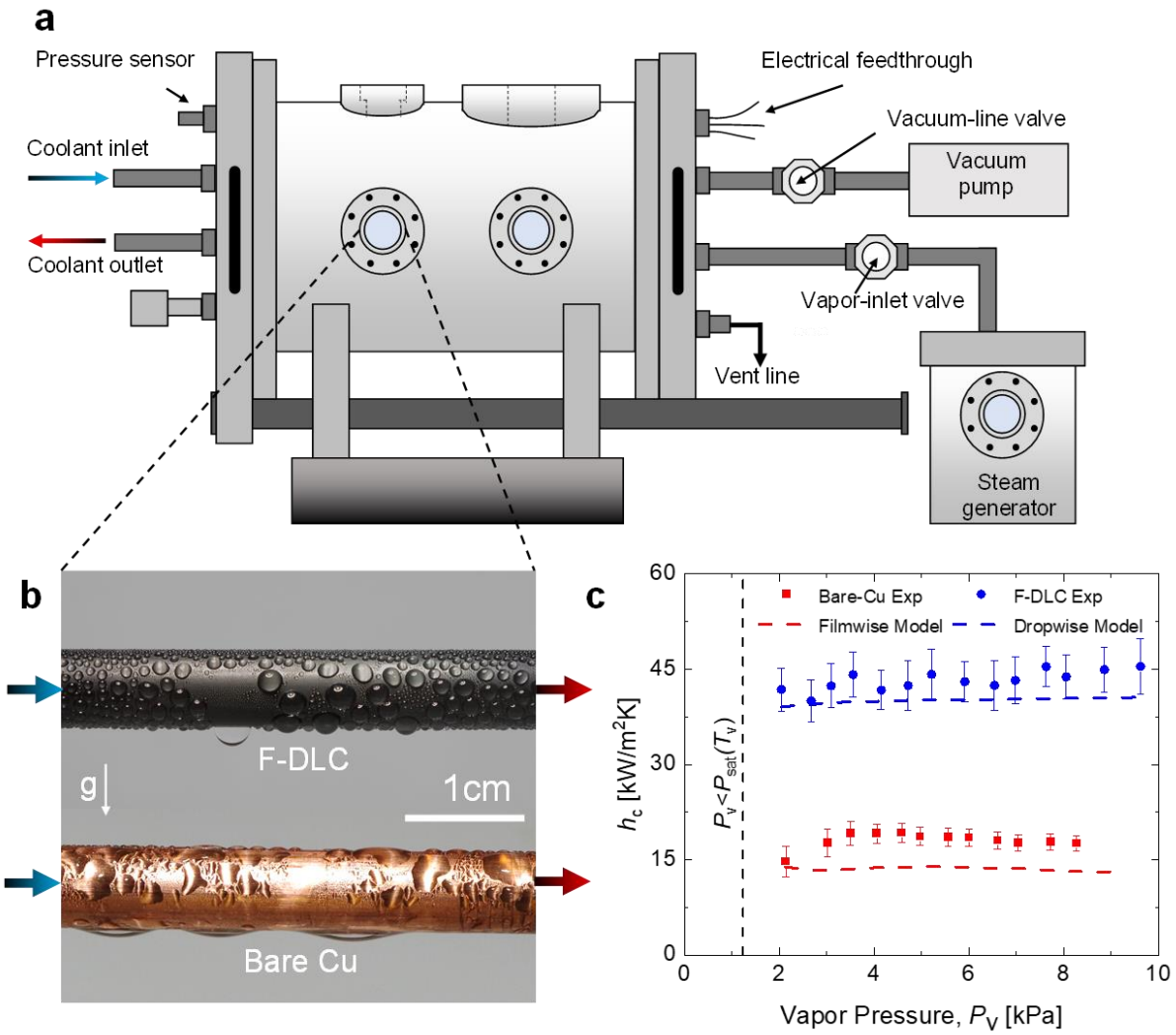

Figure 3.5. Enhanced condensation heat transfer of F-DLC. (a) Schematic of the chamber (not to scale) used for the condensation heat transfer experiments. The Cu tube sample having outer diameter D_{OD} = 9.53 mm, inner diameter D_{ID} = 8.0 mm, and length L = 134.6 mm was cooled via chilled water flowing inside of the tube at 8 ± 0.2 L/min. (b) Optical images during condensation showing (top) dropwise condensation on the F-DLC coated smooth Cu tube, and (bottom) filmwise condensation on the smooth un-coated hydrophilic Cu tube. The chamber vapor pressure P_v = 2.67 ± 0.15 kPa was identical for both tests. (c) Experimentally measured and theoretically computed steady-state condensation heat transfer coefficient (h_c) as a function of saturated steam vapor pressure (P_v) on the F-DLC coated Cu (dropwise) and bare Cu (filmwise) tubes. Error bars were computed using the propagation of error. The theoretical prediction for dropwise condensation (red dotted line) was obtained using the classical droplet growth and distribution model. The theoretical prediction for filmwise condensation (blue dotted line) was obtained using the Nusselt filmwise condensation model for a single horizontally oriented tube.

3.6.1. Heat Transfer Calculations and Error Analysis

Overall heat transfer coefficient ($\bar{U}$). The overall condensation heat transfer rate (Q) was calculated using an energy balance on the cooling water flowing inside the tube, as shown in Equation 3.2:

$$Q = \dot{m} c_{\mathrm{p}} (T_{\mathrm{out}} - T_{\mathrm{in}}) \,, \tag{3.2}$$

where Q is the overall condensation heat transfer rate, $\dot{m}$ is the cooling water mass flow rate, c_{p} is the liquid cooling water specific heat, and T_{out} and T_{in} are the outlet and inlet temperatures, respectively. The overall heat transfer rate (Q) was then balanced with the overall heat transfer coefficient, $\bar{U}$ as:

$$\dot{m} c_{\mathrm{p}} (T_{\mathrm{out}} - T_{\mathrm{in}}) = \bar{U} A_{\mathrm{o}} \Delta T_{\mathrm{LMTD}} \,, \tag{3.3}$$

where A_{o} is the tube outer surface area ($A_{\mathrm{o}} = \pi d_{\mathrm{OD}} L$, where d_{OD} = 9.35 mm, L = 134.62 mm) and ΔT_{LMTD} is the log mean temperature difference defined by:[218]

$$\Delta T_{\mathrm{LMTD}} = \frac{(T_{\mathrm{v}} - T_{\mathrm{in}}) - (T_{\mathrm{v}} - T_{\mathrm{out}})}{\ln\left[\frac{(T_{\mathrm{v}} - T_{\mathrm{in}})}{(T_{\mathrm{v}} - T_{\mathrm{out}})}\right]} \,, \tag{3.4}$$

where T_{v} is the temperature of the surrounding saturated vapor inside the chamber ($T_{\mathrm{v}} = T_{\mathrm{sat}}(P_{\mathrm{v}})$). The overall heat transfer coefficient ($\bar{U}$), which is only a function of experimentally obtained parameters, can thus be calculated as:

$$\bar{U} = \frac{\dot{m} c_{\mathrm{p}} (T_{\mathrm{out}} - T_{\mathrm{in}})}{A_{\mathrm{o}} \Delta T_{\mathrm{LMTD}}} \,. \tag{3.5}$$

Internal convection heat transfer coefficient (h_i). The calculated $\overline{U}$ is a measure of the overall heat transfer performance from the vapor to the cooling water. It includes the convective resistances on the inner and outer walls and the conductive resistance through the copper wall and hydrophobic coating. Further calculations were performed to isolate the thermal resistance on the outer wall to quantify the condensation heat transfer coefficient, h_c, as measured from the vapor to the tube outer surface.

To extract h_c, the conductive resistance was calculated using the thermal conductivity of hollow conductive cylinder assembly and the internal resistance was calculated by estimating the internal heat transfer coefficient. The water-side heat transfer coefficient (h_i) was estimated by the Petukhov correlation (Equations 3.6-3.8), which is relevant to the coolant flow conditions and has an accuracy of approximately 6%:[219]

$$h_i = \frac{k_i}{d_{ID}} \frac{\left(\frac{f}{8}\right)\mathrm{RePr}}{\left(1.07 + 12.7\left(\frac{f}{8}\right)^{\frac{1}{2}}\left(\mathrm{Pr}^{\frac{2}{3}} - 1\right)\right)} \left(\frac{\mu_b}{\mu_s}\right)^n . \tag{3.6}$$

$$\mathrm{Re} = \frac{\rho v d_{ID}}{\mu} . \tag{3.7}$$

$$f = [0.79\ln(\mathrm{Re}) - 1.64]^{-2}. \tag{3.8}$$

In Equations 3.6 to 3.8, f represents the pipe friction factor, Re is the cooling water Reynolds number, Pr is the cooling water Prandtl number, ρ is the cooling water density, k_i is the cooling water thermal conductivity, and μ_b and μ_s are the cooling water dynamic viscosities at the bulk and tube wall temperatures, respectively.

Thermal resistances. The overall heat transfer performance from vapor-to-cooling water can be expressed as a series sum of four individual thermal resistances: the internal convective resistance R_{conv}, the radial conduction tube wall resistance R_{wall}, the conductive resistance through the coating, R_{coating}, and condensation heat transfer thermal resistance $R_{\mathrm{condensation}}$, as shown in Fig. 3.6.

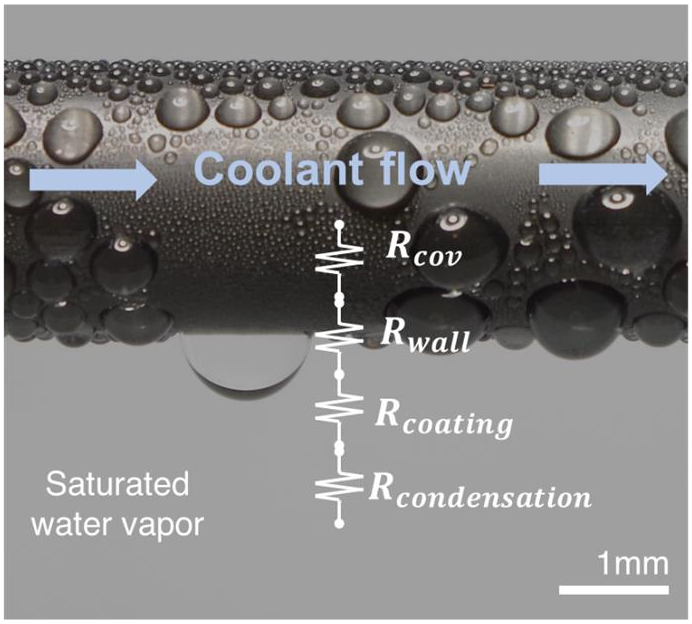

Figure 3.6. Thermal resistance network for condensation of steam on an F-DLC coated tube sample. Resistors not to scale.

Considering the coating thickness of the F-DLC as *h*, the thermal resistance of the coating on a tube with length, *L* is:

$$R_{\mathrm{coating}} = \frac{\ln\left(\frac{d_{\mathrm{OD}} + h}{d_{\mathrm{OD}}}\right)}{2\pi L k_{\mathrm{F-DLC}}}, \tag{3.9}$$

where d_{OD} is the outer diameter of the bare copper tube and $k_{\mathrm{F-DLC}}$ is the thermal conductivity of the F-DLC multilayer coating. Similarly, the conductive tube wall resistance can be calculated as:

$$R_{\text{wall}} = \frac{\ln\left(\frac{d_{\text{OD}}}{d_{\text{ID}}}\right)}{2\pi L k_{\text{Cu}}}, \tag{3.10}$$

where d_{OD} and d_{ID} are the outer and inner bare tube diameters, respectively and k_{Cu} is the thermal conductivity of multipurpose copper. The internal convection resistance and external condensation resistance can be calculated as:

$$R_{\text{conv}} = \frac{1}{h_{\text{i}}\pi d_{\text{ID}} L}. \tag{3.11}$$

$$R_{\text{condensation}} = \frac{1}{h_{\text{c}}\pi d_{\text{OD}} L}. \tag{3.12}$$

Condensation heat transfer coefficient (h_c).

The overall heat transfer coefficient can be expressed as Equation 3.13 by considering all four thermal resistances in series:

$$\frac{1}{\bar{U}A_{\text{o}}} = R_{\text{conv}} + R_{\text{wall}} + R_{\text{coating}} + R_{\text{condensation}}, \tag{3.13}$$

where A_{o} is the tube outer surface area ($A_{\text{o}} = \pi d_{\text{OD}} L$). Knowing h_{i}, a closed form solution can be obtained for h_{c} by combining all the relevant thermal resistances (internal convection and radial conduction through the tube wall and coating):

$$h_{\text{c}} = \left(\frac{1}{\bar{U}} - A_{\text{o}}(R_{\text{conv}} + R_{\text{wall}} + R_{\text{coating}})\right)^{-1}. \tag{3.14}$$

Tube surface temperature (T_{surf}). The tube surface outer temperature, T_{surf}, was used to calculate the supersaturation for each test condition. The outer wall temperature was calculated using the total heat transfer rate and the conductive and water-side convective thermal resistances, as shown in Equation 3.15:

$$Q = \frac{T_{\mathrm{surf}} - T_{\mathrm{avg}}}{\frac{1}{h_{\mathrm{i}} A_{\mathrm{i}} L} + \frac{\ln\left(\frac{d_{\mathrm{OD}}}{d_{\mathrm{ID}}}\right)}{2\pi L k_{\mathrm{t}}}}, \tag{3.15}$$

where $T_{\mathrm{avg}} = (T_{\mathrm{out}} + T_{\mathrm{in}})/2$. Rearranging Eq. 3.15, the tube surface temperature can be calculated as:

$$T_{\mathrm{surf}} = T_{\mathrm{avg}} + \dot{m} c_{\mathrm{p}} (T_{\mathrm{out}} - T_{\mathrm{in}}) \left[\frac{1}{h_{\mathrm{i}} A_{\mathrm{i}} L} + \frac{\ln\left(\frac{d_{\mathrm{OD}}}{d_{\mathrm{ID}}}\right)}{2\pi L k_{\mathrm{Cu}}} \right]. \tag{3.16}$$

Finally, the supersaturation, S, defined as the ratio of the vapor pressure to the saturation pressure corresponding to the tube sample surface temperature is given by:

$$S = \frac{P_{\mathrm{v}}}{P_{\mathrm{sat}}(T_{\mathrm{surf}})}. \tag{3.17}$$

Error analysis. The uncertainty of the overall heat transfer coefficient, $\bar{U}$, was calculated by propagating the instrument uncertainty of each measured variable (Table 3.1), as shown in Equation 3.18:

$$E_{\bar{\mathrm{U}}} = \bar{U} \sqrt{\left(\frac{E_{\dot{\mathrm{m}}}}{\dot{m}}\right)^2 + \left(\frac{E_{(T_{\mathrm{out}} - T_{\mathrm{in}})}}{(T_{\mathrm{out}} - T_{\mathrm{in}})}\right)^2 + \left(\frac{-E_{\mathrm{A}}}{A}\right)^2 + \left(\frac{-E_{\Delta T_{\mathrm{LMTD}}}}{\Delta T_{\mathrm{LMTD}}}\right)^2}. \tag{3.18}$$

As the condensation heat transfer coefficient, h_{c} is a product of powers, the error is determined as a function of the first partial derivatives of h with respect to its components:

$$E_{h_c} = h_c \sqrt{\left(\frac{\partial h_{\mathrm{c}}}{\partial h_{\mathrm{i}}} \frac{E_{\mathrm{h_i}}}{h_{\mathrm{i}}}\right)^2 + \left(\frac{\partial h_{\mathrm{c}}}{\partial \overline{U}} \frac{E_{\overline{\mathrm{U}}}}{\overline{U}}\right)^2}, \tag{3.19}$$

$$\frac{\partial h_c}{\partial h_{\mathrm{i}}} = \frac{-(A_{\mathrm{o}}/A_{\mathrm{i}})\overline{U}^2}{(h_{\mathrm{i}} - (A_{\mathrm{o}}/A_{\mathrm{i}})\overline{U} - R_{\mathrm{t}} A_{\mathrm{o}} \overline{U} h_{\mathrm{i}})^2}, \tag{3.20}$$

$$\frac{\partial h_c}{\partial \overline{U}} = \frac{{h_{\mathrm{i}}}^2}{(h_{\mathrm{i}} - (A_{\mathrm{o}}/A_{\mathrm{i}})\overline{U} - R_{\mathrm{t}} A_{\mathrm{o}} \overline{U} h_{\mathrm{i}})^2}, \tag{3.21}$$

where $R_{\mathrm{t}}$is the thermal resistance of the tube wall given by:

$$R_{\mathrm{wall}} = \frac{\ln\left(\frac{d_{\mathrm{OD}}}{d_{\mathrm{ID}}}\right)}{(2\pi k_{\mathrm{Cu}})}. \tag{3.22}$$

Table 3.1. Uncertainties corresponding to experimental measurements.

Experimental Measurement	**Uncertainty**
Cooling water temperature (T_{out}, T_{in})	0.15°C + 0.12%
Saturated vapor pressure (P_{v})	1%
Saturated vapor temperature (T_{v})	$T_{sat}(1.01(P_{\mathrm{v}}))$-$T_{sat}(P_{\mathrm{v}})$
Cooling water mass flow rate ($\dot{m}$)	1%
Sample surface area (A_{OD})	2%
Petukhov correlation heat transfer coefficient (h_{i})	6%

3.6.2. Dropwise Condensation Model

To calculate the overall condensation heat transfer, we first calculate the heat transfer through a water droplet. Then, we multiply the individual droplet heat transfer with the droplet distribution density to get the overall condensation heat flux. To calculate the droplet heat transfer, we study the thermal resistance network. For a droplet residing on a surface, the dominating thermal resistances are the conduction resistance within the droplet, the surface conduction thermal resistance (coating), and the interfacial thermal resistance at the liquid-vapor interface. The conduction resistance is determined by following our previous study.[220] Due to the sufficiently

small size of condensing droplets, convection inside of the droplet is low and is neglected.[221] Here we consider a droplet with radius R on a plain surface which is coated with F-DLC, as shown in Fig. 3.7. The contact angle θ of the F-DLC coated hydrophobic surface is assumed to be fixed regardless of the droplet size, surface temperature and vapor temperature. Knowing the vapor saturation temperature, T_{sat} and F-DLC coated tube surface temperature, T_{surf}, the heat transfer rate Q can be calculated by considering all thermal resistances.

Considering the droplet nucleation site density, N_{s},[222] the effective coalescence radius of the droplets, R_{e} above which droplets starts to coalesce can be calculated by:

$$R_{\mathrm{e}} = 1/\sqrt{4N_{\mathrm{s}}}\,. \tag{3.23}$$

Droplet critical nucleation radius (R_{min}) was calculated by:[221]

$$R_{\mathrm{min}} = \frac{2T_{\mathrm{sat}}\sigma}{h_{\mathrm{fg}}\rho(T_{\mathrm{sat}} - T_{\mathrm{surf}})}\,. \tag{3.24}$$

where σ, ρ, and h_{fg} are the liquid-vapor surface tension, density, and latent heat of vaporization of water, respectively.

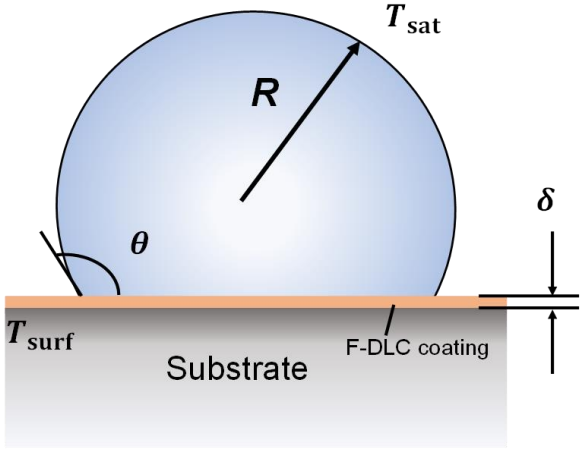

Figure 3.7. Schematic of a condensate water droplet with radius R growing on the F-DLC coated (hydrophobic) condensing surface having a total coating thickness of δ.

The heat transfer rate through a single droplet with radius R is:

$$q(R) = \frac{\pi R^2 (T_{\mathrm{sat}} - T_{\mathrm{surf}}) \left(1 - \frac{R_{\min}}{R}\right)}{\frac{1}{2h_{\mathrm{i}}\left(1 - \cos\theta_{\mathrm{a}}^{\mathrm{app}}\right)} + \frac{R\theta_{\mathrm{a}}^{\mathrm{app}}}{4k_{\mathrm{w}}\sin\theta_{\mathrm{a}}^{\mathrm{app}}} + \frac{\delta}{k_{\mathrm{HC}}\sin^2\theta_{\mathrm{a}}^{\mathrm{app}}}} \tag{3.25}$$

where, k_{w}, and k_{HC} are thermal conductivity of water and F-DLC, respectively. Here $\theta_{\mathrm{a}}^{\mathrm{app}}$ is the apparent advancing contact angle of condensate droplets, h_{i} is the interfacial heat transfer coefficient and is determined by the Schrage equation:[220, 221, 223]

$$h_{\mathrm{i}} = \frac{2\alpha}{2-\alpha}\frac{1}{\sqrt{2\pi R_{\mathrm{g}} T_{\mathrm{sat}}}}\frac{h_{\mathrm{fg}}^2}{\nu_{\mathrm{g}} T_{\mathrm{sat}}}, \tag{3.26}$$

where a is the accommodation coefficient ranging from 0 to 1, representing the ratio of vapor molecules that will be captured by the liquid phase to the total number of vapor molecules reaching the liquid phase, and R_{g} is the specific gas constant of vapor.

To calculate the overall condensation heat flux we combined the individual droplet heat transfer with the total number distribution of droplets on the condensing surface. For a hydrophobic surface, a droplet distribution theory to account for the fraction of droplets on the surface of a given radius $\boldsymbol{R}$ for surfaces undergoing shedding and jumping is used. For small droplets ($\boldsymbol{R} \leq \boldsymbol{R_e}$), the size distribution $\boldsymbol{n}(\boldsymbol{R})$ is determined by:[224]

$$n(R) = \frac{1}{3\pi R_{\mathrm{e}}^3 \hat{R}}\left(\frac{R_{\mathrm{e}}}{\hat{R}}\right)^{-\frac{2}{3}} \frac{R(R_{\mathrm{e}} - R_{\min})}{R - R_{\min}} \frac{A_2 R + A_3}{A_2 R_{\mathrm{e}} + A_3} \exp(B_1 + B_2), \tag{3.27}$$

where, where $\hat{R}$ is the effective maximum droplet radius. For large droplets ($R \geq R_{\mathrm{e}}$) growing due to coalescence, the droplet distribution $N(R)$ is determined from:[225]

$$N(R) = \frac{1}{3\pi R_{\mathrm{e}}^2 \hat{R}}\left(\frac{R_{\mathrm{e}}}{\hat{R}}\right)^{-\frac{2}{3}}. \tag{3.28}$$

The parameters A_1, A_2, A_3, B_1, B_2 are constants defined as:[220]

$$A_1 = \frac{\Delta T}{h_{\mathrm{fg}}\rho_{\mathrm{w}}\left(1-\cos\theta_{\mathrm{a}}^{\mathrm{app}}\right)^2\left(2+\cos\theta_{\mathrm{a}}^{\mathrm{app}}\right)}, \tag{3.29}$$

$$A_2 = \frac{\theta_{\mathrm{a}}^{\mathrm{app}}}{4k_{\mathrm{w}}\sin\theta_{\mathrm{a}}^{\mathrm{app}}}\ , \tag{3.30}$$

$$A_3 = \frac{1}{2h_i(1-\cos\theta_{\mathrm{a}}^{\mathrm{app}})} + \frac{\delta}{k_{\mathrm{HC}}\sin^2\theta_{\mathrm{a}}^{\mathrm{app}}}\ , \tag{3.31}$$

$$B_1 = \frac{A_2}{\tau A_1}\left[\frac{R_{\mathrm{e}}^2 - R^2}{2} + R_{\mathrm{min}}(R_{\mathrm{e}} - R) - R_{\mathrm{min}}^2\ln\left(\frac{R-R_{\mathrm{min}}}{R_{\mathrm{e}}-R_{\mathrm{min}}}\right)\right], \tag{3.32}$$

$$B_2 = \frac{A_3}{\tau A_1}\left[R_e - R - R_{\mathrm{min}}\ln\left(\frac{R-R_{\mathrm{min}}}{R_{\mathrm{e}}-R_{\mathrm{min}}}\right)\right], \tag{3.33}$$

$$\tau = \frac{3R_{\acute{e}}^2(A_2R_{\mathrm{e}} + A_3)^2}{A_1(11A_2R_{\mathrm{e}}^2 - 14R_{\mathrm{e}}R_{\mathrm{min}} + 8A_3R_{\mathrm{e}} - 11A_3R_{\mathrm{min}})}. \tag{3.34}$$

The total surface steady state condensation heat flux (q") for a hydrophobic surface is obtained by incorporating the individual droplet heat transfer obtained from Equation 3.25, with the droplet size distributions (Eqns. 3.27 and 3.28):

$$q" = \int_{R_{\mathrm{min}}}^{R_{\mathrm{e}}} q(R)n(R)dR + \int_{R_{\mathrm{e}}}^{\hat{R}} q(R)N(R)dR\ . \tag{3.35}$$

The overall condensation heat transfer coefficient is calculated by:

$$h_{\mathrm{c}} = \frac{q_{\mathrm{tot}}}{\Delta T}, \tag{3.36}$$

where ΔT is the temperature difference between the ambient vapor saturation temperature, T_{sat} and the condensing surface temperature, T_{surf} (i.e. $\Delta T = T_{\mathrm{sat}} - T_{\mathrm{surf}}$).

3.6.3. Filmwise Condensation Heat Transfer Model

To model filmwise condensation of steam on the hydrophilic copper tube samples, the classical Nusselt model was used:[218, 226]

$$h_{\mathrm{c,filmwise}} = 0.729\left[\frac{g\rho_{\mathrm{l}}(\rho_{\mathrm{l}}-\rho_{\mathrm{v}}){k_{\mathrm{l}}}^{3}{h_{\mathrm{fg}}}'}{\mu_{\mathrm{l}}d_{\mathrm{OD}}\Delta T}\right]^{0.25}, \tag{3.37}$$

$${h_{\mathrm{fg}}}' = h_{\mathrm{fg}} + 0.68c_{\mathrm{p,l}}\Delta T\,, \tag{3.38}$$

where g is acceleration due to gravity (g = 9.81 m/s^2), ρ_{v} is the vapor density, ρ_{l} is the condensate liquid density, μ_{l} is the condensate liquid dynamic viscosity, ${h_{\mathrm{fg}}}'$ is the modified latent heat of vaporization accounting for the change in specific heat of the condensate and $c_{\mathrm{p,l}}$ is the condensate liquid specific heat.

Figure 3.5b shows optical images obtained during dropwise condensation on the smooth F-DLC-coated hydrophobic Cu tube (top image) and during filmwise condensation on the clean, uncoated hydrophilic Cu tube (bottom image). As expected, on the bare Cu tube, vapor condensed and formed a thin liquid film that covered the entire surface. On the F-DLC coated Cu tube, stable dropwise condensation ensued. To maximize the tube internal heat transfer coefficient, the cooling water mass flow rate was held constant at 8 ± 0.2 L/min for all experiments ($1.01 < S \leq 1.7$, $8.5 < T_{\mathrm{s}} < 25$ °C, where S is the supersaturation and T_{s} is the extrapolated tube surface temperature. The condensation heat transfer coefficient (h_{c}) was calculated from the measured condensation heat flux and overall heat transfer coefficient. By calculating the well-validated thermal resistances of the internal tube single-phase forced convection, radial conduction through the Cu tube wall, and F-DLC coating thermal resistance using the measured thermal conductivity, the steady-state condensation heat transfer coefficient at the tube outer surface, h_{c}, was calculated. Figure 3.5c shows calculated and predicted heat transfer coefficient as a function of vapor pressure. The F-DLC coated Cu sample showed a ~3X higher condensation heat transfer compares to the uncoated Cu tube over a wide range of vapor pressures. To compare the experimental results to theoretical predictions, we calculated the dropwise condensation heat transfer coefficient (red dotted line in Fig. 3.5c) using the droplet growth and distribution model and the filmwise condensation heat

transfer coefficient (blue dotted line in Fig. 3.5c) using the Nusselt condensation model on a horizontal tube. The experimentally measured dropwise and filmwise heat transfer coefficient are in good agreement with the well-validated dropwise and filmwise condensation models, respectively.

3.7. Long-Term Steam Condensation Durability

The F-DLC coating provides a conformal, pin-hole free, adherent solution for the rational design of multiple layers that can enable enhanced condensation heat transfer (Fig. 3.8). The demonstrated condensation heat transfer results are not unique, showing similar performance with previously developed hydrophobic materials[33, 210, 227, 228]. However, the potential durability of F-DLC when compared to classical hydrophobic coatings makes it beneficial. To evaluate the long-term durability of the F-DLC coating during steam condensation, we built a separate vacuum-compatible condensation chamber (Fig. 3.8a and b). To accelerate the condensation process and increase the condensation heat flux, the testing samples were mounted on an aluminum cold plate (Fig. 3.8c) and placed in the custom-built environmental chamber commissioned in 2017. The environmental chamber was first evacuated to $P < 5$ Pa to remove non-condensable gases, then, hot steam was injected into the chamber from a boiler after following a detailed degassing procedure. Cold water at ~10°C was supplied to the cold plate inlet via a chiller, which reduces the surface temperature of the mounted samples. As the steam comes in contact with the F-DLC surfaces it forms water droplets and initiates dropwise condensation. Due to the good droplet mobility on the hydrophobic F-DLC surfaces, the condensed water droplets shed from the surface

toward the condensate collector at the bottom of the chamber and finally the condensate returns to the boiler by gravity. During the long-term test, the chamber pressure ranged from 2 to 3 kPa.

A total of three F-DLC coated substrates consisting of a polished silicon wafer, a Cu tab, and an Al tab were tested in the chamber system for the full-time duration. The condensation conditions of each sample were recorded at least twice a week via visual observation, which has been used in the past to identify the condensation mode (dropwise or filmwise condensation). Due to inherent leaks into the chamber from the pressure difference arising from the atmosphere and the saturated steam at lower pressure, the system had to be shut down periodically (once every month) in order to vacuum out the chamber and ensure pure saturated conditions. During shutdown, the chamber was not opened and simply was vacuumed to remove non condensables, with shutdown lasting no more than 3 hours.

Figure 3.8d shows time-lapse images of condensation on each sample mounted in the vertical orientation. The images show that condensing droplets on the F-DLC surfaces have clear circular shapes and grew to 3.2 to 3.5 mm in diameter prior to departing the surface throughout the testing period, which lasted for 3 years (> 1095 days). Even after the long-term exposure to saturated steam conditions, the F-DLC coating exhibited continued dropwise condensation during tests, regardless of the base substrate. This was not true for control samples consisting of Cu and Al tabs coated with self-assembled monolayers of heptadecafluorodecyl-trimethoxy-silane (HTMS), which failed via transition to filmwise condensation after less than one month of testing (Table 3.2). After exposing to steam for 3 years, the DI water contact angle on the F-DLC coating changed from θ_a/θ_r = 99.1°/86.2° to $\theta_a/\ \theta_r$ = 70.5°/57.1° (Table 3.2).

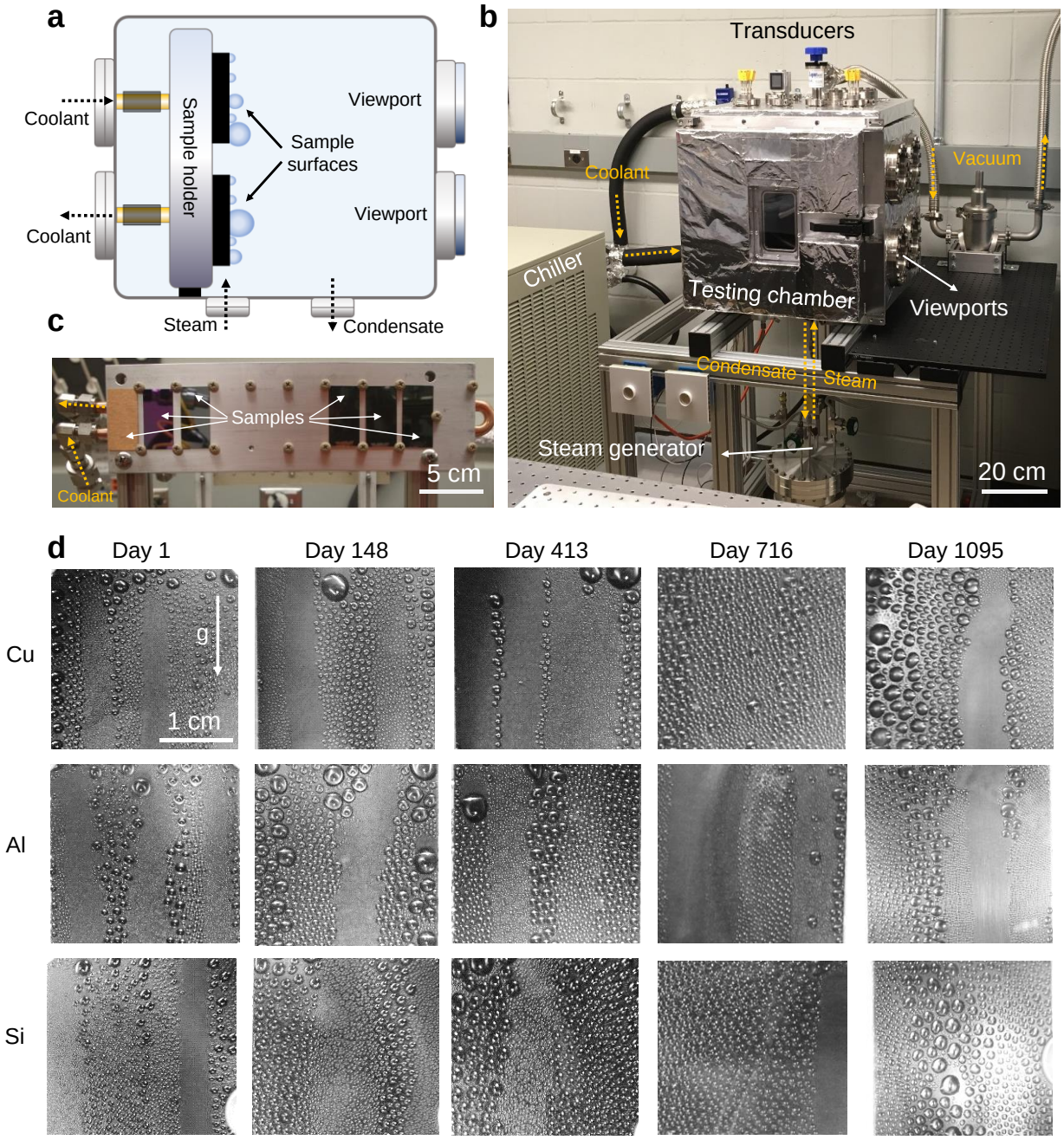

Figure 3.8. **Long-term steam dropwise condensation on F-DLC.** (a) Schematic and (b) photograph of the facility used to conduct long-term condensation experiments. (c) Image of the cold plate and sample assembly placed inside of the vacuum chamber for experiments. Throughout the experiment, the surface temperature of the samples was maintained by supplying coolant at 10°C to the cold plate from a dedicated chiller. Steam is generated inside a separate degassing chamber connected to the bottom of the chamber. (d) Time lapse images of steam dropwise condensation on the vertically oriented surfaces consisting of F-DLC coated: (top row) polished Cu, (middle row) polished Al, and (bottom row) polished Si wafer. All results showed hydrophobicity of the F-DLC coating irrespective of substrate for a period lasting more than 3 years at the time of writing this manuscript (March 2022).

Table 3.2. Condensation durability test samples and summary of test results.

Coating	Thickness	Substrate	θ_a	θ_r	$\Delta\theta$	Operation Time [days]	Durability
F-DLC	1.65 μm	Si	99.1° ± 0.4°	86.2° ±0.4°	13°	>1095	Good
		Polished Cu	98.4° ± 0.8°	82.7° ±1.1°	15°	>1095	Good
		Polished Al	99.0° ± 0.5°	85.3° ±0.8°	14°	>1095	Good
HTMS	2 nm	Polished Cu	120° ± 0.8°	94.6° ±1.2°	26°	<29	Poor
		Polished Al	111° ± 1.9°	71.1° ±0.5°	41°	<29	Poor

Post-experiment XPS analysis was conducted on the tested samples to investigate the possible surface chemistry change after continual 3 years of condensation. The results show the content of fluorine of the top f-DLC layer reduced from 9.5% to 4.9% during the 3-year test (see Table 3.3), which indicates that the surface energy increases during long exposure to water vapor, thus reducing the apparent contact angle. However, the F-DLC surfaces still maintain a low droplet Bond number ($\mathrm{Bo} = R_f^2/l_y^2$, where R_f is the characteristic lateral length of the liquid droplet, taken to be its final equilibrium radius immediately before departure, and l_y is the capillary length) representing the ratio of equilibrium droplet radius immediately before departure to capillary length scale of water. The Bo number mediated dropwise-to-filmwise transition occurs at $\mathrm{Bo}_{crit} = 1.4$, with $\mathrm{Bo} > 1.4$ predicting gravitationally dominated puddle formation and filmwise condensation.[154] Calculations of Bo for each F-DLC surface tested for durability (after 3 years) based on the final surface contact angle measurements reveal a maximum Bo ~ 0.5 (Table 3.4). Since $\mathrm{Bo} < \mathrm{Bo}_{crit}$, capillary-dominated hemispherical droplet shapes are maintained at departure, ensuring dropwise condensation and high droplet mobility.

Furthermore, TDTR measurements of the post-experiment samples show insignificant change (<1%) in the thermal conductivity of the coating (Table 3.3). The ability to conserve similar droplet mobility and thermal conductivity indicates that even after three years of steam exposure, the F-DLC coatings will provide similar heat transfer performance as freshly prepared surfaces. As of March 2022, the long-term durability test are still ongoing and will continue indefinitely until transition to filmwise condensation is achieved.

Table 3.3. Surface property comparison of the F-DLC coated fresh sample and samples after exposing in the steam environment for 1095 days. The sample substrates were polished Si wafers.

Coating property	**As coated**					**After 1095 condensation days**				
$\boldsymbol{\theta_a/\theta_r}$	99.1°± 0.4° / 86.2°±0.4°					70.5°± 1.0° / 57.1°±1.3°				
Chemical composition	F %	O %	N %	C %	Si %	F %	O %	N %	C %	Si %
	9.5	27.5	2	38.9	24.1	4.9	33.7	0	38.5	22.9
Thermal conductivity k [W/(m·K)]	0.46 ± 0.05					0.42 ± 0.04				

Table 3.4. Bond number (Bo) comparison between fresh F-DLC coated samples and condensation durability tested samples after 1095 days. Durability tested samples still maintain Bo smaller than the critical Bond number, $Bo_{crit} = 1.4$, ensuring dropwise condensation.

Substrate	**Before Test**			**After 1095 condensation days**		
	$\boldsymbol{\theta_a}$	$\boldsymbol{\Delta\theta}$	**Bo**	$\boldsymbol{\theta_a}$	$\boldsymbol{\Delta\theta}$	**Bo**
Si	99.1° ± 0.4°	≈13°	0.2	70.5° ± 1.0°	≈14°	0.47
Polished Cu	98.4° ± 0.8°	≈15°	0.26	73.2° ± 0.6°	≈16°	0.51
Polished Al	99.0° ± 0.5°	≈14°	0.22	71.0° ± 1.1°	≈14°	0.49

3.8. Thermal Stability

Abrasion resistance and stability at elevated temperatures is required for a broader array of hydrophobic coating applications. The thermal stability of the F-DLC coating was tested by heating samples in a furnace (Lindberg 2" Tube Furnace) with a flow of inert gas for various times and temperatures. A continuous flow of N_2 gas (~ 3 LPM) in the tube furnace was used. After heating for a prescribed time and allowing the sample to cool back down to room temperature, the apparent advancing (θ_a) and receding (θ_r) DI water droplet contact angles were measured using a microgoniometer (MCA-3, Kyowa Interface Science). The heating temperature ranged from 100°C to 600°C and at each temperature, five identical F-DLC coated samples were placed in the furnace. After 1 h, the first sample was taken out, followed by the rest of the samples taken out sequentially at 2, 4, 8, and 16 hours. The change in apparent contact angle represents an indication of coating integrity due to the intrinsic hydrophilicity of the substrate (metal or native oxide) beneath the F-DLC coating.

To characterize the effects of potential oxidation in non-inert (atmospheric pressure) conditions, identical experiments were also conducted in an atmospheric pressure oven (Lindberg/Blue M Moldatherm Box Furnace). The thermal stability of the F-DLC coating was compared to a control sample consisting of a HTMS SAM hydrophobic coating deposited on identical substrates. As shown in Figs. 3.9a and 3.9b, the F-DLC coating maintains consistent hydrophobicity up to 300°C exposure temperatures both in N_2 and air environments, with air exposure creating slight degradation in hydrophobicity due to substrate oxidation. However, on the HTMS coated control samples, 300°C exposure resulted in complete degradation (hydrophilicity) after 2 h of heating due to silane desorption. In the inert N_2 environment, the F-DLC coating maintained continual hydrophobicity up to 450°C (Figs. 3.10a and 3.10b). In air at

350°C (Fig. 3.10c) and 400°C (Fig. 3.10d), F-DLC degrades at a similar rate for 2 h of heating time. Then, at later times (> 2h), the oxidation rate was observed to significantly accelerate for the 400°C case.

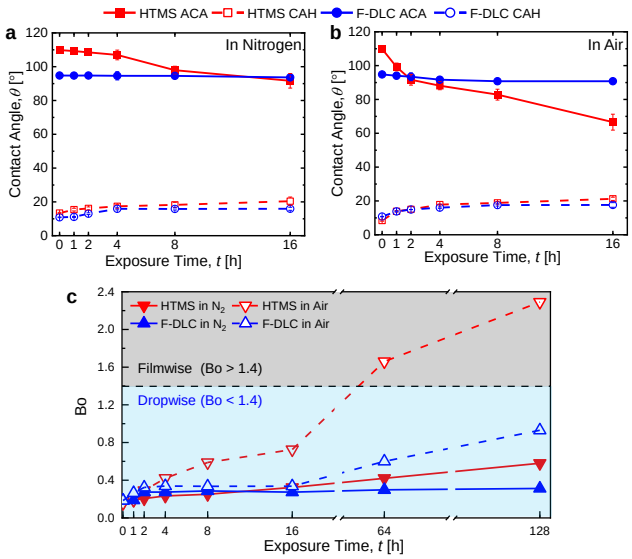

Figure 3.9. Thermal stability of F-DLC. Thermal stability of the F-DLC coating compared with HTMS SAM at 300°C in (a) Nitrogen (N_2) and (b) air environments as measured by the change in apparent advancing contact angles (ACA) and receding contact angles (RCA) with DI water droplets. Contact angle hysteresis (CAH) represents the arithmetic difference between ACA and RCA. Legends are same for (a) and (b). (c) During high temperature exposure in 300°C conditions (air), the HTMS surface in transitions to filmwise condensation, while the F-DLC coating maintains dropwise condensation.

Consistent with the previous wettability characterization during heating in air at 300°C, the HTMS coated surface showed a drastic increase in droplet Bo with little change for the F-DLC coating (Fig. 3.9c). In the inert environment, the F-DLC coating did not show filmwise transition ($Bo < 1.4$) until exposure to 600°C for ~10 h (Fig. 3.10e). However, the filmwise transition on the F-DLC coating is predicted to occur after exposure to 400°C in air after ~ 10h (Fig. 3.10f). Since the F-DLC coating showed good hydrophobicity in both air and inert environments for up to 16 hours of exposure at 300°C, we extended the heating time up to 128 hours to try to observe the

filmwise transition. As shown in Fig. 3.9c, even after 128 hours of exposure to hot air (300°C) the F-DLC coating maintain dropwise condensation (Bo ~ 0.9 < 1.4).

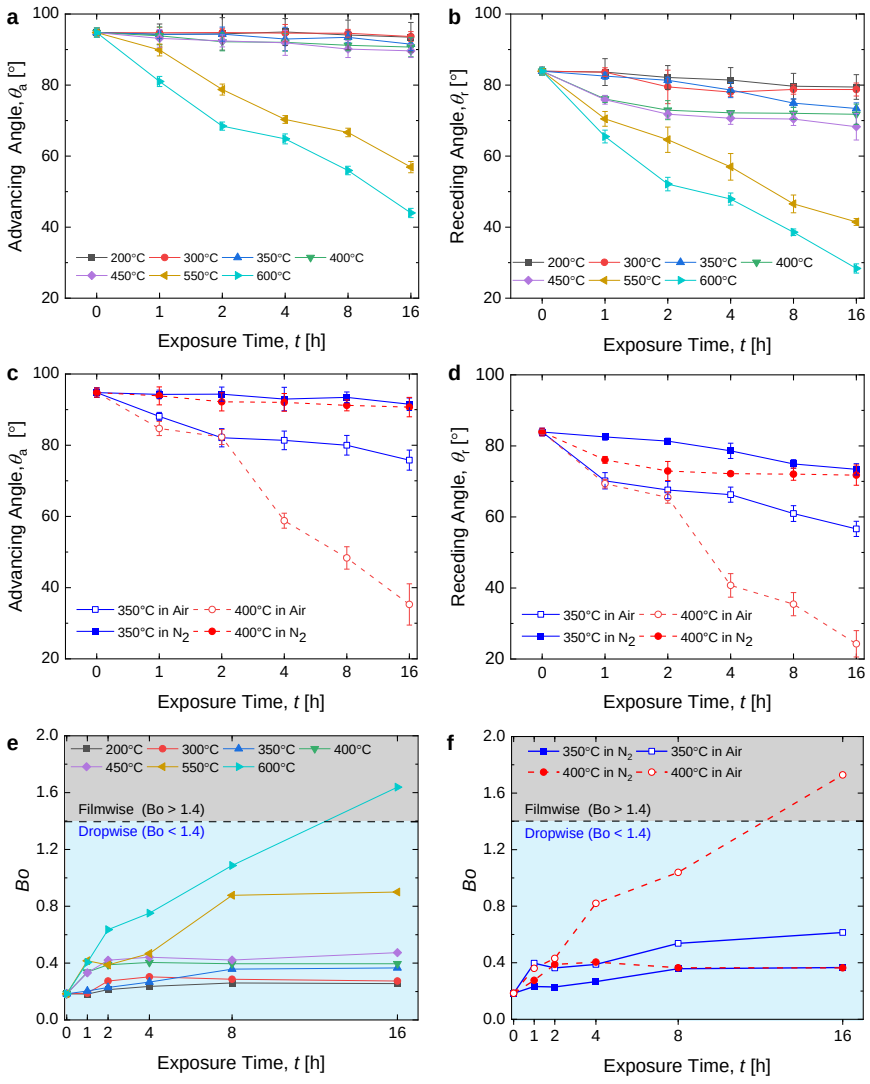

Figure 3.10. Stability of the F-DLC coating in different thermal environments. (a) Advancing, and (b) receding DI water droplet contact angle of the F-DLC coating in inert environments (N_2 gas) for different temperatures showing good hydrophobic properties up top 450°C. (c)-(d) Comparison of F-DLC degradation process in air and N_2. Calculated Bond number (Bo) for the F-DLC coated surfaces in different thermal environments, showing a filmwise transition (Bo_{crit} > 1.4)[154] temperature in the (e) 600°C inert environment, and (f) 400°C non-inert environment.

3.9. Mechanical Robustness

To evaluate long-term mechanical durability of the F-DLC film against abrasion and wear, cyclic abrasion resistance tests were performed on a Taber abrasion tester (Figure 3.11). The abrasion resistance of the F-DLC coating on the polished silicon substrate was tested using a Taber Reciprocating abraser (Model-5900). A sliding specimen platform moves in a horizontal, reciprocating motion under a stationary abradant (Calibrase® CS-10, Taber Industries). A silicon wafer coated with F-DLC was placed underneath an abrasive tip with a defined preload of 1 N on the tested surface. Then, a fixed speed linear reciprocating motion was applied to the sample stage to model abrasion, followed by DI water contact angle measurements on the abraded surface area at a prescribed number of abrasion cycles. Prior to contact angle measurement, residuals consisting of mainly abrasive nanoparticles and binder material on the test surface from the abrasion tips were cleaned by sonication of samples in ethanol. This ensured that the measured change in contact angle was due to damage during abrasion, and not parasitic material deposition.

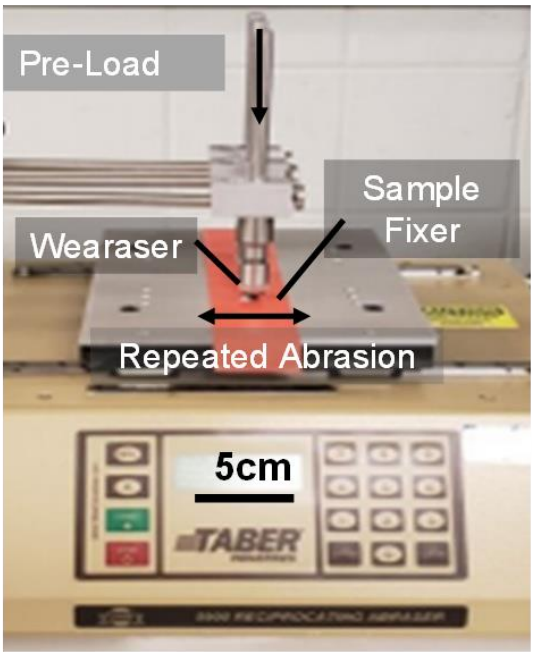

Figure 3.11. Photograp of a reciprocating abrasion tester used to characterize the mechanical stability of the F-DLC coated samples.

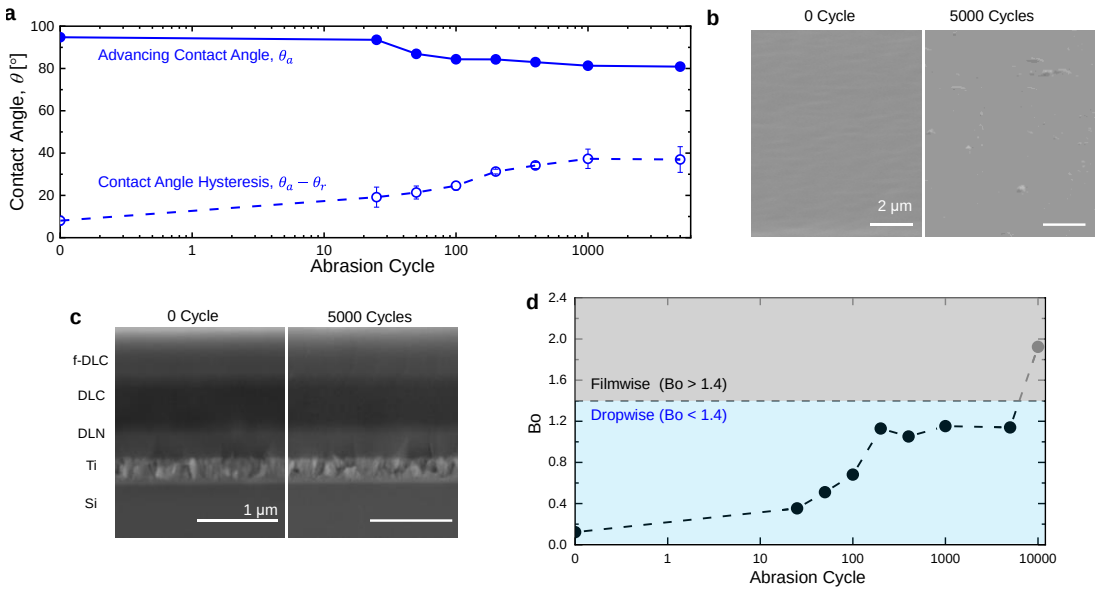

Figure 3.12. Mechanical robustness of F-DLC. To characterize the effects of abrasion, the (a) DI water droplet apparent advancing contact angle (blue solid curve) as well as the contact angle hysteresis (blue dashed curve) is plotted as a function of abrasion cycle. The apparent advancing contact angle on F-DLC reduced to ~81° after 5000 abrasion cycles due to (b) increased surface roughness and (c) reduced thickness of the top f-DLC layer after abrasion. After 5000 abrasion cycles, the thickness of the F-DLC coating reduces from ~ 1.65 μm to ~ 1.61 μm, resulting in exposure to lower fluorine content regions and reduced hydrophobicity. (f) Dropwise condensation modelling reveals that the droplet Bond number (Bo) is ~ 1.14 after 5000 abrasion cycles, less than the critical Bond number ($Bo_{crit} = 1.4$) for dropwise to filmwise transition.

Figure 3.12a demonstrates that after 5000 abrasion cycles, θ_a on the tested F-DLC surface decreased gradually from ~97.5° (fresh F-DLC surface) to ~81.0°. The contact angle hysteresis ($\Delta\theta = \theta_a - \theta_r$) of the tested surface increased from ~8.0° to ~37.0°. The wettability changes due to the combined effects of increment of local surface energy from partial removal of the top fluorinated layer (f-DLC), and formation of local micro-scale surface roughness (Fig. 3.12b). The EDS line scan (Fig. 3.13) of the F-DLC cross section shows the concentration of fluorine in the top f-DLC layer decreases from top to bottom, resulting in a surface energy gradient along the thickness of the f-DLC layer. Cross-sectional SEM analysis shows that after 5000 abrasion cycles, the total coating thickness reduces from ~ 1.65 μm to ~ 1.61 μm, only a removal of ~ 40 nm of the top f-DLC layer, exposing the surface to the lower fluorine content depth, and reducing

hydrophobicity (Fig. 3.12c). Here we observe that < 10% the material was removed after 5000 abrasion cycles, mainly due to the wear resistance originating from the coefficient of friction (COF) DLC material.[229] The observed abrasion resistance of our F-DLC coating is even better than H-terminated DLC because the two fluorine terminated DLC surfaces sliding against each other would exert higher repulsive forces compared to two H-terminated surfaces. Thus, the mutual interaction of two F-DLC surfaces results in a lower COF.[230]

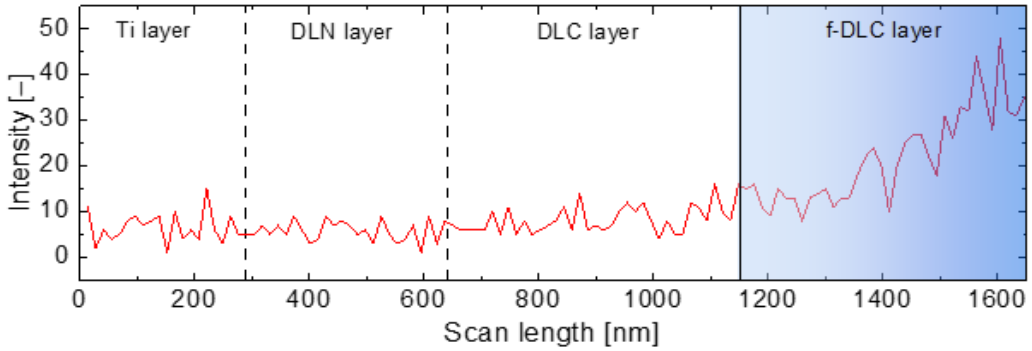

Figure 3.13. EDS line scan result for Fluorine at a cross-section of the multi-layer F-DLC coating. The blue colored area indicates the f-DLC top layer.

Although the F-DLC surface can be characterized as hydrophilic (θ_a < 90°) after 50 abrasion cycles, dropwise condensation and exceptional droplet mobility is maintained due to the maintenance of low contact angle hysteresis.[154] In fact, the F-DLC surface is predicted to maintain dropwise condensation even after 5000 abrasion cycles due to the maintenance of low droplet Bond number (Bo $<$ 1.4). Calculations of Bo for each tested surface based on the abraded surface contact angle measurements reveal a maximum Bo ~ 1.14 after 5000 abrasion cycles. Since Bo $<$ $\mathrm{Bo_{crit}}$ dropwise condensation and high droplet mobility are predicted for the abraded samples. Continued abrasion experiments up to 10000 cycles show that our F-DLC coating eventually transitions to droplet pinning and filmwise condensation behavior with Bo ~ 1.9 (Fig. 3.12d).

3.10. Discussion

Many exciting applications requiring hydrophobicity are limited to laboratory scale experiments simply due to durability limitations. Low surface energy hydrophobic coatings are needed in condensation applications, with the majority of coatings developed in the past decades have been shown to degrade within one month of exposure to moist environments. In addition to wet conditions and condensation, hydrophobic coating resiliency to mechanical deformation or abrasion during application, handling, manufacturing, and operation is a critical bottleneck to coating implementation. Hydrophobic coatings capable of maintaining low surface energy and good thermo-mechanical robustness for an extended period of time in harsh environments or manufacturing conditions are needed in order to finally enable industrial utilization.

When compared to previously reported coatings[39, 231-233], our developed F-DLC coating represents a synergistic combination of parameters required to achieve robust hydrophobicity. Moreover, our F-DLC coating presents a pathway to improve the longevity of low energy coatings not only in applications undergoing harsh thermo-mechanical degradation, but also in manufacturing, biomedical, and marine applications, owing to its tribological and mechanical properties as well as demonstrated corrosion resistance, biocompatibility, and hemocompatibility.[234-239]

Achieving stable dropwise condensation on hydrophobic surfaces has a profound impact on global energy production, water conservation, and hence the carbon footprint of industrialized and developing nations. The Electric Power Research Institute (EPRI) reports that a 1% heat rate increase of a 500 MW_e power plant operating at 80% capacity saves approximately $700,000 in annual costs and reduces CO_2 emissions by 40,000 tons per year[240]. Seventy percent of global electricity is produced by steam power plants (natural gas, coal, nuclear, biofuel), which use an

estimated 100 trillion gallons of water each year for cooling[241]. Power plant efficiency highly depends on the condenser performance. Dropwise condensation enhances the vapor-side heat transfer coefficient of the condenser and increases the difference between the evaporation and condensation temperatures across the power cycle. Thus, the overall system can operate at a higher efficiency or a decrease in overall size, weight and ultimately capital cost[242]. However, while designing the hydrophobic condenser, greater focus is needed to enhance the hydrophobic coating durability rather than the coating hydrophobicity. The overall power plant efficiency gains stagnate after a certain threshold of condensation heat transfer coefficient in achieved[242, 243]. As a clear and economically viable use case, integration of our durable F-DLC surfaces within condensers of steam-cycle power plants represents an opportunity for long-term power cycle efficiency enhancement, societal greenhouse gas emissions reduction, as well as reduced levelized cost of electricity (LCOE). Implementation of our F-DLC coating on a power cycle condenser has the potential to reduce LCOE by 1.9% by enhancing the overall power plant efficiency by 2%.[243]

3.11. Conclusions

In summary, our developed multilayer F-DLC coating has low surface energy characteristic of non-polar polymers, with a high Young's modulus approaching that of pure metals. We demonstrate the versatility of F-DLC on a wide range of substrates including crystalline, non-crystalline and common engineering metals, all showing similar surface energy after coating. The F-DLC not only demonstrates enhanced dropwise condensation heat transfer, but also unprecedented durability in wet environments for a period of more than three years. Characterization of the compatibility of F-DLC in elevated temperature environments exceeding 300ºC and sustainability after 5000 mechanical abrasion cycles demonstrates extreme resiliency.

The outcomes of our work not only develop a low surface energy coating capable of implementation for a plethora of versatile applications, it solves the decades-old problem of generating hydrophobic surfaces that can achieve extended lifetime during exposure to harsh thermo-mechanical environments.

CHAPTER 4

The Lifespan of Slippery Lubricant Infused Surfaces

4.1. Introduction

Usage of low surface tension liquid has grown substantially in recent years due to their implementation as alternative energy sources, biofuels, and refrigeration applications.[11, 43-47] Traditional hydrophobic or superhydrophobic surfaces fail to repel low surface tension liquids,[48, 49] with adsorption of organic contaminants such as proteins, cells or bacteria compromising repellency.[50-52] Although complex re-entrant geometries can achieve repellency of deposited low surface- tension liquids,[53-55] they fail during condensation, where the presence of random nucleation sites leads to flooding and film formation.[56, 57] Hence, the development of durable surfaces that are repellant to low surface tension fluids are needed.

Inspired by the Nepenthes pitcher plant, a new class of surface called the slippery liquid-infused porous surface (SLIPS) has been proposed.[58] Here, a textured solid is infiltrated with a physically and chemically confined immiscible lubricant to create a smooth liquid over layer capable of addressing the challenges associated with maintaining stable air-pockets. SLIPS are omniphobic, exhibit essentially no contact line pinning, are stable at high pressures,[58, 244] and display self-healing to mechanical damage.[58] Moreover, SLIPS have ultralow contact angle hysteresis and show rapid droplet shedding of low-surface tension liquids owing to the presence of a chemically homogeneous and atomically smooth interface for both deposited and condensing

*This chapter was mostly reprinted (adapted) from *ACS Applied Material Interfaces.* 2022, 14, 3, 4598–4611. Copyright © 2020 American Chemical Society. Muhammad Jahidul Hoque is the first author and he contributed to the study via conducting experiments, analyzing data and writing the manuscript. Dr. Nenad Miljkovic guided the research and revised the manuscript and is the corresponding authors.

liquid droplets.[158, 245, 246] Due to their superior repellant properties to a variety of liquids, SLIPS have been demonstrated to promote stable dropwise condensation of low surface tension organic vapors and enhanced dropwise condensation heat transfer.[59-62] Dropwise condensation of ethanol and hexane on SLIPS in pure vapor environments shows a 200% heat transfer enhancement when compared to smooth hydrophobic or hydrophilic metal surfaces during continual 7-hour tests.[217, 247] However, the majority of technologies promising for SLIPS implementation have longevity timescales at a minimum of months (consumer products), with the majority having operating lifetime requirements of multiple years (industrial equipment).

The life span of SLIPS is of crucial importance for both system performance and economic considerations. A lack of fundamental understanding of condensation-induced degradation mechanisms has held back the successful development and demonstration of surfaces capable of achieving stable dropwise condensation. One of the largest barriers to success is the long experimental timescale required to quantify life span. A limited number of studies have focused on conducting long-term condensation durability tests on functional surfaces.[63-69] To the best of our knowledge, no study has quantified the long-term (multi-month) condensation durability of SLIPS. The majority of past work has focused on short term robustness quantification for icing/frosting, biofouling, corrosion, and ageing.[70-77] In this chapter, we show rigorous multi-month durability studies of SLIPS during relevant steam and ethanol condenser conditions. We focus our degradation conditions to condensers given the clear and promising use case for SLIPS. Specifically, we design and test a holistic array of durability conditions which aim to emulate realistic scenarios that SLIPS would encounter if implemented within large scale shell and tube condensers. These include: single-phase vapor shear (condenser inlet), elevated temperature exposure to air (manufacturing), long-term condensation tests (condensation), and immersion for

prolonged periods within water and ethanol (condenser outlet). We use rationally designed ultra-scalable nanostructured copper oxide (CuO) SLIPS impregnated with vacuum grade lubricants covering a wide range of viscosity (9.7 mPa·s to 5216 mPa·s). Our work forms the basis for science-based fabrication of durable SLIPS.

4.2. Fabrication and Wettability of SLIPS

To fabricate the SLIPS, we used Copper (Cu) as a base substrate. Commercially available Cu tubes with outer diameters, d_{OD} = 9.52 mm, inner diameters, d_{ID} = 8.73 mm, and lengths L = 108 mm were used as the test samples. The fabrication process starts with cleaning the un-capped Cu tube by dipping it for 15 min in acetone, ethanol, isopropanol, and deionized (DI) water, in succession, followed by rinsing with DI water. The tubes were then dipped into a 2.0 M hydrochloric acid solution for 2 min to remove the native oxide layer on the surface, then rinsed multiple times with DI water and dried with clean nitrogen gas stream. Afterwards, dense blade-like nanostructured CuO surfaces were formed by immersing the capped cleaned tubes into a hot (90 ± 5°C) alkaline bath of $NaClO_2$, NaOH, $Na_3PO_4 \cdot 12H_2O$, and DI water (3.75:5:10:100 wt%).[132] Surfaces were then functionalized using atmospheric pressure chemical vapor deposition (CVD) of a fluorinated silane (heptadecafluorodecyltrimethoxy-silane, HTMS, Gelest, CAS #83048-65-1).[248] Lubricants of choice were next impregnated into the functionalized superhydrophobic CuO samples by dipping them into the lubricant. After dipping the samples in the lubricant for 10 mins, drainage of the excess lubricant from the surface was ensured by leaving the tubes in a vertical position for 24 hours in ambient conditions followed by drying in a clean nitrogen stream. Gravitational drainage of excess oil from the surfaces for 24 hours ensures the presence of lubricant only within the nanostructures, which was shown to be independent on the oil viscosity.[217] From a

theoretical perspective, we estimate the amount of oil retained in the CuO structure by considering that irrespective of the oil viscosity, the lubricant fills the CuO microstructures (structure height h ≈ 2 μm, solid fraction $\varphi \approx 0.023$). Thus, at initiation of the experiments, the SLIPSs have ≈ 2 mL/m^2 (≈ 3.8 g/m^2) of lubricant per unit condenser surface area.[249]

Here we used, Krytox 16256 (5216 mPa·s at 20°C), Fomblin 25/6 (524 mPa·s at 20°C), Krytox 1525 (496 mPa·s at 20°C), Carnation oil (9.7 mPa·s at 20°C), and GPL 101 (14.7 mPa·s at 20°C), as the infusing lubricants. These lubricants were rationally selected to cover a wide range of vapor pressures at room temperature (4.0×10^{-15} kPa to 1.3×10^{-8} kPa), viscosity (9.7 mPa·s to 5216 mPa·s), and to some extent surface tension (18 to 28 mN/m).

Table 4.1. Physical Properties of Different Infused Oil at Room Temperature (~20ºC).

Infused Oil	Oil Type	Density [Kg/m^3]	Oil Dynamic Viscosity [mPa·s]	Surface Tension [mN/m]	Vapor Pressure at 20ºC [kPa]	Spreading Coefficient	
						Water	Ethanol
Carnation Oil	Mineral	810	9.7	28	10^{-2}	-6.6	-10.11
GPL101	Fluorinated	1890	14.7	18.8	N/A	2.9	0.0
Fomblin Y25/6		1900	524	20	6×10^{-8}	1.76	-1.22
Krytox 1525		1900	496	19	1.3×10^{-8}	2.70	-0.20
Krytox 16256		1920	5216	19	4×10^{-15}	2.70	-0.20

Fluorinated and mineral oils were selected as lubricants due to their immiscibility with water and ethanol, as well as their differing spreading behavior at the condensate/oil interface (Table 4.1).[250] Figures 4.1(a), and 4.1(b) show scanning electron micrographs (SEM) of a

functionalized CuO and lubricant (Krytox 1525) infused CuO SLIPS, respectively. The contact angle of water and ethanol on each sample was measured using microgoniometry (MCA-3, Kyowa Interface Science), where liquid droplets (100 nL) were dynamically grown to measure the apparent advancing contact angles. The microgoniometer droplet dispenser was then turned off and the deposited droplets were allowed to continuously evaporate to obtain the apparent receding contact angle.[141, 159, 251] All SLIPS surfaces showed < 5º contact angle hysteresis (Figure 4.1c). Ethanol droplets made a thin film after impacting the superhydrophobic CuO surface, making it difficult to measure the contact angle (Figure 4.1c). Similarly, condensation of ethanol on the superhydrophobic CuO surface resulted in liquid film formation (Figure 4.1d). As expected,[217] all SLIPS showed dropwise condensation during short term (< 1 day) condensation experiments.

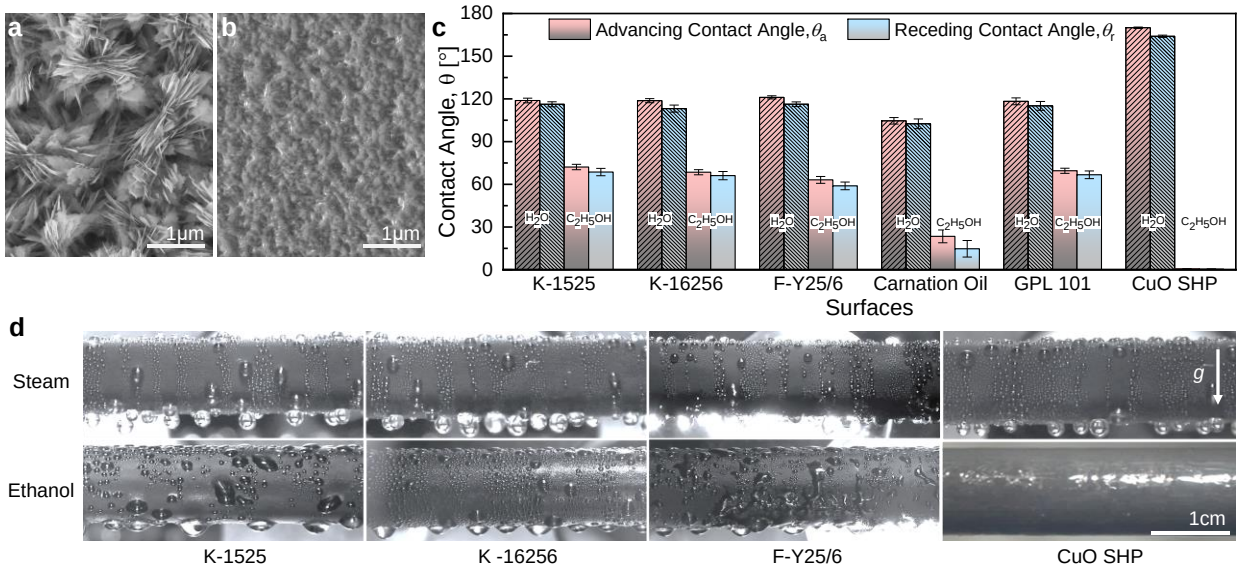

Figure 4.1. Surface wettability characterization of different SLIPS. Scaning electron microscopy (SEM) images of a (a) superhydrophobic CuO surface and (b) Krytox 1525 infused CuO SLIPS. (c) Goniometric contact angle measurements of DI water and ethanol droplets on the studied samples. (d) Optical images of external condensation of steam and ethanol vapor on different SLIPS and the superhydrophobic CuO surface. SLIPS infused with Krytox 1525, Krytox 16256, and Fomblin are named K-1525, K-16256, and F-Y25/6, respectively. Sueprhydrophobic CuO is termed CuO SHP. Contact angle of ethanol on the CuO SHP surface is difficult to measure and is not reported as as ethanol completey wets the surface.

4.3. Experimental Setup and Approaches

Condensation Durability Test Setup. To evaluate the condensation durability of SLIPS for prolonged periods of time, we built a customized vacuum chamber which was mounted on a stainless-steel frame integrated on a movable cart (Figure 4.2a). The main environmental cylindrical chamber (16.5" diameter and 26" long) consists of a top opening, three customized side optical view ports, and six apertures for various components around the side walls. The top opening was sealed with a rubber gasket and a custom-made stainless-steel view port (Kurt J. Lesker) which has three circular glass windows (2 with a 6" diameter and the third with a 4.5" diameter). The top windows were used for visualization of the condensation phenomena inside the chamber. Among the six apertures, two were used as feedthrough connections to the chiller inlet and outlet, one was connected to the vacuum pump line, one was connected to a tee-joint for sensors and venting, other the remaining two were sealed. All feedthroughs used high-vacuum compatible CF flanges having silver plated copper gaskets. Other KF flanges were sealed with stainless steel centering rings accompanied by nitrile rubber O-rings.

A Cu tube in the form of a water jacket was soldered around the entire body of the chamber helically in the axial direction (Figure 4.2a and 4.2g) through which tap water at 65°C was supplied from a hot water bath (1C1551256, PolyScience, Figure 4.2b). The hot water jacket helped to maintain the chamber wall temperature at ≈55°C throughout the long-term experiment, which helped to reduce the amount of condensation occurring on the inside the chamber wall and side view ports. A heater (3631K44, McMaster-Carr) with an adjustable temperature controller was wrapped around the outer wall of the chamber near the base occupied by the working fluid inside of the vessel (Figure 4.2g). A second tape heater (AWH-171-020, HTS/Amptek) controlled with a variable voltage controller was attached to the outer-bottom surface of the chamber. These two

heaters were calibrated and adjusted at voltages to maintain constant boiling of the working fluid inside of the chamber. The heating water jacket and all the heaters were insulated to limit heat losses to the ambient environment.

Cooling tap water was supplied to the chamber from a high-capacity chiller (N0772046, PolyScience) *via* the KF fluid feedthroughs (Kurt J. Lesker, Figure 4.2a and 4.2b). To monitor the water flow rate, an electromagnetic flow meter (FMG93-PVDF, Omega) with an accuracy of ±1% of the reading was integrated in series with the coolant inflow line (Figure 4.2e). To remove non-condensable gases prior to the experiments, a bellows valve (Ideal Vacuum) was attached to top of the environmental chamber for connection to a rotary vane vacuum pump (KJLC-RV212, Kurt J. Lesker, Fig.4.2c). An in-line liquid nitrogen (LN2) cooled trap (Kurt J. Lesker) was incorporated into the evacuation line from the environmental chamber to the vacuum pump *via* bellows tube connection (Kurt J. Lesker). The LN2 trap enabled removal of moisture from the air which also helped to produce a lower base pressure and faster pump down time (Figure 4.2b).

To monitor the pressure within the chamber, a vacuum pressure transducer (925 Micro Pirani, MKS) was installed (Figure 4.2d). A secondary valve (Kurt J. Lesker) was integrated with a tee flange between the pressure transducer and capped end to release the vacuum to ambient once the experiment was finished (Figures 4.2a and 4.2b). As the working fluid was poured into the chamber prior to pump down, complete removal of non-condensable gases (NCGs) was not possible. To monitor temperatures within the system, K-type thermocouple bundles were connected to the chamber *via* the thermocouple feedthroughs (Kurt J. Lesker). Outside of the chamber, two thermocouples monitored the inlet and outlet temperatures of the coolant. Inside of the chamber, the temperature of the side walls, vapor and ambient, and working fluid/condensate were monitored throughout experiment.

The thermocouples, flow meter and pressure transducer were electrically connected to a data acquisition (DAQ) system (cDAQ-9174, National Instruments), and data was continuously recorded throughout the experiment with all collected data was analyzed with LabVIEW. The DAQ system included a thermocouple input module (NI-9213, National Instruments), a digital module (NI-9423, National Instruments), a voltage input module (NI-9209, National Instruments), and a terminal block (NI-9923, National Instruments). A stainless steel manifold (Swagelok) was built to hold the test samples. Care was taken while making the manifold so that none of the samples resided in the same vertical plane (Figure 4.2h). Furthermore, manifold design was such that close hydraulic balancing (equivalent flow lengths) was achieved for each sample to ensure similar coolant flow rates for all tube samples. This prevented condensate drainage from top samples to lower samples. Finally, a DSLR camera (K-50, Pentax) was placed outside of the top view port of the chamber for visual observation of coating degradation (Figure 4.2a).

A set of strict test procedures were followed to ensure consistency throughout the experiments. First, the chamber interior was thoroughly cleaned with isopropyl alcohol (IPA) to remove any contaminants. Then the chamber was filled with 15 liters of the working fluid (DI water or ethanol). The hot water bath (Cu jacket heater) and tape heaters were turned on to heat up the chamber walls for drying out inside of the chamber prior to pump down and to prevent condensation during the experiments. The test samples were fixed using Swagelok connections to the customized manifolds holding the samples. The manifolds were then connected to the coolant loop via the inlet and outlet feedthroughs (Figure 4.2h). Simultaneously, thermocouples were attached to the chamber walls using Cu tape and placed inside the working fluid residing on bottom.

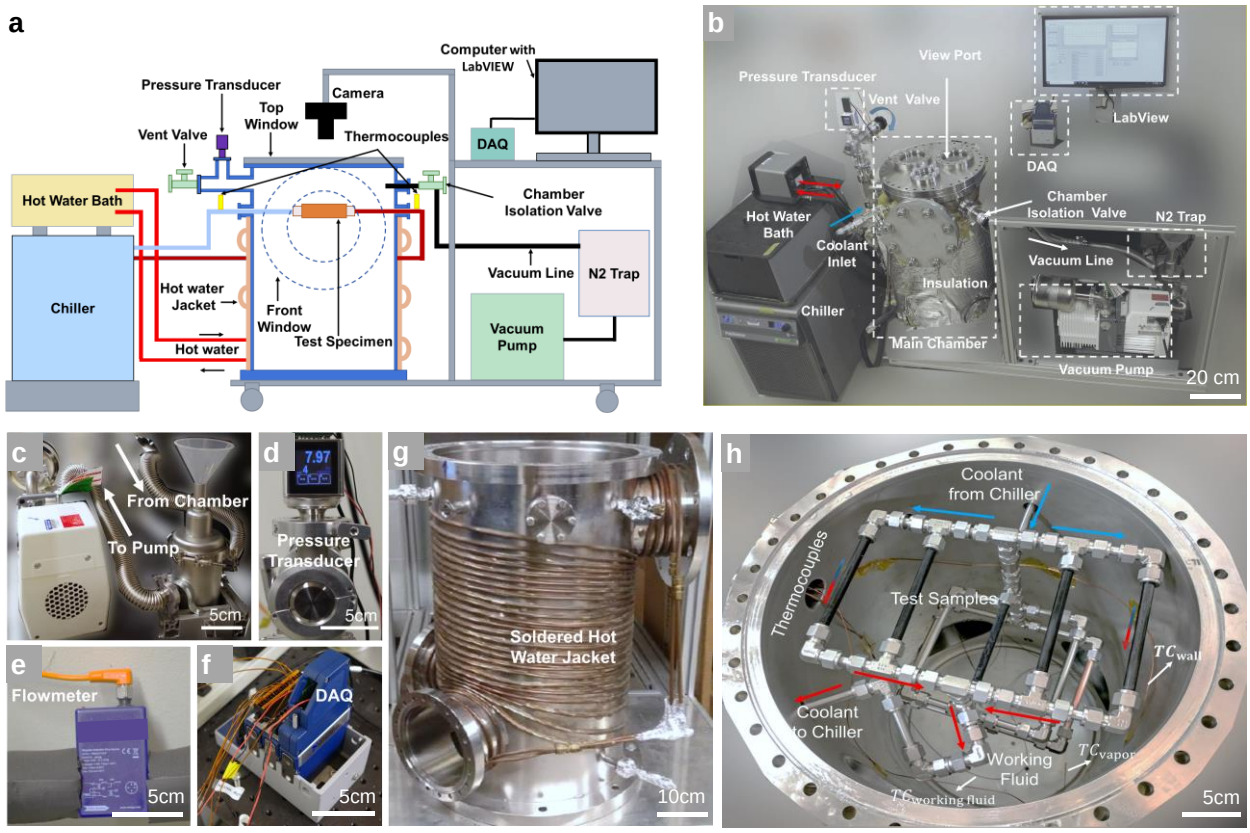

Figure 4.2. Condensation chamber for durability experiments. (a) Schematic and (b) image of the test rig showing all system components. (c) Vacuum line showing the flow path from the main chamber to the vacuum pump, where the LN2 trap is placed. Photograph of the (d) pressure transducer, (e) flowmeter, and (f) DAQ system. (g) Photograph showing the Cu tube water jacket soldered on the main chamber, helping to reduce condensate accumulation on the chamber walls. (h) Photograph of the Swagelok manifold built for holding the test tube samples.

Condensation Durability Testing Protocols. Given the long period of continuous condensation (> 1 month), a leak test was performed to ensure no leaks were present before each experimental trial. After sealing all openings, all valves of the chamber were closed. The LN2 trap was first filled with liquid nitrogen. After closing the vent valve, the pump is turned on and then the valve connecting the bellows the vacuum pump via the LN2 trap is slowly opened to initiate the pump down process. The chamber pressure was monitored using pressure transducer. In the middle of pump down process, the chiller was turned on, and the water temperature was set to 5°C. The inflow rate of the coolant was monitored using the electromagnetic flowmeter and was maintained

at 10 LPM. The pump down process took approximately 30 minutes to achieve a vacuum level of $P \sim 5$ kPa. Due to the presence of the working fluid in the chamber, it is not possible to completely remove all NCGs unless a full freeze pump thaw cycle was enacted. However, the partial vacuum conditions reached were maintained in the chamber which reduced the amount of heat required to boil the working fluids. Whenever necessary during pump down, the LN2 trap was refilled. The LN2 trap was cleaned midway, since frost formed on the LN2 trap and blocked the vacuum line during the pump down process.

When a steady base pressure was achieved, the valve connecting the environmental chamber and the LN2 trap was closed, and the pump was turned off. Then, the valve connecting the vacuum pump and the ambient was opened to release vacuum in the pump line. Before conducting the experiment, the leak test was performed. At that time, the chamber was filled with required amount of working fluid and dummy samples were connected to the Swagelok manifolds. For the leak test, the chamber was left in the vacuum state for >24 hours, and the chamber pressure was monitored with the pressure transducer. The leak rate was characterized to acquire the leak rate of air into the chamber. When the leak test was finished, the vacuum was released by opening the valve connecting the environmental chamber and the ambient. Once the leak test was finished, an actual experiment was performed. In actual experiments, steady state conditions were typically reached after approximately 30-40 minutes of operation. Throughout the experiments, data (temperatures, pressure, and flow rate) was collected, and the images of each sample were recorded using the DSLR camera. To maintain the same level of pressure though the long-tern durability test, the condensation rig had to be shut down once per month in order to pump down the chamber to the desired pressure level to remove non-condensable gases. This was done due to air leaking into the chamber at a slow rate from the atmosphere-to-saturated vapor (sub-atmospheric pressure)

pressure difference. During shutdown, the chamber was not opened and only the cooling water flowing through the tubes was arrested. During shutdown, the chamber was vacuumed through a valve feedthrough to remove non condensable gases, with shutdown lasting no more than 3 hours per month. For the remaining time, continual 24-hour a day condensation occurred in the chamber.

4.4. Long-Term Durability during Steam Condensation

To conduct condensation durability studies on SLIPS relevant to thermoelectric power generation applications, we exposed the samples to continual steam condensation. Four SLIPSs infused with Carnation Oil, Fomblin (F-Y25/6), Krytox 1525 (K-1525), Krytox 16256 (K-16256) and one superhydrophobic (SHP) CuO sample were placed in the chamber. Condensation experiments and visualization was continuously conducted. The long-term condensation durability experiments were conducted in a customized chamber maintaining a pressure of ~ 5 kPa.

Condensation of steam on the surfaces was visualized over long periods of time to evaluate surface degradation (Figure 4.3). For steam condensation, degradation or loss of hydrophobicity indicates that the DI water apparent advancing droplet contact angle decreases below 90 degrees along with significant reduction of the receding contact angle. As a result, the contact angle hysteresis increases when compared to the freshly made sample. Visualization of the condensation transition from regular spherical shaped droplets (dropwise) to a surface flooded with irregular shaped droplets or thin condensate films provided a qualitative measure of surface degradation. The superhydrophobic CuO surface and Carnation oil infused SLIPS degraded after 10 days of exposure to steam condensation, with both surfaces flooding with a three-week period of initiating steady condensation (Figure 4.3).

In contrast, the F-Y25/6 and K-1525 infused SLIPS showed good shedding behavior for up to one month of steady-state steam condensation. Among all samples, K-16256 infused SLIPS showed no sign of degradation after 45 days of exposure to steam condensation. The viscosity and spreading coefficient of the impregnated oils play a vital role on the long-term durability of SLIPS during condensation. Variation in the longevity among the different SLIPS stems from the difference in oil ridge formation, cloaking phenomena (right schematic in Fig. 4.3 and Fig. 4.4), and contrast in the rate of oil depletion with shedding condensate droplets resulting from the viscosity differences of the infused oils. Condensate encapsulation or cloaking of the condensate droplets by the infused oil was observed when the spreading coefficient of the oil on the condensate (S_{oil}) is positive ($S_{\text{oil}} > 0$).[252-254] The spreading coefficient S_{oil} is defined as, $S_{\text{oil}} = \gamma_{\text{droplet}} - \gamma_{\text{oil}} - \gamma_{\text{oil-droplet}}$, where γ_{droplet}, γ_{oil}, $\gamma_{\text{oil-droplet}}$ represent the surface tension of the condensing droplet, lubricant oil, and interfacial tension between the droplet and oil, respectively. Cloaked condensate sheds from the surface and over time reduces the slipperiness of the surfaces by depleting the infused oil layer (right schematic in Figure 4.3). Carnation oil has a negative spreading coefficient ($S_{\text{carnation}} = -6.6 < 0$), which prevents cloaking.[250] However, both K-1525 and K-16256 have positive spreading coefficients ($S_{\text{Krytox}} = 2.7 > 0$). Hence, the oil can spread and encapsulate the condensed water droplet.[250] Even though K-16256 has positive spreading coefficient, the shedding of the cloaked droplets from the K-16256 infused SLIPS had the lowest oil depletion rate due to the highest viscosity (μ = 5216 mPa·s) among the tested samples. Due to its negative spreading coefficient, carnation oil hinders cloaking. However, the surface loses its slipperiness in a very short period of time because the infused carnation oil has a very low viscosity (μ = 9.7 mPa·s) and is removed via shear induced drainage.

Our results show that even in the presence of droplet cloaking, the viscosity of the infused oil plays a more dominant role on the lifespan of SLIPS during condensation. Past studies have shown that a major source of oil depletion happens during oil ridge formation near the base of the departing droplet.[255, 256] To evaluate the effects of oil viscosity variation on the droplet wetting ridge-driven oil depletion, we performed a scaling analysis to compare with cloak-layer-driven oil depletion. The volume of a condensate droplet (V_{droplet}) with an apparent advancing contact angle, θ and radius R, can be expressed as,**[220]** $V_{\mathrm{droplet}} = (\pi/3)[(1-\cos\theta)^2(2+\cos\theta)R^3]$. The volume of a cloak layer ($V_{\mathrm{cloak\,layer}}$) on the condensate droplet can be calculated from the difference between original droplet size and size increment due to a cloak layer with a thickness t. Thus, $V_{\mathrm{cloak\,layer}} = (\pi/3)[(1-\cos\theta)^2(2+\cos\theta)]\,[(R+t)^3 - R^3]$. Assuming, a 2 mm diameter condensate droplet with a contact angle of 120° having a 10 nm cloak layer, the volume of the cloak layer becomes, $V_{\mathrm{cloak\,layer}} = 1.06 \times 10^{-13}$ m^3. The volume of the oil ridge around a condensate droplet can be expressed as,[256] $V_{\mathrm{ridge}} = R_{\mathrm{b}}{h_{\mathrm{i}}}^2/\mu_1 Ca^{\frac{4}{3}}$, where R_{b} is the base radius of the droplet, h_{i} is the initial lubricant film thickness, $\mu_1 \sim 0.5$, is the limiting size of the wetting ridge for a given set of experimental conditions,[256] and $Ca = \eta U / \gamma$ is the capillary number. Here η is the oil viscosity, γ is the surface tension of the oil, and U is the droplet shedding velocity. For a departing condensate droplet ($R_{\mathrm{b}} = 2$ mm) shedding at 2 mm/s on K-16256 (η = 5216 mPa·s; γ = 19 mN/m) and K-1525 (η = 496 mPa.s ; γ = 19 mN/m) infused SLIPS with an initial oil layer thickness, h_{i} = 2 μm, the oil ridge volumes are, $V_{\mathrm{ridge,K-16256}} = 1.78 \times 10^{-14}$ m^3 and, $V_{\mathrm{ridge,K-1525}} = 4.09 \times 10^{-13}$ m^3. Our analysis shows that for SLIPS with high viscosity oil (K-16256), the cloak-layer-driven oil depletion dominates ridge-induced oil depletion ($V_{\mathrm{cloak\,layer}} = 1.06 \times 10^{-13}$ m^3 > $V_{\mathrm{ridge,K-16256}} = 1.78 \times 10^{-14}$ m^3). However, this ratio of depletion rates

becomes smaller for lower viscosity oils ($V_{\text{ridge,K}-1525} = 4.09 \times 10^{-13}$ m^3 ~ $V_{\text{cloak layer}}$). Due to having the same order of magnitude oil viscosities, both K-1525 and F-Y25/6 show similar behavior.

Lifespan Prediction. By combining the estimated volume of oil drainage per droplet with the experimentally observed droplet count, we can predict the idealized lifespan of a SLIPS surface. In our condensation experiments in pure steam conditions, we observed that the number of droplet shedding events from a SLIPS infused with K-16256 was approximately 30 droplets/min. In pure ethanol condensation, this number was ~60 droplets/min. For both cases, the vapor pressure was maintained at ~6 kPa in an environmental chamber and experiments performed on a SLIPS tube sample having 3/8" (0.0095m) external diameter with 3" (0.0762 m) length. In our simplified scaling analysis, we showed that for K-16256 infused SLIPS, the volume of oil drainage due to the cloak layer and oil-ridge induced droplet shedding are, $V_{\text{cloak layer}} = 1.06 \times 10^{-13}$ m^3 and $V_{\text{ridge}} = 1.78 \times 10^{-14}$ m^3, respectively.

Due to the negative spreading coefficient of K-16256 ($S_{\text{K}-16256,\text{ethanol}} = -0.20$) with ethanol condensate, we assume only the wetting-ridge-induced oil drainage is present. Hence, the amount of oil drainage during ethanol condensation is (60 droplets/min) × (1.78×10^{-14} m^3) = 1.07×10^{-12} m^3/min.

Due to the positive spreading coefficient of K-16256 ($S_{\text{K}-16256,\text{steam}} = 2.70$) with steam condensate, extra oil will drain with shedding droplets due to cloak layer formation along with the presence of the oil-ridge. Hence, the amount of oil drainage during steam condensation is (30 droplets/min) × (1.78×10^{-14} m^3 + 1.06×10^{-13} m^3) = 3.7×10^{-12} m^3/min.

Furthermore, at the initiation of the experiments, SLIPS with CuO microstructures (structure height $h \approx 2$ μm, solid fraction $\varphi \approx 0.023$) have approximately 2 mL/m^2 ($\approx 2 \times 10^{-6}$

m^3/m^2) of lubricant per unit condenser surface area.[249] So, the total amount of impregnated oil on a 3" long and 3/8" diameter SLIPS is $\pi \times 0.0095\, m \times 0.0762\, m \times\ 2 \times 10^{-6}\, m^3/m^2$ = $4.55 \times 10^{-9}\ m^3$

Hence, the ideal lifespan ($t_{\text{working fluid}}$) for a K-16256 infused SLIPS during ethanol and steam condensation are:

t_{ethanol} = $(4.55 \times 10^{-9}\ m^3) / (1.07 \times 10^{-12}\ m^3/\text{min})$ = 4252.34 min = **2.95 days**.

t_{steam} = $(4.55 \times 10^{-9}\ m^3) / (3.7 \times 10^{-12}\ m^3/\text{min})$ = 1229.73 min = **0.85 days**.

Similarly, the lifespan of a SLIPS infused with an order of magnitude lower viscosity oil (K-1525) is:

$t_{\text{ethanol,K}-1525}$ = $(4.55 \times 10^{-9}\ m^3) / (3.7 \times 10^{-11}\ m^3/\text{min})$ = 122.97 min = **2.05 hours**,

where 90 ethanol condensate droplets shed per minute maintaining a negative spreading coefficient ($S_{\text{K}-1525,\text{ethanol}} = -0.20$) with the infused oil. And the oil-ridge volume for K-1525 is, $V_{\text{ridge}} = 4.09 \times 10^{-13}\ m^3$.

The predicted lifespan of SLIPSs is far less than the actual timeline observed in the experiments. Although qualitatively the scaled lifetimes are in agreement (i.e. ethanol condensation results in lower SLIPS drainage and lower viscosity oil drains faster), multiple factors lead to the variation between the experimentally observed and theoretical estimated lifetime of the SLIPS. Although our scaling analysis is elucidating in identifying the volumetric contribution of lubricant loss due to cloaking and oil ridge formation, it does not consider kinetics. The cloak layer formation timescale or oil ridge formation timescale depend on the viscosity of the infused oils, the method of condensate formation (deposition vs condensation), as well as the shedding rate and droplet lifetime on the surface. Past work has shown that the initial cloak layer formation timescale for higher viscosity oils (K-16256) is an order of magnitude higher than

moderate viscosity oils (K-1525, F-Y25/6).[253] Also, the theoretical model assumed a uniform cloak layer thickness irrespective to the droplet size and oil viscosity. However, the cloaking layer is spatially and temporally non-uniform when compared to the lubricant underneath and behind a moving droplet.[255, 256] Moreover, for simplification, we assumed same shedding droplet size, and similar droplet shedding velocity irrespective to the SLIPS surfaces and condensation environments (steam/ethanol). Oil depletion due to the oil ridge formation is a function of the departure velocity and oil viscosity. As the viscosity of the infused oil increases, the departure velocity decreases.[255] Depending on the droplet size, not only will the shedding velocity change, but so will the cloak layer thickness and oil-ridge pattern.

Moreover, the model used assumes a scenario of a single droplet moving on a SLIPS surface at a relatively constant velocity. This condition differs from that of droplet being formed, coalescing, and shedding during long-term condensation experiments (as conducted in this study). The droplet dynamics studied here involve multi-droplet coalescence, departure, and re-nucleation. In reality, continuous droplet-nucleation-re-nucleation, multi-droplet coalescence, and restoring/wicking phenomena exist[257], which together lead to the continuous formation-rupture-reformation of the cloaking layer and oil-ridge. The existing theoretical framework used for the scaling analysis and lifespan estimate do not capture these kinetics.

In addition, we assume that the total volume of oil present in the cloak layer and oil ridge drain with the shedding droplet and that all droplets shedding from a surface contribute equally to the oil depletion throughout the lifespan of the surface. In reality, these are simplified assumptions. As the infused oil starts to drain, it leads to the gradual exposure of the CuO microstructure tips, changing the interfacial phenomena between the condensate and underlying oil-infused microstructures. We hypothesize that overtime, due to this reduction of oil volume fraction, the

timescale of the cloak layer and oil-ridge formation increases, which decreases the oil drainage rate and results in enhanced lifespan of the surfaces as observed in our experiments.

Future studies are needed to validate our hypotheses and to develop higher fidelity models of SLIPS lifespan that focus on the effects of oil viscosity, type of working fluid, and multi-droplet coalesce dynamics on cloaking oil layer formation, oil ridge formation, droplet shear dynamics, and time dependent oil-drainage, which all holistically combine to govern lubricant depletion dynamics on SLIPS.

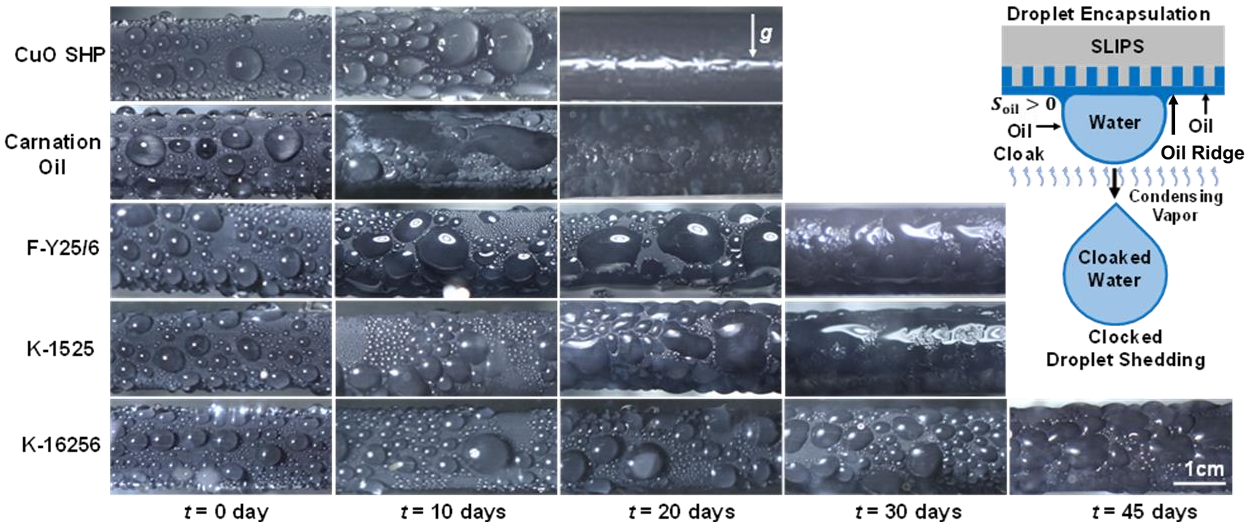

Figure 4.3. Steam condensation durability. Time-lapse optical images of the samples during steady steam condensation. The superhydrophobic (CuO SHP) tube surface and the carnation oil infused SLIPS sample degraded after 10 days, with both surfaces transitioning to filmwise condensation within 20 days after test initiation. The F-Y25/6 and K-1525 infused SLIPS performs well for approximately 21 days, with transition to filmwise condensation within 28 days. The highly viscous K-16256 infused SLIPS did not show filmwise condensation after 45 days of continuous steam condensation. Schematics (not to scale) on right: Oil with positive spreading coefficient forms an oil cloak around the condensate, clocked condensate shedding increases the oil depletion rate results in reduction of slippery lifespan.

4.5. Long-Term Durability during Ethanol Condensation

To conduct condensation durability studies on SLIPS relevant to organic Rankine cycle and petrochemical separations condenser applications, we exposed the samples to continual ethanol vapor condensation conditions. In addition to the high viscosity SLIPS (F-Y25/6, K-1525, and K-16256), we also tested a SLIPS infused with a very low viscosity oil (GPL-101, 14.7 mPa·s). Although the carnation oil has a negative spreading coefficient in both water and ethanol ($S_{\text{carnation,water}} = -6.6$; $S_{\text{carnation,ethanol}} = -10$), it was not included in the ethanol condensation tests due to its demonstrated poor durability during steam condensation (Figure 4.3). Similarly, GPL-101 was not used during steam condensation due to its positive spreading coefficient ($S_{\text{GPL101,water}} = 2.9 > 0$) and low viscosity (μ = 14.7 mPa·s). For ethanol condensation, we included GPL-101 because of its unique spreading coefficient with ethanol condensate ($S_{\text{GPL101,ethanol}} = 0$, Table 4.1).

Experiments revealed that the low surface tension ethanol condensate (24.8 mN/m) forms a film on the superhydrophobic (SHP) surface immediately after condensation initiation (Figure 4.4). As expected, due to its low viscosity, the GPL-101 infused SLIPS degraded within 14 days of continuous exposure to ethanol condensation. For ethanol, since the apparent advancing contact angle was already below 90º on the fresh surfaces, the indication of loss of ethanol-repellency was measured by the increase in contact angle hysteresis stemming from the substantial decrease in the receding contact angle, which leads to irregular droplet shape (or film) formation during condensation.[154] The Krytox oil infused SLIPS (K-1525 and K-16256), and Fomblin (F-Y25/6) have negative spreading coefficients with ethanol condensate (Table 4.1), resulting in the absence of cloaking and delayed oil depletion. By preventing cloaking, high viscosity SLIPSs show longer durability to ethanol condensation when compared to steam condensation (Figure 4.4

and Table 4.2). Due to the negative spreading coefficient, the condensates are not cloaked. Furthermore, evaporation of the infused oil is negligible as the volatility is low at ambient temperatures. Hence, oil mainly depletes due to oil ridge formation and condensate shear beneath shedding droplets (right schematic in Figure 4.4). As shown in Figure 4.4, compared to steam condensation, SLIPS infused with high viscosity oils (K-1525, K-16256, and F-Y25/6) showed continuous ethanol condensate shedding for more than 5 months of continual testing. In agreement with the steam condensation experiments, the K-16256 infused SLIPS had the greatest longevity, demonstrating stable dropwise condensation for more than 8 months (250 days) of continual ethanol condensation.

Condensate droplet dynamics of ethanol differ from water due to two different reasons. The first is that ethanol condensate and water have different surface tensions. The second is due to oil layer depletion from the underlying structure and resulting exposure of the underlying structure. The latter acts to decrease the lubricant-condensate interface area and increase the structure condensate interfacial area, which acts to alter the condensate-sample surface energy during long term exposure to condensation. As seen in Figure 4.3, after 20 days of steam condensation, F-Y25/6, K-1525, and K-16256 showed the formation of irregular shaped droplets, demonstrating a slow transition to filmwise condensation within a week for the low viscosity SLIPS. Ethanol showed regular small condensate droplet formation at the very early stages of condensation (Figure 4.4, < 1 day). For longer condensing times, the surfaces transitioned to a hybrid dropwise-filmwise condensation mode (Figure 4.4) which was stable in time. As seen in Figure 3, after 60 days of exposure to ethanol condensation, the high viscosity SLIPS showed the hybrid mode of condensation which is stable for K-1525, and F-Y25/6 for up to 5 months of exposure. The SLIPS

impregnated with the highest viscosity oil (K-16256) held this hybrid stability for more than 8 months.

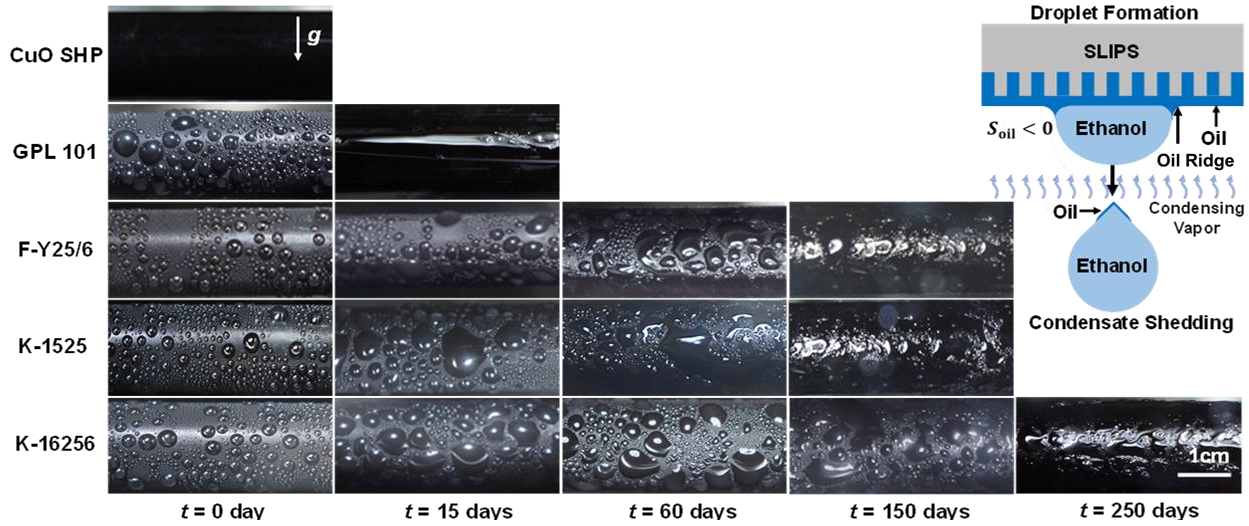

Figure 4.4. Ethanol condensation durability. Time-lapse optical images of the samples during steady ethanol condensation. The superhydrophobic (CuO SHP) tube surface shows filmwise condensation immediately after starting condensation (t = 0). The GPL-101 infused SLIPS degrades in 14 days, showing filmwise transition. The F-Y25/6, and K-1525 infused SLIPSs degraded at 5 months of continual ethanol condensation exposure, with the highly viscous K-16256 infused SLIPS degrading after 8 months. Unlike steam condensation, SLIPSs samples exposed to ethanol condensation show stable filmwise-dropwise hybrid condensation before eventual transition to filmwise. Schematics (not to scale) on right: oil with negative spreading coefficient does not cloak the condensate, however, due to condensate shear, oil depletes at a very slow rate delaying the oil depletion and hence increased the lifespan of the SLIPS. The oil layer on the trailing edge of the shedding droplet does not imply the actual mechanism of oil depletion.

To quantify if the continual condensation durability tests affected the dropwise condensation heat transfer, the condensation heat transfer was measured after completing the 150 day ethanol condensation durability test. The condensation heat transfer coefficient measurement for pure ethanol was conducted in a separate controlled environmental chamber.[36] The K-16256 SLIPS sample, which showed the best condensation durability, was measured to maintain the same condensation heat transfer coefficient as that of a freshly made sample, which was measured to be 7.3 ± 3.1 kW/(m^2·K). The result is in line with the observations of continual dropwise

condensation. Although we observed that oil viscosity significantly alters SLIPSs durability, variation in oil viscosity does not affect the condensation heat transfer coefficient, as the coating thermal resistance for varying oils are significantly lower than the condensation heat transfer and internal single-phase convection heat transfer resistances (See section 4.5.1).

Table 4.2. Characterization of samples after steam and ethanol condensation durability tests. The measured $\Delta\theta_{\mathrm{water}}$ and $\Delta\theta_{\mathrm{ethanol}}$ characterize the water droplet and ethanol droplet contact angle hysteresis prior to conducting condensation experiments. Lifetime is defined as the condensation exposure time required to transition the condensation mode from dropwise or hybrid dropwise-filmwise to classical filmwise condensation.

Surface	**Infused Oil**	$\boldsymbol{\mu}$ **[mPa·s]**	$\boldsymbol{\Delta\theta_{\mathrm{water}}}$ **[◦]**	$\boldsymbol{\Delta\theta_{\mathrm{ethanol}}}$ **[◦]**	**Steam**	**Ethanol**
					Lifetime [Days]	**Lifetime [Days]**
CuO-HTMS	N/A	N/A	4.1	N/A	20	1
CuO-HTMS	Carnation Oil	9.7	2.8 ± 1.1	8.7 ± 1.3	20	N/A
	GPL101	14.7	3.2 ± 1	2.8 ± 1.2	N/A	10
	Fomblin	524	2.9 ± 2.7	2.2 ± 3.1	30	150
	Krytox 1525	496	2.7 ± 2.6	2.3 ± 2.9	30	150
	Krytox 16256	5216	3.2 ± 2.9	2.8 ± 3.2	45	250

4.5.1 Effect of Oil Viscosity to the Heat Transfer Coefficient

The overall heat transfer performance from the vapor to the cooling water can be expressed as a series sum of four individual thermal resistances: the internal convective resistance R_{conv}, the conduction copper tube wall resistance R_{wall}, the conductive resistance imposed by the nanostructures and infused lubricant oil R_{coating}, and the condensation heat transfer resistance $R_{\mathrm{condensation}}$.

Considering the maximum coating resistance, *i.e.* t = 2 μm layer (≈ height of CuO nanostructures) of lubricant on the tube outer surface given $\mathrm{k_{Krytox}} \ll \mathrm{k_{CuO}}$ ($\mathrm{k_{Krytox}} \sim 0.25\ \mathrm{W/}$

$(\mathrm{m}\cdot\mathrm{K})$, $\mathrm{k_{CuO}} \sim 33\ \mathrm{W/(m\cdot K)}$), the thermal resistance of the coating for a Cu tube with outer diameters, d_{OD} = 9.52 mm, inner diameters, d_{ID} = 8.73 mm, and lengths L = 108 mm is:

$$R_{\mathrm{coating}} = \frac{\ln\left(\frac{d_{\mathrm{OD}}+t}{d_{\mathrm{OD}}}\right)}{2\pi L k_{\mathrm{Krytox}}} \approx 1.23\times10^{-3}\,\frac{\mathrm{K}}{\mathrm{W}}. \tag{4.1}$$

Similarly, the conductive tube wall resistance can be calculated by knowing the thermal conductivity of the wall ($k_{\mathrm{Cu}} = 386\ \mathrm{W/(m\cdot K)}$, and using:

$$R_{\mathrm{wall}} = \frac{\ln\left(\frac{d_{\mathrm{OD}}}{d_{\mathrm{ID}}}\right)}{2\pi L k_{\mathrm{Cu}}} \approx 3.3\times10^{-4}\,\frac{\mathrm{K}}{\mathrm{W}}. \tag{4.2}$$

Compared to these two resistances, for a standard experimental conditions ($\mathrm{h_i} \approx 25\ \mathrm{kW/(m^2\cdot K)}$, $\mathrm{h} \approx 10\ \mathrm{kW/(m^2\cdot K)}$) the internal convective resistance and condensation heat transfer resistance are significantly larger.[217, 258]

$$R_{\mathrm{conv}} = \frac{1}{h_{\mathrm{i}}\pi d_{\mathrm{ID}} L} \approx 0.0135\,\frac{\mathrm{K}}{\mathrm{W}}, \tag{4.3}$$

$$R_{\mathrm{condensation}} = \frac{1}{h\pi d_{\mathrm{OD}} L} \approx 0.03\,\frac{\mathrm{K}}{\mathrm{W}}, \tag{4.4}$$

Thus, both the tube wall and the additional coating thermal resistances are significantly lower than condensation and internal convection resistances.

Moreover, the thermal conductivity of the lubricant oils does not vary with oil viscosity. For all viscosities of the oil tested here, the thermal conductivity of the oils ranges from 0.1 $\mathrm{W/(m\cdot K)}$ to 0.25 $\mathrm{W/(m\cdot K)}$, even though the viscosity ranges by orders of magnitude.

4.6. Durability to High-Speed Gas Shear

In a real shell-and-tube condenser to be used in large-scale energy applications, vapor comes in contact via impingement with the condenser tubes at a certain velocity.[259] To ensure durability, SLIPS should withstand the potential vapor shear stemming from the incoming high velocity vapor to the condenser tubes. To evaluate the vapor shear resistance of SLIPS tubes, we performed high velocity air (N_2 gas) shear tests on our fabricated tube samples. As shown in Figure 4.5(a), SLIPS were first attached to a sample holder and placed horizontally to a stiff optical table. Clean N_2 gas was supplied from a pressurized gas cylinder and guided on the top surface of the SLIPS (pointing down to the ground with gravity) through a nozzle. The oil layer deformation and possible oil depletion was monitored with a high-speed camera (Phantom v7.1, Vision Research) from the side (Figs. 4.5a and b). Prior to testing, the flow velocity was measured and calibrated using a hot wire anemometer. A flow velocity of U_{gas} = 10 m/s was used during testing based on the typical values of steam inlet velocity encountered in large scale power generation surface condensers as well as petrochemical separations condensers.[260, 261] A SLIPS infused with K-1525 oil was selected due to its proven durability in both steam and ethanol condensation. As shown in Figure 4.5(c), even after exposing the surface to 10 m/s N_2 gas flow for a continual 90 minutes, no oil depletion was observed from the SLIPS. Only localized wrinkles formed (Figures 4.5c and 4.5d) due to gas shear forces at the N_2 gas exposed area due to the pressure distribution. These wrinkles disappeared after gas shear was removed due to self-healing of the lubricant driven by capillary pressure. Micro-goniometric DI water contact angle measurement of a fresh sample and a 10 m/s N_2 gas exposed sample showed identical values of approximately 120°.

The lack of lubricant displacement from the tube can be understood through an analysis of the driving force for lubricant breakup, which can be quantified by the flow Weber number (We =

$\rho_{gas}U_{gas}^2 l/\gamma_{K-1525}$, where ρ_{gas} is the N_2 gas density, l is the structure pore radius (~ 2 μm), and γ_{K-1525} is the lubricant liquid-vapor surface tension (≈ 0.019 N/m). Here, We represents a ratio of the gas inertia force leading to lubricant breakup to the surface tension based capillary force keeping the lubricant within the structured surface pores. For the gas velocities tested here and the SLIPS surfaces chosen (K-1525), We < 0.009, well below $We_{crit} = 0.75$ required to break up the liquid film and entrain lubricant droplets in the gas flow.[262] In fact, scaling reveals that the required gas velocities needed to initiate failure are U_{crit} > 95 m/s which approaches the velocity at the exhaust of the steam turbine and which is limited by the National Electrical Manufacturers Association to 137 m/s.[260]

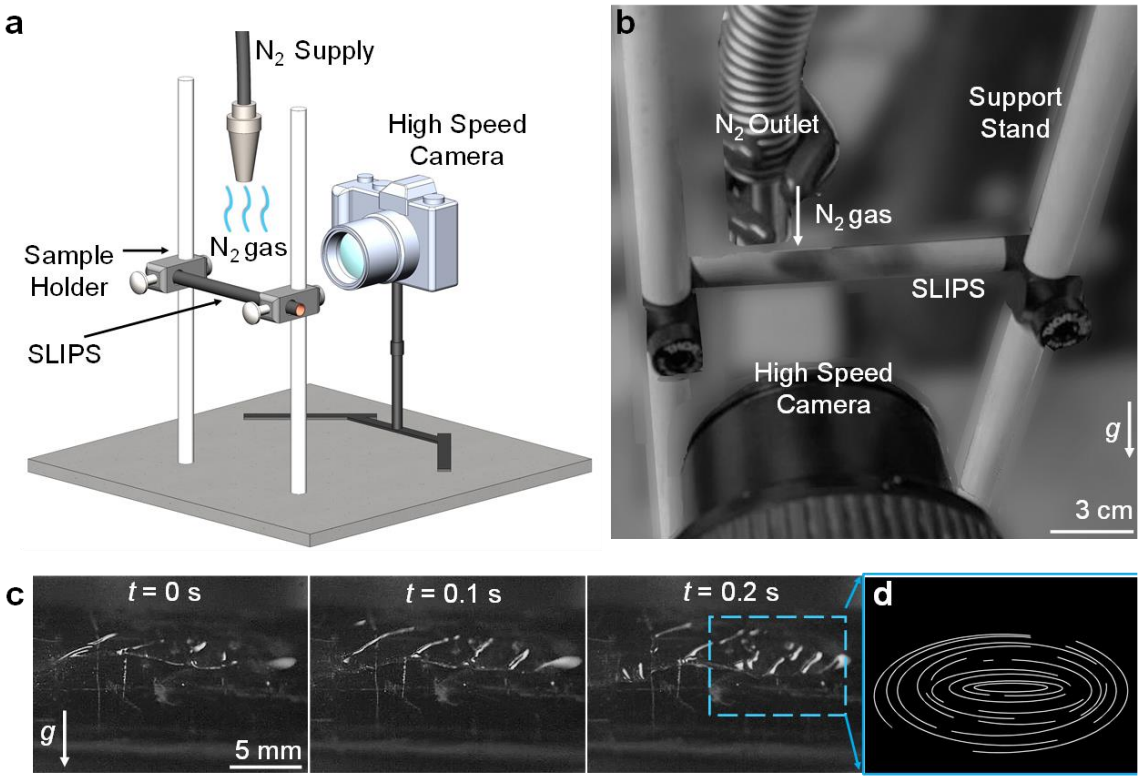

Figure 4.5. Gas shear durability testing. (a) Schematic (not to scale) and (b) Image of the N_2 gas shear test apparatus for SLIPS tube samples. The N_2 gas is supplied on top of SLIPS from a gas cylinder through a nozzle having a 20 mm diameter and visualization was performed with a high-speed camera from the side. (c) Time-lapse high-speed images of the SLIPS after exposed to (N_2 gas impingement with a 10 m/s speed (pointing downward). The images show wrinkles forming in the thin oil layer due to the pressure distribution with no oil depletion (entrainment) observed. (d) Simplified schematic (not to scale) of oil wrinkles.

4.7. Thermal Stability in Air

In addition to condensation durability, condensers undergoing manufacture or operation may encounter conditions where low or elevated ambient temperatures are encountered. For example, condenser tubing located near the shell-and-tube inlet can encounter superheated steam at high face velocities, significantly heating the surface and leading to degradation.[263] To evaluate the durability of SLIPSs at both low and elevated temperatures, we selected and focused on the oils that were demonstrated to be durable to steam and ethanol condensation, F-Y25/6, K-1525, and K-16256. For the elevated temperature exposure experiments (50℃ to 250℃), the samples were placed in an atmospheric pressure oven (Lindberg/Blue M Moldatherm Box Furnace). For low temperature exposure experiments (-50℃ to 10℃) the samples were placed in a freezer (Ult390-3-a31, Revco). At each temperature, five identical samples of each SLIPS were placed in the furnace or freezer. After 1 h of thermal exposure, the first sample was taken out, followed by the rest of the samples taken out sequentially at 2, 4, 8, and 16 hours. After exposing the samples for a prescribed time and allowing the samples to equilibrate with the room temperature, the apparent advancing (θ_a) and receding (θ_r) DI water droplet contact angles were measured on the microgoniometer (MCA-3, Kyowa Interface Science).

As demonstrated in Figure 4.6(a), the surfaces did not show any significant change in contact angle after exposing for 16 hours at -50℃ to 150℃. However, samples exposed higher temperatures (>150℃) showed changes in hydrophobicity. The observed wettability change at high temperatures was independent of oil viscosity tested, and did not result due to oil degradation. To verify this, we measured the room temperature oil viscosity after exposing the oils to elevated temperatures using a commercial rheometer (Table 4.3). Figure 4.6(b) shows that the F-Y25/6 and K-1525 infused SLIPSs become superhydrophobic after exposing the samples to 200℃ conditions

for 1 hour. The infused oil film evaporates at the elevated temperature,[264] leaving the silane coated CuO exposed (Figure 4.6e). However, the K-16256 exposed to 200℃ did not lose all of its infused oil, showing only reduced hydrophobicity for longer exposure times (Figure 4.6b). This is due to the lower evaporation rate (vapor pressure) of more viscous Krytox 16256 oil, which fails to expose the CuO-HTMS base surface. After exposing the samples to higher temperatures (250℃) for 1 hour, all samples became superhydrophilic (Figure 4.6b and Figure 4.6e, inset). The transition to superhydrophilicity occurs due to the majority of the oil evaporating (Figure 4.6e) in addition to the reference substrate CuO-HTMS desorbing its hydrophobic HTMS promoter.

Table 4.3. Experimentally measured viscosity of two oils after exposure to different temperatures and allowing them to settle back to room temperature.

Exposure Temperature [°C]	Measured Viscosity after Exposure [mPa·s]	
	Carnation Oil	Krytox 16256
-50	9.689	5216.008
20	9.693	5215.987
200	9.702	5215.991

To test our hypothesis, we fabricated a CuO-HTMS superhydrophobic surface and placed it in the same atmospheric pressure oven at 250℃. As shown in Figure 4.6(c), the superhydrophobic surface (CuO SHP) starts to degrade (reduced hydrophobicity) after 30 minutes of exposure to 250℃ air, failing completely within 1 hour. To understand if the elevated temperature degradation is substrate dependent, we did the same experiments on a silicon wafer based superhydrophobic surface. A thin layer (~50 nm) of aluminum (Al) was sputtered (AJA3 Sputter) on a polished silicon wafer, which was then boehmized by immersing it in hot DI water at ~90℃ for one hour, followed by HTMS salinization.[248] Unlike CuO-HTMS, the Si-based

superhydrophobic surface maintained excellent superhydrophobicity after 250℃ exposure due to stronger bonding of the silane to the native AlO(OH). Similar behavior was also observed on the SHP samples made from Al tubing following the same boehmite formation and salinization process. The results indicate that boehmite-HTMS has better thermal stability when compared to CuO-HTMS. Due to the better thermal stability of the Si-substrate boehmite surface, we also fabricated Si-based boehmite SLIPS by infusing Krytox 16256 (Si K-16256) following the same Si-based superhydrophobic boehmite fabrication process described previously. As shown in Figure 4.6(c), after exposing the Si-based boehmite SLIPS to 250℃ for 16 hours, the surface maintained hydrophobicity.

The reason for the better SLIPS thermal stability of Si-based boehmite SLIPSs when compared to the CuO-based SLIPSs is due to two possible reasons. The first is due to the inherently different structure length scales of boehmite (< 150 nm) and CuO-based (2 μm) SLIPSs. The configuration of the lubricant infused in the microstructures is different, with the boehmite confining the lubricant to a much thinner region near the substrate.[245] From our experimental observation of oil evaporation differences between the CuO microstructure and boehmite nanostructure, we note that the structure solid fraction of boehmite samples is higher than CuO (~0.023),[249] due to nanoscale porosity of boehmite,[265] resulting in slower oil evaporation rates. Although we hypothesize that slower oil evaporation occurs due to increased interaction between the structure and oil (closer proximity and higher interfacial area and capillary pressure), further work is needed to confirm this mechanism. The second reason for greater thermal stability is the higher surface coverage of the HTMS silane with boehmite when compared to CuO, which acts to slow the degradation of the underlying HTMS layer. As in the first mechanism, the second needs further work to verify the proposed hypothesis.

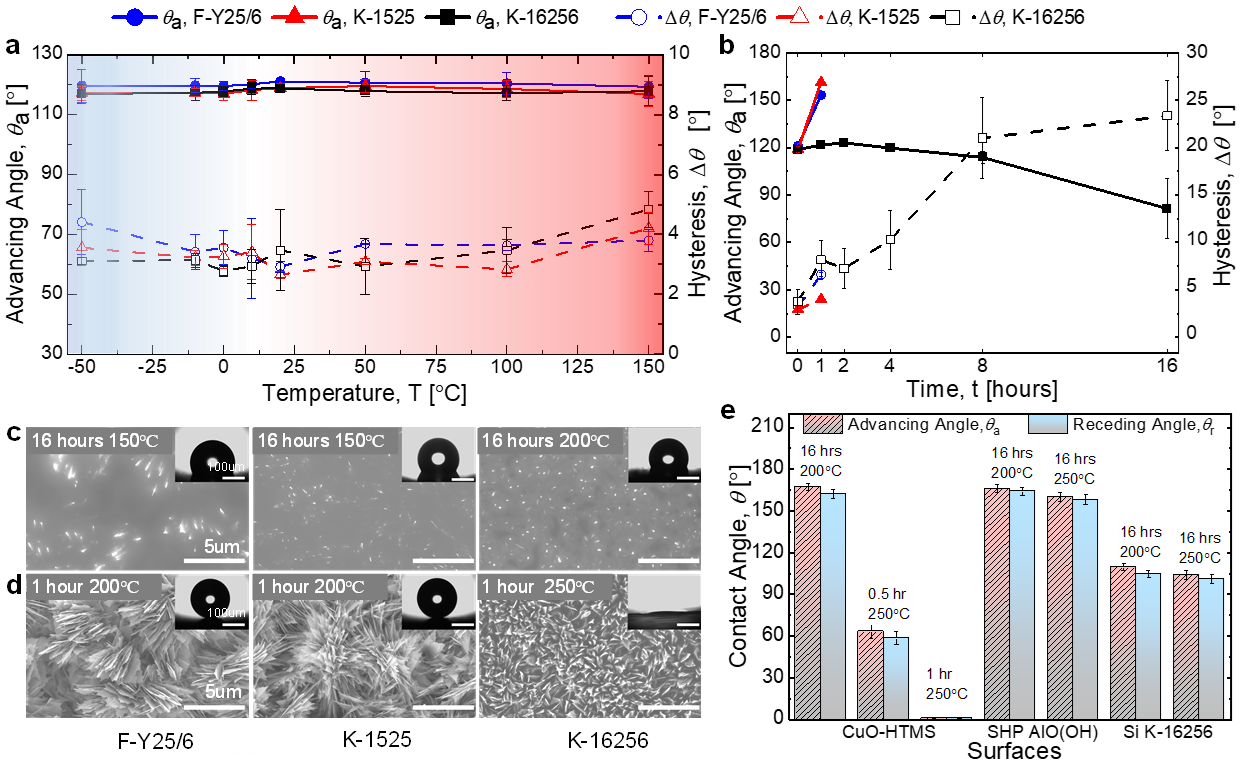

Figure 4.6. SLIPSs thermal stability in air. (a) Apparent advancing DI water contact angle (θ_a) and contact angle hysteresis ($\Delta\theta = \theta_a - \theta_r$) of F-Y256/6, K-1525, and K-16256 SLIPS for a wide range of air temperatures (-50℃ to 150℃). (b) The F-Y25/6 and K-1525 infused SLIPS become superhydrophobic (SHP) after exposing then to 200℃ air for 1 hour. The K-16256 SLIPS begins to lose hydrophobicity at 200℃, with complete failure at 250℃. SEM images of (c) F-Y25/6 SLIPS after 16 hours of exposure to 150℃ air, K-1525 SLIPS after 16 hours of exposure to 150℃ air, and K-16256 SLIPS after 16 hours of exposure to 200℃ air. The SEM images show the presence of oil infused within the CuO structured surfaces. SEM images of (d) F-Y25/6 SLIPS after 1 hour of exposure to 200℃ air, K-1525 SLIPS after 1 hour of exposure to 200℃ air, and K-16256 SLIPS after 16 hours of exposure to 200℃. (e) Contact angle change of Cu and Si based superhydrophobic and silicon based SLIPSs. At 250℃, the CuO surface starts to lose hydrophobicity and become completely superhydrophilic within one hour of exposure.

4.8. Durability to Condensate Flooding

Large shell and tube condensers collect the condensate product at the bottom of the shell section sometimes termed the hotwell. During operation, parts of the tubes near the hotwell may be inundated or completely immersed in the collecting condensate, resulting in prolonged times of direct immersion within the condensate,[266] requiring rigorous degradation quantification to

single-phase liquid immersion conditions. To test SLIPSs durability during prolonged condensate exposure, we submerged the SLIPSs in a variety of different working fluids for extended time periods to characterize any change in functionality (contact angle). We simplified our tests by keeping the fluid stagnant while the surfaces were completely immersed in the fluid in a sealed container to reduce the rate of evaporation of the working fluid. For the test liquids, we selected room temperature (~20°C) water and ethanol. Test samples included the CuO based SLIPSs infused with K-1525, K-16256, and F-Y25/6. During the room temperature water and ethanol test, five identical samples of each SLIPS were immersed in each liquid and sealed in separate glass bottles. After 1 day, the first sample of each type from each liquid was taken out followed by 2, 4, 8, and 16 days. Before submerging the samples, the working fluids were changed after each run to avoid possible contamination. After removing the samples, drying was done on a hot plate at ~60°C for 15 minutes followed by resting the samples at room temperature. After each test, when all samples reached room temperature, the apparent advancing (θ_a) and receding (θ_r) DI water droplet contact angles were measured on the microgoniometer (MCA-3, Kyowa Interface Science). More quantifiable methods of sample changes such as mass difference before and after immersion were difficult to measure due to limitations of available analytical balance mass scale sensitivity for the differences in mass obtained in the experiment. As shown in Figures 4.7(a-b), no observable change in contact angle of the SLIPS surfaces was observed in the tested immersion conditions. The SEM images showed the presence of the infused lubricant on the different SLIPS surfaces even after immersing them into the working fluids for 16 days (Figure 4.7d). To study the degradation of the infusing oil, we performed an oil aging experiment where each type of oil (K-1525, K-16256, and F-25/6) was mixed (50 v%) with ethanol and kept in a sealed glass bottle for ~12 months. After the test, SLIPS samples were fabricated following the same CuO-HTMS surface

fabrication then immersing them in the aged oil mixtures followed by the same post immersion treatment (oil drainage and drying). Then, the DI water contact angle of these samples was measured. As shown in Figure 4.7(c), comparison of the SLIPS made with fresh infused oil with the SLIPS infused with the 12 months aged oil did not show any discernable difference in apparent contact angle behavior.

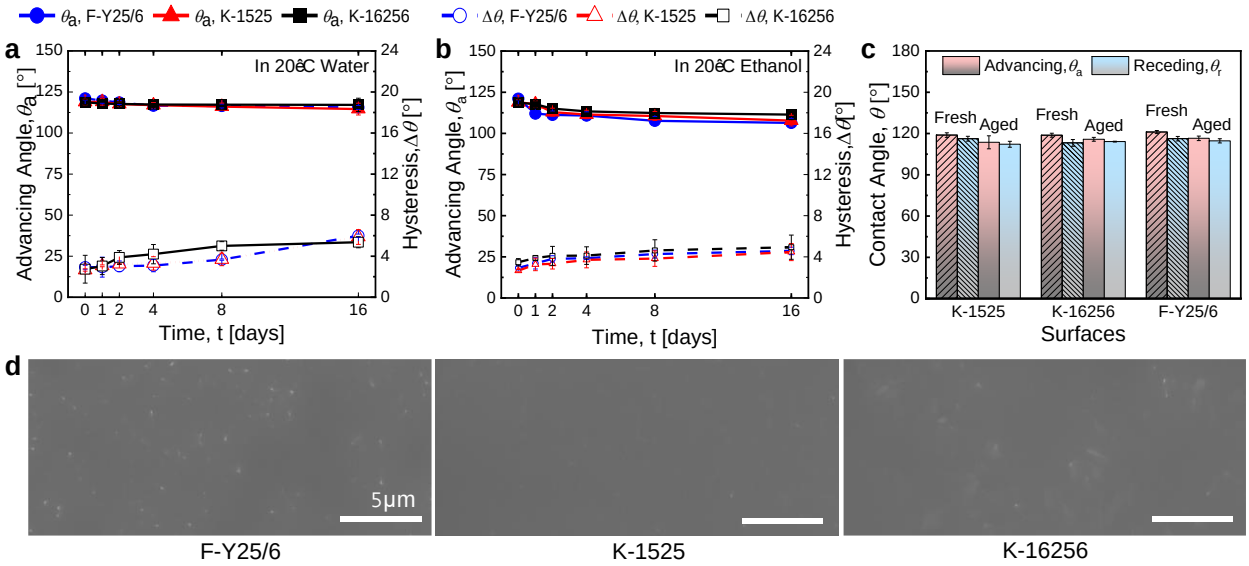

Figure 4.7. SLIPSs durability to prolonged condensate immersion. Advancing contact angle ($\boldsymbol{\theta_a}$) and contact angle hysteresis ($\Delta\boldsymbol{\theta}$) of the SLIPSs surfaces after submerging in (a) 20ºC water, and (b) 20ºC ethanol for a variety of different times. Legend is the same for (a) and (b) and is shown on top of a-b. (c) Contact angle comparison of SLIPS infused with fresh oil and aged oil. Oil was aged by mixing it with ethanol and allowing it to rest for 12 months. Comparison shows no significant change in contact angle, depicting no property change of the oil as a response to prolonged ethanol exposure. (d) SEM images of SLIPSs samples after submerging them in ethanol for 16 days showing no apparent degradation of surface quality. Scale bars all represent 5 μm.

4.9. Discussion

The results reported here have important implications for the potential development of scalable and robust surfaces for long-term dropwise condensation applications, both for steam and for low-surface-tension fluids. Systems that use refrigerants,[267, 268] and hydrocarbon fluids[269-271], stand to significantly benefit from dropwise condensation. Achieving stable dropwise

condensation of steam on hydrophobic surfaces has a profound impact on global energy production, water conservation, and hence the carbon footprint of industrialized and developing nations. Dropwise condensation on durable hydrophobic condenser surfaces in shell and tube condensers of a thermoelectric or nuclear power plant has the potential to lead to ~2% increase in overall power plant energy efficiency.[272] Although the clear advantages of dropwise condensation have been understood for over a century, designing robust hydrophobic surfaces that can survive long-term operation with unchanged heart transfer performance has not been successful, severely limiting practical application.

Our work demonstrates the rational design of SLIPS for long-term stable dropwise condensation of both steam and ethanol condensation, indicating the importance of lubricant selection and degradation conditions. Our low temperature exposure durability study showed no change in wettability after exposure. However, exposing the surfaces to lower temperatures for extended periods (months) may alter these findings. Especially if the surfaces are exposed for a long time near the pour point of the lubricant or at a lower temperature which may change the physical properties of the lubricant. The pour point of a lubricant is the lowest point at which it becomes too viscous and loses its flow properties. Pour points of K-1525, K-16256, and F-Y25/6 are - 48ºC, - 15ºC and - 35ºC, respectively. SLIPSs infused with these oils may show altered surface wettability if they are exposed to their respective pour point or lower temperatures for prolonged periods.

The condensation results demonstrating multi-month durability present a promising approach to enable the long-term operation of SLIPS condensers. Typical large scale condenser systems require multi-year longevity with continual operation. Some require more than a decade of operation prior to shut down. The lack of miscibility between the lubricants studied here and

the condensates tested presents an interesting opportunity to use active re-lubrication of the surfaces after prescribed timeframes.[249] Compared to brushed lubricant impregnation,[273] our proposed contactless re-lubrication is attractive due to its simplicity. For example, the installation of spray nozzles capable of injecting lubricant into the steam inlet section of the condenser for re-lubrication presents a promising route to multi-year durability. The lack of miscibility enables the relatively easy separation of any drained lubricant outside of the condenser, which can be re-used and re-sprayed on the external condenser tubing. In fact, past approaches to achieve durable dropwise condensation and corrosion protection have developed methods to apply additives to external condenser tubes using similar approaches, demonstrating the added benefit of corrosion protection in addition to heat transfer enhancement.[274]

To evaluate the reusability of the multi-month durability tested samples after failure, we recoated the tested samples following the same SLIPS fabrication processes to emulate the proposed re-spray technique. For recoating, we selected the durable samples, F-Y25/6, K-1525, and K-16256 from the ethanol condensation experiments. We conducted the same ethanol condensation experiment with the recoated samples, which showed stable dropwise condensation as was observed with the fresh samples (Fig. 4.8). The findings indicate that long-term condensation exposure does not degrade the silane layer or underlying CuO structure. In fact, the oil layer acts as a protective shield to the silane layer and the performance degradation of SLIPS mainly occurs due to oil depletion, which can be remedied by re-coating. Although the revival of SLIPS performance with recoating reveals a clear added benefit of SLIPS over solid hydrophobic coatings, further studies are needed to compare the surface chemistry change between the freshly fabricated and re-coated SLIPSs after prolonged exposure and spray cycles.

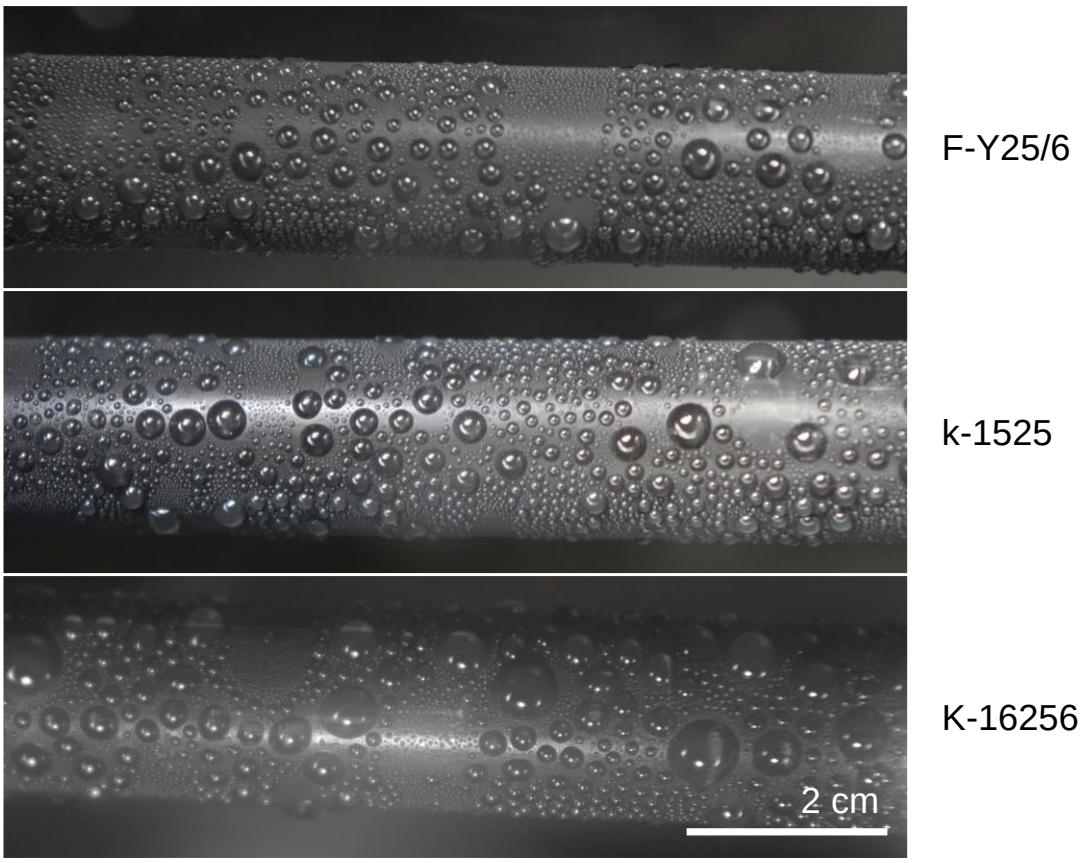

Figure 4.8. Ethanol condensation on re-lubricated LIPSs after log-term durability test. After continuous durability test the failed SLIPS samples were re-lubricated with fresh oil and condensation experiment was conducted in the same chamber. Re-lubricated samples show similar condensation behavior as of fresh samples.

Past studies have quantified the effect of oil viscosity on shear-driven surface failure focusing on external single-phase fluid flow.[275, 276] Here, we experimentally prove that high viscosity oils can delay SLIPSs failure in the presence of condensate droplet shedding-driven oil depletion. Although higher oil viscosity enhances the lifespan of SLIPSs, future studies are needed which focus on the effects of oil viscosity, type of working fluid, and multi-droplet coalesce dynamics on cloaking oil layer formation, oil ridge formation, and droplet shear dynamics, which all govern the coupled mechanics of lubricant depletion. Moreover, our study focused on CuO-based superhydrophobic surfaces infused with different oils. Our high temperature air stability

tests indicated that boehmite structures, due to their inherently different structure length scale when compared to CuO, result in enhanced lifespan at elevated temperatures. We hypothesize that this phenomenon occurs simply due to the higher surface roughness, nanoscale pore geometry, and enhanced surface interaction potential (thinner films). Future studies which can decouple the oil viscosity effects and nanostructure effects[277] (such as hierarchical surfaces with variable length scale roughness[278]) are needed to evaluate the combined effect of oil viscosity and optimized structure on the improved lifespan of SLIPS in different degradation conditions.

4.10. Conclusions

In this chapter, we rigorously demonstrate the lifespan of a variety of SLIPSs in both water and ethanol condenser applications. The majority of SLIPSs show short lifespans (<1 month) during steam condensation due to cloaking of the condensate by the infused lubricant. Among the tested samples, surfaces infused with highest viscosity lubricants (Krytox-16256) exhibited dropwise condensation for up to 45 days. During ethanol condensation, SLIPSs infused with high viscosity lubricants (K-1525, F-Y25/6, and K-16256) showed stable dropwise condensation for multiple months due to the absence of cloaking, reducing oil depletion. Similar to steam condensation, the Krytox-16256 infused SLIPS was the most durable during ethanol condensation, demonstrating stable dropwise condensation for more than 8 months. To quantify durability to elevated temperatures as encountered by superheated gases in condensers, the K-1525 and F-Y25/6 infused SLIPSs showed good durability after exposure to 150℃ air for 16 hours. The K-16256 infused surface was shown to be durable to 200℃, finally degrading at 250℃ within 1 hour. To quantify durability to immersion in a liquid, we subjected the SLIPSs to water and ethanol immersion conditions. All SLIPSs showed stable hydrophobicity even after 16 days of continual immersion.

Our work presents design guidelines for the rational selection of lubricants for fabricating durable SLIPSs having wide applicability with both steam and ethanol condensation. Our results outline future directions towards the development of next generation durable SLIPSs.

CHAPTER 5

Modular Heat Sinks for Enhanced Thermal Management of Electronics

5.1. Introduction

In the last three chapters we showed that micro-nanoscale manufacturing considerations have profound impact on performance improvement of energy systems. In this chapter we focus on macroscale device level advanced manufacturing. We develop innovative thermal solution for power electronics focusing on volumetric and gravimetric power density enhancement.

The design of power electronics involves consideration of many factors such as size, noise, cost, maintenance requirements, complexity, and robustness [279, 280]. Although silicon (Si) devices are the most popular material for power semiconductor applications, wide band gap materials such as silicon carbide (SiC) and gallium nitride (GaN) are gaining popularity due to their ability to operate at elevated junction temperatures [279]. Furthermore, these materials enhance efficiency by providing lower parasitics, such as on-state resistance, package inductance, and output capacitance, and smaller physical package size [281, 282]. Currently available solder materials, reliability considerations, packaging technologies, and cost constraints limit the maximum junction temperature of SiC and GaN devices to approximately 175°C [91, 283]. As the package size decreases and the power processed remains the same (or possibly increases), the surface area to cool the device dramatically decreases and the capacity to extract heat with conventional

*This chapter was mostly reprinted (adapted) with permission from *Journal of Electronic Packaging*, Jun 2021, 143(2): 020903. Copyright © ASME. Muhammad Jahidul Hoque is the first author of the publication. Dr. Nenad Miljkovic guided the research and revised the manuscript and is the corresponding author.

methods decreases. For example, employing thermal interface materials (TIMs) constrains improvements in power density and specific power of the complete system due to the necessity for a large heat sink [284]. Furthermore, poor thermal management of electronics not only lowers device performance but also significantly shortens lifespan, with 55% of power electronics failures due to elevated temperature [285].

Current thermal management strategies for power electronics cooling include air [78, 286-290], liquid [291-294], and two-phase cooling [295-305]. Although air as a coolant is less attractive due to its low thermal conductivity (~ 0.026W/(m·K)) and small Prandtl number (~0.70), air cooling approaches have a number of advantages when compared to other cooling strategies. There advantages include: simplicity and low cost to implement, easy to maintain, highly reliable, do not require complex and expensive sealing, air is not electrically conducting, lower pumping power, and air is readily available from the ambient in most applications. Hence, for decades, air cooling has been the preferred method for managing heat in power electronics applications [306]. Recently, ambient-air-cooled converters [307] and inverters [308] have been demonstrated to have reduced overall system complexity compared to single-phase liquid cooling [309, 310]. Although forced air cooling is a good option for low power (< 1 MW) converters [311], the need for a finned heat sink results in decreased power density [312, 313]. Furthermore, the need for higher power density of modern devices is pushing the limits of conventional heat sink designs [314-316]. Therefore, air-cooled heat sink optimization is needed [317-320]. In the past, researchers have optimized different parameters of air-cooled heat sink topologies focusing on heat sink design [78-81], heat sink fabrication processes [82-84], different power electronics system layouts [85, 86], various heat sink geometries [87, 88], heat sink materials [89], hybrid cooling approaches [90, 91], coolant flow modifications [92], and overall thermal performance [93-95].

With the integration of power converters into mobile machinery such as aircraft, ships, on-road vehicles, or off-road equipment, a desire exists to enhance converter power density and performance without integration penalty [96, 97]. The heat sink in an air-cooled power converter is typically the heaviest part [92, 98]. A key parameter governing the required heat sink is the thermal performance of the gap pad between the PCB and heat sink. Although gap pads are required for electrical isolation and mechanical compliance, their added thermal impedance stemming from their poor thermal conductivity (< 5 W/(m·K)) ensures oversizing of heat spreading components to minimize non-pad thermal resistances and hence enhance overall junction-to-air heat transfer. The need for coupling of the heat sink with multiple heat generating components operating at different voltage potentials inherently increases complexity and mass. To ensure compliance, the heat sink is oversized to overlap with all components to and to ensure that the gap pad material is present at the interface of all devices to provide electrical isolation.

In this chapter, we study modular and electrically-floating heat sinks (MHSs) to achieve ultra-efficient thermal management of power converters. The MHS approach utilizes a finite number of discrete and disconnected MHSs strategically placed on hot spots (devices), removing the need for gap pads. Elimination of the gap pad ensures better cooling performance due to direct contact between the devices and heat sinks, while also reducing overall volume and mass due to downsizing of the heat sink. We demonstrate our approach by benchmarking MHS cooling with two conventional copper (Cu) pin fin heat sinks mounted on a 650 V, 5-level 2 kW_e power converter utilizing gallium nitride (GaN) switches cooled from the back side with Cu thermal vias. Benchmarking of the prototype was achieved by using two conventional Cu pin-fin heat sinks having short (4 ± 0.05mm) and tall (23 ± 0.05 mm) pins with center-to-center spacing of 1 ± 0.1mm and 1.2 ± 0.12 mm, respectively, which were mounted using a conventional gap pas material. To

investigate the heat transfer physics from junction-to–fluid, and to help co-design the MHS solution, we used three-dimensional (3D) finite volume method simulations coupling the fluid flow and converter heat transfer. Infrared imaging was used to validate simulations and provide loss model estimates for power distribution within the converter. To test the modular approach, MHSs were machined from same Cu heat sinks and prototype characterization was performed. In addition to direct contact mounting with and without a TIMs, the best performing heat sink assembly was chosen to test direct soldering to the Cu vias for further improvement of thermal performance. Volumetric and gravimetric power density improvement of the MHS approach was characterized when compared to the benchmark approaches, showing 22% and 73% improvements, respectively. Our work not only demonstrates the use of MHSs as a power dense thermal management option for power converter cooling in applications, it offers insights into alternate avenues for performance improvement and multi-functional design of components for power electronics.

5.2. Electrical Prototype

An experimental power converter was developed as a test platform to benchmark and demonstrate the effectiveness of the MHS air-cooling solution. Due to their modular nature and reduced commutation loops, flying capacitor multi-level (FCML) converters have demonstrated high power density power conversion when paired with GaN power switches. For this experiment, we tested a bi-directional 5-level FCML with 650 V GS66508B GaN systems transistors. Table 5.1, shows the converter specifications and Table 5.2, lists the components used. To improve the mechanical assembly and to enable MHS integration, bottom side cooled transistors were included in the design and a single sided electrical design was implemented, as shown in Figure 5.1.

Table 5.1. FCML converter specifications.

Specification	Value
Input Voltage	500 VDC to 1000 VDC
Output Voltage	25 VDC to 200 VDC
Peak Output Power	2.0 kW
GaN Switching Frequency	167 kHz

Table 5.2. Used components in the FCML converter.

Component	Manufacturer and Part Number	Parameters
GaN FETs (S)	GaN Systems GS66508B	650 V, 50 mΩ
Capacitors (C_1 & C_2)	TDK C5750X6S2W225K250KA × 10	450 V, 2.2 μF
Capacitors (C_{in})	TDK C5750X6S2W225K250KA × 12	450 V, 2.2 μF
Capacitors (C_{out})	TDK C5750X6S2W225K250KA × 4	450 V, 2.2 μF
Inductors (L)	Vishay IHLW5050EZER56M01 × 2	22 A, 5.6 μH

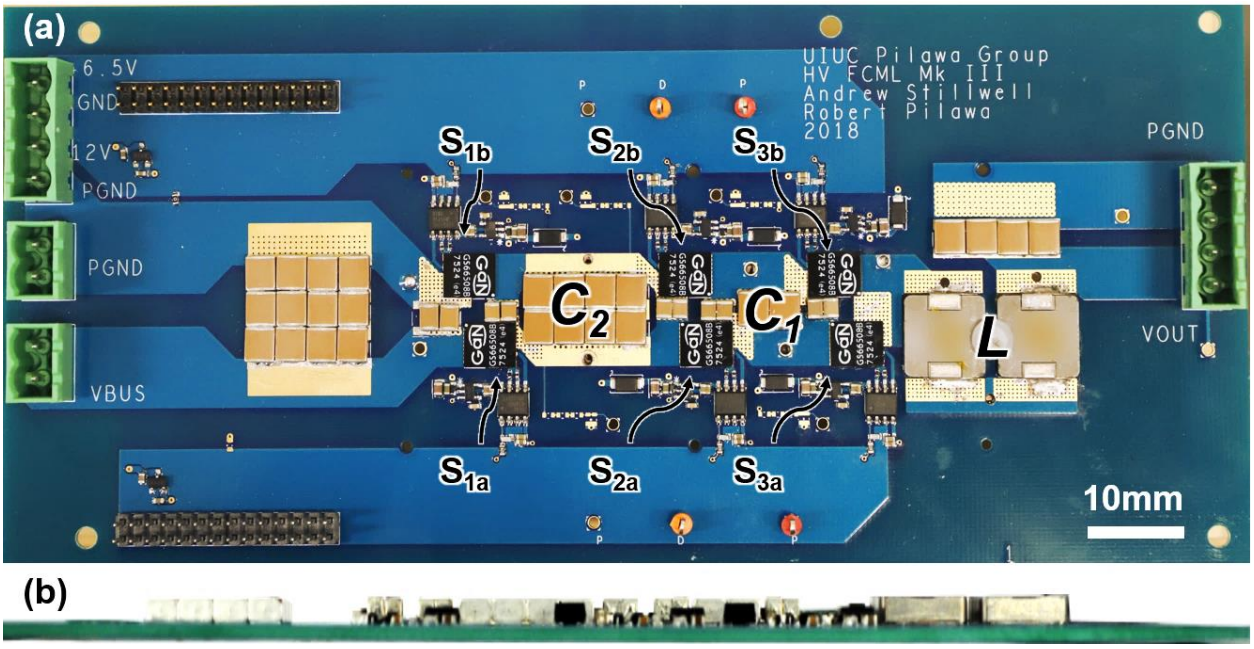

Figure 5.1. (a) Top and (b) front view of the FCML power converter electrical prototype. The views do not show the thermal management system (heat sink), which is mounted on the backside (opposite side of image in (a)). Components labeled on the pictures are identified in Table 5.2.

To provide a thermal path to the backside of the PCB, Cu thermal vias were included under the source pad of the GaN transistors (S_1 to S_3 in Fig. 5.1). One of the tradeoffs faced during layout electro-thermal co-design were the switching commutation loops, shown in Figure 5.2. Electrically, a small commutation loop is desired to reduce parasitic inductance and thus reduce switch voltage ringing [321]. In addition to reducing the commutation loop area, we implemented an inner layer shielding plane in the first Cu layer below the switching commutation loop [322] to further reduce parasitic inductance and improve electromagnetic interference (EMI). However, the tightly packed GaN switches and inner Cu layer reduced the area available for thermal vias. As a compromise, the inner Cu layer was reduced to minimize the interference with the thermal vias, and additional thermal vias were placed beyond the bounds of the GaN device package. With these design choices, we placed over 120 thermal vias for each GaN switch, well within design guidelines [323].

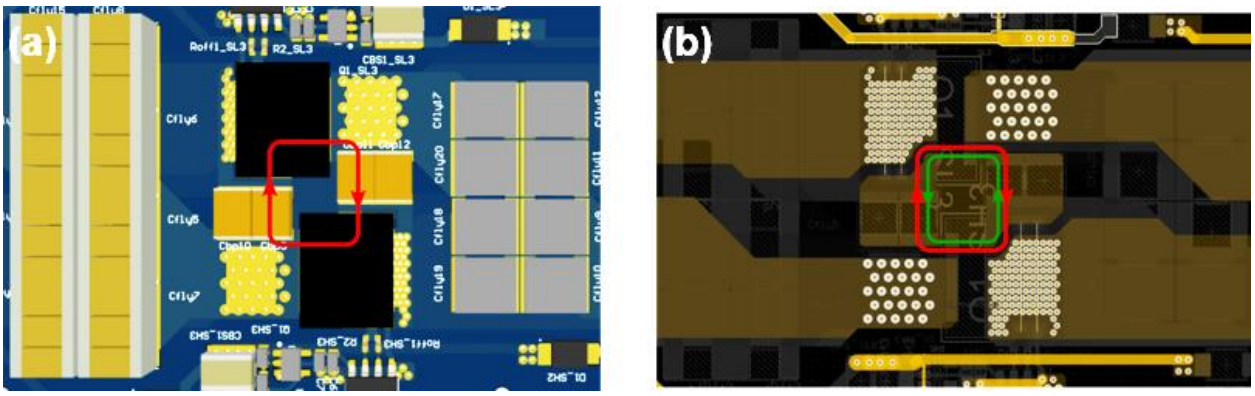

Figure 5.2. (a) Complementary GaN switches form a commutation loop (current path shown in red) through local bypass capacitors. (b) An inner copper layer acts as a shield plane (induced current shown in green) underneath the commutation loop to reduce EMI and switching noise. Thermal vias provide a path for heat to transfer to the backside of the PCB.

5.3. Thermal Management

Conventional thermal management for the developed power converter would involve integration with a single full metallic heat sink (FHS) that covers all Cu footprints as well as additional non-metallic FR4 material on the backside of the PCB (back of Fig 5.1a). As shown in Fig. 5.3(a), the area within the white dotted border encompasses all Cu footprints as well as large non-metallic portions of the PCB. Here, the Cu footprints were separated based on their electrical potentials, which demands electrical isolation when using a FHS. As shown in Fig. 5.3(b), to achieve electrical isolation between the Cu pads and the FHS, a gap pad is required. Conversely, employing MHS ensures individual Cu pads are not connected (Fig. 5.3c). Due to the same potential of each Cu pad, the MHS approach does not require the use of a gap pad, reducing the junction-to-air thermal resistance. As depicted in Fig. 5.3(d), a thin layer (≈100 µm) of thermal paste or TIM

between the MHSs and Cu pads ensures better thermal contact by overcoming possible microscale gaps due to roughness. It is important to note, the removal of the gap pad results in electrical connection between the Cu pad and MHS, resulting in safety considerations that need to be accounted for due to the heat sinks becoming electrically live (at a fixed voltage). Another advantage of the MHS approach is in top side cooled applications where component height varies across the PCB. Utilization of a FHS results in significant complexity with alignment and ensuring good thermal contact between multiple components having variable height, typically resulting in milling of a negative of the PCB structure on the base plate of the heat sink. However, use of MHSs obfuscates these issues as individual heat sinks are mounted to components on the front.

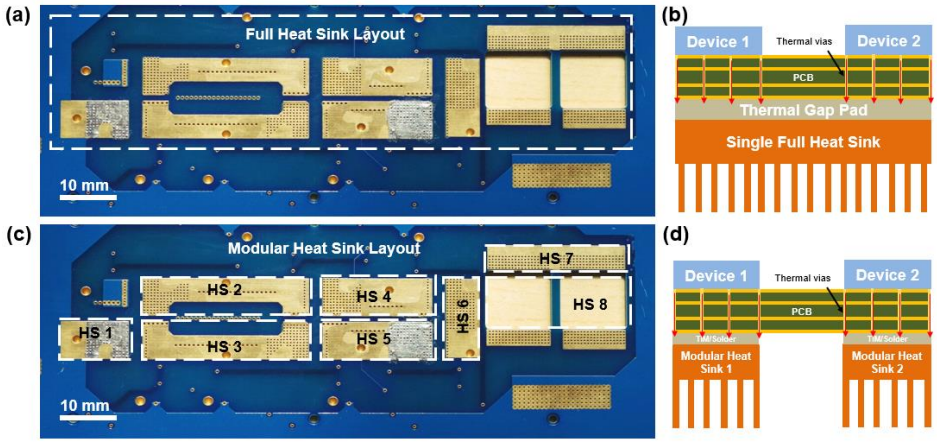

Figure 5.3. Images and schematics of heat sink design approach. (a) A conventional FHS covers the entire backside (back of Fig 1a) as depicted by the white dotted line, which includes Cu footprints and bare FR4 on the PCB. (b) Schematic depicting the thermal gap pad mounted between the PCB and FHS. (c) A MHS layout includes multiple disconnected heat sinks for each Cu footprint. (d) The MHS approach does not require the use of a gap pad, with only a thin layer of thermal paste (TIM) or direct soldering of the Cu heat sink to the thermal vias possible. Devices 1 and 2 in (b) and (d) represent any active or passive heat generating component on the PCB.

To gain a better understanding of the key thermal resistances of the MHS approach as well as the more conventional FHS approach, we considered different assemblies of the converter prototype thermal management layout with their corresponding 1D thermal resistance circuits

(Fig. 5.4). Depending on the heat sink arrangement, design, and TIM application method, the overall thermal resistance (R_{total}) from junction-to-air is shown in Table 5.3. To enable comparison of different Cu fin designs, we utilized two finned heat sink profiles in our calculations and experiments: a low profile Cu pin-fin heat sink (Enzotech, SLF-1) and a high aspect ratio Cu pin-fin heat sink (Enzotech, CNB-S1) delineated in Table 5.3 as 'short' and 'tall', respectively. Furthermore, given the range of possible air flow rates, fin resistance calculations were done for two average air side heat transfer coefficients, h = 50 W/(m^2·K) and 100 W/(m^2·K). The chosen h values were based on previous experimental studies of pin-fin heat sinks assuming reasonable air flow rates (1 to 5 m/s) [310, 324, 325]. The thermal resistance analysis revealed that the heat sink resistance presents the major bottleneck in the overall junction-to-air thermal pathway for both low and high airside heat transfer coefficients. Although the airside thermal resistance for the MHS approach is higher compared to the FHS due to higher spreading resistance and lower fin number, our analysis reveals that using MHSs and eliminating the gap pad reduces the interfacial resistance (GaN and heat sink interface) by 84% and 99% for TIM thermal paste and solder, respectively.

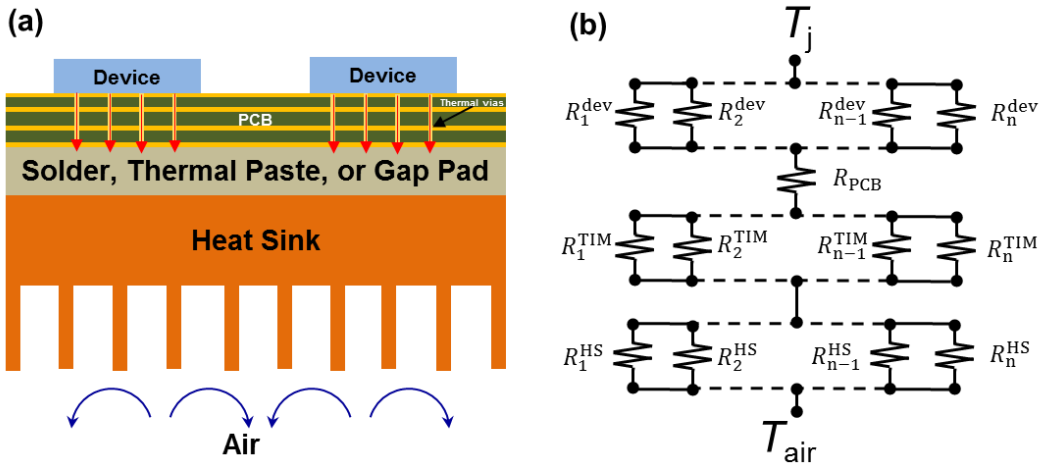

Figure 5.4. (a) Cross-sectional schematic of two GaN devices mounted on a PCB with a FHS assembly for different interface materials (solder, TIM, or gap pad) representing a multi-component converter thermal management layout. (b) Schematic of a 1D thermal resistance circuit showing the equivalent resistance approach for the converter system with temperature difference from device junction (T_j) to air (T_{air}), where "n" varies with the number of devices (dev), corresponding TIM layers (TIM) and heat sinks (HS).

Table 5.3. Calculated thermal resistances for different heat sink arrangements. All thermal resistances are in units of K/W. Schematic shown in Fig. 5.4(a) depicts the thermal resistance circuit used in the analysis.

Design	$^{1}R_{eq}^{dev}$	$^{2}R_{PCB}$	$^{3}R_{eq}^{TIM}$	$^{4}R_{eq}^{HS}$	R_{total}
	Air-side heat transfer coefficient h = 50 W/(m^2·K)				
Tall MHS Soldered	0.08	0.029	0.001	0.87	0.98
Tall MHS with TIM			0.025	0.87	1.00
Tall FHS with Gap Pad			0.16	0.47	0.70
Short MHS with TIM			0.025	3.50	3.60
Short FHS with Gap Pad			0.16	1.50	1.75
	Air-side heat transfer coefficient h = 100 W/(m^2·K)				
Tall MHS Soldered	0.08	0.029	0.001	0.45	0.56
Tall MHS with TIM			0.025	0.45	0.58
Tall FHS with Gap Pad			0.16	0.23	0.50
Short MHS with TIM			0.025	1.74	1.87
Short FHS with Gap Pad			0.16	0.74	1.00

[1]Device thermal resistance was obtained from the device manufacturer [326] and equivalent resistance was calculated considering six GaN and two inductors (Fig. 5.1a) and corresponding resistance circuit (Fig. 5.4b).
[2]PCB thermal resistance was calculated by considering maximum heat sink face area (Fig. 5.5) and 2 oz board thermal conductivity [327].
[3]Pad thickness was assumed to be 2 mm with a thermal conductivity of 3 W/(m·K), while the paste and solder had thickness of 100 µm. Equivalent TIM resistance for each assembly was calculated considering the face area of each heat sink (Fig. 5.5) and corresponding resistance circuit (Fig. 5.4b).
[4]Equivalent heat sink resistance corresponds to each assembly (Fig. 5.5) and respective thermal circuit (Fig. 5.4b). This includes the material and fin resistance of each heat sink.
The 1D conduction resistance was calculated using $R_{cond} = t/kA$, where *t*, *k*, and *A* are the thickness, thermal conductivity and face area of the medium. Fin resistance was calculated by considering the convective fin tip condition and using: $R_{fin} = f(\eta_{fin})$, where η is the fin efficiency.

5.4. Experiments

Two different fin profiles (short and tall) were used to develop the FHS and MHS thermal management approach. The low profile (short) heat sinks (Enzotech, SLF-1) were made of Cu and had fin radii of 600 ± 50 µm, fin center-to-center spacing of 1 ± 0.1 mm, fin height of 4 ± 0.05 mm, with a heat sink base thickness of 2 ± 0.05 mm. The high aspect ratio (tall) heat sinks (Enzotech, CNB-S1) had fin radii of 850 ± 50 µm, fin center-to-center spacing of 1.2 ± 0.12 mm, fin height of 23 ± 0.05 mm, with a heat sink base thickness of 2 ± 0.05 mm . The two distinct designs yielded

four different heat sink arrangements for the prototype converter, as demonstrated in Figure 5. Due to the finite size of the procured heat sinks, assembly of three heat sinks adjacent to one another formed the FHS as depicted in Fig. 5.5(a, b) and 5.5(c, d) for the tall and short FHS, respectively. To fabricate the MHS for each backside pad, we cut the procured heat sinks to the required dimensions of each individual Cu pad such that overlap was ensured when mounting on the back. To mount the FHSs to the prototype, a double-sided sticky thermal pad (BERGQUIST GAP PAD HC 3.0) was used with a 3D printed (Lulzbot TAZ 6, with polylactic acid, PLA) mount used to apply pressure to the heat sinks at the extended edges (Fig. 5.5a and c) to ensure good thermal contact with the PCB Cu pads on the backside. To mount the MHS, tapped through holes were manufactured on the PCB and on the MHS. Thin screws (94690A711, McMaster-Carr) were used through the PCB to the threaded holes of the MHSs to ensure a tight hold.

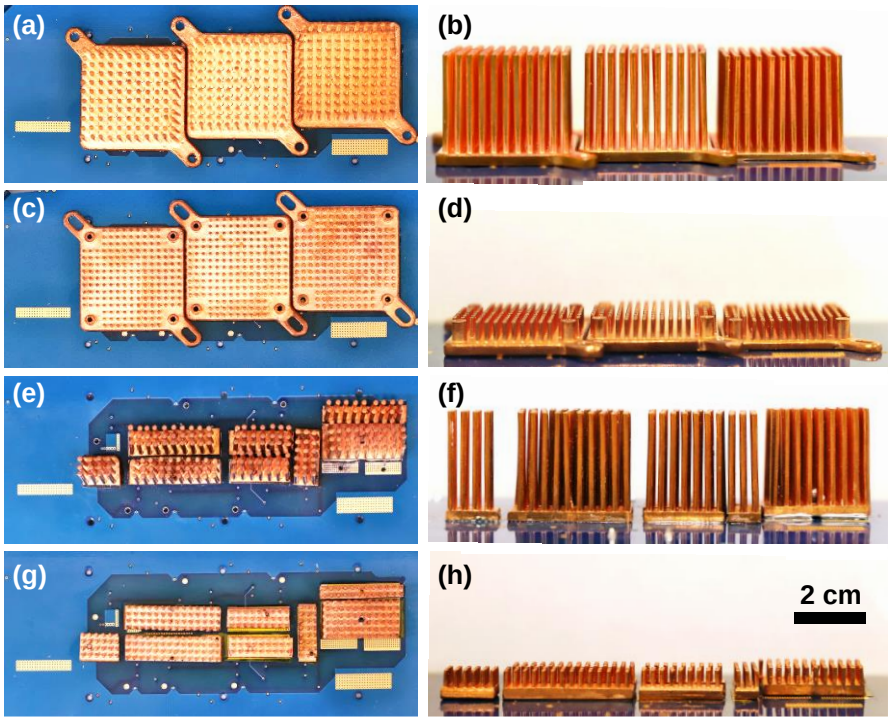

Figure 5.5. Images of the FHS and MHS arrangements. Photograph of (a) top and (b) side views of the tall FHS, (c) top and (d) side views of the short FHS, (e) top and (f) side views of the tall MHS, and (g) top and (h) side views of the short MHS. Scale bar in (h) is representative for all images.

To characterize the electro-thermal performance of the converter, an experimental testbed was developed (Fig. 5.6a). Table 5.4 lists the instruments used for the experiments and corresponding specifications and measurement uncertainties. The converter was operated at a fixed switching frequency and conversion ratio for all tests. The test section had the FCML converter (Fig. 5.1) integrated with the heat sink, with fans supplying air guided towards the heat sinks from the side through a 3D printed air duct (Fig. 5.6b). Ambient temperature room air was supplied by fans which were installed at a distance of 12 ± 2 cm to achieve an air velocity of 2 ± 0.2 m/s as measured with an anemometer (HHF-SD1, Omega). The air duct was designed and 3D printed (LulzBot TAZ 6) with polylactic acid (PLA). The air duct ensured that only the bottom side of the PCB was cooled by guiding the air to the backside of the PCB through the heat sinks. Experiments were conducted in a laboratory having room temperature of 22 ± 0.6°C and relative humidity of 45 ± 2.5%. As shown in Fig. 5.6(a), an infrared camera (FLIR A600-series) was installed to monitor the thermal profile of the converter from the backside (top down in Fig. 5.6b) during testing. The top side of the FCML converter was painted black with a thin layer (≈ 50 μm) of spray paint to ensure a high spectrally averaged emissivity (≈0.94) for IR thermal measurements. Temperature measurements were recorded using FLIR software for thermal videos at a sample rate of 1Hz.

For the short and tall FHS assemblies (Fig 5.5a-d), a thermal gad pad (BERGQUIST GAP PAD HC 3.0) was used. The short and tall MHS assemblies were tested with a thin layer (100 ± 50 μm) of thermal paste (OMEGATHERM “201”) to ensure good thermal contact between the MHSs and PCB Cu pads. Furthermore, the MHS assemblies were also tested by soldering the MHSs directly to the Cu pads. In doing so, a thin layer (~ 100 μm) of Sn42/Bi57.6/Ag0.4 solder (SMDLTLFP10, Chipquik) was applied in between the PCB and each modular heat sink area. Hot

air at 300°C from an air gun (SEEKONE 1800W) was used to melt the solder and allow it to spread in the gap while pacing the MHSs in their respective locations. Once spread, the solder joints were allowed to cool down to room temperature for permanent bonding. In addition to soldering the Cu MHS base to the Cu pad, the MHS edges were soldered using lead free solder (Kester SAC305 48) to the Cu pad for secure bonding. The metal alloy soldering paste reduced the interfacial resistance by improving the contact between the MHSs and PCB. It is important to note, the applied paste and solder goes into the hollow Cu thermal vias on the PCB, resulting in increased thermal flow paths and lower conduction and spreading resistance on the FCML PCB. In contrast, the solid gap pad used for the FHS approach has poorer compliance and flexibility, resulting in poorer heat conduction due to the trapped air in the hollow vias.

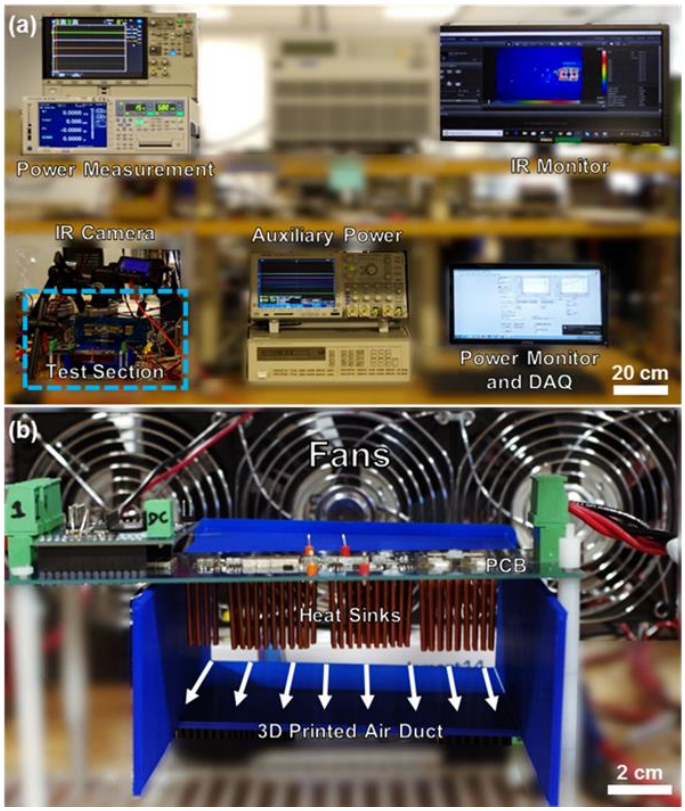

Figure 5.6. Photographs of the (a) experimental facility and (b) test section (dotted blue box in (a)). The test section consisted of fans, FCML-heat sink assembly, and 3D printed air duct (blue material) to ensure only bottom side cooling of the PCB.

Table 5.4. List of experimental sensors with measurement uncertainties for the experimental setup depicted in Fig. 5.6.

Measurement	Instrument	Range	Uncertainty
Ambient Temperature	OMEGA-HX93BDCTemp/RH Transmitter	-30°C to 75°C	±0.6°C
Relative Humidity		0 to 100%	±2.5%
Air Velocity	Hot Wire Anemometer	0.2 to 20 m/s	±5.0%
Mass	AND FX-300i	0 to 320 g	±0.001 g
Surface Temperature	FLIR T62101 Infrared Camera	-40°C to 650°C	±2°C
Input Voltage	Keysight PA2200	500 V	±0.05%
Input Current		2 A	±0.05%
Power		1 kW	±0.1%
Losses		-	±0.1%

5.5. Results and Discussion

Figure 5.7 shows the experimentally characterized efficiency (black solid line) and power loss profile (blue dotted line) of the FCML converter as a function of input power. The range tested was for low voltage testing, where the converter is current/thermally limited. The converter is rated for 10 A output current (I) due to inductor limitations, with 50 V output used for our tests. Due to this constraint the current experiment was conducted up to a power of 500W. For the full load ($2kW_e$) converter testing, a 200 V and 10 A output current were used. As observed from Fig. 5.7, the efficiency decreases with higher power/current due to higher losses at higher powers stemming from conduction (I^2R) losses, where R is the device electrical resistance. As conduction losses increase, GaN devices heat up, further increasing the switching resistance and losses.

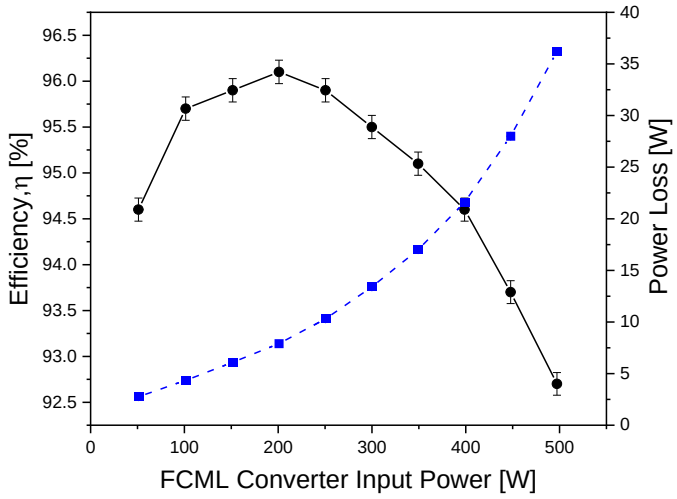

Figure 5.7. Power loss (thermal, blue dotted curve, right axis) and energy-conversion efficiency (black solid line, left axis) of the FCML converter system (Fig. 5.1) as a function of input power with soldered tall MHS. Power loss error bars (right axis) are smaller than the symbols and hence are not plotted for clarity.

Figures 5.8(a) and (b) show the experimental and simulated temperature distributions on the FCML front side (Fig 5.1a), respectively for the tall FHS assembly. The simulation geometry included the GaN devices, the multi-layer PCB, Cu vias, inductors, capacitors, and cabling connected to the electronics. The GaN devices (S_1 to S_3) shown in Fig. 5.1(a) dissipated heat, creating hot spots on the front side of the PCB, as shown in Fig. 5.8. Converter device heat dissipations were input parameters and varied in the simulations. The simulations were conducted using ANSYS Icepack commercial software with airflow modeled past the backside to determine convective losses and local heat transfer coefficients. The boundary conditions of the fluid flow domain included a uniform inlet air velocity of 2 m/s on the backside with uniform inlet temperature of 22ºC and ambient pressure outlet. The front side boundary condition was quiescent ambient air. The backside airflow cabinet size was set to be equivalent to the 3D printed flow guidance structure (13 cm x 6 cm face area).

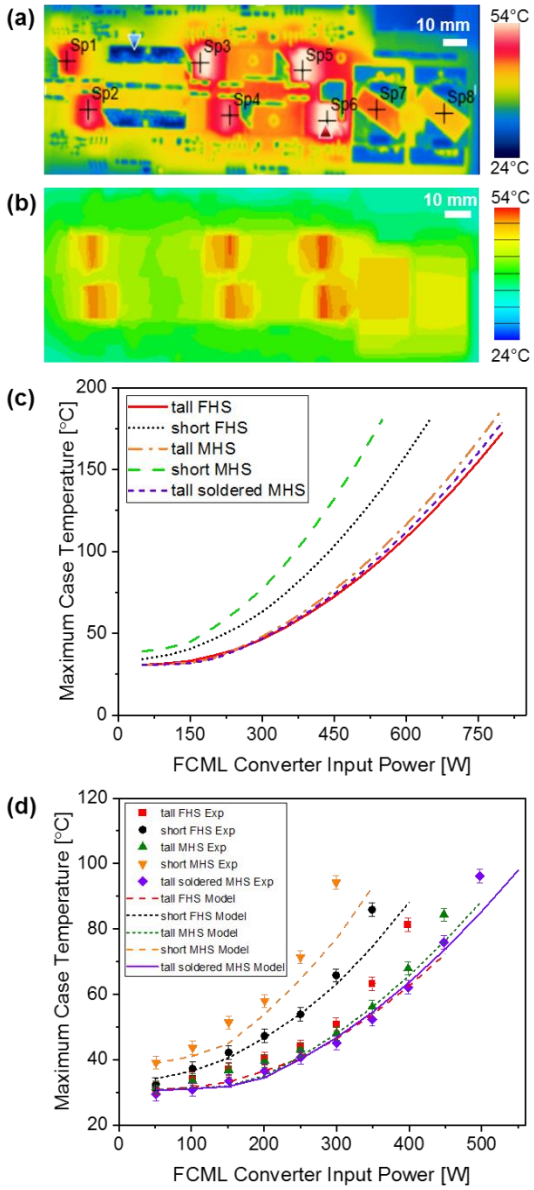

Figure 5.8. Steady-state (a) top-view IR thermal image and (b) simulated temperature contour of the FCML front side (exposed to ambient air, Fig 1a) with the tall MHS assembly mounted on the back. (c) Simulated maximum case temperatures on the FCML converter as a function of input power for different heat sink assembly configurations. (d) Comparison of the modeling results with the experimentally measured maximum converter front side local case temperature for the different heat sink arrangements as a function of FCML converter input power level. The data points were obtained using the IR images as shown in (a). Maximum temperatures were always observed to occur on the GaN switches. For the images shown in (a) and (b), gravity points into the page. The temperature error bars for the experimental data was ±2ºC stemming from the calibrated IR thermal measurement. Range of individual color band is different for simulation and experimental scale bars.

The PCB along with electronic components were imported into the software, and heatsinks with TIM were integrated based on the chosen heatsink assembly for different modeling cases. Meshing was performed in ANSYS Icepack whereby a physics-controlled hexahedral mesh was used for the fluid as well as FCML PCB domains. Through control of mesh parameters, face alignment (< 0.15) and skewness (< 0.95) of the mesh were achieved with mesh independence satisfied. Flow over the backside was modelled using a turbulent model and the enhanced two equation k-ε (k-epsilon) model, due to its better suitability for near wall and low Reynold number flows. We used the stationary solver with a relative tolerance of 0.001 for flow and 10^{-7} for energy, with temperature fields for surfaces generated. As part of the post processing, heat flows into the heatsinks and heat transfer coefficient over the heatsinks was found using the post processing tool. All heat sink arrangements were simulated in order to enable experimental comparison. The excellent agreement between simulation and experiment (Fig. 5.8c and d) demonstrated that the simulation was successful at predicting the heat spreading effects inside the FCML PCB and to the heat sinks on the backside, and could be used to determine and validate key thermal resistances and heat transfer coefficients used in the 1D thermal resistance network (Fig. 5.4). As shown in Fig. 5.8(c and d), the short MHS had the worst thermal performance (maximum GaN case temperature) for a wide range of power inputs, which stems from its highest overall thermal resistance (Table 5.3). However, the thermal resistance for the TIM or solder interface is lower than the gap pad, with a further 50% lower heat sink thermal resistance of the tall FHS, leading to a lower overall resistance (Table 5.3) and better thermal performance, as verified in Figs. 5.8(c and d).

Figure 5.8(d), shows the comparison of the modeling results with the experimentally measured (IR) FCML converter maximum local case temperature for the different heat sink

arrangements as a function of input power. Interestingly, comparison of the experimental maximum temperatures among the four heat sink arrangements (Fig. 5.5) show that the tall MHS had the best thermal performance. The short FHS and MHS reach temperatures >80°C at input power of 300 W due to smaller air side surface area and larger overall junction-to-air thermal resistance (Table 5.3). The short MHS design had the worst performance (highest temperatures) due to airside heat transfer limitations present in the short pin fin design. Although having less overall area for heat transfer when compared to the FHS, the tall MHS design showed better thermal performance than the tall FHS due to the ~6.5X smaller interfacial thermal resistance between the Cu pads and heat sinks (Table 5.3). Our experiments revealed the inability of the simulations to consider the enhancement in thermal pathway (lower thermal resistance) due to the flow of TIM or solder into Cu vias on the FCML PCB. As shown in Fig.5.9, the ability of the thermal paste (TIM or solder) to fill the 700 hollow Cu vias (individual diameter ~330 µm, and Cu thickness ~25 µm) located on the FCML PCB results in significant reduction of the effective PCB thermal resistance. The solid, less compliant, thermal gap pad used for the FHS tests cannot fill the Cu vias and hence has a poorer effective PCB thermal conductivity due to the presence of trapped air. Although this is also the case for short pin fins, the short MHS has a 71% higher air side thermal resistance when compared to the short FHS, which dominates the overall junction to air thermal resistance and hence overshadows any improvement due to conduction in the PCB. Conversely, for the tall MHS, the air side thermal resistance is only 40% higher than the FHS (Fig. 5.10), reducing the overall junction to air thermal resistance. Hence, the tall MHS showed the best performance among the four arrangements in terms of minimizing the maximum GaN case temperature. When comparing the use of thermal paste (TIM) or solder to attach the tall MHS to the PCB, soldering resulted in a lower thermal resistance with a further 8°C reduction in maximum

GaN case temperature when compared to the tall MHS attached with a commercial thermal paste (Fig. 5.8d). This is due to the fact that soldering facilitates the air tight bonding of the MHSs to the PCB owing to capillary wicking of highly wetting solder-flux combinations, eliminating possible microscale air gaps while using screws to hold the MHSs. Furthermore, the Sn42/Bi57.6/Ag0.4 solder thermal conductivity is much higher (≈ 20 to 60 W/(m·K)) than that of the thermal paste (≈ 1 W/(m·K)), resulting in lower thermal resistance and better overall performance.

Figure 10 shows that the surface averaged heat transfer coefficient values vary for different heat sink assemblies. Here, we define heat transfer coefficient as $h = q_f/(\int_{Af}[T(x) - T_\infty]dA_S)$, where q_f is the fin transfer rate and A_f is the total, including the fin tip, fin surface area. Differences in h among the assemblies stem from the different heat transfer area, amount of heat flux from the heat sink base and corresponding heat sink base temperature for the same ambient conditions. At a particular power, as the full and modular heat sink of both short and tall profiles had different surface areas for air-side heat transfer, hence h varied for each one. The minimum and maximum values of h corresponding to the full and modular heat sinks for the tall pin fins are 95 and 126 W/(m^2·K), respectively and for the short pin fins are 41 and 60 W/(m^2·K), respectively. The variation of the heat transfer coefficient among heat sink assemblies yields different overall heat sink resistances (Fig. 5.10). However, the surface averaged heat transfer coefficient for the tall and short pin-fins is estimated to be approximately 110 and 50 W/(m^2·K), respectively, in close agreement with our previous modeling assumptions based on previous experimental studies of pin-fin heat sinks (Table 5.3). Furthermore, the simulations revealed fin efficiencies approaching 90% and 98% for the tall and short fins, respectively. The simulations revealed that the tall MHS have a 40% higher surface averaged heat transfer coefficient (h) due to their shorter lateral dimensions

and thinner boundary layer development length, with a 50% lower heat transfer area (A), when compared to tall FHS.

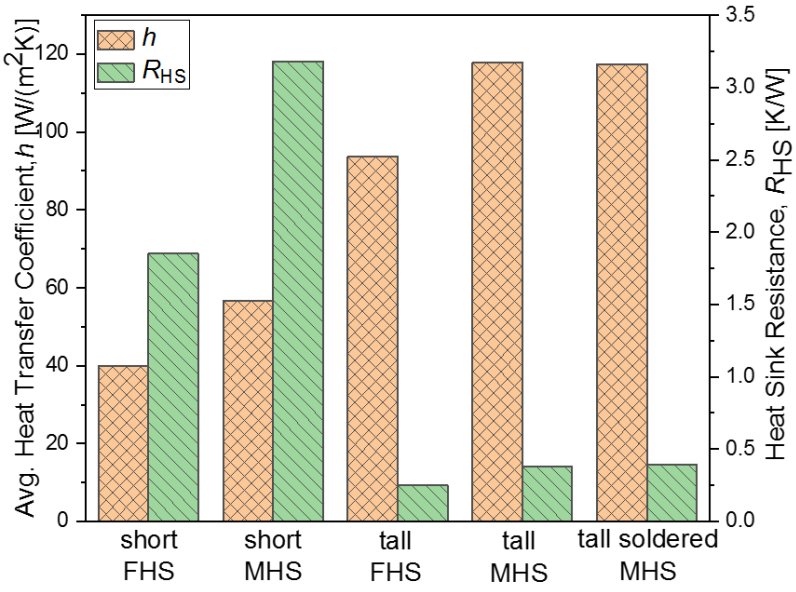

Figure 5.9. Simulated surface averaged heat transfer coefficient (h) and corresponding overall heat sink thermal resistance (R_{HS}) for different heat sink assemblies.

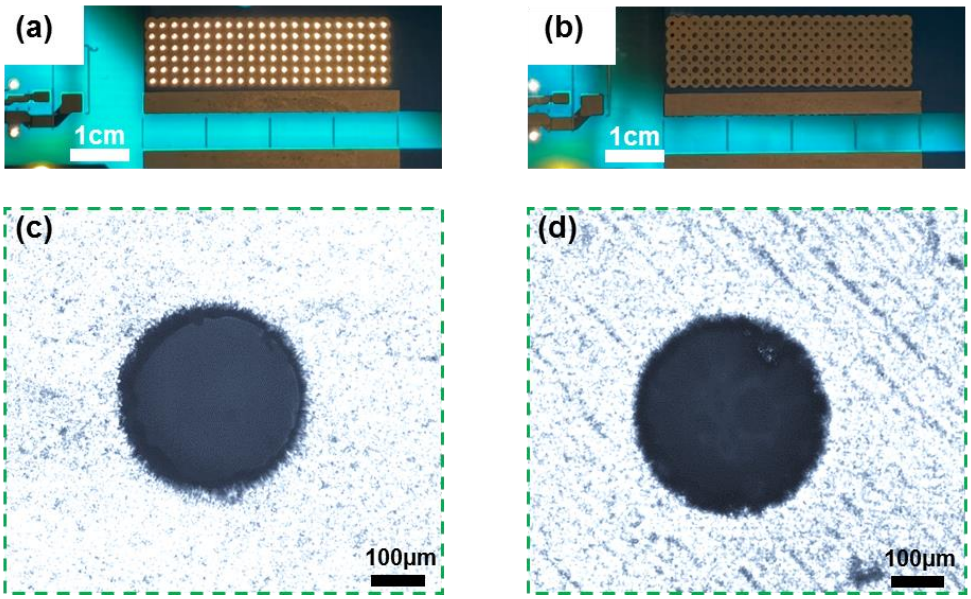

Figure 5.10. Optical images of thermal vias on the PCB (a) before and (b) after being filled with thermal paste. Microscopic images of a (c) hollow via showing the halo of light passing through it, and (d) filled via with a darker shade due to filling with thermal paste.

To estimate the effect of the differing thermal management strategies, we considered the effect of overall system level (electrical and thermal) FCML converter gravimetric and volumetric power density. For specific power calculation, the power of the converter was divided by the mass of the whole system including the components of the FCML converter and individual heat sink assembly with respective TIM. When comparing the short and tall FHS system mass, utilization of short and tall MHSs results in a mass reduction of 33% and 42%, respectfully. This mass reduction leads to specific power enhancement of the MHS FCML converter. Figure 5.11(a), shows the specific power comparison among the heat sink arrangements of the converter system. The short MHS assembly has the lowest system mass, which leads to highest specific power improvement with sub-optimal thermal performance. However, in addition to the best thermal performance, the tall MHS assembly showed a 73% specific power enhancement resulting from a 42% reduction of the system mass in comparison to the conventional tall FHS design. The observed trends were also promising when considering volumetric power density improvement. Volumetric power density variation was obtained by taking the ratio of the FCML converter power to overall system volume. Though dominated by the volume of the FCML PCB and electronics components, an overall 18% volume reduction for the tall MHS design resulted in an average 22% volumetric power density enhancement in comparison with the conventional tall FHS design. It is important to note, when computing overall volume of the FCML converter, we used maximum boxed volume of the converter, and did not consider the individual boxed volume of all components and heat sinks. This was done as it is the norm in power electronics volumetric power density benchmarking. As seen from Figure 5.11(c), when considering individual boxed volumes for the components and heat sinks, the volumetric power density for the tall MHS approach would be 175% higher than the tall FHS approach, due to mainly ~77% reduction of redundant heat sink

volume owing to modularity. Another point to note here, this sudden jump of the volumetric density resulted from the elimination of ~90% empty space volume of the maximum boxed volume case. However, modularity effect stemming from the heat sink material reduction is more definite while actual heat sinks volume is considered. As shown in Figure 5.11(c), while considering the actual volume, the tall MHS shows ~35% enhancement of the volumetric density compared to the tall FHS design, this is stemming from the ~62% reduction of heat sink material. The improvement of specific and volumetric power density was the same for the tall soldered MHS, due to the insignificant change of system mass and volume compared to tall MHS with thermal paste (TIM). Among all heat sink arrangements considered here, the tall soldered MHS showed the best overall FCML performance in terms of both specific and volumetric power density enhancement.

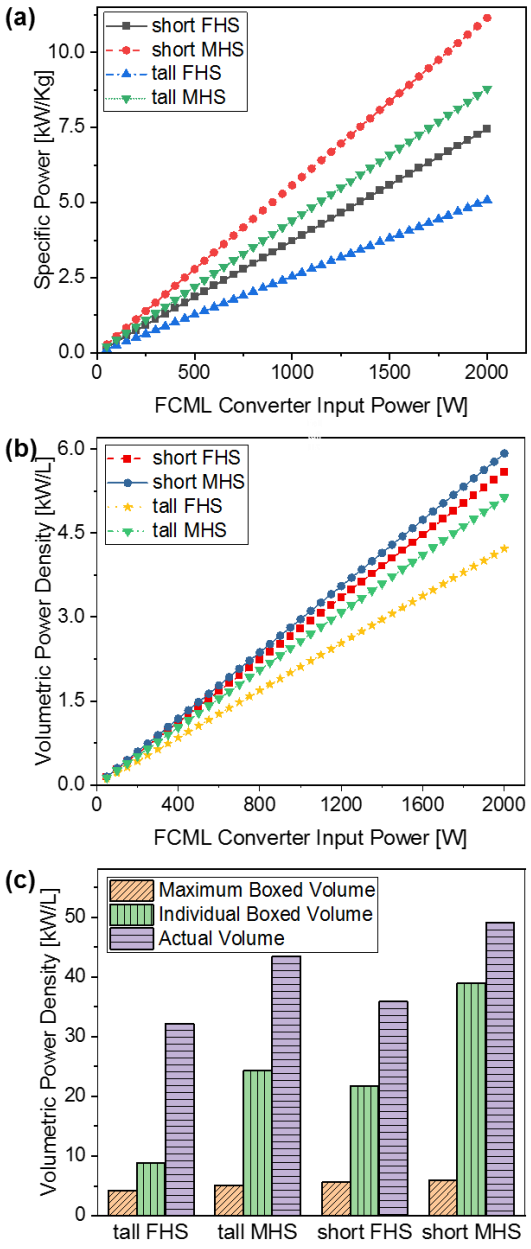

Figure 5.11. Comparison of the (a) specific and (b) volumetric power density of FCML power converter integrated with the varying thermal management approaches. (c) Comparison of the volumetric power density among different thermal management approaches while considering maximum boxed volume, individual boxed volume, and actual volume of all components of the FCML converter at the full load (2 kW_e) condition. The tall soldered MHS assembly was excluded from the plot due to its insignificant difference when compared to the tall MHS assembly (the curves can be considered identical).

5.6. Discussion

Although the current study outlines a readily available method to further enhance the power density of air-cooled power converters in addition to reducing cost due to heat sink material minimization, more work is needed. The proposed modularization technique results in higher performance at the expense of potential safety considerations. The floating of the modular heat sinks at different voltage potentials requires the development of powering protocols when considering maintenance issues related to power converter usage. The approach is naturally advantageous in environments where power converter access is not readily available to the user, and were strict protocols on usage are available. In addition, although demonstrated here for an air cooled FCML power converter, the approach has utilization for a variety of other cooling methods including dielectric fluid single phase cooling, where the fluid side heat transfer coefficients will be higher and hence weight on the interface and mounting method increasing. In addition, although demonstrated here for cooling, the developed approach can be readily integrated for multi-functional electronics component development. For example, given that the voltage potentials of each pad are different and isolated from one another, the mounted conducting heat sinks can both act as thermal management tools in addition to providing current to devices. This can eliminate the use of Cu traces in the FCML PCB, further simplifying converter layout and enhancing reliability and performance.

The proposed approach here is similar to recent work investigating modularization of heat sinks on isolated individual power devices. Although past studies have not used electrically floating heat sinks, much can be learned in terms of heat sink design using individual and modular small-scale fans to further limit pressure drop and maximize performance [328]. Furthermore, the heat sink performance results presented here are valid for the FCML power converted used in this

study, and do not represent the best design for any power converter in the literature. Our work develops the method and design methodology, rather than suggesting one particular design for any and all converters.

We show that soldered modular heat sinks yield better thermal and power density performance irrespective of the via configuration (assuming a reasonable via design). This is because the thermal resistance through the vias is not the major thermal resistance in the network (junction to air) for the designs considered in our work. Both simulations and experiments demonstrate that the thermal interface material and the air side thermal resistance dominate the heat transfer, hence the via design is insensitive assuming reasonable via implementation. In a real system, the main limitation on modular heat sink design is proximity to other areas having differing voltage potential. Though the purpose of the current study focusing on the FCML converter prototype was not to optimize vias of the Cu pad design, it leaves much to be investigated to achieve a more holistic optimization considering different via configurations, via layouts (which affect the heat sink design as well), minimization of spreading resistance in the PCB, and variable heat sink topologies (pin design, height, density). These considerations may become very important if alternate cooling fluids are used (i.e. liquid cooling) with the modular approach, which may put more emphasis on via design and spreading thermal resistance. Detailed electro-thermal co-design and optimization is required to develop these design guidelines considering loop inductances, parasitic capacitances, EMI considerations, and reliability limitations.

Furthermore, it is important to clarify here, the main advantage of using modular heat sinks may not be lower device junction temperature. The use of a full heat sink with gap pad may result in equivalent or lower junction temperature depending on board layout and heat sink selection. One of the main advantages of the modular approach developed here is that the power density can

be increased for similar thermal performance. For example, the mass of the integrated system can be reduced by 50% as the heat sink typically constitutes the heaviest component of the power converter assembly for air cooled designs. Power density and junction temperature are two interdependent variables, both of which are considered as output metrics of a particular power converter design, hence, focusing on one without considering the other may not be beneficial.

Lastly, the presence of modularization of heat sinks opens up a secondary approach not considered here to enhance air-side heat transfer. In addition to the observed lower boundary layer thickness, and enhanced developing length for modular heat sinks, the use of individual modular heat sink structures to induce secondary flow structures along the PCB opens us a new avenue of thermal-hydraulic design for the modular heat sinks considered here. Our work not only demonstrates the use of modular heat sinks as a power dense thermal management option for power converter cooling in applications, it offers insights into alternate avenues for performance improvement and multi-functional design of components for power electronics.

5.7. Conclusions

We propose, design, simulate and experimentally study modular heat sinks that are electrically floating to achieve thermal management of highly power dense power conversion systems. Thermal performance of the modular and full heat sink approaches was compared considering two different pin-fin heat sink profiles (tall and short). Using finite volume method simulations, we showed that for high power converter operation ~1kW, the converter system requires a certain fin profile to maintain GaN device temperatures within reasonable operating ranges < 175°C (junction temperature). Among the four different heat sink assemblies, the tall modular heat sink showed the best thermal performance when it was soldered to the FCML

converter PCB. The tall soldered modular heat sink reduced the maximum system temperature up to 8°C by increasing heat transfer through the PCB. Moreover, the tall modular assembly reduced the system (FCML converter and thermal management) mass by 42% and volume by 18%, resulting in a 73% higher specific power with 22% higher volumetric power density when compared to the tall full heat sink. The proposed modular heat sink design approach promises thermal performance improvement of electronics by removing the need for electrically isolating and thick thermal gap pads, and hence reduces system mass and volume through elimination of heat sink oversizing to compensate for the added gap pad thermal resistance. Our work not only demonstrates the successful integration of modular heat sinks to a prototype power converter with enhanced power density, it develops design guidelines for the performance enhancement of electronics in different mobile applications in addition to developing additional directions for multi-functional component electro-thermal co-design.

CHAPTER 6:

Additively Manufactured Hybrid Cold Plates for Efficient Thermal Management of High-Power Density Electronics

6.1 Introduction

Power electronics use different cooling approaches including natural convection air cooling [329] , forced air cooling [330], single phase liquid cooling [331-333], air [334] and liquid jet impingement [19], and solid-to-liquid phase change [303]. In last chapter, we demonstrated air cooled based thermal solution. However, many applications, especially for high-power density electronics, air cooling is not a sufficient thermal solution, instead it requires liquid cooling. A common mode of liquid cooled based thermal solution is all metal cold plate. The heat transfer performance of liquid cooled thermal solutions can be enhanced by introducing microchannels or fins. Pioneering work by Tuckerman and Pease showed the exciting promise of how microchannel heat sinks dissipate high heat fluxes [335]. The flow channel geometry can be modified to obtain trade-offs between thermal-hydraulic performance. The performance of a microchannel is very sensitive to the magnitude of its hydraulic diameter. Reducing the hydraulic diameter yields higher heat transfer performance at the expense of a non-linear increase in pressure drop [336]. A commercial off-the-shelf cold plate developed by Wieland offers good thermal solutions for high heat flux applications with the integration of high-power density Wolfspeed XM3 half-bridge SiC power module [337]. However, this all metal cold plate has limited scope to reduce system mass and improve power density for mobile applications.

In addition to that, the device reliability represents yet another design constraint for thermal management systems. Multi-chip power electronics modules can suffer from differences in device-

to-device junction temperatures, which can lead to lateral temperature gradients, increased stresses, and premature failure [338, 339]. Device-to-device junction temperature inhomogeneity where devices are used in parallel can also lead to imbalanced current sharing [340], creates the necessity for additional electronics control approaches [341]. Therefore, any successful thermal management solution should not only reduce the overall junction-to-coolant thermal resistance, but also the chip-to-chip temperature difference.

In this chapter, we demonstrate an aggressive thermal solution which is metal-polymer hybrid cold plate (HCP). We characterize the leak proof HCP design in harsh operating condition such as high-pressure fluid flow and elevated shock-vibration conditions. Compared with the commercial off-the-shelf (COTS) cold plate, our developed HCP can reduce ~40% of the system mass leading to specific power enhancement. Moreover, HCP shows comparable thermal performance to COTS cold plate. In addition, due to its design freedom, the HCP has the potential to provide inter-module isothermal profile. By integrating the lab scale experiments with the ANSYS Icepak modeling we show that the HCP provides an efficient thermal solution for high power density electronics and can enhance the system reliability by ensuring module level isothermalization.

6.2 Design

A common method to achieve high-performance cooling of multi-chip power modules is to mount the module on a liquid cooled all-metal heat sinks or cold plate as shown in Figure 6.1(a). For example, the reference design for the high-power density Wolfspeed XM3 half-bridge SiC power module family uses Microcool-series cold plates from Wieland [337]. This commercial off-the-shelf (COTS) cold plate provides good the thermal solution for high power density liquid cooled

electronics. However, COTS has limited scope to improve system's power density and reliability improvement. In portable electronics such as in mining vehicles, aviation industry, system level mass reduction can significantly reduce the operating cost, moreover, maintaining isothermal profile in electronics.

To overcome the challenges of COTS cold plate, we propose a metal-polymer coupled hybrid thermal solution. Our developed hybrid cold plate (HCP) consists of an additively manufactured (AM) fluid manifold, while has the similar heat sink design on top as of COTS for thermal conduction path (Fig. 6.1b). The interface between the top heat sink and the liquid flow manifold is fitted with a sealing gasket to ensure leak-proof performance. We employ polymer manifold manufactured using AM. The manifold was fabricated from Nylon PA12 with Selective Laser Sintering (SLS). We use PA12 as the build material as it offers the benefits of low density ($\sim$930 kg/m^3) compared to its metal counterparts ($\sim$2700 kg/m^3 for Al-6061), reasonable tensile strength ($\sim$48 MPa tensile strength) when compared to other common polymeric materials ($\sim$20 MPa for Polyethylene). AM using PA12 provides enough packing density to prevent leaks and enable high glass transition temperature (up to 163ºC), ideal for operation with a coolant at elevated temperatures ($\sim$105ºC). A simple calculation reveals that if the cold plate manifold was made from PA12 instead of Al, a reduction in cold plate mass of 70% is achievable when compared to a commercial cold plate (Wieland Microcool). This cold plate mass reduction results in an overall power module and heatsink mass reduction by 40% when compared to the COTS design.

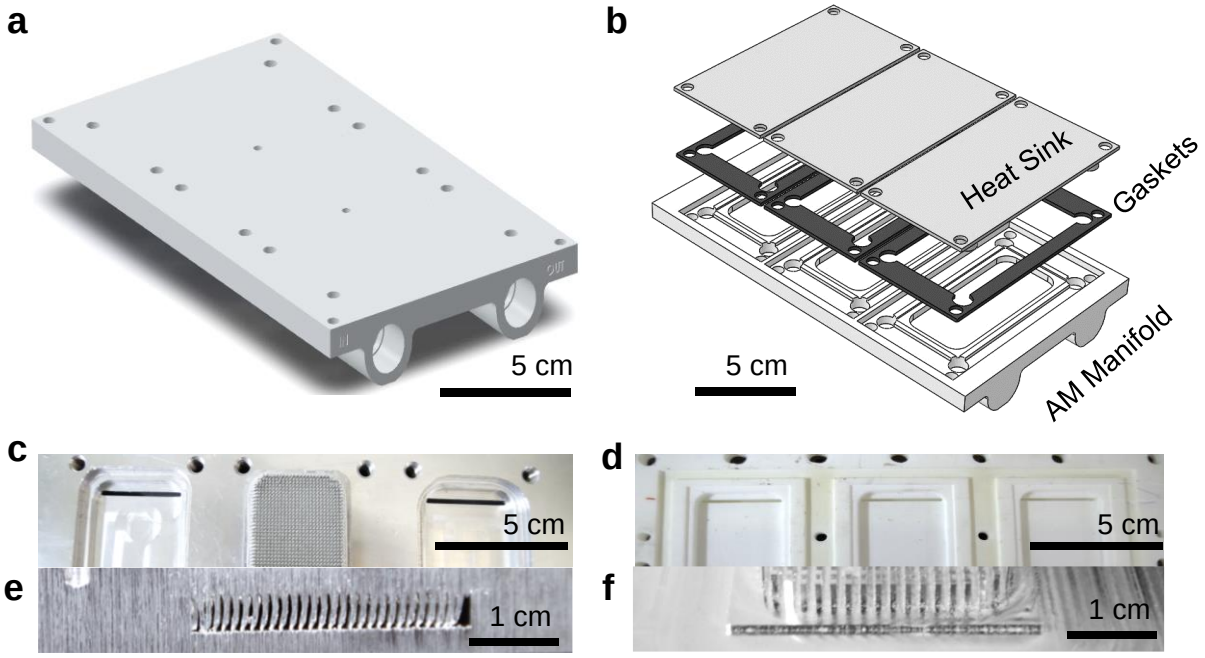

Figure 6.1. (a) Photograph of the conventional thermal management approach of an all-aluminum cold plate developed by Wieland [56]. (b) 3D exploded view of the proposed thermal management approach using a polymer additively manufactured coolant manifold, gaskets, and top heat sinks. Internal-top view of the (c) COTS cold plate, and (d) HCP, cross-sectional view of the fin section of (e) COTS cold plate, and (f) HCP.

To characterize the performance of the cold plates, a customized characterization loop was developed (Fig. 6.2a). The cooling loop consists of a chiller (Durachill 1.5HP, Polyscience), flow loop and sensors. A bypass line was designed to add flexibility to the fluid flow control (Fig. 6.2a). A magnetic flow meter (MIM, kobold) monitors the coolant flow through the loop. An absolute (PX605, Omega) and a differential pressure transducer (PXM409, Omega) monitor the absolute pressure and pressure drop in the loop. Two RTDs are installed at the inlet and outlet of the cold plate two monitor the coolant temperature. All sensors are connected to data acquisition system (CompactDAQ, National Instrument)

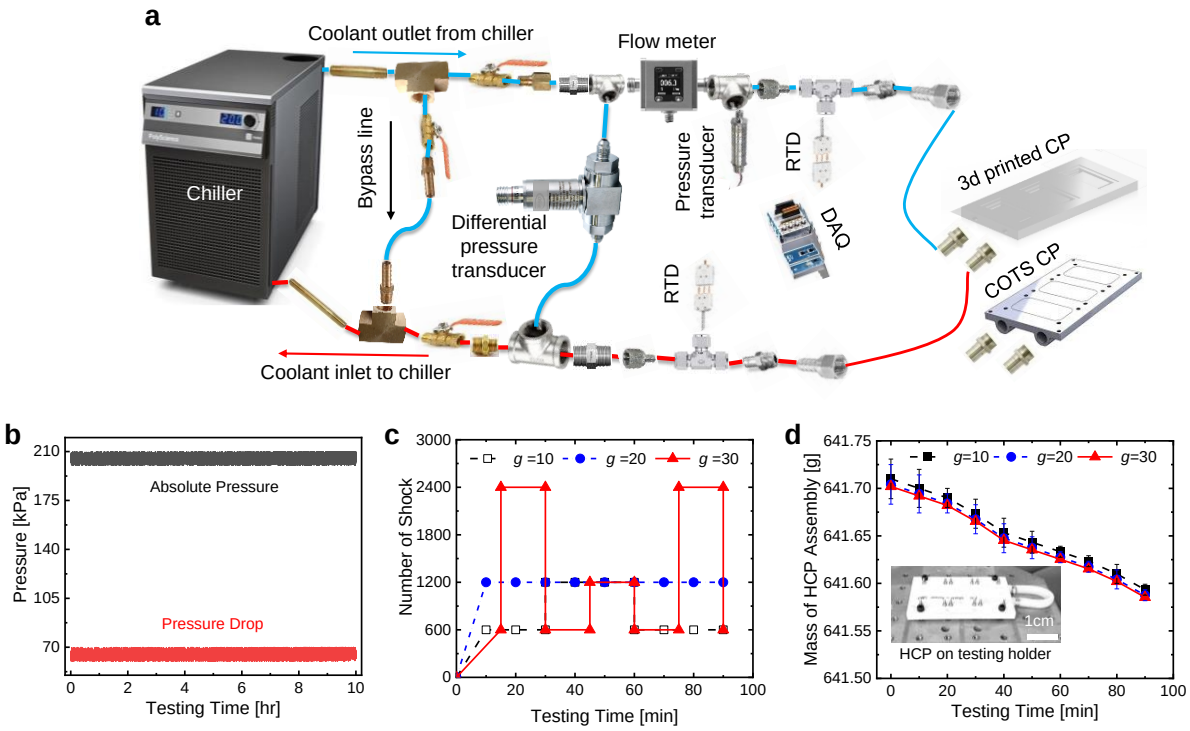

Figure 6.2. (a) Schematic (not to scale) of the experimental cooling loop for cold plate characterization. (b) Hydraulic characterization of the HCP showing leak poof design (no sudden jump in pressures). (c) Shock profile and (d) corresponding mass profile of HCP assembly (HCP-liquid) after shock test. Even under high acceleration (*g)*, the HCP assembly did not show any liquid leak, the slight change in mass comes from the polymer material loss due to the friction between the mounting screw and HCP while in operation.

For leak testing, hybrid cold plate assembly was connected to the cooling loop and water-Ethelyn glycol (WEG) mixture (50v%) was supplied at a flow rate of 16LPM. Test was continued for 10 hours, and values from both absolute and differential pressure transducers were monitored and recorded with the DAQ interfaced LabView program. During the testing period, no sudden jump in pressure was observed which depicts no leak of the coolant (Fig. 6.2b). To evaluate the compatibility of the HCP in high shock and vibration environment such as in mining vehicle or airplane, we also performed the shock testing. We selected high acceleration which are common in such elevated shock environment (Fig. 6.2c). For the shock testing, HCP assembly filled with

working fluid (WEG) is arranged as a closed loop and securely fastened to the shock testing bed (inset in Fig. 6.2d). At 10 minutes interval, HCP assembly was disconnected from the shock testing bed and mass was monitored on a sensitive mass scale (EX24001, Ohaus Explorer). Irrespective to the shock profile (Fig. 6.2c), no loss of fluid was monitored, however, there is a gradual reduction in assembly mass. This mass reduction comes from the material loss of the polymer due to the friction with fastening screw, as after each run HCP assembly was disconnected from the bed to measure the mass.

6.3 Thermal Characterization

As shown in Fig. 6.1b, there are three different fin section of the cold plate, on top of which the power modules (HT3000, Wolfspeed) are placed [342]. To emulate the power source of the module, we develop a simple alternative heating source using a copper block and heaters (Fig. 6.3a). Copper block was designed in a way so that it covers the same surface area of the devices in the module. A cylindrical hole was generated in the copper block to place cartridge heater (Fire rod, Watlow). Copper block-heater assembly was then placed on a power module without having any active devices. This is done to replicate the exact thermal resistance due to the presence of the base plates of the module. Fig. 6.3b shows the schematic of the heating arrangement. A thin layer (~100μm) of thermal paste (Arctic MX-4) is placed at the interface between the base plate-cold plate and copper block-base plate. To monitor the cold plate surface temperature, thermocouple slots were prepared on the cold plate (Fig. 6.3c). For each module location, there are two thermocouples and average of these two are taken as that module temperature. In total, three such assembly were placed on the cold plate and to ensure thermal insulation a Teflon block was designed and placed on the top (Fig. 6.3d). In real applications, modules are operated at different

power loss [342]. Here, we selected 7:1:7 ratio of losses among module 1,2, and 3 (M1:M2:M3) to emulate a standard loss distribution profile of an inverter system [342]. For thermal characterization we selected two different fluid inlet temperatures, 25ºC and 35ºC and total loss of 500W and 700 W, which was distributed among the heaters covering each module location. For controlling the thermal loss, two different heaters having 500W and 300 W power rating are used at each module location. At the middle location, due to low thermal load, one heater was used. Variable transformers (Beeleb Variac) were used to control the amount of heating from each heater for individual module location. Similar heating and controlling arrangement were maintained for COTS cold plate. As shown in Figures 6.3d and 6.3e, as the fluid flow rate increases, the maximum temperature of the cold plate is decreases due to enhanced convection heat transfer. Maximum temperature indicates the highest temperature obtained from the six thermocouples assembled on the cold plate. The farthest thermocouple from the inlet always shows the hot spot, due to the highest pressure drop at the region. Compared with the COTS cold plate, the HCP shows slightly higher temperature profile (~5°C), this is because of the less heat conduction path of the HCP due to the presence of polymer manifold.

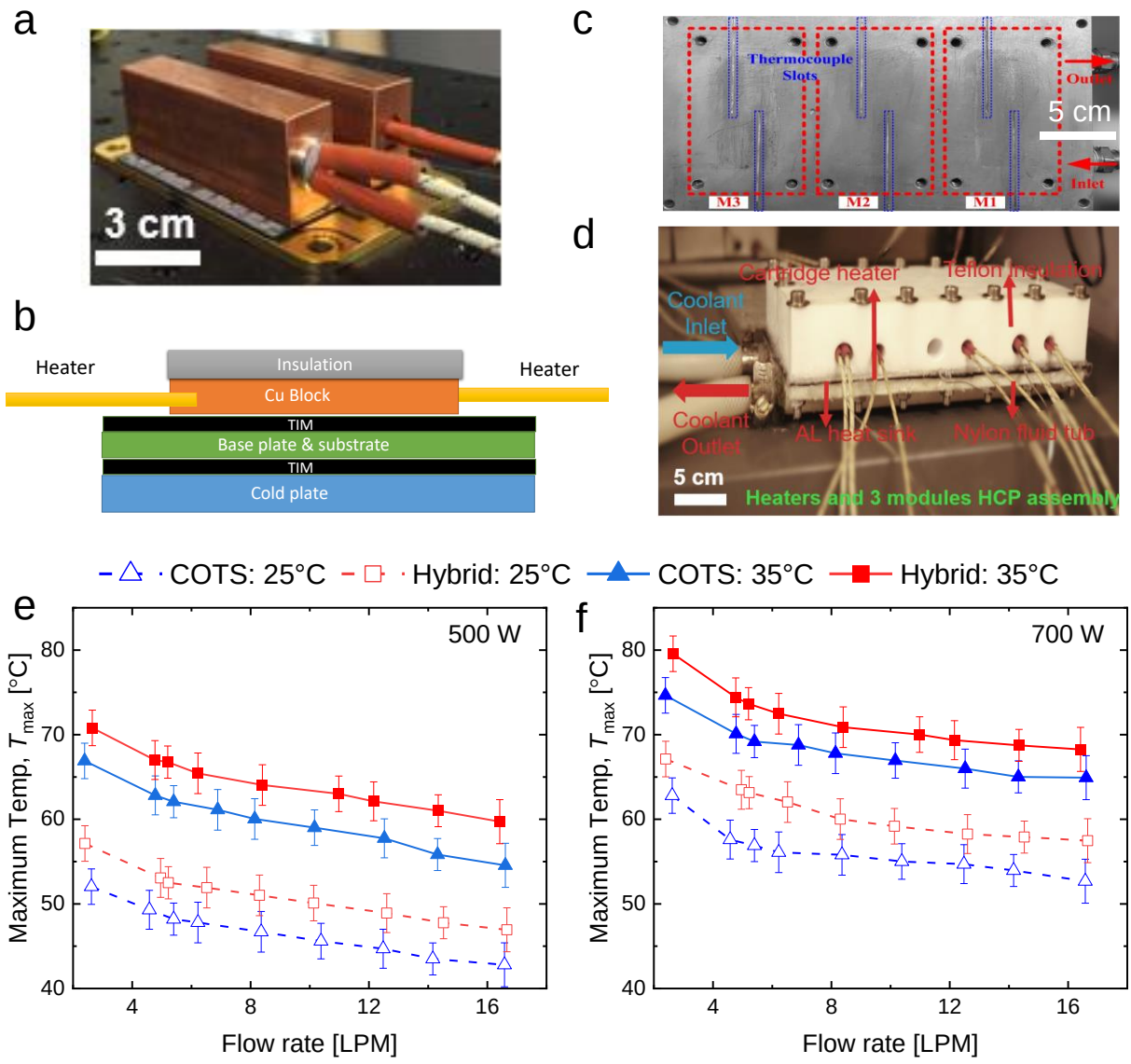

Figure 6.3. (a) Image and (b) schematic of copper-heater assembly for the cold plate at each module location. (c) Image of the thermocouple arrangement for monitoring the cold plate temperature. (D) Image of the experimental section (heating-insulating assembly). Thermal profile comparison of the HCP and COTS cold plate for total (e) 500W and (f) 700 W loss distributed among three-module locations. Legends shown on top are same for both (e) and (f).

6.4 Modeling and High-Power Applications

We also developed an ANSYS Icepak model of the cold plate assembly to predict temperature profile at different operating conditions. For modeling we assumed same 700W loss distributed as 7:1:7 ratio among M1:M2:M3. Model predicted temperatures similar trend with the experimentally measured temperature readings at same operating conditions (Fig. 6.4a). Observed slight deviation in the model is due to the difference in temperature measurement location between the model and experiments. As shown in Fig. 6.3 c, thermocouples are placed on the cold plate center and the maximum temperature is the reading of the sixth cold plate (farthest from the inlet). However, in the model, it is observed that the hot spot is not in the middle of the third module, rather it is towards the outlet flow channel (fig. 6.4b). This is because of the higher pressure drop (less coolant flow) and heat accumulation of the coolant towards to flow direction. In high density power electronics, losses from the modules are much higher. To evaluate the performance of the HCP we conducted modeling at higher thermal load. The considered power modules in this study are used in real inverter system and they are usually operated at higher efficiency (>95%) [342]. still the power loss of these inverters is in kW scale. A 6-module inverter system with 99% efficiency has a power loss ~3kW [342]. Assuming half of the loss in a three-module system we have ~1500W loss. Distributing 1500 W loss among three modules yields, 700 W loss for M1 and M3, and 100 W loss for M2 (following 7:1:7 ratio). The reason of the same thermal load for M1 and M3 is that the modules function as a pair. For a 6-module inverter system, pairs are like, M1-M2, M3-M4, M5-M6, where first module of each pair (M1,M3 and M5) operates at ~ 7X higher loss than second module of each pair (M2,M4, and M6). In real inverter cooling, the working fluid (WEG) is used from an existing cooling loop in the system, often time this fluid comes from the outlet of a secondary loop at high temperature (70ºC up to 105ºC). Here, we used WEG as working fluid at

an inlet temperature 105ºC to emulate the performance in harsh environments. Our thermal modeling and comparison with the COTS show that the HCP gives comparable but a bit higher temperature profile than the COTS (Figs. 6.4c-d),similarly as we observed in our experiments (Figs. 6.3e and 6.3f). For both cold plates, due to larger pressure drop at third module location (M3) the temperature is highest. Similarly, compared to significantly lower thermal load, M2 shows lowest temperature for both cases.

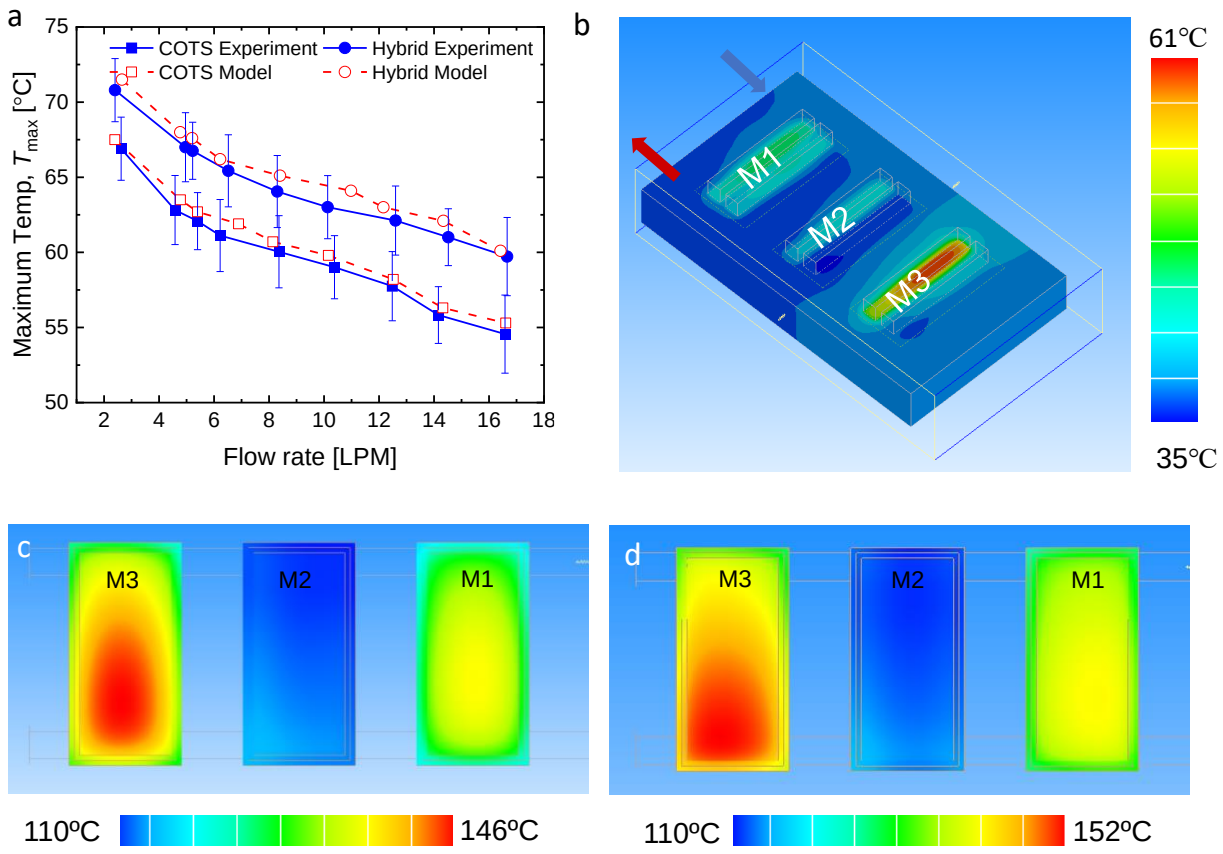

Figure 6.4. (a) Comparison of model and experimental results for COTS and hybrid cold plate. Total loss was 700W and distributed as 7:1::7 ratio among M1:M2:M3. Coolant was WEG at an inlet temperature of 35°C. (b) Ansys Icepak modeled thermal profile for a COTS cold plate for 700W total loss with 35°C coolant (WEG) flowing at 7.5LPM rate. Icepak modeled thermal profile at power application for (c) COTS cold plate, and (d) HCP. For both cases, total loss was 1500 W and distributed as 7:1::7 ratio among M1:M2:M3. Coolant was WEG at an inlet temperature of 105°C and flow rate of 7.5 LPM.

6.5. Isothermal Temperature Profile

More closer observations on the Icepack generated thermal profiles (Figs. 6.4b, 6.4c and 6.5a) reveal that even the modules (M1 and M3) are dissipating same thermal load, however, the cooling solution cannot maintain same temperature profile among them. Which leads to inter-module non-isothermal profile. Though M1 and M3 has similar losses, due to the pressure drop in the cold plate channels leads to flow imbalance among modules. As M3 is the farthest from the flow inlet, it experiences highest pressure drop, which results in lowest coolant flow at M3, thus is the hot spot. This is also true M2, even it has significantly lower thermal load compare to M3, the difference in temperature between M2 and M3 is just ~10°C. This inter-module temperature mismatch among modules can lead to the failure of devices in the module due to overheating emerging from poor thermal management. Which can drastically reduce the reliability of the systems. Generation of isothermal temperature profile can improve the system reliability. Hydraulic flow balancing is a potential route to overcome the pressure drop among modules. Standard design of the cold plates has a primary flow channel and equal sized opening for secondary flow toward each module location (Fig. 6.5b). By tuning these secondary flow openings, it is possible to make sure that hot spot (M3) gets highest flow among the three modules. This hydraulic flow balancing is challenging for COTS cold plate as it comes a single piece of metal. Whereas our HCP allows us simply tuning the AM manifold design for isothermal profile generation while keeping the other components of the assembly same. Fig. 6.5d shows isothermal temperature profile of the HCP, where maximum flow was allowed for the M3 and the opening size of the other two modules (M1 and M3) are tuned.

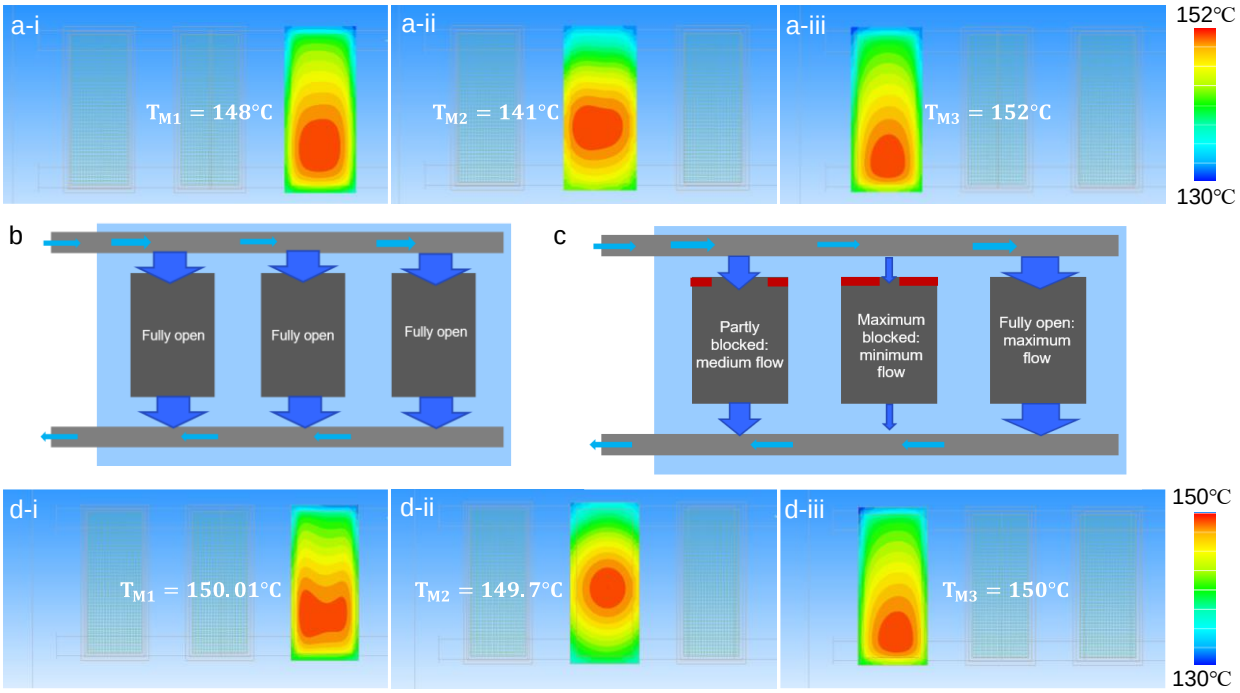

Figure. 6.5. (a-i)-(a-iii) Icepak modeled thermal profile showing different temperature at different module locations indicating non-isothermal temperature profile. (b) Standard coolant profile inside a hybrid cold plate which generates non-isothermal profile as shown in (a). (c) Hydraulically balanced flow profile for inter-module isothermalization. (d-i) –(d-iii) Icepak modeled isothermal temperature profile after implementing the flow balancing as shown in (c). Simulation was done for total loss of 1500 W loss distributed among modules as 7:1::7 (M1:M2:M3). Coolant was WEG at an inlet temperature of 105°C and flow rate of 7.5 LPM.

6.6. Conclusions

Single phase liquid cooled cold plates are a preferred for thermal management in many power dense electronics cooling applications. However, traditional cold plates offer limited scope for system level performance improvement. Here, we show how an additively manufactured (AM) polymer-metal hybrid cold plate can provide high performance cooling for power electronic converters. From experimental thermal characterization we show that HCP provides comparable thermal performance with state-of-the-art (SOA) all metal cold plates. However, HCP reduces ~40% mass of the power converter subsystem. We develop an ANSYS Icepak model to predict

the performance of HCP at high power density applications. For high power application inter-module power losses leads to the non-isothermal profile generation, which raises reliability concern of the electronics. Conventional all metal cold plates cannot offer isothermal profile in such condition due to lack of design freedom. By adapting a simple flow balancing, we show that our HCP cold plate can provide inter-module isothermal profile leading to system level reliability enhancement. Our developed HCP not only provides an aggressive light wight thermal solution for high power density electronics but also improve the lifespan of the electronics.

CHAPTER 7

Conclusion and Outlook

7.1. Scalable Hybrid surfaces

To overcome the challenges of the state off the art techniques, we demonstrated a simple, scalable and rapid stamping technique to fabricate hybrid surfaces. The technique involves using a pre-fabricated stamp, which is reusable and can be used to stamp various coated hydrophobic/superhydrophobic surfaces. The hybrid surfaces fabricated here show approximately 44X higher droplet nucleation site density enhancement. Atmospheric vapor condensation and coalescence-induced droplet jumping experiments showed that superhydrophobic hybrid surfaces possess global superhydrophobicity with local hydrophilicity, resulting in an almost 14X improvement in multi-droplet jumping compared to homogenous superhydrophobic surfaces. The hybrid surfaces fabricated here demonstrate spatially controlled heterogeneous nucleation of condensation, enhance droplet nucleation density, and a narrower droplet distribution. Our study not only presents an effective and high-throughput approach to fabricating hybrid surfaces using a facile stamping technique, but also provides insights into the interplay between the dual wettability of the hybrid functional surfaces during condensation heat transfer.

7.2. Durable Hydrophobicity for Steam Condensation

From the fundamental understanding of the coating robustness, the developed multilayer F-DLC coating shows low surface energy characteristic of non-polar polymers, with a high Young's modulus approaching that of pure metals. We demonstrate the versatility of F-DLC on a wide range of substrates including crystalline, non-crystalline and common engineering metals, all showing similar surface energy after coating. The F-DLC not only demonstrates enhanced

dropwise condensation heat transfer, but also unprecedented durability in wet environments for a period of more than three years. Characterization of the compatibility of F-DLC in elevated temperature environments exceeding 300ºC and sustainability after 5000 mechanical abrasion cycles demonstrates extreme resiliency. The outcomes of our work not only develop a low surface energy coating capable of implementation for a plethora of versatile applications, it solves the decades-old problem of generating hydrophobic surfaces that can achieve extended lifetime during exposure to harsh thermo-mechanical environments.

7.3. Durable Hydrophobicity for Low Surface Tension Liquid

Here, we rigorously demonstrate the lifespan of a variety of SLIPSs in both water and ethanol condenser applications. The majority of SLIPSs show short lifespans (<1 month) during steam condensation due to cloaking of the condensate by the infused lubricant. Among the tested samples, surfaces infused with highest viscosity lubricants (Krytox-16256) exhibited dropwise condensation for up to 45 days. During ethanol condensation, SLIPSs infused with high viscosity lubricants (K-1525, F-Y25/6, and K-16256) showed stable dropwise condensation for multiple months due to the absence of cloaking, reducing oil depletion. Similar to steam condensation, the Krytox-16256 infused SLIPS was the most durable during ethanol condensation, demonstrating stable dropwise condensation for more than 8 months. To quantify durability to elevated temperatures as encountered by superheated gases in condensers, the K-1525 and F-Y25/6 infused SLIPSs showed good durability after exposure to 150℃ air for 16 hours. The K-16256 infused surface was shown to be durable to 200℃, finally degrading at 250℃ within 1 hour. To quantify durability to immersion in a liquid, we subjected the SLIPSs to water and ethanol immersion conditions. All SLIPSs showed stable hydrophobicity even after 16 days of continual immersion. Our work presents design guidelines for the rational selection of lubricants for fabricating durable

SLIPSs having wide applicability with both steam and ethanol condensation. Our results outline future directions towards the development of next generation durable SLIPSs.

7.4. Modular Heat Sink

We propose, design, simulate and experimentally study modular heat sinks that are electrically floating to achieve thermal management of highly power dense power conversion systems. Thermal performance of the modular and full heat sink approaches was compared considering two different pin-fin heat sink profiles (tall and short). Using finite volume method simulations, we showed that for high power converter operation ~1kW, the converter system requires a certain fin profile to maintain GaN device temperatures within reasonable operating ranges < 175°C (junction temperature). Among the four different heat sink assemblies, the tall modular heat sink showed the best thermal performance when it was soldered to the FCML converter PCB. The tall soldered modular heat sink reduced the maximum system temperature up to 8°C by increasing heat transfer through the PCB. Moreover, the tall modular assembly reduced the system (FCML converter and thermal management) mass by 42% and volume by 18%, resulting in a 73% higher specific power with 22% higher volumetric power density when compared to the tall full heat sink. The proposed modular heat sink design approach promises thermal performance improvement of electronics by removing the need for electrically isolating and thick thermal gap pads, and hence reduces system mass and volume through elimination of heat sink oversizing to compensate for the added gap pad thermal resistance. Our work not only demonstrates the successful integration of modular heat sinks to a prototype power converter with enhanced power density, it develops design guidelines for the performance enhancement of electronics in different mobile applications in addition to developing additional directions for multi-functional component electro-thermal co-design.

7.5. Hybrid Cold Plate

Single phase liquid cooled cold plates are a preferred for thermal management in many power dense electronics cooling applications. However, traditional cold plates offer limited scope for system level performance improvement. Here, we show how an additively manufactured (AM) polymer-metal hybrid cold plate can provide high performance cooling for power electronic converters. From experimental thermal characterization we show that HCP provides comparable thermal performance with state-of-the-art (SOA) all metal cold plates. However, HCP reduces ~40% mass of the power converter subsystem. We develop an ANSYS Icepak model to predict the performance of HCP at high power density applications. For high power application inter-module power losses leads to the non-isothermal profile generation, which raises reliability concern of the electronics. Conventional all metal cold plates cannot offer isothermal profile in such condition due to lack of design freedom. By adapting a simple flow balancing, we show that our HCP cold plate can provide inter-module isothermal profile leading to system level reliability enhancement. Our developed HCP not only provides an aggressive light wight thermal solution for high power density electronics but also improve the lifespan of the electronics.

7.6. Societal Impact

Over the last two decades, the share of global electricity generation provided by solar photovoltaic (PV) and wind energy installations has risen from 0.2% in 2000 to 10.1% in 2021.[343] However, as much as 70% of global electrical power generation is still generated using traditional steam power cycles which use either a fossil fuel or nuclear fission to create the energy source. Therefore, increasing the overall efficiency of steam power plants has a profound impact on global energy production and the carbon footprint of developing and developed nations. Among the several strategies proposed to increase power plant efficiency, such as deploying supercritical steam

cycles[344], and optimizing power station infrastructure[243], a relatively simple, well known, and promising path is to maximize the steam condensation heat transfer inside the power cycle condenser. Doing so has been shown to result in a 2% net increase in power plant energy efficiency and reduce the levelized cost of electricity by 1.9% [243]. In 2022, this efficiency enhancement is equivalent to: an additional 700 billion kWh/year electrical power generation, 83% of the global electricity produced by solar photovoltaics, a decrease of 460 million tons of CO_2 emissions/year, and a decreased use of 2 trillion gallons of cooling water per year [240]..

A key process of the steam power cycle is the condensation of steam on metallic shell-and-tube condensers. The hydrophilicity of these metal tube surfaces results in the condensate forming a water film on the condenser surface, termed filmwise condensation, which slows thermal transport[345]. However, it has been well established for multiple decades that the filmwise condensation rate can be enhanced by modifying the condenser surface with a thin hydrophobic coating. On hydrophobic surfaces, steam condensate forms discrete droplets that easily shed due to dropwise condensation resulting in up to a 2000% enhanced condensation rate. This enhanced condensation rate translates into the potential 2% net increase in power plant energy efficiency stemming from the ability to run the condenser at a lower steam pressure, and to extract more enthalpy from the working fluid[14, 222]. Furthermore, use of hydrophobic surfaces in power plants also provides valuable corrosion and erosion protection for condenser tubing[346], increasing up-time for power plant condensers, and decreasing power plant operating expense. This research proposed robust wettability surface design and implementation in actual ssytem can make profound impact on global power production, economy, and environment.

Electrical systems are ubiquitous in today's world and it is necessary that they do not fail due to overheating. Regardless of the cause of overheating, the general and primary effect of overheating

on an electronic component is damage. Circuit systems within electronics work best at lower temperatures. Allowing systems to run for prolonged periods of time in high temperatures can decrease the longevity and reliability of devices. It is generally accepted that operating temperatures above this range reduce life expectancy: Every ten-degree rise in temperature shortens the average reliability of electrical/electronic components by 50%. So, proper thermal management of electronics is necessary to ensure its prolonged functionality and at the same time advanced thermal solution is needed to increase power density requirement, especially for mobile applications. This research shows new avenue to develop advanced thermal solutions for high power density electronics to enhanced system level power density and reliability improvement, which can provide greater impact on economy.

7.7. Outlook

This research clearly shows the benefit of hydrophobicity of the condenser surface and advanced thermal management of electronic devices to enhance performance of different energy systems. However, there is a need for proper interfacing with industrial research, applications and evaluation of performance on real systems. Robust hydrophobicity and hybrid wettability show the condensation performance improvement. Integration hybrid wettability and durable hydrophobic surfaces (F-DLC/Durable SLIPS) in real condenser prototype and operation in actual power generation environment is needed. Similarly, coupling the developed thermal solutions in real environments such as mining vehicles, electric airplane and evaluation of performance in such conditions for prolonged time is necessary. This integration can further bring new challenges and open new avenue of research for both academia and industry. In parallel, it is more important to do detailed economic analysis or develop a prediction model to evaluate the benefit of integration with real systems.

References

1. Kim, M.H. and C.W. Bullard, *Air-side performance of brazed aluminum heat exchangers under dehumidifying conditions.* International Journal of Refrigeration-Revue Internationale Du Froid, 2002. **25**(7): p. 924-934.
2. Beer, J.M., *High efficiency electric power generation: The environmental role.* Progress in Energy and Combustion Science, 2007. **33**(2): p. 107-134.
3. Peters, T.B., et al., *Design of an Integrated Loop Heat Pipe Air-Cooled Heat Exchanger for High Performance Electronics.* IEEE Transactions on Components Packaging and Manufacturing Technology, 2012. **2**(10): p. 1637-1648.
4. Cassie, A. and S. Baxter, *Wettability of porous surfaces.* Transactions of the Faraday Society, 1944. **40**: p. 546-551.
5. Wenzel, R.N., *Resistance of solid surfaces to wetting by water.* Industrial & Engineering Chemistry, 1936. **28**(8): p. 988-994.
6. Le Fevre, E.J. and J.W. Rose, *Heat-Transfer Measurements During Dropwise Condensation of Steam.* International Journal of Heat and Mass Transfer, 1964. **7**: p. 272-273.
7. Rose, J.W., *On the Mechanism of Dropwise Condensation.* International Journal of Heat and Mass Transfer, 1967. **10**: p. 755-762.
8. Attinger, D., et al., *Surface engineering for phase change heat transfer: A review.* MRS Energy & Sustainability, 2014. **1**(1): p. 1-40.
9. Boreyko, J.B. and C.H. Chen, *Self-propelled dropwise condensate on superhydrophobic surfaces.* Phys Rev Lett, 2009. **103**(18): p. 184501.
10. Enright, R., et al., *Condensation on superhydrophobic surfaces: the role of local energy barriers and structure length scale.* Langmuir, 2012. **28**(40): p. 14424-32.
11. Ma, J., et al., *Recent developments, challenges, and pathways to stable dropwise condensation: A perspective.* Applied Physics Letters, 2020. **116**(26): p. 260501.
12. Nam, Y., H. Kim, and S. Shin, *Energy and hydrodynamic analyses of coalescence-induced jumping droplets.* Applied Physics Letters, 2013. **103**(16): p. 161601.
13. Nam, Y., et al., *Droplet coalescence on water repellant surfaces.* Soft Matter, 2015. **11**(1): p. 154-60.
14. Miljkovic, N., et al., *Jumping-Droplet-Enhanced Condensation on Scalable Superhydrophobic Nanostructured Surfaces.* Nano Letters, 2013. **13**(1): p. 179-187.
15. Ryan Enright, N.M., Nicholas Dou, Youngsuk Nam, Evelyn N. Wang, *Condensation on Superhydrophobic Copper Oxide Nanostructures.* Journal of Heat Transfer, 2013. **135**(9): p. 091304-091315.
16. Hou, Y.M., et al., *Recurrent Filmwise and Dropwise Condensation on a Beetle Mimetic Surface.* Acs Nano, 2015. **9**(1): p. 71-81.
17. Bai, H., et al., *Efficient water collection on integrative bioinspired surfaces with star-shaped wettability patterns.* Adv Mater, 2014. **26**(29): p. 5025-30.
18. Choo, S., H.-J. Choi, and H. Lee, *Water-collecting behavior of nanostructured surfaces with special wettability.* Applied Surface Science, 2015. **324**: p. 563-568.
19. Gerasopoulos, K., et al., *Effects of Engineered Wettability on the Efficiency of Dew Collection.* ACS Appl Mater Interfaces, 2018. **10**(4): p. 4066-4076.

20. Liu, H., et al., *Constructing hierarchically hydrophilic/superhydrophobic ZIF-8 pattern on soy protein towards a biomimetic efficient water harvesting material.* Chemical Engineering Journal, 2019. **369**: p. 1040-1048.
21. Sharma, V., et al., *Gladiolus dalenii Based Bioinspired Structured Surface via Soft Lithography and Its Application in Water Vapor Condensation and Fog Harvesting.* ACS Sustainable Chemistry & Engineering, 2018. **6**(5): p. 6981-6993.
22. Wang, Y., et al., *A facile strategy for the fabrication of a bioinspired hydrophilic–superhydrophobic patterned surface for highly efficient fog-harvesting.* Journal of Materials Chemistry A, 2015. **3**(37): p. 18963-18969.
23. Hou, Y., et al., *Suppressing Ice Nucleation of Supercooled Condensate with Biphilic Topography.* Phys Rev Lett, 2018. **120**(7): p. 075902-6.
24. Mishchenko, L., et al., *Spatial Control of Condensation and Freezing on Superhydrophobic Surfaces with Hydrophilic Patches.* Advanced Functional Materials, 2013. **23**(36): p. 4577-4584.
25. Van Dyke, A.S., et al., *Droplet coalescence and freezing on hydrophilic, hydrophobic, and biphilic surfaces.* Applied Physics Letters, 2015. **107**(14): p. 141602-4.
26. Betz, A.R., et al., *Boiling heat transfer on superhydrophilic, superhydrophobic, and superbiphilic surfaces.* International Journal of Heat and Mass Transfer, 2013. **57**(2): p. 733-741.
27. Olceroglu, E. and M. McCarthy, *Self-Organization of Microscale Condensate for Delayed Flooding of Nanostructured Superhydrophobic Surfaces.* ACS Appl Mater Interfaces, 2016. **8**(8): p. 5729-36.
28. Shang, Y., et al., *Modeling and optimization of condensation heat transfer at biphilic interface.* International Journal of Heat and Mass Transfer, 2018. **122**: p. 117-127.
29. Shen, B., et al., *Enhanced pool boiling of ethanol on wettability-patterned surfaces.* Applied Thermal Engineering, 2019. **149**: p. 325-331.
30. Yamada, M., et al., *Enhancement of boiling heat transfer under sub-atmospheric pressures using biphilic surfaces.* International Journal of Heat and Mass Transfer, 2017. **115**: p. 753-762.
31. Yuan, J., et al., *Convective dropwise condensation heat transfer in mini-channels with biphilic surface.* International Journal of Heat and Mass Transfer, 2019. **134**: p. 69-84.
32. Cho, H.J., et al., *Nanoengineered materials for liquid–vapour phase-change heat transfer.* Nature Reviews Materials, 2016. **2**(2): p. 16092-17.
33. Miljkovic, N., et al., *Jumping-droplet-enhanced condensation on scalable superhydrophobic nanostructured surfaces.* Nano Lett, 2013. **13**(1): p. 179-87.
34. Attinger, D., et al., *Surface engineering for phase change heat transfer: A review.* MRS Energy & Sustainability, 2014. **1**(e4): p. 1-40.
35. de Gans, B.J., P.C. Duineveld, and U.S. Schubert, *Inkjet Printing of Polymers: State of the Art and Future Developments.* Advanced Materials, 2004. **16**(3): p. 203-213.
36. Zhang, L., et al., *Inkjet printing for direct micropatterning of a superhydrophobic surface: toward biomimetic fog harvesting surfaces.* Journal of Materials Chemistry A, 2015. **3**(6): p. 2844-2852.
37. Yang, Y., X. Chen, and Y. Huang, *Spreading Dynamics of Droplet Impact on a Wedge-Patterned Biphilic Surface.* Applied Sciences, 2019. **9**(11): p. 2214-15.
38. Ma, J.C., et al., *Recent developments, challenges, and pathways to stable dropwise condensation: A perspective.* Applied Physics Letters, 2020. **116**(26).

39. Ma, J., et al., *Condensation Induced Delamination of Nanoscale Hydrophobic Films.* Advanced Functional Materials, 2019. **29**(43): p. 1905222.
40. Peng, C.Y., Z.Y. Chen, and M.K. Tiwari, *All-organic superhydrophobic coatings with mechanochemical robustness and liquid impalement resistance.* Nature Materials, 2018. **17**(4): p. 355-+.
41. Wang, D., et al., *Design of robust superhydrophobic surfaces.* Nature, 2020. **582**(7810): p. 55-59.
42. Deng, X., et al., *Candle Soot as a Template for a Transparent Robust Superamphiphobic Coating.* Science, 2012. **335**(6064): p. 67-70.
43. Jay S. Golden, R.H., Janire Pascual-Gonzalez, Ben Agsten, Taylor Brennan, Lina Khan and Emily True, *Indicators of the U.S. Biobased Economy*. 2018, United States Department of Agriculture. p. 1-74.
44. Lammens, T.M., et al., *Availability of Protein-Derived Amino Acids as Feedstock for the Production of Bio-Based Chemicals.* Biomass and Bioenergy, 2012. **44**: p. 168-181.
45. Miao, X. and Q. Wu, *Biodiesel Production from Heterotrophic Microalgal Oil.* Bioresour Technol, 2006. **97**(6): p. 841-846.
46. Agonafer, D., M.S. Spector, and N. Miljkovic, *Materials and Interface Challenges in High-Vapor-Quality Two-Phase Flow Boiling Research.* IEEE Transactions on Components, Packaging and Manufacturing Technology, 2021. **11**(10): p. 1583-1591.
47. Suh, Y., et al., *A Deep Learning Perspective on Dropwise Condensation.* Adv Sci (Weinh), 2021: p. e2101794.
48. Wen, L., Y. Tian, and L. Jiang, *Bioinspired Super-Wettability from Fundamental Research t Practical Applications.* Angew Chem Int Ed Engl, 2015. **54**(11): p. 3387-3399.
49. Wu, Y., et al., *Superwettability-Based Interfacial Chemical Reactions.* Adv Mater, 2019. **31**(8): p. 1800718.
50. George B. Sigal, M.M., and George M. Whitesides, *Effect of Surface Wettability on the Adsorption of Proteins and Detergents.* Journal of the American Chemical Society 1998. **120**: p. 3464-3473.
51. Darouiche, R.O., *Device-Associated Infections: A Macroproblem that Starts with Microadherence.* Clinal Infectious Diseases, 2001. **33**: p. 1567-1572.
52. Nguyen, T.P., et al., *Quantitative Testing of Robustness on Superomniphobic Surfaces by Drop Impact.* Langmuir, 2010. **26**(23): p. 18369-18373.
53. Anish Tuteja, W.C., Minglin Ma, Joseph M. Mabry, Sarah A. Mazzella, Gregory C. Rutledge, Gareth H. McKinley, Robert E. Cohen1, *Designing Superoleophobic Surfaces.* Sceince, 2007. **318**: p. 1618-1622.
54. Kim, T.L.L.a.C.-J.C., *Turning a Surface Superrepellent Even to Completely Wetting Liquids.* Science, 2014. **346**(6213): p. 1096-1100.
55. Weisensee, P.B., et al., *Hydrophobic and Oleophobic Re-Entrant Steel Microstructures Fabricated Using Micro Electrical Discharge Machining.* Journal of Micromechanics and Microengineering, 2014. **24**(9): p. 095020.
56. Enright, R., et al., *Condensation on Superhydrophobic Surfaces: The Role of Local Energy Barriers and Structure Length Scale.* Langmuir, 2012. **28**(40): p. 14424-14432.
57. Wilke, K.L., et al., *Toward Condensation-Resistant Omniphobic Surfaces.* ACS Nano, 2018. **12**(11): p. 11013-11021.

58. Wong, T.S., et al., *Bioinspired Self-Repairing Slippery Surfaces with Pressure-Stable Omniphobicity.* Nature, 2011. **477**(7365): p. 443-447.
59. Preston, D.J., et al., *Heat Transfer Enhancement During Water and Hydrocarbon Condensation on Lubricant Infused Surfaces.* Sci Rep, 2018. **8**(1): p. 540.
60. Rykaczewski, K., et al., *Dropwise Condensation of Low Surface Tension Fluids on Omniphobic Surfaces.* Sci Rep, 2014. **4**: p. 4158.
61. Sushant Anand, A.T.P., Rajeev Dhiman, J. David Smith, and Kripa K. Varanasi, *Enhanced Condensation on Lubricant-Impregnated Nanotextured Surfaces.* Acs Nano, 2012. **6**(11): p. 10122-10129.
62. Liu, Z. and D.J. Preston, *Enhanced Condensation for Improved Energy Efficiency.* Joule, 2019. **3**(5): p. 1182-1184.
63. Erb, R. and E. Thelen, *Promoting Permanent Dropwise Condensation.* Industrial & Engineering Chemistry, 1965. **57**(10): p. 49-52.
64. Marto, P.J., et al., *Evaluation of organic coatings for the promotion of dropwise condensation of steam.* International Journal of Heat and Mass Transfer, 1986. **29**(8): p. 1109-1117.
65. Holden, K.M., et al., *The Use of Organic Coatings to Promote Dropwise Condensation of Steam.* Journal of Heat Transfer, 1987. **109**(3): p. 768-774.
66. Erb, R.A., *Dropwise condensation on gold.* Gold Bulletin, 1973. **6**(1): p. 2-6.
67. Haraguchi, T., et al., *The effect of polyvinylidene chloride coating thickness on promotion of dropwise steam condensation.* International Journal of Heat and Mass Transfer, 1991. **34**(12): p. 3047-3054.
68. Vemuri, S., et al., *Long term testing for dropwise condensation using self-assembled monolayer coatings of n-octadecyl mercaptan.* Applied Thermal Engineering, 2006. **26**(4): p. 421-429.
69. Ma, J., et al., *Ultra-Thin Self-Healing Vitrimer Coatings for Durable Hydrophobicity.* Nature Communications, 2021. **12**(1): p. 5210.
70. Ouyang, Y., et al., *Bioinspired Superhydrophobic and Oil-Infused Surface: Which is the Better Choice to Prevent Marine Biofouling?* Colloids and Surfaces A: Physicochemical and Engineering Aspects, 2018. **559**: p. 297-304.
71. Tenjimbayashi, M., et al., *In Situ Formation of Slippery-Liquid-Infused Nanofibrous Surface for a Transparent Antifouling Endoscope Lens.* ACS Biomater Sci Eng, 2018. **4**(5): p. 1871-1879.
72. Bandyopadhyay, S., et al., *High Temperature Durability of Oleoplaned Slippery Copper Surfaces.* Langmuir, 2020. **36**(15): p. 4135-4143.
73. Yu, P., et al., *Slippery Liquid Infused Porous Surfaces with Corrosion Resistance Potential on Aluminum Alloy.* RSC Advances, 2021. **11**(2): p. 847-855.
74. Goodband, S.J., et al., *Effect of Ageing on the Structure and Properties of Model Liquid-Infused Surfaces.* Langmuir, 2020. **36**(13): p. 3461-3470.
75. Lee, J., et al., *Oil‐Impregnated Nanoporous Oxide Layer for Corrosion Protection with Self‐Healing.* Advanced Functional Materials, 2017. **27**(15).
76. Gurav, A.B., et al., *Highly transparent, hot water and scratch resistant, lubricant-infused slippery surfaces developed from a mechanically-weak superhydrophobic coating.* Chemical Engineering Journal, 2021. **416**: p. 127809.
77. Khodakarami, S., et al., *Scalable Corrosion-Resistant Coatings for Thermal Applications.* ACS Appl Mater Interfaces, 2021. **13**(3): p. 4519-4534.

78. Dede, E.M., S.N. Joshi, and F. Zhou, *Topology Optimization, Additive Layer Manufacturing, and Experimental Testing of an Air-Cooled Heat Sink.* Journal of Mechanical Design, 2015. **137**(11).
79. Castelan, A., et al., *3D analytical modelling of plate fin heat sink on forced convection.* Mathematics and Computers in Simulation, 2019. **158**: p. 296-307.
80. Sakanova, A., et al., *Optimization and comparison of double-layer and double-side micro-channel heat sinks with nanofluid for power electronics cooling.* Applied Thermal Engineering, 2014. **65**(1-2): p. 124-134.
81. Tong Wu, B.O., Madhu Chinthavali , Zhiqiang Wang , Suman Debnath , Steven Campbell, *Design and optimization of 3D printed air-cooled heat sinks based on genetic algorithms,* in *IEEE Transportation Electrification Conference and Expo (ITEC)*. 2017: Chicago, IL, USA.
82. Deepak Shamvedi, O.J.M., Cyril Danilenkoff, Eoghan O'Donoghue, Paul O'Leary, Ramesh Raghavendra, *3D Metal printed heat sinks with longitudinally varying lattice structure sizes using direct metal laser sintering.* Virtual and Physical Prototyping 2018. **13**(4): p. 301-310.
83. Collins, I.L., et al., *A permeable-membrane microchannel heat sink made by additive manufacturing.* International Journal of Heat and Mass Transfer, 2019. **131**: p. 1174-1183.
84. Kempers, R., et al., *Experimental characterization of a hybrid impinging microjet-microchannel heat sink fabricated using high-volume metal additive manufacturing.* International Journal of Thermofluids, 2020. **5-6**.
85. M.M. Ohadi, S.V.D., K. Choo , M. Pecht , John V. Lawler, *A comparison analysis of air, liquid, and two-phase cooling of data centers,* in *28th Annual IEEE Semiconductor Thermal Measurement and Management Symposium (SEMI-THERM)*. 2012: San Jose, CA, USA.
86. Zhao, C.Y. and T.J. Lu, *Analysis of microchannel heat sinks, for electronics cooling.* International Journal of Heat and Mass Transfer, 2002. **45**(24): p. 4857-4869.
87. Tan, H., et al., *Heat transfer improvement in microchannel heat sink by topology design and optimization for high heat flux chip cooling.* International Journal of Heat and Mass Transfer, 2019. **129**: p. 681-689.
88. Kumar, S., et al., *Study of thermal and hydraulic performance of air cooled minichannel heatsink with novel geometries.* International Communications in Heat and Mass Transfer, 2019. **103**: p. 31-42.
89. Drofenik, U., A. Stupar, and J.W. Kolar, *Analysis of Theoretical Limits of Forced-Air Cooling Using Advanced Composite Materials With High Thermal Conductivities.* IEEE Transactions on Components, Packaging and Manufacturing Technology, 2011. **1**(4): p. 528-535.
90. Sahoo, S.K., M.K. Das, and P. Rath, *Hybrid Cooling System for Electronics Equipment During Power Surge Operation.* IEEE Transactions on Components, Packaging and Manufacturing Technology, 2018. **8**(3): p. 416-426.
91. Ali, H.M., et al., *Thermal management of electronics: An experimental analysis of triangular, rectangular and circular pin-fin heat sinks for various PCMs.* International Journal of Heat and Mass Transfer, 2018. **123**: p. 272-284.

92. Sakanova, A. and K.J. Tseng, *Comparison of pin-fin and finned shape heat sink for power electronics in future aircraft.* Applied Thermal Engineering, 2018. **136**: p. 364-374.
93. Krueger, W.B. and A. Bar-Cohen, *Optimal Numerical Design of Forced Convection Heat Sinks.* IEEE Transactions on Components and Packaging Technologies, 2004. **27**(2): p. 417-425.
94. Xiaobing Luo, Wei Xiong, Ting Cheng1 and Sheng Liu, *Design and Optimization of Horizontally-located Plate Fin Heat Sink for High Power LED Street Lamps*, in *Electronic Components and Technology Conference*. 2009: San Diego, CA, USA.
95. Drofenik, U., Laimer, G. , Kolar, J. W, *Theoretical Converter Power Density Limits for Forced Convection Cooling*, in *International conference, Power electronics, intelligent motion, power quality; PCIM* 2005: Nuremberg, Germany. p. 608-619.
96. Drofenik, U., G. Laimer, and J.W. Kolar, *Pump Characteristic Based Optimization of a Direct Water Cooling System for a 10-kW/500-kHz Vienna Rectifier*. IEEE Transactions on Power Electronics, 2005. **20**(3): p. 704-714.
97. Drofenik, U., and Kolar, J.W. *Thermal Analysis of a Multi-Chip Si/SiC-Power Module for Realization of a Bridge Leg of a 10kW Vienna Rectifier*. in *Proceedings of the 25th IEEE International Telecommunications Energy Conference (INTELEC)*. 2003. Yokohama, Japan.
98. Dunford, D.G.D.W.F.M.M.E.W.E.W.G., *A review of thermal management in power converters with thermal vias*, in *2013 Twenty-Eighth Annual IEEE Applied Power Electronics Conference and Exposition (APEC)*. 2013: Long Beach, CA, USA.
99. Barthlott, W. and C. Neinhuis, *Purity of the sacred lotus, or escape from contamination in biological surfaces.* Planta, 1997. **202**(1): p. 1-8.
100. Feng, L., et al., *Super-hydrophobic surfaces: From natural to artificial.* Advanced Materials, 2002. **14**(24): p. 1857-1860.
101. Wisdom, K.M., et al., *Self-cleaning of superhydrophobic surfaces by self-propelled jumping condensate.* Proc Natl Acad Sci U S A, 2013. **110**(20): p. 7992-7.
102. Miljkovic, N., et al., *Jumping-droplet electrostatic energy harvesting.* Applied Physics Letters, 2014. **105**(1): p. 013111-5.
103. Gao, X., et al., *The Dry-Style Antifogging Properties of Mosquito Compound Eyes and Artificial Analogues Prepared by Soft Lithography.* Advanced Materials, 2007. **19**(17): p. 2213-2217.
104. Mouterde, T., et al., *Antifogging abilities of model nanotextures.* Nat Mater, 2017. **16**(6): p. 658-663.
105. Li, J., et al., *Subcooled-Water Nonstickiness of Condensate Microdrop Self-Propelling Nanosurfaces.* ACS Appl Mater Interfaces, 2015. **7**(48): p. 26391-5.
106. Xu, Q., et al., *Energy-effective frost-free coatings based on superhydrophobic aligned nanocones.* ACS Appl Mater Interfaces, 2014. **6**(12): p. 8976-80.
107. Zhang, Q., et al., *Anti-icing surfaces based on enhanced self-propelled jumping of condensed water microdroplets.* Chem Commun (Camb), 2013. **49**(40): p. 4516-8.
108. Qu, M., J. Liu, and J. He, *Fabrication of copper-based ZnO nanopencil arrays with high-efficiency dropwise condensation heat transfer performance.* RSC Advances, 2016. **6**(64): p. 59405-59409.

109. Wen, R., et al., *Hydrophobic copper nanowires for enhancing condensation heat transfer.* Nano Energy, 2017. **33**: p. 177-183.
110. Zhao, Y., et al., *Copper-Based Ultrathin Nickel Nanocone Films with High-Efficiency Dropwise Condensation Heat Transfer Performance.* ACS Appl Mater Interfaces, 2015. **7**(22): p. 11719-23.
111. Zhu, J., et al., *Clustered ribbed-nanoneedle structured copper surfaces with high-efficiency dropwise condensation heat transfer performance.* ACS Appl Mater Interfaces, 2015. **7**(20): p. 10660-5.
112. Cheng, P. and H.Y. Wu, *Mesoscale and Microscale Phase-Change Heat Transfer*. 2006. p. 461-563.
113. Beér, J.M., *High efficiency electric power generation: The environmental role.* Progress in Energy and Combustion Science, 2007. **33**(2): p. 107-134.
114. Peters, T.B., et al., *Design of an Integrated Loop Heat Pipe Air-Cooled Heat Exchanger for High Performance Electronics.* IEEE Transactions on Components, Packaging and Manufacturing Technology, 2012. **2**(10): p. 1637-1648.
115. Li, B. and R. Yao, *Urbanisation and its impact on building energy consumption and efficiency in China.* Renewable Energy, 2009. **34**(9): p. 1994-1998.
116. Man-Hoe Kim, C.W.B., *Air-side performance of brazed aluminum heat exchangers under dehumidifying conditions.* International Journal of Refrigeration, 2002. **25**: p. 924–934.
117. Pérez-Lombard, L., J. Ortiz, and C. Pout, *A review on buildings energy consumption information.* Energy and Buildings, 2008. **40**(3): p. 394-398.
118. Enright, R., et al., *How Coalescing Droplets Jump.* Acs Nano, 2014. **8**(10): p. 10352-10362.
119. Liu, F., et al., *Numerical simulations of self-propelled jumping upon drop coalescence on non-wetting surfaces.* Journal of Fluid Mechanics, 2014. **752**: p. 39-65.
120. Liu, F., et al., *Self-propelled jumping upon drop coalescence on Leidenfrost surfaces.* Journal of Fluid Mechanics, 2014. **752**: p. 22-38.
121. Nam, Y., H. Kim, and S. Shin, *Energy and hydrodynamic analyses of coalescence-induced jumping droplets.* Applied Physics Letters, 2013. **103**(16): p. 161601-5.
122. Miljkovic, N., et al., *Electric-Field-Enhanced Condensation on Superhydrophobic Nanostructured Surfaces.* Acs Nano, 2013. **7**(12): p. 11043-11054.
123. Lafuma, A. and D. Quere, *Superhydrophobic states.* Nat Mater, 2003. **2**(7): p. 457-60.
124. Liu, X. and P. Cheng, *Dropwise condensation theory revisited: Part I. Droplet nucleation radius.* International Journal of Heat and Mass Transfer, 2015. **83**: p. 833-841.
125. Varanasi, K.K. and T. Deng, *Controlling nucleation and growth of water using hybrid hydrophobic-hydrophilic surfaces*, in *2010 12th IEEE Intersociety Conference on Thermal and Thermomechanical Phenomena in Electronic Systems*. 2010. p. 1-5.
126. Varanasi, K.K., et al., *Spatial control in the heterogeneous nucleation of water.* Applied Physics Letters, 2009. **95**(9): p. 094101-3.
127. Hamilton, W.J., J.R.H. , and M.K. Seely, *Fog collection by Namid Desert beetles.* South African Journal of Science, 2003. **99**: p. 181.
128. Parker, A.R. and C.R. Lawrence, *Water capture by a desert beetle.* Nature, 2001. **414**(6859): p. 33-34.
129. Kim, S. and K.J. Kim, *Dropwise Condensation Modeling Suitable for Superhydrophobic Surfaces.* Journal of Heat Transfer, 2011. **133**(8): p. 081502-8.

130. Keum, H., et al., *Silicon micro-masonry using elastomeric stamps for three-dimensional microfabrication.* Journal of Micromechanics and Microengineering, 2012. **22**(5): p. 055018-7.
131. Kim, S., et al., *Microstructured elastomeric surfaces with reversible adhesion and examples of their use in deterministic assembly by transfer printing.* Proc Natl Acad Sci U S A, 2010. **107**(40): p. 17095-100.
132. Hoque, M.J., et al., *High-Throughput Stamping of Hybrid Functional Surfaces.* Langmuir, 2020. **36**(21): p. 5730-5744.
133. Yang, Z., et al., *A simple way to fabricate an aluminum sheet with superhydrophobic and self-cleaning properties.* Chinese Physics B, 2012. **21**(12): p. 126801-6.
134. Drelich, J., et al., *Contact angles for liquid drops at a model heterogeneous surface consisting of alternating and parallel hydrophobic hydrophilic strips.* Langmuir, 1996. **12**(7): p. 1913-1922.
135. Fan, P., et al., *Broadband High-Performance Infrared Antireflection Nanowires Facilely Grown on Ultrafast Laser Structured Cu Surface.* Nano Lett, 2015. **15**(9): p. 5988-94.
136. Jiang, X.C., T. Herricks, and Y.N. Xia, *CuO nanowires can be synthesized by heating copper substrates in air.* Nano Letters, 2002. **2**(12): p. 1333-1338.
137. Kumagai, S., et al., *On the Enhancement of Filmwise Condensation Heat Transfer by Means of the Coexistence with Dropwise Condensation Sections.* Experimental Heat Transfer, 2007. **4**(1): p. 71-82.
138. Moon-Kyung Kim, E.C.K., Junyoung Ahn , Young Seong Kim , Hyeongyun Cha , Nenad Miljkovic *Condensation Limits on Biphilic Surfaces,* in *6th Micro and Nano Flows Conference, 9-12 September 2018*. 2018: Atlanta, USA.
139. Morita, M., et al., *Macroscopic-wetting anisotropy on the line-patterned surface of fluoroalkylsilane monolayers.* Langmuir, 2005. **21**(3): p. 911-918.
140. Raj, R., et al., *Unified model for contact angle hysteresis on heterogeneous and superhydrophobic surfaces.* Langmuir, 2012. **28**(45): p. 15777-88.
141. Yan, X., et al., *Atmosphere-Mediated Superhydrophobicity of Rationally Designed Micro/Nanostructured Surfaces.* ACS Nano, 2019. **13**(4): p. 4160-4173.
142. Yao, C.W., et al., *Droplet contact angle behavior on a hybrid surface with hydrophobic and hydrophilic properties.* Applied Physics Letters, 2012. **101**(11): p. 111605-5.
143. Ru¨he, C.D.a.J.r., *Mimicking the Stenocara BeetlesDewetting of Drops from a Patterned Superhydrophobic Surface.* Langmuir, 2008. **24**: p. 6154-6158.
144. Lee, A., et al., *Water harvest via dewing.* Langmuir, 2012. **28**(27): p. 10183-91.
145. Li, J.S., et al., *Printable Superhydrophilic–Superhydrophobic Micropatterns Based on Supported Lipid Layers.* Langmuir, 2012. **28**(22): p. 8286-8291.
146. Lai, Y., et al., *In situ surface-modification-induced superhydrophobic patterns with reversible wettability and adhesion.* Adv Mater, 2013. **25**(12): p. 1682-6.
147. Hatton, B.D. and J. Aizenberg, *Writing on superhydrophobic nanopost arrays: topographic design for bottom-up assembly.* Nano Lett, 2012. **12**(9): p. 4551-7.
148. Krumpfer, J.W. and T.J. McCarthy, *Dip-coating crystallization on a superhydrophobic surface: a million mounted crystals in a 1 cm2 array.* J Am Chem Soc, 2011. **133**(15): p. 5764-6.
149. Hou, Y., et al., *Tunable Water Harvesting Surfaces Consisting of Biphilic Nanoscale Topography.* ACS Nano, 2018. **12**(11): p. 11022-11030.

150. Kumar, A. and G.M. Whitesides, *Patterned Condensation Figures as Optical Diffraction Gratings.* Science, 1994. **263**(5143): p. 60-62.
151. Ma, J., et al., *Condensation Induced Delamination of Nanoscale Hydrophobic Films.* Advanced Functional Materials, 2019. **29**(43): p. 1905222-10.
152. Wang, L. and T.J. McCarthy, *Covalently Attached Liquids: Instant Omniphobic Surfaces with Unprecedented Repellency.* Angew Chem Int Ed Engl, 2016. **55**(1): p. 244-8.
153. Boyina, K.S., et al., *Condensation frosting on meter-scale superhydrophobic and superhydrophilic heat exchangers.* International Journal of Heat and Mass Transfer, 2019. **145**: p. 118694.
154. Cha, H., et al., *Dropwise condensation on solid hydrophilic surfaces.* Sci Adv, 2020. **6**(2): p. eaax0746.
155. Zhao, H., et al., *Extreme Antiscaling Performance of Slippery Omniphobic Covalently Attached Liquids.* ACS Appl Mater Interfaces, 2020. **12**(10): p. 12054-12067.
156. Kim, M.K., et al., *Enhanced Jumping-Droplet Departure.* Langmuir, 2015. **31**(49): p. 13452-66.
157. Chavan, S., et al., *Heat Transfer through a Condensate Droplet on Hydrophobic and Nanostructured Superhydrophobic Surfaces.* Langmuir, 2016. **32**(31): p. 7774-87.
158. Weisensee, P.B., et al., *Condensate droplet size distribution on lubricant-infused surfaces.* International Journal of Heat and Mass Transfer, 2017. **109**: p. 187-199.
159. Yan, X., et al., *Droplet Jumping: Effects of Droplet Size, Surface Structure, Pinning, and Liquid Properties.* ACS Nano, 2019. **13**(2): p. 1309-1323.
160. Rykaczewski, K., J.H.J. Scott, and A.G. Fedorov, *Electron beam heating effects during environmental scanning electron microscopy imaging of water condensation on superhydrophobic surfaces.* Applied Physics Letters, 2011. **98**(9): p. 093106-3.
161. Hoque, M.J., et al., *Visualization of Droplet Nucleation on Patterned Hybrid Surfaces.* Journal of Heat Transfer, 2019. **141**(10): p. 100902-1.
162. Anderson, D.M., et al., *Using Amphiphilic Nanostructures To Enable Long-Range Ensemble Coalescence and Surface Rejuvenation in Dropwise Condensation.* Acs Nano, 2012. **6**(4): p. 3262-3268.
163. Eral, H.B., D.J.C.M. 't Mannetje, and J.M. Oh, *Contact angle hysteresis: a review of fundamentals and applications.* Colloid and Polymer Science, 2012. **291**(2): p. 247-260.
164. Alizadeh-Birjandi, E., A. Alshehri, and H.P. Kavehpour, *Condensation on Surfaces With Biphilic Topography: Experiment and Modeling.* Frontiers in Mechanical Engineering, 2019. **5**(38): p. 1-8.
165. Liu, X. and P. Cheng, *Dropwise condensation theory revisited Part II. Droplet nucleation density and condensation heat flux.* International Journal of Heat and Mass Transfer, 2015. **83**: p. 842-849.
166. Meakin, P., *Droplet deposition growth and coalescence.* Rep. Prog. Phys. , 1992. **55** p. 157-240.
167. Mu, C., et al., *Effects of surface topography of material on nucleation site density of dropwise condensation.* Chemical Engineering Science, 2008. **63**(4): p. 874-880.
168. Gunay, A.A., et al., *Steady Method for the Analysis of Evaporation Dynamics.* Langmuir, 2017. **33**(43): p. 12007-12015.
169. Chen, X., et al., *Coalescence-Induced Jumping of Multiple Condensate Droplets on Hierarchical Superhydrophobic Surfaces.* Sci Rep, 2016. **6**: p. 18649.

170. Rykaczewski, K., et al., *Multimode multidrop serial coalescence effects during condensation on hierarchical superhydrophobic surfaces.* Langmuir, 2013. **29**(3): p. 881-91.
171. Liu, J., et al., *Guided Self-Propelled Leaping of Droplets on a Micro-Anisotropic Superhydrophobic Surface.* Angew Chem Int Ed Engl, 2016. **55**(13): p. 4265-9.
172. Lv, C., et al., *Condensation and jumping relay of droplets on lotus leaf.* Applied Physics Letters, 2013. **103**(2): p. 021601-5.
173. Qu, X., et al., *Self-propelled sweeping removal of dropwise condensate.* Applied Physics Letters, 2015. **106**(22): p. 221601-4.
174. Zhang, P., et al., *Enhanced Coalescence-Induced Droplet-Jumping on Nanostructured Superhydrophobic Surfaces in the Absence of Microstructures.* ACS Appl Mater Interfaces, 2017. **9**(40): p. 35391-35403.
175. Cheng, Y., et al., *Macrotextures-induced jumping relay of condensate droplets.* Applied Physics Letters, 2019. **114**(9): p. 093704-5.
176. Kuan-Chia Chen, W.-W.W., Chien-Neng Liao, Lih-Juann Chen, K. N. Tu, *Observation of Atomic Diffusion at Twin-Modified Grain Boundaries in Copper.* SCIENCE, 2008. **321**(22): p. 1066-1069.
177. Kumar, A., et al., *Anomalous diffusion along metal/ceramic interfaces.* Nat Commun, 2018. **9**(1): p. 5251.
178. Mondal, B., et al., *Design and Fabrication of a Hybrid Superhydrophobic-Hydrophilic Surface That Exhibits Stable Dropwise Condensation.* ACS Appl Mater Interfaces, 2015. **7**(42): p. 23575-88.
179. Motezakker, A.R., et al., *Optimum ratio of hydrophobic to hydrophilic areas of biphilic surfaces in thermal fluid systems involving boiling.* International Journal of Heat and Mass Transfer, 2019. **135**: p. 164-174.
180. Zupančič, M., et al., *Enhanced pool-boiling heat transfer on laser-made hydrophobic/superhydrophilic polydimethylsiloxane-silica patterned surfaces.* Applied Thermal Engineering, 2015. **91**: p. 288-297.
181. Clark, A.T., et al., *A 54mm x 54mm -1.8Megapixel CMOS image sensor for medical imaging*, in *2008 IEEE Nuclear Science Symposium Conference Record*. 2008. p. 4540-4543.
182. Wang, K., K.W. Leong, and Y. Yang, *Expanding Nanopatterned Substrates Using Stitch Technique for Nanotopographical Modulation of Cell Behavior.* J Vis Exp, 2016. **e54840**(118): p. 1-6.
183. Park, S.H., et al., *Bioinspired superhydrophobic surfaces, fabricated through simple and scalable roll-to-roll processing.* Sci Rep, 2015. **5**: p. 15430.
184. Schleunitz, A., et al., *Hybrid working stamps for high speed roll-to-roll nanoreplication with molded sol–gel relief on a metal backbone.* Microelectronic Engineering, 2011. **88**(8): p. 2113-2116.
185. Søndergaard, R.R., M. Hösel, and F.C. Krebs, *Roll-to-Roll fabrication of large area functional organic materials.* Journal of Polymer Science Part B: Polymer Physics, 2013. **51**(1): p. 16-34.
186. Alwazzan, M., et al., *Condensation on hybrid-patterned copper tubes (I): Characterization of condensation heat transfer.* International Journal of Heat and Mass Transfer, 2017. **112**: p. 991-1004.

187. Alwazzan, M., et al., *Condensation on hybrid-patterned copper tubes (II): Visualization study of droplet dynamics.* International Journal of Heat and Mass Transfer, 2017. **112**: p. 950-958.
188. Chen, X., et al., *Nanograssed Micropyramidal Architectures for Continuous Dropwise Condensation.* Advanced Functional Materials, 2011. **21**(24): p. 4617-4623.
189. Yamada, Y., et al., *Droplet nucleation on a well-defined hydrophilic-hydrophobic surface of 10 nm order resolution.* Langmuir, 2014. **30**(48): p. 14532-7.
190. Marder, M., R.D. Deegan, and E. Sharon, *Crumpling, buckling, and cracking: Elasticity of thin sheets.* Physics Today, 2007. **60**(2): p. 33-38.
191. Molian, P.A., B. Janvrin, and A.M. Molian, *Laser Chemical-Vapor Deposition of Fluorinated Diamond Thin-Films for Solid Lubrication.* Wear, 1993. **165**(2): p. 133-140.
192. Nobili, L. and A. Guglielmini, *Thermal stability and mechanical properties of fluorinated diamond-like carbon coatings.* Surface and Coatings Technology, 2013. **219**: p. 144-150.
193. Liangliang Liu, W.T., Qingdong Ruan, Zhongcan Wub, Chao Yang, Suihan Cui,, R.K.Y.F. Zhengyong Ma, Xiubo Tian, Ruijun Wang, Zhongzhen Wub,, and P.K. Chu, *Robust and durable surperhydrophobic F-DLC coating for anti-icing in aircrafts engineering.* Surface & Coatings Technology 2020. **404**: p. 126468.
194. Grischke, M., et al., *Application-oriented modifications of deposition processes for diamond-like-carbon-based coatings.* Surface & Coatings Technology, 1995. **74-75**(1-3): p. 739-745.
195. Gilmore, R. and R. Hauert, *Control of the tribological moisture sensitivity of diamond-like carbon films by alloying with F, Ti or Si.* Thin Solid Films, 2001. **398**: p. 199-204.
196. Sullivan, J.P., T.A. Friedmann, and A.G. Baca, *Stress relaxation and thermal evolution of film properties in amorphous carbon.* Journal of Electronic Materials, 1997. **26**(9): p. 1021-1029.
197. Ferrari, A.C., et al., *Stress reduction and bond stability during thermal annealing of tetrahedral amorphous carbon.* Journal of Applied Physics, 1999. **85**(10): p. 7191-7197.
198. Hübsch, H.D.a.H., *Applying low-friction wear-resistant thin solid films by physical vapour deposition.* Philips Tech. Rev. 4, 1983/84. **41**(6): p. 186-197.
199. K. Bewilogua, C.V.C., C. Specht , J. Schroder , R. Wittorf and M. Grischke, *Effect of target material on deposition and properties of metal-containing DLC Me-DLC coatings.* Surface and Coatings Technology 2000. **132**: p. 275-283.
200. Grischke, M., et al., *Variation of the wettability of DLC-coatings by network modification using silicon and oxygen.* Diamond and Related Materials, 1998. **7**(2-5): p. 454-458.
201. K. TROJANM, G., n d H. DIMIGEN, *Network Modification of DLC Coatings to Adjust a Defined Surface.* phys. stat. sol. (a) 1994. **145**: p. 575
202. E. Dekempeneera, K.V.A., K. Vercammen, J. Meneve, . Neerinck, S. Eufinger, W. Pappaert, M. Sercu, J. Smeets, *Abrasion resistant low friction diamond-like multilayers.* Surface and Coatings Technology 2001. **142**: p. 669-673.
203. Bertran, E., et al., *Mechanical properties of nanometric structures of Si/SiC, C/SiC and C/SiN produced by PECVD.* Diamond and Related Materials, 2001. **10**(3-7): p. 1115-1120.
204. Chouquet, C., et al., *Mechanical properties of a-C:H/Si-containing a-C:H multilayered coatings grown by LF-PECVD.* Surface and Coatings Technology, 2008. **203**(5-7): p. 745-749.

205. Morath, C.J., et al., *Picosecond optical studies of amorphous diamond and diamondlike carbon: Thermal conductivity and longitudinal sound velocity.* Journal of Applied Physics, 1994. **76**(5): p. 2636-2640.
206. Ma, J., D.G. Cahill, and N. Miljkovic, *Condensation Induced Blistering as a Measurement Technique for the Adhesion Energy of Nanoscale Polymer Films.* Nano Letters, 2020. **20**(5): p. 3918-3924.
207. Han, J., et al., *Surface energy approach and AFM verification of the (CF)ntreated surface effect and its correlation with adhesion reduction in microvalves.* Journal of Micromechanics and Microengineering, 2009. **19**(8).
208. Zhou Yang, Y.-Z.W., Yi-Fan Ye, Mao-Gang Gong, Xiao-Liang Xu, *A simple way to fabricate an aluminum sheet with superhydrophobic and self-cleaning properties.* Chinese Physics B, 2012. **21**(12).
209. Hakovirta, M., et al., *Heat capacity of hydrogenated diamond-like carbon films.* Applied Physics Letters, 2000. **77**(15): p. 2340-2342.
210. Rose, J.W., *Dropwise condensation theory and experiment: a review.* Proc Instn Mech Engrs J Power and Energy, 2002. **216** p. 115-128.
211. Ma, X.-H., et al., *Condensation heat transfer enhancement in the presence of non-condensable gas using the interfacial effect of dropwise condensation.* International Journal of Heat and Mass Transfer, 2008. **51**(7-8): p. 1728-1737.
212. Rose, J.W., *Heat-transfer coefficients, Wilson plots and accuracy of thermal measurements.* Experimental Thermal and Fluid Science, 2004. **28**(2-3): p. 77-86.
213. Rose, J.W., *Dropwise Condensation 2019 Max Jakob Memorial Award Paper.* Journal of Heat Transfer, 2020. **142**(4).
214. Amir vosough, A.f., Sadegh vosough , Hasan nasr esfehani,Azam behjat and Roya naseri rad, *Improvement Power Plant Efficiency with Condenser Pressure.* International Journal of Multidisciplinary Sciences and Engineering, 2011. **2**(3): p. 38-43.
215. Bejan, A., *Fundamentals of exergy analysis, entropy generation minimization, and the generation of flow architecture.* International Journal of Energy Research, 2002. **26**(7): p. 0-43.
216. Sett, S., et al., *Transient pulse condensation.* Applied Physics Letters, 2020. **117**(9).
217. Sett, S., et al., *Stable Dropwise Condensation of Ethanol and Hexane on Rationally Designed Ultrascalable Nanostructured Lubricant-Infused Surfaces.* Nano Lett, 2019. **19**(8): p. 5287-5296.
218. Bergman, T.L., et al., *Fundamentals of heat and mass transfer*. 2011: John Wiley & Sons.
219. Petukhov, B. *An investigation of heat transfer to fluids flowing in pipes under supercritical conditions*. in *International Developments in Heat Transfer: Proceedings of the 1961-62 Heat Transfer Conference, August 28-September 1, 1961, University of Colorado, Boulder, Colorado USA, January 8-12, 1962, Continued discussions, Central Hall Lecture Theatre, Westminster, London, England*. 1963. The American Society of Mechanical Engineers.
220. Miljkovic, N., R. Enright, and E.N. Wang, *Modeling and Optimization of Superhydrophobic Condensation.* Journal of Heat Transfer, 2013. **135**(11).
221. Kim, S. and K.J. Kim, *Dropwise Condensation Modeling Suitable for Superhydrophobic Surfaces.* Journal of Heat Transfer, 2011. **133**(8).

222. Miljkovic, N., R. Enright, and E.N. Wang, *Effect of Droplet Morphology on Growth Dynamics and Heat Transfer during Condensation on Superhydrophobic Nanostructured Surfaces.* ACS Nano, 2012. **6**(2): p. 1776-1785.
223. Scharge, R.W., *A Theoretical Study of Interphase Mass Transfer*. 1953, Columbia University, New York.
224. Kim, S. and K.J. Kim, *Dropwise Condensation Modeling Suitable for Superhydrophobic Surfaces.* Journal of Heat Transfer, 2011. **133**(8): p. 081502.
225. Le Fevre, E.J. and J.W. Rose. *A Theory of Heat Transfer by Dropwise Condensation*. in *Proceedings of the Third International Heat Transfer Conference*. 1966. Chicago, IL: ASME.
226. Miljkovic, N., et al., *Jumping-droplet-enhanced condensation on scalable superhydrophobic nanostructured surfaces.* Nano letters, 2012. **13**(1): p. 179-187.
227. Adera, S., et al., *Enhanced condensation heat transfer using porous silica inverse opal coatings on copper tubes.* Sci Rep, 2021. **11**(1): p. 10675.
228. Preston, D.J., et al., *Scalable graphene coatings for enhanced condensation heat transfer.* Nano Lett, 2015. **15**(5): p. 2902-9.
229. Donnet, C. and A. Erdemir, *Tribology of diamond-like carbon films: fundamentals and applications*. 2007: Springer Science & Business Media.
230. Bhowmick, S., et al., *Friction and adhesion of fluorine containing hydrophobic hydrogenated diamond-like carbon (FH-DLC) coating against magnesium alloy AZ91.* Surface and Coatings Technology, 2015. **267**: p. 21-31.
231. Ma, J., et al., *Ultra-thin self-healing vitrimer coatings for durable hydrophobicity.* Nat Commun, 2021. **12**(1): p. 5210.
232. Ma, J., et al., *A Lipid-Inspired Highly Adhesive Interface for Durable Superhydrophobicity in Wet Environments and Stable Jumping Droplet Condensation.* ACS Nano, 2022. **In press**.
233. K.M.Holden, A.S.W., P. J. Marto, D. H. Boone, J. W. Rose, *The Use of Organic Coatings to Promote Dropwise Condensation of Steam.* Journal of Heat Transfer, 1987. **109**: p. 768-774.
234. Cao, L., et al., *Corrosion and tribocorrosion behavior of W doped DLC coating in artificial seawater.* Diamond and Related Materials, 2020. **109**.
235. Falub, C.V., et al., *A quantitative in vitro method to predict the adhesion lifetime of diamond-like carbon thin films on biomedical implants.* Acta Biomater, 2009. **5**(8): p. 3086-97.
236. Roy, M.E., et al., *Diamond-like carbon coatings enhance the hardness and resilience of bearing surfaces for use in joint arthroplasty.* Acta Biomater, 2010. **6**(4): p. 1619-24.
237. Hasebe, T., et al., *Fluorine doping into diamond-like carbon coatings inhibits protein adsorption and platelet activation.* J Biomed Mater Res A, 2007. **83**(4): p. 1192-9.
238. Liao, W.H., et al., *Concurrent improvement in biocompatibility and bioinertness of diamond-like carbon films with nitrogen doping.* J Biomed Mater Res A, 2012. **100**(11): p. 3151-6.
239. Roy, R.K. and K.R. Lee, *Biomedical applications of diamond-like carbon coatings: a review.* J Biomed Mater Res B Appl Biomater, 2007. **83**(1): p. 72-84.
240. Korellis, S., *Range and Applicability of Heat Rate Improvements*. 2014, ELECTRIC POWER RESEARCH INSTITUTE: Palo Alto, CA,USA.
241. Agency, I.E., *World Energy Outlook 2020*. 2020.

242. Karim Khalil, D.S., Taylor Farnham, Adam Paxson, Asli Ugur Katmis, Karen Gleason, Kripa K. Varanasi, *Grafted Nanofilms Promote Dropwise Condensation of Low-Surface-Tension Fluids for High-Performance Heat Exchangers.* Joule, 2019. **3**: p. 1377–1388.
243. Champlin, P.A., *Techno-Economic Evaluation of Cross-Cutting Technologies for Cost Reduction in Nuclear Power Plants*, in *Department of Nuclear Science and Engineering*. 2018, Massachusetts Institute of Technology.
244. Lafuma, A. and D. Quéré, *Slippery Pre-Suffused Surfaces.* EPL (Europhysics Letters), 2011. **96**(5): p. 56001.
245. Smith, J.D., et al., *Droplet Mobility on Lubricant-Impregnated Surfaces.* Soft Matter, 2013. **9**(6): p. 1772-1780.
246. Ge, Q., et al., *Condensation of Satellite Droplets on Lubricant-Cloaked Droplets.* ACS Appl Mater Interfaces, 2020. **12**(19): p. 22246-22255.
247. Park, K.C., et al., *Condensation on Slippery Asymmetric Bumps.* Nature, 2016. **531**(7592): p. 78-82.
248. Zhou Yang , Y.-Z.W., Yi-Fan Ye, Mao-Gang Gong and Xiao-Liang Xu., *A Simple Way to Fabricate an Aluminum Sheet with Superhydrophobic and Self-Cleaning Properties.* Chinese Physics B, 2012. **21**(12): p. 126801.
249. Sett, S., et al., *Lubricant-Infused Surfaces for Low-Surface-Tension Fluids: The Extent of Lubricant Miscibility.* ACS Appl Mater Interfaces, 2021. **13**(19): p. 23121-23133.
250. Sett, S., et al., *Lubricant-Infused Surfaces for Low-Surface-Tension Fluids: Promise versus Reality.* ACS Appl Mater Interfaces, 2017. **9**(41): p. 36400-36408.
251. Yan, X., et al., *Hierarchical Condensation.* ACS Nano, 2019. **13**(7): p. 8169-8184.
252. Harkins, W.D.F., A. Films. , *The Spreading of Liquids and the Spreading Coefficient* J. Am. Chem. Soc., 1922. **44**: p. 2665-2685.
253. Günay, A.A., et al., *Cloaking Dynamics on Lubricant‐Infused Surfaces.* Advanced Materials Interfaces, 2020. **7**(19): p. 2000983.
254. Preston, D.J., et al., *Design of Lubricant Infused Surfaces.* ACS Appl Mater Interfaces, 2017. **9**(48): p. 42383-42392.
255. Adera, S., et al., *Depletion of Lubricant from Nanostructured Oil-Infused Surfaces by Pendant Condensate Droplets.* ACS Nano, 2020. **14**(7): p. 8024-8035.
256. Kreder, M.J., et al., *Film Dynamics and Lubricant Depletion by Droplets Moving on Lubricated Surfaces.* Physical Review X, 2018. **8**(3): p. 031053.
257. Junyoung Lee, S.S., and Nenad Miljkovic, *Opto-Hydrodynamic Characterization of Lubricant Infused Surfaces Degradation*. 2022.
258. Sett, S., et al., *Transient pulse condensation.* Applied Physics Letters, 2020. **117**(9): p. 091602.
259. Yau, K.K., J.R. Cooper, and J.W. Rose, *Effect of Fin Spacing on the Performance of Horizontal Integral-Fin Condenser Tubes.* Journal of Heat Transfer-Transactions of the Asme, 1985. **107**(2): p. 377-383.
260. Spencer, E., *Specifying Steam Surface Condensers*. Graham Mfg.Co., Inc.: Great Neck, Long Island, N.Y.
261. Silver, R.S., *An Approach to a General Theory of Surface Condensers.* Proc Instn Mech Engrs, 1963. **178**(14): p. 339-357.
262. Faghri, A., *Heat Pipe Science and Technology*. 2016: Global Digital Press.
263. Saunders, E.A.D., *Heat Exchanges: Selection, Design and Construction*. 1988: New York: Longman Scientific and Technical.

264. Zhang, J., et al., *Evaporation-induced transition from Nepenthes pitcher-inspired slippery surfaces to lotus leaf-inspired superoleophobic surfaces.* Langmuir, 2014. **30**(47): p. 14292-9.
265. Li, L., et al., *Fabrication Optimization of Ultra-Scalable Nanostructured Aluminum-Alloy Surfaces.* ACS Appl Mater Interfaces, 2021. **13**(36): p. 43489-43504.
266. Armstrong Fluid Handling, I., *Understanding and Solving Equipment Stall*. 2021.
267. Park, K.-J., T. Seo, and D. Jung, *Performance of alternative refrigerants for residential air-conditioning applications.* Applied energy, 2007. **84**(10): p. 985-991.
268. Cavallini, A., et al., *Condensation inside and outside smooth and enhanced tubes—a review of recent research.* International Journal of Refrigeration, 2003. **26**(4): p. 373-392.
269. Allen, D.T. and D.R. Shonnard, *Green engineering: environmentally conscious design of chemical processes*. 2001: Pearson Education.
270. Koppejan, J. and S. Van Loo, *The handbook of biomass combustion and co-firing*. 2012: Routledge.
271. Sun, D.-W. and L. Zheng, *Vacuum cooling technology for the agri-food industry: Past, present and future.* Journal of food engineering, 2006. **77**(2): p. 203-214.
272. Khalil, K., et al., *Grafted Nanofilms Promote Dropwise Condensation of Low-Surface-Tension Fluids for High-Performance Heat Exchangers.* Joule, 2019. **3**(5): p. 1377-1388.
273. Seo, D., et al., *Brushed lubricant-impregnated surfaces (BLIS) for long-lasting high condensation heat transfer.* Sci Rep, 2020. **10**(1): p. 2959.
274. Sean H. Hoenig, M.B., Gregory Robinson, Claudia Pierce, Donald Meskers, Michael C. Ellis, and Richard W. Bonner III, *Technoeconomic Benefits of Film-Forming Amine Products Applied to Stea, Surface Condensers.* PPCHEM Journal 2021. **23**(1): p. 4-16.
275. Wexler, J.S., I. Jacobi, and H.A. Stone, *Shear-driven failure of liquid-infused surfaces.* Phys Rev Lett, 2015. **114**(16): p. 168301.
276. Liu, Y., et al., *Effect of viscosity ratio on the shear-driven failure of liquid-infused surfaces.* Physical Review Fluids, 2016. **1**(7).
277. Laney, S.K., et al., *Delayed Lubricant Depletion of Slippery Liquid Infused Porous Surfaces Using Precision Nanostructures.* Langmuir, 2021. **37**(33): p. 10071-10078.
278. Kim, P., et al., *Hierarchical or not? Effect of the length scale and hierarchy of the surface roughness on omniphobicity of lubricant-infused substrates.* Nano Lett, 2013. **13**(4): p. 1793-9.
279. Benda, V., *Power semiconductors – state of the art and future trends*, in *Proceedings of the fourth global conference on power control and optimization.* . 2011. p. 16-24
280. Vobecky, J. *Future Trends in High Power Devices* in *Proc. 27th international conference on microelectronics*. 2010.
281. Kaplar, R.J., et al., *Generation-After-Next Power Electronics: Ultrawide-bandgap devices, high-temperature packaging, and magnetic nanocomposite materials.* IEEE Power Electronics Magazine, 2017. **4**(1): p. 36-42.
282. Kassakian, J.G. and T.M. Jahns, *Evolving and Emerging Applications of Power Electronics in Systems.* IEEE Journal of Emerging and Selected Topics in Power Electronics, 2013. **1**(2): p. 47-58.
283. Biela, J., et al., *SiC versus Si—Evaluation of Potentials for Performance Improvement of Inverter and DC–DC Converter Systems by SiC Power Semiconductors.* IEEE Transactions on Industrial Electronics, 2011. **58**(7): p. 2872-2882.

284. Prasher, R., *Thermal Interface Materials: Historical Perspective, Status, and Future Directions.* Proceedings of the IEEE, 2006. **94**(8): p. 1571-1586.
285. Khattak, Z. and H.M. Ali, *Air cooled heat sink geometries subjected to forced flow: A critical review.* International Journal of Heat and Mass Transfer, 2019. **130**: p. 141-161.
286. Kwon, B., et al., *Air Jet Impingement Cooling of Electronic Devices Using Additively Manufactured Nozzles.* IEEE Transactions on Components, Packaging and Manufacturing Technology, 2019: p. 1-1.
287. Alexander Hensler, T.B., Stephan Neugebauer, Stefan Pfefferlein, *Air Cooled SiC Three Level Inverter with High Power Density for Industrial Applications*, in *PCIM Europe 2017* 2017: Nuremberg, Germany.
288. Meyer, S.C.W.Y.D., *Design and Implementation of Forced Air-cooled, 140kHz, 20kW SiC MOSFET based Vienna PFC*, in *2019 IEEE Applied Power Electronics Conference and Exposition (APEC)*. 2019, IEEE: Anaheim, CA, USA, USA
289. Kercher, D.S., et al., *Microjet cooling devices for thermal management of electronics.* IEEE Transactions on Components and Packaging Technologies, 2003. **26**(2): p. 359-366.
290. Wrzecionko, B., et al., *High-Temperature (250 °C / 500 °F) 19 000 min^{-1} BLDC Fan for Forced Air-Cooling of Advanced Automotive Power Electronics.* IEEE/ASME Transactions on Mechatronics, 2015. **20**(1): p. 37-49.
291. Matioli, R.v.E.G.K.E., *A manifold microchannel heat sink for ultra-high power density liquid-cooled converters*, in *2019 IEEE Applied Power Electronics Conference and Exposition (APEC)*. 2019, IEEE: Anaheim, CA, USA, USA.
292. Jorg, J., et al., *Direct Single Impinging Jet Cooling of a mosfet Power Electronic Module.* IEEE Transactions on Power Electronics, 2018. **33**(5): p. 4224-4237.
293. Liang, Z., *Integrated double sided cooling packaging of planar SiC power modules*, in *2015 IEEE Energy Conversion Congress and Exposition (ECCE)*. 2015, IEEE: Montreal, QC, Canada.
294. Klaus Olesen, D.R.B., Dr. Prof. Ronald Eisele, *"ShowerPower" New Cooling Concept for Automotive Applications*, in *Automotive Power Electronics*. 2006: Paris, France.
295. Campbell, J.B., et al., *Two-Phase Cooling Method Using the R134a Refrigerant to Cool Power Electronic Devices.* IEEE Transactions on Industry Applications, 2007. **43**(3): p. 648-656.
296. Mudawar, I., et al., *Two-Phase Spray Cooling of Hybrid Vehicle Electronics.* IEEE Transactions on Components and Packaging Technologies, 2009. **32**(2): p. 501-512.
297. Bostanci, H., et al., *Thermal Management of Power Inverter Modules at High Fluxes via Two-Phase Spray Cooling.* IEEE Transactions on Components, Packaging and Manufacturing Technology, 2012. **2**(9): p. 1480-1485.
298. Wang, P., P. McCluskey, and A. Bar-Cohen, *Two-Phase Liquid Cooling for Thermal Management of IGBT Power Electronic Module.* Journal of Electronic Packaging, 2013. **135**(2).
299. Oh, J., et al., *Jumping-droplet electronics hot-spot cooling.* Applied Physics Letters, 2017. **110**(12).
300. Foulkes, T., et al., *Fundamental limits of jumping droplet heat transfer.* Applied Physics Letters, 2020. **116**(9).
301. Foulkes, T., et al., *Self-assembled liquid bridge confined boiling on nanoengineered surfaces.* International Journal of Heat and Mass Transfer, 2019. **133**: p. 1154-1164.

302. Birbarah, P., et al., *Water immersion cooling of high power density electronics.* International Journal of Heat and Mass Transfer, 2020. **147**.
303. Moon, H., N. Miljkovic, and W.P. King, *High power density thermal energy storage using additively manufactured heat exchangers and phase change material.* International Journal of Heat and Mass Transfer, 2020. **153**.
304. Foulkes, T., et al., *Jumping droplets electronics cooling: Promise versus reality.* Applied Physics Letters, 2020. **116**(20).
305. Barth, C., et al., *Design, Operation and Loss Characterization of a 1 kW GaN-based 3-level Converter at Cryogenic Temperatures.* IEEE Transactions on Power Electronics, 2020: p. 1-1.
306. M. Ohadi, j.Q., *Thermal management of harsh-environment electronics*, in *Twentieth Annual IEEE Semiconductor Thermal Measurement and Management Symposium*. 2004: San Jose, CA, USA.
307. Foller Renken, R.K., *High Temperature Electronic for Future Hybrid Powertrain Applications*, in *2005 European Conference on Power Electronics and Applications*. 2005: Dresden, Germany.
308. Wrzecionko, B., D. Bortis, and J.W. Kolar, *A 120 °C Ambient Temperature Forced Air-Cooled Normally-off SiC JFET Automotive Inverter System.* IEEE Transactions on Power Electronics, 2014. **29**(5): p. 2345-2358.
309. Christen, D., M. Stojadinovic, and J. Biela, *Energy Efficient Heat Sink Design: Natural Versus Forced Convection Cooling.* IEEE Transactions on Power Electronics, 2017. **32**(11): p. 8693-8704.
310. Pua, S.W., et al., *Natural and forced convection heat transfer coefficients of various finned heat sinks for miniature electronic systems.* Proceedings of the Institution of Mechanical Engineers, Part A: Journal of Power and Energy, 2018. **233**(2): p. 249-261.
311. Blinov, A., D. Vinnikov, and T. Lehtla, *Cooling Methods for High-Power Electronic Systems.* Scientific Journal of Riga Technical University. Power and Electrical Engineering, 2011. **29**(1): p. 79-86.
312. Dang, B., et al., *Integrated Microfluidic Cooling and Interconnects for 2D and 3D Chips.* IEEE Transactions on Advanced Packaging, 2010. **33**(1): p. 79-87.
313. Koo, J.-M., et al., *Integrated Microchannel Cooling for Three-Dimensional Electronic Circuit Architectures.* Journal of Heat Transfer, 2005. **127**(1): p. 49-58.
314. Mahajan, R., C. Chia-pin, and G. Chrysler, *Cooling a Microprocessor Chip.* Proceedings of the IEEE, 2006. **94**(8): p. 1476-1486.
315. Chowdhury, I., et al., *On-chip cooling by superlattice-based thin-film thermoelectrics.* Nat Nanotechnol, 2009. **4**(4): p. 235-8.
316. Krishnan, S., et al., *Towards a Thermal Moore's Law.* IEEE Transactions on Advanced Packaging, 2007. **30**(3): p. 462-474.
317. Khan, W.A., J.R. Culham, and M.M. Yovanovich, *Optimization of Microchannel Heat Sinks Using Entropy Generation Minimization Method.* IEEE Transactions on Components and Packaging Technologies, 2009. **32**(2): p. 243-251.
318. Shah, A., et al., *A Numerical Study of the Thermal Performance of an Impingement Heat Sink—Fin Shape Optimization.* IEEE Transactions on Components and Packaging Technologies, 2004. **27**(4): p. 710-717.
319. P. Ning, G.L., F. Wang, and K. D. T. Ngo. *Selection of Heatsink and Fan for High-Temperature Power Modules under Weight Constraint* in *IEEE APEC*. 2008.

320. U. Drofenik, G.L., and J. W. Kolar. *Theoretical converter power density limits for forced convection cooling*. in *Int. PCIM Eur.Conf.* 2005.
321. Pilawa-Podgurski, N.P.T.M.R.C.N., *Electrically thin approach to switching cell design for flying capacitor multilevel converters*, in *2017 IEEE 5th Workshop on Wide Bandgap Power Devices and Applications (WiPDA)*. 2017, IEEE: Albuquerque, NM, USA. p. 411-416.
322. Kueck, C., *Power Supply Layout and Emi.* Electronics World, 2014. **120**(1935): p. 12-22.
323. Systems, G., *PCB-Thermal-Design-Guide-Enhancement-Mode-031815*, in *GaN Systems Application Note* 2016.
324. Khan, W.A., *Modeling of Fluid Flow and Heat Transfer for Optimization of Pin-Fin Heat Sinks*, in *Mechanical Engineering*. 2004, University of Waterloo: Waterloo, Ontario, Canada.
325. Jaffri, A.S.T.N.B., *Thermal analysis of perforated pin-fins heat sink under forced convection condition.* Procedia Manufacturing, 2018. **24**: p. 290-298.
326. Systems, G., *GS66508B Bottom-side cooled 650 V E-mode GaN transistor Preliminary Datasheet*.
327. Wenjing Zhang, G.F., *A Quick PCB Thermal Calculation for Power Electronic Devices with Exposed Pad Packages*, in *PCIM Asia* 2019, VDE: Shanghai, China.
328. Pilawa-Podgurski, N.P.C.K.T.M.J.S.M.A.K.G.R., *Modular Heat Sink for Chip-Scale GaN Transistors in Multilevel Converters*, in *2018 IEEE Applied Power Electronics Conference and Exposition (APEC)*. 2018: San Antonio, TX, USA.
329. Lazarov, B.S., et al., *Experimental validation of additively manufactured optimized shapes for passive cooling.* Applied Energy, 2018. **226**: p. 330-339.
330. Ho, J.Y., et al., *Convective heat transfer performance of airfoil heat sinks fabricated by selective laser melting.* International Journal of Thermal Sciences, 2017. **114**: p. 213-228.
331. Moon, H., et al., *Heat Transfer Enhancement of Single-Phase Internal Flows using Shape Optimization and Additively Manufactured Flow Structures.* International Journal of Heat and Mass Transfer, 2021. **177**.
332. Moon, H., et al., *Ultra-power-dense heat exchanger development through genetic algorithm design and additive manufacturing.* Joule, 2021. **5**(11): p. 3045-3056.
333. Kwon, B., et al., *Heat transfer enhancement of internal laminar flows using additively manufactured static mixers.* International Journal of Heat and Mass Transfer, 2019. **137**: p. 292-300.
334. Kwon, B., et al., *Air Jet Impingement Cooling of Electronic Devices Using Additively Manufactured Nozzles.* IEEE Transactions on Components, Packaging and Manufacturing Technology, 2020. **10**(2): p. 220-229.
335. Tuckerman, D.B. and R.F.W. Pease, *High-Performance Heat Sinking for Vlsi.* Electron Device Letters, 1981. **2**(5): p. 126-129.
336. Peng, X.F. and G.P. Peterson, *The Effect of Thermofluid and Geometrical Parameters on Convection of Liquids through Rectangular Microchannels.* International Journal of Heat and Mass Transfer, 1995. **38**(4): p. 755-758.
337. Al-Neama, A.F., et al., *An experimental and numerical investigation of the use of liquid flow in serpentine microchannels for microelectronics cooling.* Applied Thermal Engineering, 2017. **116**: p. 709-723.

338. Chen, Y., et al., *Investigation of heat transfer and thermal stresses of novel thermal management system integrated with vapour chamber for IGBT power module.* Thermal Science and Engineering Progress, 2019. **10**: p. 73-81.
339. Boteler, L., et al., *A System to Package Perspective on Transient Thermal Management of Electronics.* Journal of Electronic Packaging, 2020. **142**(4).
340. Rahimi, T., et al., *Unbalanced currents effect on the thermal characteristic and reliability of parallel connected power switches.* Case Studies in Thermal Engineering, 2021. **26**.
341. Carsten Nesgaard, M.A.E.A., *Optimized Load Sharing Control by means of Thermal-Reliability Management*, in *2004 35th Anna1 IEEE Power Electronics Specinlists Conference*. 2004: AacheR Germany.
342. Wu, Y., et al., *Electrothermal-Control Co-Design of an All Silicon Carbide 2×250 kW Dual Inverter for Heavy-Duty Traction Applications.* IEEE Transactions on Industry Applications, 2022. **58**(1): p. 505-516.
343. IEA, *World Energy Outlook 2021*. 2021: Paris. France.
344. Dostal, V., P. Hejzlar, and M.J. Driscoll, *The supercritical carbon dioxide power cycle: Comparison to other advanced power cycles.* Nuclear Technology, 2006. **154**(3): p. 283-301.
345. El Fil, B., G. Kini, and S. Garimella, *A review of dropwise condensation: Theory, modeling, experiments, and applications.* International Journal of Heat and Mass Transfer, 2020. **160**.
346. Khodakarami, S., et al., *Scalable Corrosion-Resistant Coatings for Thermal Applications.* Acs Applied Materials & Interfaces, 2021. **13**(3): p. 4519-4534.